Ductility analysis of aluminum alloy connections

Schellekens, Tim

Award date:
2020

Ductility Analysis of Aluminum Alloy Connections

T.J.M. (Tim) Schellekens

April 2020

Version: final

Eindhoven University of Technology

Department of the Built Environment

Master Architecture Building and Planning

Unit Structural Design

Ductility Analysis of Aluminum Alloy Connections

Master's thesis

Date: 28-04-2020

Report number: A-2018.254

Version: Final 2.0

Author: T.J.M. (Tim) Schellekens

Student number: 0789337

Email address: timschellekens_@hotmail.com

Graduation committee:	Prof.dr.ir. J. (Johan) Maljaars,	Eindhoven University of Technology (Chairman)
	Prof.ir. H.H. (Bert) Snijder,	Eindhoven University of Technology
	Ing. J.M. (Johan) van Loon,	Bayards

Preface

More than one and a half year ago, I faced a graduation topic which fulfilled both my interests; numerical analyses and experimental research. The initial plan was to fulfill this graduation project about the ductility of aluminum alloy structures in one year. However, partly due to a board year for study association KOers, this was extended to a total of just over a year and a half. Nevertheless, I think this total time can be marked as one of the most enlightening years of my total, and already long, study career, especially on a personal level.

First of all, I would like to thank my first supervisor Prof.dr.ir. J. (Johan) Maljaars for bringing me this perfect research topic and for encouraging me to do a board year. Also, thanks for motivating me during this research project and the always enthusiasm but critical view during the meetings. Additionally, many thanks to Prof.ir. H.H. (Bert) Snijder for the critical and very helpful reviews and advice. Also, many thanks to Ing. J.M. (Johan) van Loon for his practical views and advice during this research. Furthermore, a lot of thanks to the company Bayards and all the colleagues who were always willing to answer my questions and provide me with advice. Moreover, thank you for taking care of the production of the test specimens.

Additionally, I would like to thank Marc van Maris from the multi-scale lab of the Departement of Mechanical Engineering to have me in their laboratory. Also, many thanks to the people of the structures lab of our own department. Special thanks to Eric Wijen and Theo van de Loo for assisting me during the experiments.

Furthermore, special thanks to my friends Tom Leenen en Derk Bos, for proofreading my thesis. I would also thank all my colleague students of graduation floor 5, for the advisory but also the funny moments, which made this an unforgettable time.

Last, but not least, many thanks to my family, friends, and Anne Derks, who always supported and encouraged me even though I wasn't always the nicest person during the hard times in the process. Without you all, I would never have succeeded in providing this thesis.

Tim Schellekens

Liempde, April 2020.

Abstract

Ductility is an essential aspect of designing safe and reliable structures. The ductility of a structure is dependent on the geometry and the used material properties. The essential material properties regarding ductility include the ultimate strength to 0.2% proof stress ratio ($f_u/f_{0.2}$) and the strain at rupture. The ratio $f_u/f_{0.2}$ is relatively low for many heat-treated alloys. This thesis considers the influence of this ratio on the ductility at the structure level for aluminum alloys.

When welds are applied at heat-treated aluminum alloy members, the mechanical properties are affected by the heat input of welding. This affection results in degrading strength properties and is usually associated with a higher $f_u/f_{0.2}$ ratio as compared to the base material, and hence it may positively affect the ductility of a structure. On the other hand, the extent of the HAZ is relatively small as compared to the structural dimensions. Since the HAZ has lower strength than the base metal, the extent of the plastic zone may be limited, resulting in a relatively brittle performance at the structural level. Currently, proper guidelines are present in the available standards related to the decreased strength properties caused by welding. However, clear engineering and design guidelines regarding ductility performance are lacking. In this research, a literature review and an experimental study are performed to investigate the effect of welding on the ductility performance. In addition, a foundation has been created for a numerical model to easy and quickly examine the influence of welding on several aluminum alloy connections.

The outcomes of the literature study show that welding of heat-treated aluminum alloys will result in poor ductility performance when a tensile member is transversely welded. This was also shown by others for bending members with welds applied in the tensile zone. Therefore, several studies recommend avoiding transverse welds in tensile zones of members when possible. In the field of ductility of longitudinally welded members, extensive studies are still limited.

With the help of experiments, the performance of transversely welded dogbones, longitudinally welded cruciforms, and bolted joints are examined. The transversely welded dogbones are welded over the entire width of the specimens and hence containing a fully heat-affected cross-section. The longitudinally welded cruciforms containing a weld over the longitudinal axis of the member. Depending on the size of the member, the HAZ extends partially or entirely over the width of the member. A deformation capacity measure is defined for tensile members to compare the ductility of the different connections. This deformation capacity measure is analogous to the rotation capacity measure as known for bending members.

The results of the experimental tests show that transverse welds indeed resulted in a significant loss of deformation capacity for a heat-treated aluminum alloy 6082T6. Also, the longitudinally welded cruciform with a limited member width showed a relatively low deformation capacity. In both cases, the critical cross-section was fully heat-affected. For the longitudinally welded cruciform with a larger member width and hence a partly heat-affected zone, a better ductility performance is experienced. The welded cruciforms, which are dimensioned based on failure in a plate invulnerable to the heat input from welding, resulted in the best ductility performance. This plate consisted out of a cold worked aluminum alloy 5083H111 and was therefore not affected by welding. The bolted experiment results show that net section failure leads to an expected poor ductility performance. The deformation capacity values of the fully heat-affected members were in the range of this poorly engineered bolted variant. The bolted variant which failed by bearing showed the best ductility performance of all tested connections.

A numerical model is developed in order to easily and quickly investigate a large amount of different aluminum alloy connections in the future. These numerical models are based on the experiments of

the welded cruciforms and a bolt hole plate and are validated with the corresponding experimental results. The implemented material models were calibrated based on the dogbone experiment results. With the established numerical model, a good first approach is obtained of the experimental results of the welded cruciforms with failure in the Heat Affected Zone. However, more research into the fracture model and behavior is needed to improve the numerical model. This also yields for the numerical model of the welded cruciforms with failure in the non-heat treated finger plate. By these numerical models, yet not a proper approach of the experiments is obtained.

From this research, it is concluded that when a member is heat-affected over the full critical cross-section, it will result in relatively low ductility performance of the structure. This applies to both transversely welded and longitudinally welded connections. It is also concluded that the impact of the changed ratio $f_u/f_{0.2}$ was less than expected. It is experienced that the extent of the zone of changed material properties had a more significant impact on ductility performance than the material properties themselves. It is also shown that a low $f_u/f_{0.2}$ ratio did not lead to early failure by a possible inability of stress concentrations redistribution in a bolted joint suffering from bearing failure.

Since transversely welded members contain a fully heat-affected critical cross-section, it is recommended to avoid transverse welds where possible. For longitudinally welded members, it is recommended to apply a member width larger than the extent of the HAZ in order to ensure not the entire cross-section is heat-affected. In this case, a larger ductility performance will be achieved. Another recommendation is to ensure that failure will occur in a cold worked or fully annealed finger plate. Since this plate is not affected by welding and usually contains a high $f_u/f_{0.2}$ ratio, significant plastic deformation can occur before failure. For bolted connections using an aluminum alloy with a very low $f_u/f_{0.2}$ ratio, it must be guaranteed that bearing failure occurs before net section failure occurs. This is important since net section failure will result in minimal plastic deformation.

Content

List of symbols and abbreviations

Abbreviations

AA	Aluminum Alloy
CV	Coefficient of Variation
FEM	Finite Element Method
HAZ	Heat Affected Zone
HV	Hardness in Vickers
LVDT	Linear Variable Differential Transformer
RO	Ramberg Osgood

Symbols

Latin lower case:

b	width
b_{haz}	width of the Heat Affected Zone
$f_{0.2}$	0.2% proof stress
$f_{0.2,haz}$	0.2% proof stress of the Heat Affected Zone material
f_u	ultimate strength
$f_{u,haz}$	ultimate strength of the Heat Affected Zone material
f_x	adjustable stress value parameter
f_y	yield stress
l	length
n	material hardening exponent from the Ramberg Osgood relation
$\bar{n}$	hardening exponent from the power-law
t	thickness
u	displacement
$u_{0.2}$	displacement corresponding to the elastic limit strength
u_{el}	displacement corresponding to the drop below elastic limit strength
u_{max}	displacement at the point of the maximal applied load

Latin upper case:

A	cross-sectional area
A_0	original cross-section area
A_{50}	ultimate strain at rupture measured with 50 mm gauge length
$A_{5,65\sqrt{A}}$	ultimate strain at rupture measured with a gauge length corresponding to $5{,}65\sqrt{A}$
A_{60}	ultimate strain at rupture measured with 60 mm gauge length
E	modulus of elasticity
G_f	fracture energy
U_c	deformation capacity
$U_{c,s}$	stable deformation capacity

Greek lower case:

ε	strain
$\tilde{\varepsilon}$	true strain
ε_u	ultimate strain corresponding to maximal stress
ε_f	fracture strain at the onset of damage initiation
$\bar{\varepsilon}_f$	equivalent fracture strain
η	stress triaxiality
σ	stress
$\bar{\sigma}$	equivalent stress
$\tilde{\sigma}$	true stress
σ_m	mean stress

1. Introduction

Ductility is an essential aspect in the process of designing safe and reliable structures. Ductility can be defined at the material level and at the entire structure level. At the material level, ductility is related to the stress-strain relationship and the fracture toughness. At the structure level, not only the material itself is of importance but also the applied geometry, for example. This thesis considers the ductility at the structure level of statically loaded structures.

The ductility at the material level is mainly defined by the strain at rupture, defined as the ratio between the elongated length at the moment of failure and the original length in a uniaxial stress state. A high strain at rupture implies that the material can elongate to a great extent before it eventually breaks. The strain at rupture for ductile materials, like structural steels and structural aluminum alloys, as mentioned in the standards EN-1993-1-1[2] and EN-1999-1-1[3] respectively, is in the range of 1% up to 30%. For a brittle material like concrete, the strain at rupture in tension is only about 0.02%.

When examining the ductility of a structure, not only the material, but the whole structure is considered. The ductility at the structure level defines the extent to which a structure can plastically deform until it collapses. Therefore, it is also known as the deformation capacity. By large deformations of a structure, a warning mechanism is obtained, which can prevent human casualties. Besides the warning mechanism, other important benefits can be achieved using ductile structures such as increased resistance, force redistribution, and energy dissipation. Thus, by gaining insight into the ductility on both the material and the structure level, structures can be designed in a safe manner.

The ductility of structures subjected to bending is mostly defined by occurring rotations up to failure and hence expressed as the rotation capacity[14]. A significant rotation capacity and corresponding plastic deformation ensures that stress redistribution can be realized over the cross-section. If the rotation capacity is sufficient, it is allowed to calculate with a fully plastic cross-sectional resistance[3]. Generally, the rotation capacity is dependent on the cross-section dimensions of the member. Therefore, a cross-sectional classification is introduced in the standards. For the ductile classified members of the standards, it is allowed to calculate with a fully plastic cross-sectional resistance since it is assumed that enough rotation capacity is present. A low ultimate to yield strength ratio (f_u/f_y) or a small strain at rupture may have an impact on the rotation capacity. When the desired and expected rotation capacity is not present, the risk exists that the actual resistance is lower than the initially considered resistance. In previous studies of Steenbergen et al. (1996)[20], Moen et al. (1999)[16], and Van Es et al. (2018)[23] it was already mentioned that the f_u/f_y ratio significantly influences the ductility behavior of both steel and aluminum alloy structures. The results of these studies implied that the rotation capacity does, besides the geometry, also depends on the material properties. However, studies concerning aluminum alloys are limited, especially parametric studies focusing on the influence of the $f_u/f_{0.2}$ ratio on the rotation capacity are missing. This $f_u/f_{0.2}$ ratio is equivalent to the f_u/f_y ratio known for steel and is further explained in Section 2.1.

As mentioned, the ductility of a structure in bending is expressed by the rotation capacity, and it depends in turn on the ratio $f_u/f_{0.2}$. Obviously, in the tension zone of a member, the ductility depends on the strain at rupture. However, when it contains welds, bolts, or other geometry changes, another aspect must be considered in addition. In these situations, stress concentrations occur. Examples of stress concentrations are visible in Figure 1.1 and Figure 1.2 for a weld toe and the edge of a bolt hole. Structural calculations rely on the assumption that these local stress concentrations can be ignored since it is implicity assumed that plasticity can occur, and hence the internal stress redistribution can take place. However, when a very low $f_u/f_{0.2}$ ratio is present, there may be insufficient possibility for

internal redistribution of forces, which can result in early local failure. Also, the strain at rupture will influence the rate of expansion of the plastic zone. A low value of the strain at rupture can result in too small deformation required to extend the plastic zone. In summary, the rotation capacity and hence the resistance of sections in bending depends, besides the geometry, on the ratio $f_u/f_{0.2}$ and the strain at rupture. In addition, a very low ratio $f_u/f_{0.2}$ or a very low strain at rupture may result in reduced resistance and failure without warning at geometrical discontinuities as present near connections.

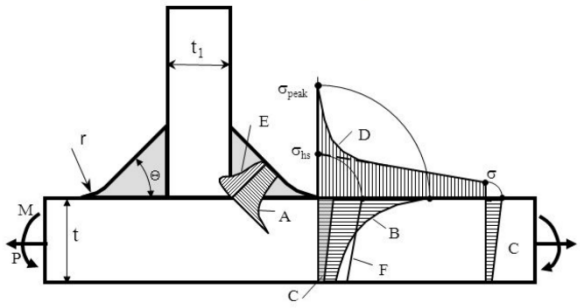

Figure 1.1: Schematization of stress distribution near a T-weldment [47].

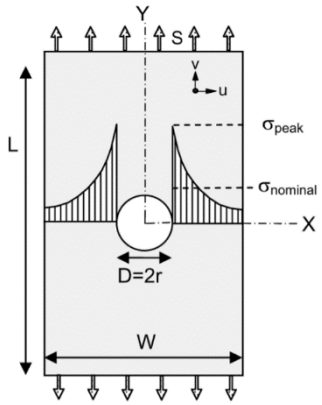

Figure 1.2: Schematization of stresses near a bolt hole [48].

In the European standard for steel structures (EN-1993-1), it is recognized that the material properties influence the ductility. In this standard, some requirements related to ductility are given. Minimum values are given for the f_u/f_y ratio, the strain at ultimate strength, and the strain at rupture. For example, the ratio f_u/f_y must be higher than 1.1, and the strain at rupture must be at least 15%[2]. However, in EN-1999-1, the European standard for aluminum structures, no specific minimum values related to ductility, are given in an apparent way as in EN-1993-1. In EN-1999-1, this is regulated by providing the calculation models only for a limited number of alloys. However, the nominal value of the $f_u/f_{0.2}$ ratio of some of these listed alloys is approaching the minimum value of 1.1 as known for steel structures[3]. For the actual tested values, the $f_u/f_{0.2}$ ratio is known to be even closer to 1.1 or may even be lower than this ratio. Also, considering the strain at rupture, it is experienced that the 15% limit as used for steel in EN-1993-1 is far from being reached.

Connecting aluminum alloy members by welding results in a Heat Affected Zone (HAZ) in the plate adjacent to the weld. In this zone, the material is affected by the heat of the welding process. This heat influence results in reduced material properties, particularly for heat-treated alloys. Especially the yield strength $f_{0.2}$ (0.2% proof stress) will be reduced[3]. This results in an increased $f_u/f_{0.2}$ ratio and may have a beneficial effect on the stress redistribution, hence the ductility of a structure. However, the extent of the HAZ is limited, especially in large scale structures. Since the 0.2% proof stress and the ultimate strength of the HAZ are lower than that of the base material for most alloys, the extent of the plastic zone may be limited, and the question arises whether it gives sufficient room for redistribution.

Another method to connect aluminum alloy members is by using bolts. When making a connection by bolts, a HAZ is not formed. However, this connection has the disadvantage that, locally, the cross-section is reduced by the bolt hole. For bolted connections, it is commonly advised to ensure that plastic deformation occurs in the gross section before failure in the net section. However, in most cases, this is impossible for heat-treated alloys with a low $f_u/f_{0.2}$ ratio.

Currently, clear guidelines are present in the standards regarding the strength of welded and bolted structures. However, the problem is that extensive information and design procedures considering the ductility of structures are lacking. This despite the evidence from earlier studies that material properties such as the ratio $f_u/f_{0.2}$ can significantly influence the ductility of a structure.

Essential information about the influence of material properties on the ductility of aluminum alloy connections is necessary for engineering safe and reliable structures. In order to be able to support future designs of aluminum alloy structures, the current study is performed. This research aims to determine the ductility of some typical aluminum alloy connections. Attention is mainly paid to welded connections and the corresponding influence of the changed material properties and the extent of the heat-affected zone. By experimental tests, the available deformation capacity of some different welded configurations is assessed and compared with some bolted connections. With the help of a numerical model, the ductility behavior can be investigated quicker and less costly for a wide variety of connection types and materials. The goal of this study is to establish a solid foundation for such a model.

The focus of this study is limited to the available deformation capacity of statically loaded structures, i.e. fatigue is not considered. This study does not examine the specific needed values for obtaining a ductile structure. Bending beams are not involved in the experimental research, and hence only connections imposed by tensile forces are examined. This because already, experiments on bending beams were executed in the past, and the research is focused at the tensile zone of a member.

In this thesis, background information about the topic is gathered first. This background information about material properties, welding, and numerical modeling is presented in Chapter 2 and is primarily related to the material ductility. Furthermore, more in-depth literature is reviewed of the latest studies about ductility at the structure level. The results of this literature study into the state of the art of deformation capacity are presented in Chapter 3. After conducting the literature study and identifying the current knowledge and research gaps, an experimental research plan is proposed to extend the current knowledge about the ductility of aluminum alloy connections. The results of the experimental program are shown and discussed in Chapter 4. With the help of the experimental results, numerical models are created, calibrated, and validated. The calibration process and the results of the numerical models are presented in Chapter 5. The conclusions that can be drawn from this study are presented in Chapter 6. Finally, attention points and topics for further research are provided in Chapter 7.

2. Theoretical background information

Background information about the topic was gathered first in this study. The most essential background information about material properties, welding, and numerical modeling is presented in this chapter. The information in this chapter is primarily related to the ductility at the material level.

2.1. Yield stress (0.2% proof-stress)

For steel materials, usually, a clear elastic limit and yield plateau is present in the stress-strain curve. For aluminum alloys, this is not the case since they have a unique curved stress-strain relationship, also called round-housed. In order to be able to calculate with an elastic limit, the value $f_{0.2}$ is introduced in EN-1999-1-1. $f_{0.2}$ stands for the 0.2% proof stress and represents a specific stress value where 0.2% plastic strain remains after removing the load. For linear elastic calculations, this value is the limit value.

For mild steel, the nominal tensile strength to yield stress ratio is about 1.5 for S235 and decreases with increasing steel strengths. For aluminum alloys, the ratio between the ultimate tensile strength and the 0.2% proof stress lies in between 1.05 and 2.5 and depends on the aluminum alloy and type of treatment. For some heat-treated alloys, this ratio can decrease to 1.05. Material treatments can increase the 0.2% proof stress and ultimate strength but reduce the strain at rupture and the ratio $f_u/f_{0.2}$. The latter is particularly important since it reduces the material's ability for redistribution of stresses, for example, near connections. This has an influence on the plastic redistribution, which forms the basis of our design rules. Therefore, alloys with a ratio of $f_u/f_{0.2}$ close to 1.0 are not always suitable for structural applications. In EN-1999-1-1 extensive tables with structural properties of various aluminum alloys are given for sheets (3.2a) and extruded profiles (3.2b). These tables include not all existing aluminum alloys since the calculation models of EN-1999-1-1 do not cover them all **[1]**.

Table 2.1 shows the frequently used aluminum alloys for extrusion profiles (table 3.2b) and their corresponding nominal values for the 0.2% proof stress, ultimate stress, and the elongation at rupture measured at a length of $5.65\sqrt{A_o}$. Additionally, the actual values from experimental tests, found in the literature, are listed in the table. For reasons of comparison, some steel grades and their structural properties are added.

Table 2.1: Structural properties of some extruded aluminum alloys and steel grades.

		Nominal values[2,3]				**Experimental values**			
Alloy	**Treatment**	**$f_{0.2}$ [N/mm²]**	**f_u [N/mm²]**	**f_u/f_0 [-]**	**$5.65\sqrt{A_o}$ [%]**	**$f_{0.2}$ [N/mm²]**	**f_u [N/mm²]**	**$f_u/f_{0.2}$ [-]**	**$5.65\sqrt{A_o}$ [%]**
5083	O/H111	110	270	2.45	12	165[21]	295[21]	1.79	15.4[21]
6060	T6	140	170	1.21	8	214[26]	239[26]	1.12	-
6061	T4	110	180	1.64	50	116[27]	260[27]	2.24	22.4[27]
6061	T6	240	260	1.08	8	298[26]	325[26]	1.09	-
6063	T6	160	195	1.22	8	225[28]	268[28]	1.19	8.9[28]
6005A	T6	200	250	1.25	8	266[29]	288[29]	1.08	-
6082	T4	110	205	1.86	14	148[15]	252[15]	1.70	19.8[15]
6082	T6	260	310	1.19	10	312[15]	324[15]	1.04	6.9[15]
7020	T6	290	350	1.21	10	326[30]	385[30]	1.18	13.6[30]
Steel	**Treatment**	**f_y [N/mm²]**	**f_u [N/mm²]**	**f_u/f_y [-]**	**$5.65\sqrt{A_o}$ [%]**	**f_y [N/mm²]**	**f_u [N/mm²]**	**f_u/f_y [-]**	**$5.65\sqrt{A_o}$ [%]**
S235		235	360	1.53	25				
S275	N/NL	275	390	1.42	24				
S355	N/NL	355	490	1.38	22	376[31]	479[31]	1.27	
S420	N/NL	420	520	1.24	19				
S460	N/NL	460	540	1.17	17	486[31]	613[31]	1.26	

2.2. Strain at rupture

As mentioned previously in Section 2.1, heat treatments increase the 0.2% proof stress and the ultimate strength. However, it reduces the ratio $f_u/f_{0.2}$ and the strain at rupture. The reduction of these factors can lead to a decrease in ductility. The strain at rupture is defined as the ratio between the elongated length at rupture and the original specimen length in a uniaxial stress state. The value of the strain at rupture is a good indication of the material ductility since ductility describes the ability of a material to undergo a large amount of plastic deformation without the occurrence of cracking. With a high elongation till rupture, much deformation occurs. By this possibility of deformation, the material can redistribute the stresses over a cross-section.

The strain at rupture depends on the type of aluminum alloy, the treatment method, and the temperature. At room temperatures, the actual values of strain at rupture of wrought alloys lie in between 3% and 35%. For heat-treated wrought alloys, this varies between 5% and 20% **[1]**.

From the point of yielding up to the ultimate strength, a strain hardening region is present. After the ultimate strength is reached, the necking process takes place, and a necking region is formed. In this region, the elongation is no longer equally distributed along the length of the specimen. The elongation will concentrate in the region where eventually failure will occur. Therefore, it is crucial which measuring length will be used for the strain at rupture. This length is standardized to 50 mm, also indicated with A_{50}. When testing several specimens with different dimensions, the measuring length is equal to $5.65\sqrt{A_o}$, where A is the initial cross-section area of the sample **[4, 5]**.

2.3. Material model and specifications

2.3.1. Material model

For structural calculations and numerical analyses, a specific material model is needed. Often global elastic analysis is used in structural engineering, which relies on the assumption that the stress-strain curve of the material is linear up to failure. When the member meets the requirements of cross-section class 1 and the aluminum alloy has sufficient ductility, a global plastic analysis may be used. For global plastic analyses, a plastic phase is considered. This plastic branch can be modeled perfectly plastic or including strain hardening. Furthermore, the transition from the elastic to the plastic region can vary from an abrupt to a smooth transition. With a generic inelastic analysis, the material model can be idealized to the actual stress-strain relationship. In this material model, the transition from elastic to plastic is gradual. This model is suited for Finite Element Method (FEM) simulations, which must represent reality **[6]**.

In the next section, more about the material model and the corresponding stress-strain curve, which can be used for the numerical analysis, is explained.

2.3.2. Stress-strain curve

Specifying the material properties and behavior is required for analyzing an element. By specifying the material parameters as close to reality as possible, a realistic model can be obtained. When a specific material is tested, actual stress-strain data is obtained, which can be used in the analysis. However, this data is not always available. Also, it is hard to model the exact behavior with a numerical material model. Therefore, some simplifications are made, and approximation models are introduced. In EN-1999-1-1, Annex E, some simplified models are present. Following this standard, one can use a multi-linear (bi- or tri-linear) model or a continuous model.

A continuous model that is frequently used and accurately approximates the actual stress-strain behavior is the Ramberg-Osgood (RO) model. This equation is supported by EN-1999-1-1 and is suited

to describe the plastic behavior of a material, with only knowing the yield strength, ultimate strength, elastic modulus, and corresponding strains **[3,5]**.

The Ramberg-Osgood equation for both elastic and plastic material behavior is formulated as

$$\varepsilon = \frac{\sigma}{E} + 0.002\left(\frac{\sigma}{f_y}\right)^n, \tag{2.1}$$

Where ε is the occurring strain, σ is the variable stress, E the elastic modulus, f_y the yield stress, and n the strain hardening exponent. The value for n can be computed by

$$n = \frac{\log\left(\frac{\varepsilon_2}{\varepsilon_1}\right)}{\log\left(\frac{\sigma_2}{\sigma_1}\right)}, \tag{2.2}$$

where $(\sigma_1; \varepsilon_1)$ and $(\sigma_2;\ \varepsilon_2)$ are two points on the plastic curve. Since the ultimate strength point and the yield point (0.2% proof stress) are commonly known, these variables can be substituted by the known material properties as follows

$$n = \frac{\log\left(\frac{\varepsilon_u}{0.002}\right)}{\log\left(\frac{f_u}{f_0}\right)}. \tag{2.3}$$

An example of a constructed RO-model is shown in Figure 2.1 for two materials with properties obtained from EN-1999-1-1 **[3]**.

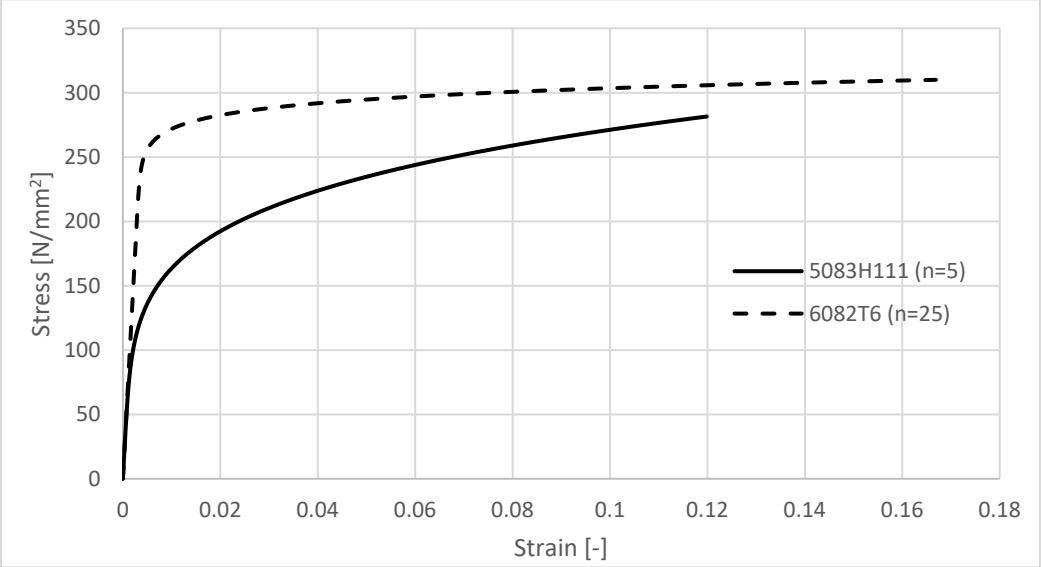

Figure 2.1: Stress-strain diagram constructed using the Ramberg Osgood model.

Some previous studies experienced significant numerical difficulties and missing convergence in the finite element analyses and, therefore, used another material model to describe the stress-strain relation, namely the Hopperstad exponential model. Also, Piluso et al. (2019) preferred the Hopperstad exponential model curve fitted on the Ramberg-Osgood curve. The simplified equation corresponding to the Hopperstad exponential model is described as follows

$$\sigma = f_{0.2} + Q\left[1 - e^{(-C\varepsilon_p)}\right], \tag{2.4}$$

where ε_p is the plastic strain, and Q and C the curve fitting parameters, which depend on the material properties. Therefore, they also are known as the material constants. Where Q is determining the strain hardening behavior and C the shape of the curve **[18]**.

2.3.3. True stress and strain

Usually, engineering stress is used for structural calculations. Engineering stress is the force divided by the original cross-section area before loading. However, by loading a material, the cross-section area will decrease. By using true stress, the actual area of the specimen will be considered. Therefore, the true stress will be higher than the engineering stress. For the linear elastic region, this difference is negligible. More distinction between the two models begins to develop from the plastic region onwards. In this region, the material faces more deformation, especially in the necking region, where locally, the cross-section decreases tremendously. In Figure 2.2, both the engineering and the true stress-strain curve are plotted. As mentioned, there is mainly a difference to be seen in the plastic phase and especially in the necking region.

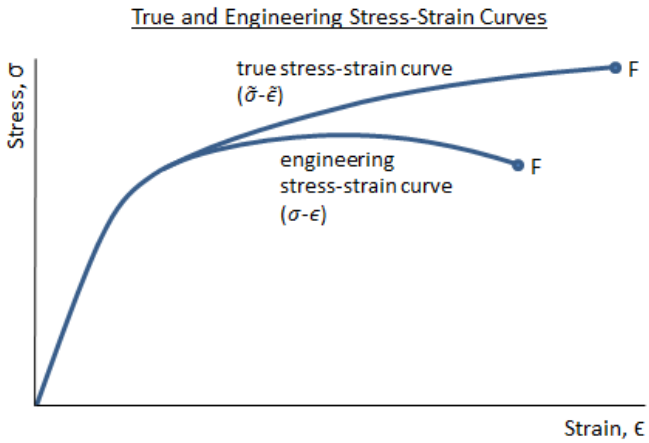

Figure 2.2: True and Engineering stress-strain curves [5].

The true stress $\tilde{\sigma}$ can be computed, based on the engineering stress σ and the assumption that the material volume remains constant. The true stress is calculated by

$$\tilde{\sigma} = \frac{P}{A} = \frac{P}{A_o} \cdot \frac{A_o}{A} = \frac{P}{A_o} \cdot \frac{L}{L_o} = \sigma(1 + \varepsilon), \tag{2.5}$$

where P is the applied force, A the actual cross-section, and A_o the original cross-section. L is defined by the actual measured length and L_o the original length. The engineering strain ε can be computed by the change in length ΔL divided by the original length following the equation

$$\varepsilon = \frac{L}{L_o} = \frac{L_o + \Delta L}{L_o}. \tag{2.6}$$

When the change in length is divided into many small increments, the summation of the strains approaches the true strain value. Therefore, the true strain can be computed by

$$\tilde{\varepsilon} = \int_{L_0}^{L} \left(\frac{dL}{L}\right) = \ln\left(\frac{L}{L_o}\right) = \ln(1 + \varepsilon). \tag{2.7}$$

2.4. Welding and HAZ

One of the methods to join different structural aluminum alloy members is by welding. By welding, the materials are connected primarily by the use of heat. This heat can lead to a degradation of the mechanical properties of the aluminum alloy, which is further discussed in Section 2.4.1. Currently, several welding techniques are available. Arc welding and friction (stir) welding are the most common techniques used nowadays.

For arc-welding, Tungsten Inert Gas (TIG) welding and Metal Inert Gas (MIG) welding are the most common methods. Both methods use an inert gas shield to protect the electrode, the arc column, and the weld pool. This gas shield prevents the welding area from making contact with the atmospheric air, which can cause porosity, fusion defects, and weld metal embrittlement. The TIG welding process is schematized in Figure 2.3. The main difference between the two welding processes is that TIG welding uses a non-consumable tungsten electrode, and MIG welding uses a consumable wire electrode. For MIG welding, this consumable wire electrode also serves as a filler metal, which is always connected to the positive polarity of the direct current. This process results in a large amount of heat generated at the end of the filler metal. For TIG welding, alternating current is used, resulting in a continuous change of the electrode or workpiece being positive. The filler metal is melted in the arc column located between the positive and negative polarity and not only in the positive polarity. This leads to significantly lower heat input as known for MIG welding. However, MIG welding has some advantages compared to TIG welding, namely faster welding speeds, excellent oxide film removal, and all positional welding capability. Therefore, MIG welding is the most widely used manual welding technique for aluminum alloys **[7,38]**.

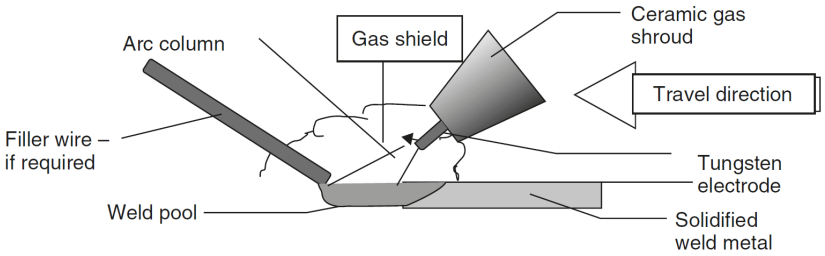

Figure 2.3: TIG Welding [6].

2.4.1. HAZ properties

The aluminum alloys used for structural applications are usually heat-treated or strain hardened. By these techniques, the strength of the aluminum alloys is increased compared to the annealed condition. However, heating of the material above a temperature of 200˚C or higher tends to decay the effects which are obtained by heat treatment or stain hardening, which results in bringing back the mechanical properties close to the original state. Welding of an aluminum alloy member will result in local heating of the metal. Hence the mechanical properties of the material will be affected in the region adjacent to the weld. This zone is called the Heat Affected Zone (HAZ). The extent of the HAZ and rate of strength reduction depends on several factors like the welding process, weld material, and the type and thickness of the base material. Despite the strength reduction, this degradation is often accompanied by an increase in ductility since usually, the $f_{0.2}$ strength decreases more than the f_u strength resulting in a higher ratio ultimate stress to yield strength. This phenomenon is also shown in Table 2.2, where the nominal mechanical properties of some aluminum alloys are listed. Besides the increased ratio, it was mentioned by some studies, including Woelke et al. (2017)[39], that the strain at rupture in the HAZ also increases in some cases. Therefore, the HAZ can have a higher material ductility than the base material. This higher ductility was also observed in the results from the tensile specimens

in the study of Wang (2006)[25], shown in Figure 2.4. From these results, it is evident that the HAZ material experienced a more ductile behavior than the parent material **[8, 33]**.

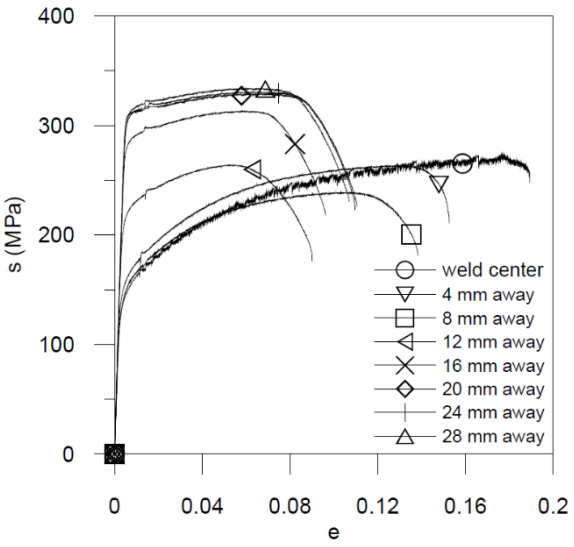

Figure 2.4: True stress-plastic strain curves from the results of the MIG welded AA6068-T6 tensile specimens [25].

Table 2.2: Extruded aluminum alloys and corresponding (HAZ) nominal structural material properties [3].

Alloy	Treatment	$f_{0.2}$	f_u	$f_u/f_{0.2}$	$5.65\sqrt{A_o}$ %	$f_{0.2,haz}$	$f_{u,haz}$	$f_{u,haz}/f_{0.2,haz}$
5083	H111	110	270	2.45	12	110	270	2.45
6060	T6	140	170	1.21	8	60	100	1.67
6061	T6	240	260	1.08	8	115	175	1.52
6063	T6	160	195	1.22	8	65	110	1.69
6005A	T6	200	250	1.25	8	115	165	1.43
6082	T6	260	310	1.19	10	125	185	1.48
7020	T6	290	350	1.21	10	205	280	1.37

As aforementioned, the strength of the material in the HAZ depends on several parameters. In the last decades, several studies have been carried out on this subject. Lakshminarayanan et al. (2007)[38] studied the effect of three different welding processes on the tensile properties of a 6061-T6 aluminum alloy with a thickness of 6 mm. In the experiments, the strength of the base material, the welding material, and the strength of the entire joint were determined for different welding processes. In Table 2.3, these values are listed.

Table 2.3: Experimental results of welded AA6061-T6 joints [38].

Type of material/joint	$f_{0.2}$	f_u	Elongation (%)	Reduction cross-section area (%)
Base metal (AA6061T6)	302	334	18	12.24
TIG weld metal (AA4043)	160	230	8	5.45
TIG welded joint	188	211	11.8	8.26
MIG weld metal (AA4043)	150	220	6	4.5
MIG welded joint	141	163	8.4	5.8
FSW weld metal	245	295	14	10.2
FSW welded joint	224	248	14.2	9.56

A similar study was carried out by Li et al. (2006)[33]. In this study, both MIG and TIG welding was investigated as well as some different welding wires. The experiments were done with aluminum alloy

6061-T6 and various thicknesses. The experiments for the plates with a thickness of 6 mm are listed in Table 2.4.

Table 2.4: Experimental results from the study of Li et al. on aluminum alloy 6061-T6 [33].

Welding process	Welded joint	Base material		HAZ		Weld metal	
	f_u	$f_{0.2}$	f_u	$f_{0.2}$	f_u	$f_{0.2}$	f_u
MIG (4043 wire)	202	323	337	116	213	121	177
MIG (5356 wire)	220	305	336	133	215	111	213
TIG (5A06 wire)	183	310	325	109	182	113	208

By looking at the different results in Table 2.3 and Table 2.4, it appears that the findings concerning the differences between MIG and TIG contradict each other. The research of Lakshminarayanan et al.[38] shows that TIG welding resulted in higher joint strength. However, contrary to the research of Li et al.[33], it was found that TIG welding results in lower strength properties of the joint compared to MIG welding. However, these differences can be a result of different welding conditions in the two studies. Usually, TIG welding results in more heat development than MIG welding due to its lower welding speed, which is also mentioned in EN-1999-1 chapter 6.1.6. This higher heat input will result in a more degrading effect on the strength properties of the material **[33,38]**.

The strength of a welded member depends on the type of welding process and the used material. But also, on the orientation of the weld. Therefore, welds are divided into two categories: transverse welds and longitudinal welds. Transverse welds are welds lying in a plane transversely to the stress direction in a member. Examples of transverse welds are welds for connecting members, welds for a stiffening panel, and welds for attaching members to a base plate. Longitudinal welds run parallel to the stress direction of the member. An example of these welds are welds for connecting the web and the flange of a plate girder. Longitudinal welds are typically applied for built-up members **[1,8]**.

The different welding categories influence the structural calculations. According to the Eurocode, for the transverse welds, one may use the ultimate HAZ strength. However, for the longitudinal welds, one should use the 0.2% proof stress of the heat-affected zone, $f_{0,haz}$. This should be done because, in the case of a transverse weld, the weld and the HAZ will be fully utilized, and the strains concentrate in this region. Therefore, enough strain can be obtained to reach its ultimate strength. In the case of a longitudinal weld, the base material affects the behavior, since it also takes a part of the strain distribution into account. Due to the contribution of the base material and its usually lower ultimate strain, the HAZ will never reach the strain corresponding to the ultimate strength **[1,3,8]**.

2.4.2. HAZ extent

As aforementioned, welding of aluminum alloy members results in a heat-affected zone. This zone must be considered for the design and calculations of aluminum alloy structures. The standard EN-1999-1-1 provides some dimensions of the HAZ for MIG and TIG welding. The dimensions for MIG welding with a maximal interpass temperature of 60˚C, according to 6.1.6.3(3), are as follows

$0 < t \leq 6$ mm $\quad b_{haz} = 20$ mm;
$6 < t \leq 12$ mm $\quad b_{haz} = 30$ mm;
$12 < t \leq 25$ mm $\quad b_{haz} = 35$ mm;
$t > 25$ mm $\quad b_{haz} = 40$ mm.

For TIG welding, the HAZ is larger since the heat input is bigger as known for MIG welding. For this welding method, the possible weld thickness is limited to 6 mm. For TIG welding, the dimensions are, according to 6.1.6.3(6) as follows

$0 < t \leq 6$ mm $\qquad b_{haz} = 30$ mm.

Next to the studies of the HAZ strength, also several studies are performed regarding the extent of the HAZ. From these studies, it was observed that the HAZ is sometimes too conservative. Following the design standards, the strength properties of the material in the HAZ are decreased over the full area, while, in reality, it is increasing gradually over the length of the zone. Due to this phenomenon, the calculated strength of the zone can be much lower as compared to reality. The strength evolution within the HAZ can be researched with the help of Vickers hardness measurements expressed by a Hardness in Vickers (HV). From this, a hardness profile can be obtained referring to the strength profile within the HAZ. In Figure 2.5, a typical example of the results from this test is shown. From this test, it can be seen that minimum hardness is achieved at some distance away from the weld center. This phenomenon is well-known for Vickers hardness curves of aluminum welded specimens and is also called the failure plane of the HAZ since it is generally the weakest spot in welded joints. In Table 2.5, a few results are listed. All of these results showed a minimum value of the hardness about 10 mm away from the weld center. Furthermore, it can be concluded that the measured extent of the HAZ zone is reasonably in line with the standards **[33]**.

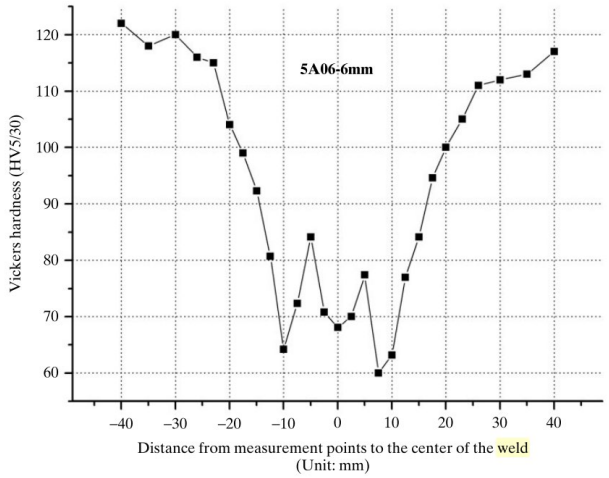

Figure 2.5: Vickers hardness curve of a TIG-welded AA6061-T6 specimen [33].

Table 2.5: HAZ extent studies overview.

Study	Alloy	Thickness	Welding type, thickness and welding material	HAZ Extent (from center)	Min. hardness (from center)	Min. HV/ base HV
Hval (1998)[34]	6005T6	15mm	MIG, butt weld, 5183 filler	25mm	10mm	55%
Zhang (2006)[33]	6061T6	6mm	TIG, 10mm buttweld, 5A06 filler metal	25 mm	10mm	50%
Zheng (2009)[35]	6061T6	3mm	MIG, butt weld	23mm	10mm	50%
Sato (1999)[36]	6063T5	6mm	FSW, 6mm fusion zone	15mm	10mm	65%
Moen (1999)[15]	6082T6	5mm	MIG, welded stiffener (no weld in specimen)	30mm	10mm	65%
Missori (2000)[37]	6082T6	10mm	MIG, 10mm butt weld, A4043 filler	20mm	10mm	55%
Wang (2006)[25]	6082T6	5mm	MIG, 5mm fillet weld, 5283 filler metal	30mm	10mm	65%

One can conclude from a typical Vickers hardness profile shown in Figure 2.5, that the strength profile gradually changes over the extent of the HAZ. Therefore, the HAZ will sometimes be modeled with varying mechanical properties instead of one uniform reduced zone. An example is the research of Farajkhah and Liu (2016)[10], where the transition from the weld to the base material was modeled with three zones with different material strengths. Namely, the HAZ, semi-HAZ, and the base metal zone. Also, de Jongh (2016)[9] used more precise modeling of the weld region. In one model, he modeled the weld, the HAZ, and the base material as three different zones. In another case, he also divided the HAZ into six different zones with different material properties. Since, in the case of the single HAZ zone, the decisive HAZ properties where used, i.e., the lowest mechanical properties, the whole zone was fully degraded compared to the six zones divided HAZ. Therefore, the single zone modeled HAZ showed a slightly lower overall resistance. However, the divided HAZ model showed less deformation due to strain concentrations in the weakest zone of the HAZ**[9, 10]**.

2.5. FEM modeling

By the use of numerical methods such as the Finite Element Method (FEM), analyses can be done for a large number of samples, without the cost and time-consuming drawbacks. The current study also explores the possibilities of applying numerical analyses. The model applicability was examined by validation of the numerical results on the experimental results. A numerical model must be created to obtain these numerical results. To make an accurate numerical representation, some specific input parameters and modeling choices must be made. For example, the type of element, the type of material model, and the type of damage modeling must be defined. The type of material model was defined earlier in Section 2.3, where the Ramberg-Osgood model was outlined. More information about the element type and damage modeling is discussed in the following paragraphs.

One of the choices that must be made for the way of setting up the model is the choice for the type of elements that will be used. The FEM software Abaqus provides a wide variety of elements. Abaqus supports, for example, beam elements, shell elements, and continuum elements. For the current study, only shell and continuum solid elements are of interest. The main feature for shell elements is that these elements approximate a three-dimensional continuum with a two-dimensional surface model. The stresses perpendicular to the shell surface are zero, and the stresses through the thickness are calculated by the help of integration points. The nodes of the elements are located on the reference surface. Continuum solid elements are 3D elements where the nodes are located at corners and edges of the volume. The trough-thickness stresses are calculated by the help of these nodes and integration points. The great advantage of shell elements is that they can lead to substantial computational time savings since it requires far fewer mesh elements and thus, fewer nodes and equations **[50]**.

In earlier studies by Matusiak (1999)[24], Chan and Porter Goff (2000)[44], and Zhang et al. (2001)[45], also numerical predictions of the deformation behavior and strength of welded aluminum alloy structures were carried out. In these studies, solid elements and an elastoplastic constitutive model were used. Wang (2006)[25] recognized this and stated that in finite element modeling of welded structures, most of the time, the weld material and base material were modeled using solid elements. Using these solid elements will result in more complicated models and more computational time compared to shell element models and is therefore not always practical for complex structures containing many welds. However, Wang (2006) stated that the existing literature on shell element modeling of welded structures is quite limited. Only in the study of Moen et al. (1999) and the study of Wang itself, shell elements were successfully applied for analyzing the behavior of aluminum alloy beam exposed to bending.

It is necessary to model the welds accurately since in the current research stress concentrations and the redistribution of stresses are the studied topics. To model this geometry, solids elements are required. Chan and Porter Goff (2000) [44] showed that this type of element could be used successfully for a similar kind of problem, as needed for the current study. A choice must be made between 8-node or 20-nodes solid elements. The quadratic 20-nodes solid elements can capture stress concentrations more effectively and give overall better results[41]. However, this comes with increased computational time. Chan et al. used 20-nodes brick elements with quadratic displacement functions. However, the good applicability of 8-nodes was also proven by the studies of Zhang et al. (2001)[45] and Farajkhah and Liu (2016)[32]. Since stress concentration occurs locally and this region is very small compared to the complete model in this study, it is more efficient to apply a finer mesh size locally with first-order 8-nodes elements compared to applying quadratic 20-nodes elements in the complete model.

2.6. Damage and failure modeling

In reality, the loaded specimens will crack and eventually fail at a particular load. Since cracking influences the failure and deformation behavior, it is important to model this also as accurately as possible in the FEM analyses. This behavior can be considered by modeling the damage and failure in the continuum elements itself by a constitutive behavior or by interface elements. For the damage and failure model using interface elements, cohesive zone modeling can be used. Failure in the continuum elements itself can be modeled in Abaqus with the help of two distinct types, namely ductile fracture of metals or necking instability in sheet metal forming. For the first type, three different criteria are featured by Abaqus: Ductile damage, Johnson-Cook damage, and the Shear damage criterion. For the necking instability of sheet metal, forming limit diagrams (FLD, FLSD, and MSFLD) are present to assess the formability of sheet metal. For numerically predicting the necking instability in sheet metal, the M-K criterion is applied, which takes the deformation history into account. Both ductile fracture and necking instability models can be used in cooperation with the von Mises and Johnson-Cook plasticity models **[40].**

Since ductile fracture is of importance in this study, the ductile damage model will be implemented in the numerical simulations. The total modeled behavior of a metal specimen from begin loading up to failure by ductile fracture can be broken down into three different parts. These three different parts are presented in Figure 2.6 and consist of the undamaged elastic-plastic response, the damage initiation point, and the damage evolution. First, the undamaged elastic-plastic response of the material must be present. This undamaged elastic-plastic response is schematized in Figure 2.6 with first the linear elastic response from point a. to b. and then the plastic phase, including yielding and strain hardening, from point b. to point d'. This part is defined by the Ramberg Osgood stress-strain relationship, as outlined earlier in Section 2.3. For the plasticity model, the Von Mises plasticity model will be used, which is the default in Abaqus. At a certain point, the material stiffness starts to degrade, this damage initiation point, marked as point c, reflects the onset of damage of the material. Once this point is reached, the damage evolution response can be considered, which is indicated as the region between c. and d. This response between c. and d. can be viewed as the damaged response of the region between c. and d'. In the following subsections, the damage initiation and the damage evolution are further discussed, which are needed for the implementation of damage and failure into the finite element model.

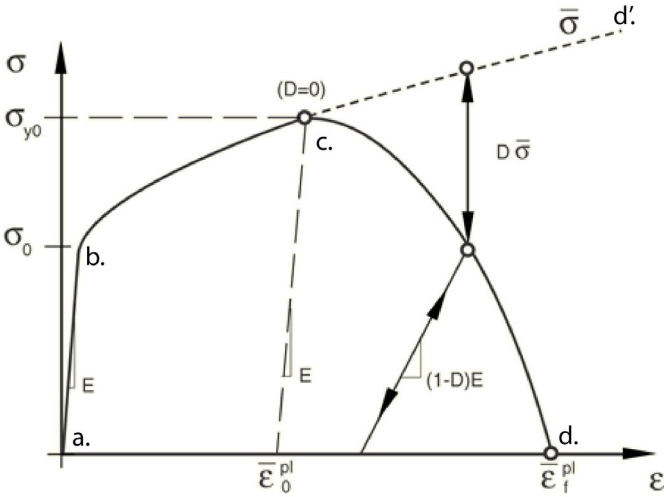

Figure 2.6: Typical stress-strain curve with progressive damage and failure implemented [5].

2.6.1. Damage initiation

The ductile fracture of metals is based on a damage initiation criterion, which defines the point of initiation and degradation of stiffness. The Ductile damage criterion can model the onset of damage due to nucleation, growth, and coalescence of voids in ductile metals. This model assumes that the plastic strain corresponding to the point at the onset of damage is a function of stress triaxiality and strain rate. This stress triaxiality η is defined by

$$\eta = \frac{\sigma_m}{\bar{\sigma}}, \tag{2.8}$$

consisting out of the mean stress defined by

$$\sigma_m = \frac{\sigma_1 + \sigma_2 + \sigma_3}{3}, \tag{2.9}$$

and the equivalent stress defined by

$$\bar{\sigma} = \sqrt{\frac{(\sigma_1 - \sigma_2)^2 + (\sigma_1 - \sigma_3)^2 + (\sigma_2 - \sigma_3)^2}{2}}, \tag{2.10}$$

in which $\sigma_1, \sigma_2, \sigma_3$ are the principal stresses.

Bao et al. (2003)[46] outlined the dependency of stress triaxiality. From the results of this study, it was clear that stress triaxiality strongly influences failure behavior. For high-stress triaxialities, void nucleation, growth, and linkage mechanism occur. For the negative range of triaxiality values, a different mechanism was observed. In this range, a crack formation mechanism described by shear fracture occurred. The dependency was also proved by Wierzbicki et al. (2005)[42] with the help of 15 experimental tests under different stress triaxialities, as shown in Table 2.6 **[42, 46]**.

Table 2.6: Summary of the experimental program by Wierzbicki et al. (2005) [42].

Test #	Specimen description	$\overline{\varepsilon_f}$	η_{av}
1	Round, smooth	0.46	0.40
2	Round, large notch	0.28	0.63
3	Round, small notch	0.17	0.93
4	Flat-grooved	0.21	0.61
5	Cylinder (d0/h0=0.5)	0.45	-0.278
6	Cylinder (d0/h0=0.8)	0.38	-0.234
7	Cylinder (d0/h0=1.0)	0.356	-0.233
8	Cylinder (d0/h0=1.5)	0.341	-0.224
9	Round notched (compression)	0.62	-0.248
10	Flat dog-bone tensile	0.21	0.012
11	Flat	0.26	0.117
12	Plate with a circular hole	0.31	0.343
13	Dog-bone	0.48	0.357
14	Pipe	0.33	0.356
15	Solid bar	0.36	0.369

Different models are available to describe the relationship of the fracture strain to stress triaxiality. One of those models is the constant equivalent strain criteria, which assumes that fracture occurs in a material when the equivalent plastic strain reaches a critical value. This critical value is defined by a constant value that is similar for every stress triaxiality. Since the fracture strain can vary for different stress triaxialities, this criterion is not very precise. However, it can give a quick indication of the possible fracture areas. Often, the constant fracture strain is also used as an adjustable parameter to obtain the best match between the experiments and numerical analyses. This method performs good results in most cases but is fundamentally wrong **[42].**

A criterion that is more specific and takes the stress triaxiality into account is the Johnson-Cook fracture model. In this model, the strain at the onset of fracture is expressed by an exponential function of the stress triaxiality and it uses three material constants. The equation of the equivalent fracture strain is described as follows

$$\overline{\varepsilon_f} = C_1 + C_2 \exp(C_3 \eta). \tag{2.11}$$

Where $\overline{\varepsilon_f}$ is the equivalent fracture strain at the onset of failure, η is the stress triaxiality, and C_i are the calibration constants. Since three unknown material constants are present, at least three tests are required for calibration. A similar criterion with the same functional form was earlier developed by Rice and Tracey (1969), where C_1 and C_3 were determined theoretically, and only C_2 is left for calibration. Values of -1.5 and 0.0 for C_1 and C_3, respectively, resulted in a good match with experimental results in the range for stress triaxialities higher than 1/3.

Next to the Johnson-Cook fracture criterion, also the Maximum Shear stress criterion takes the dependency of different stress states into account. Wierzbicki et al. (2005) stated that ductile fracture occurs on a plane where the shear stress is maximum. Therefore, a Maximum Shear stress criterion was established. Even though only one calibration constant is used in this criterion, this model shows excellent performance. The criterion assumes that fracture occurs when the shear stress reaches a specific maximum value, defined by the condition $\tau_{max} = (\tau_{max})_f$, where $\tau_{max}$is a function of the principal stresses defined by

$$\tau_{max} = \max\left\{\frac{\sigma_1 - \sigma_2}{2}, \frac{\sigma_2 - \sigma_3}{2}, \frac{\sigma_3 - \sigma_1}{2}\right\}, \tag{2.12}$$

where $\sigma_1, \sigma_2, \sigma_3$ are the principal stresses and $(\tau_{max})_f$ is the critical failure shear stress.

The fracture locus for the maximal shear stress criterion, which is based on a plane stress situation, is given by the following equations

$$\bar{\varepsilon_f} = C\left\{\frac{\sqrt{1+\alpha+\alpha^2}}{2+\alpha}\right\}^{\left(\frac{1}{\bar{n}}\right)} \quad for = -\frac{1}{2} < \alpha < 1 \; or \; \frac{1}{3} < \eta < \frac{2}{3} \tag{2.13a}$$

$$\bar{\varepsilon_f} = C\left\{\frac{\sqrt{1+\alpha+\alpha^2}}{1-\alpha}\right\}^{\left(\frac{1}{\bar{n}}\right)} \quad for = -2 < \alpha < -\frac{1}{2} \; or \; -\frac{1}{3} < \eta < \frac{1}{3} \tag{2.13b}$$

Where $\eta = (\frac{1}{\sqrt{3}})(\alpha+1)/(\sqrt{1+\alpha+\alpha^2}$, $\alpha = \frac{d\varepsilon_2}{d\varepsilon_1}$ defined as the principal strain rate, and C the calibration constant. Furthermore, $\bar{n}$ is the hardening exponent from the power law and can be calculated by

$$\bar{n} = \frac{\ln(f_{u,true}) - \ln K}{\ln(\varepsilon_{u,true})}. \tag{2.14}$$

In a recent study into aluminum weld failure conducted by Manders (2018), the Maximal Shear criterion was applied. This since the model is easy to apply while only one calibration point is needed. Also, Wierzbicki et al. (2005) showed that this model matched the experimental results with high accuracy compared to other models, which can be seen in Figure 2.7. Since the ease of use, also in this current study, the material damage model in cooperation with the maximal shear criterion will be used **[43]**.

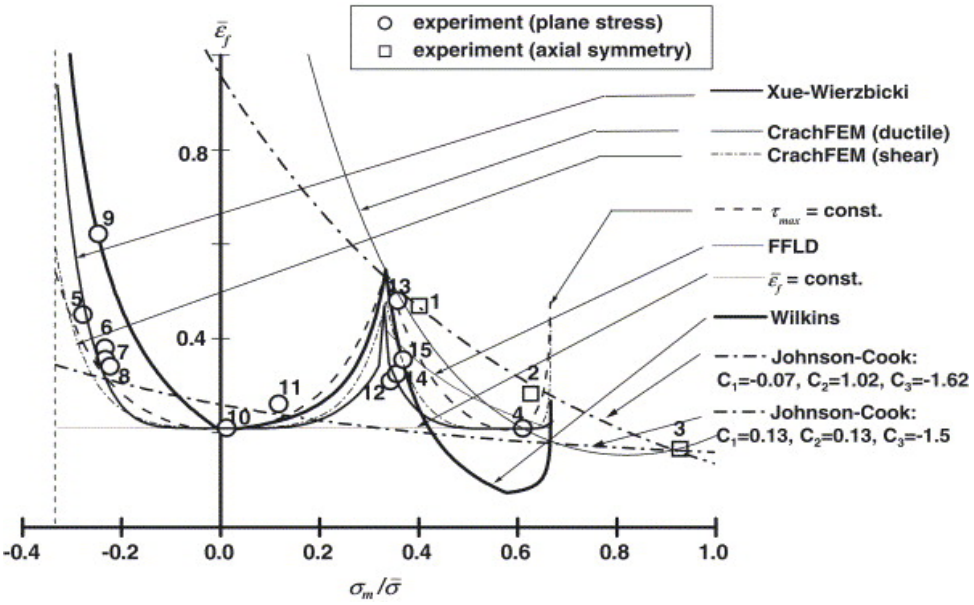

Figure 2.7: Comparison of seven different fracture criteria performed by Wierzbicki et al. (2005) [42].

2.6.2. Damage evolution

When the damage initiation point is reached, damage begins to occur. From this point on, the material loses its stiffness and load-carrying capacity up to the point of complete failure. The path of this curve is shown in Figure 2.6. From point c. up to point d. the process of this damaging process is considered using the damage evolution law. This law assumes that damage can be characterized by the progressive degradation of the material stiffness, which eventually leads to total material failure. The damage evolution is taken into account by the scalar damage equation

$$\sigma = (1 - D)\bar{\sigma}, \tag{2.15}$$

where D is defined as the damage variable and $\bar{\sigma}$ the effective stress tensor computed in the current increment. This effective stress tensor includes the stresses that would exist in the case of an undamaged material. When D is equal to 1, the material completely lost its load-carrying capacity. The damage variable can be computed and defined through an equivalent plastic displacement or in terms of fracture energy dissipation. These terms are defined as the amount of displacement or energy needed to open a crack until it lost its full stiffness. When the equivalent plastic displacement or the fracture energy reaches a critical value of $\bar{u}_f^{pl}$ or G_f, respectively, the damage variable is equal to 1. The calculation of the damage variable is explained later on in this section after introducing the fracture energy principle.

The constitutive model for continuum mechanics is typically expressed in terms of stress-strain relations, which is also the case for the damage evolution region, as can be seen in Figure 2.6. However, through the strain-softening relation, strain localization can occur. This strain localization will result in a strong mesh dependency since by applying a smaller mesh size, strains will concentrate in a smaller area. Hence, less energy is required for the element to fail.

A different approach is needed to represent the strain-softening branch after damage initiation. Therefore Hillerborg's (1976) fracture energy theory will be used to reduce the mesh dependency by using a stress-displacement response. This theory is based on the amount of energy required to open a unit area of a crack, defined as the fracture energy G_f. The principle can be explained by the help of the schematization shown in Figure 2.8, where the crack starts to open when the stress reaches the critical strength f_u. At the point the crack is propagated as much as it reaches a critical crack opening u_f, the stress has fallen to zero. The stresses between these two points are described with the curve $\sigma = f(u)$ where the stresses are a function of the crack opening displacement u. In this method, displacement is used instead of strain, since a crack will occur on a local scale and thus cannot be related in terms of strains. Because there is a stress to overcome to open the crack, energy is absorbed. The amount of energy absorbed per unit crack area for opening the crack from zero up to u_f is defined by

$$G_f = \int_0^{u_f} \sigma du\,, \tag{2.16}$$

where G_f corresponds to the area covered by the curve shown in Figure 2.9.

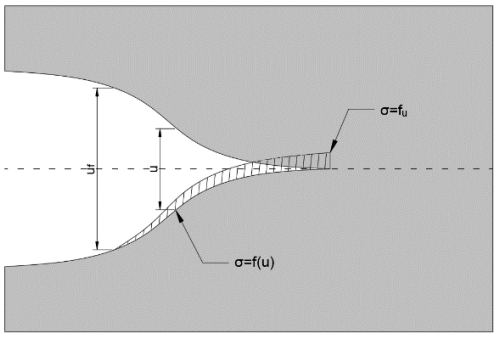

Figure 2.8: Crack opening principle schematization.

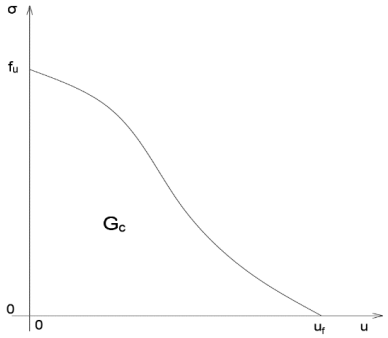

Figure 2.9: Opening versus stress curve during crack propegation.

In the Hillerborg approach, the response after damage initiation is characterized by a stress-displacement relationship instead of a stress-strain relation. In order to still be able to construct the damage evolution, the fracture energy G_f in Abaqus is defined by

$$G_f = \int_0^{\bar{u}_f^{pl}} \sigma d\bar{u}^{pl} = \int_{\bar{\varepsilon}_0^{pl}}^{\bar{\varepsilon}_f^{pl}} L\sigma d\bar{\varepsilon}^{pl} \,. \tag{2.17}$$

Here the equivalent plastic displacement, $\bar{u}^{pl}$, is substituted by the equivalent plastic strain $\bar{\varepsilon}^{pl}$, multiplied with the characteristic length of the element L. This characteristic length is defined for shell elements as the square root of the integration area and for solid elements as the cube root of the integration volume. This by the fact that the direction of the fracture is not known in advance and the elements can have different aspect ratios. When using large aspect ratios, still mesh sensitivity effects can exist. Therefore, it is recommended to use solid elements with an aspect ratio close to unity **[5].**

As mentioned, the damage variable D can be calculated using an equivalent plastic displacement or fracture energy. This value can be calculated by a function for D depending on $\bar{u}^{pl}$ or by calculation of the absorbed energy divided by the critical fracture energy. With the corresponding equations given by

$$D = D\left(\bar{u}^{pl}\right) or\ D = \frac{\int_0^{\bar{u}^{pl}} \sigma d\bar{u}^{pl}}{G_f}. \tag{2.18}$$

When the damage evolution is assumed to be linear, the fracture energy, G_f, can easily be converted to an equivalent plastic displacement at failure $\bar{u}_f^{pl}$. The damage variable in the linear form can be simply calculated by

$$D = \frac{L \cdot \bar{\varepsilon}^{pl}}{\bar{u}_f^{pl}} = \frac{\bar{u}^{pl}}{\bar{u}_f^{pl}}, \tag{2.19}$$

where

$$\bar{u}_f^{pl} = \frac{2G_f}{f_u}. \tag{2.20}$$

3. State of the art of deformation capacity

In the last three decades, numerous studies have been conducted concerning the ductility of aluminum alloy members. This is due to the emerging questions relating to the safety aspects of plastic design with aluminum alloys. The behavior of the inelastic phase is usually described by the rotation capacity or the deformation capacity. The rotation capacity is one of the most reliable parameters for estimating the inelastic behavior of a structural member [1]. This chapter outlines the latest findings on the rotation capacity and the influencing parameters. Furthermore, the influence of welding on the rotation capacity for beams but also the influence on structural members subjected to only tensile forces are discussed. Finally, a general conclusion is included regarding the most important findings of the studies.

3.1. Rotation capacity

The evaluation of the rotation capacity of aluminum alloy members has been the subject of several studies over the years. This because the underlying assumption made for the plastic design of metal structures is that members can withstand large plastic deformations without a significant reduction of strength. Therefore, it is necessary to allow redistribution of internal stresses in structures and to assure the complete development of plastic reserves. Finally, the rotation capacity is an important parameter to ensure high energy dissipation in the case of seismic actions **[11,12,13]**.

The rotation capacity is conventionally defined as a measure of the inelastic rotation that a member can suffer for a certain level of bending capacity. In the case of steel members, this bending capacity is defined by the full plastic moment $M_p = f_y W_{pl}$. However, for aluminum alloy members, this is not logical since it is a roundhouse type of material. Therefore, the fibers never reach a plateau characterized by yielding as known for mild steels. Hence, a conventional elastic moment is introduced corresponding to the elastic limit stress, also known as the 0.2% proof stress $f_{0.2}$. This means that there is some difference in the definition of the rotation capacity for steel and aluminum alloys. For steel members, the rotation capacity can be interpreted as the ability to withstand large plastic rotations before the bending resistance falls below the fully plastic moment of the section. While for aluminum alloy members this is defined as it falls below the conventional elastic limit moment $M_{0.2} = f_{0.2} W_{el}$ **[14]**.

Mazzolani and Piluso (1997)[14] defined some equations to determine the rotation capacity. They divided the rotation capacity into two parts, the stable rotation capacity R_0 and the full plastic rotation capacity R. The full plastic rotation capacity is defined as the ratio of the plastic rotation at the state the bending moment drops down the conventional elastic limit divided by the rotation when the elastic limit is reached for the first time. The full plastic rotation capacity is calculated by

$$R = \frac{\theta_p}{\theta_{0.2}} = \frac{\theta_u - \theta_{0.2}}{\theta_{0.2}} = \frac{\theta_u}{\theta_{0.2}} - 1 \,, \tag{3.1}$$

where θ_u is the ultimate rotation, i.e., the rotation corresponding to a point where the acting moment will drop down the value corresponding to the conventional elastic limit moment. $\theta_{0.2}$ corresponds to the rotation when the limit stress $f_{0.2}$ is reached for the first time. The plastic rotation θ_p is defined as the ultimate rotation minus the elastic limit rotation.

The stable branch of the rotation capacity is expressed by:

$$R_0 = \frac{\theta_{max}}{\theta_{0.2}} - 1 \,, \tag{3.2}$$

where θ_{max} is the rotation corresponding when local buckling occurs and so on the maximal moment is reached. The definition of the rotation capacity is visualized in Figure 3.1 **[14]**.

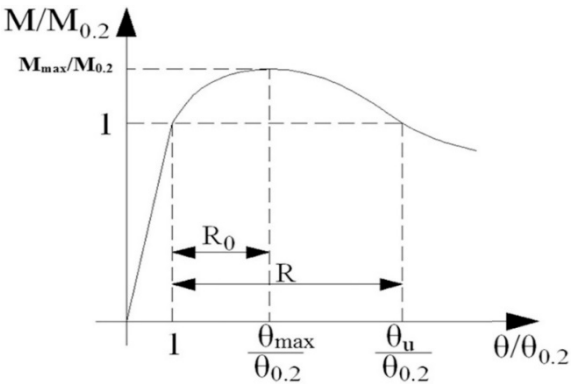

Figure 3.1: Definition of the rotation capacity [12].

In most cases, the occurrence of local buckling or lateral-torsional buckling limits the maximum rotational capacity of a beam. These occurrences depend on geometrical and material properties. Usually the calculation standards take the limiting effect of these properties into account by a cross-sectional classification system. This classification system is based on the width to thickness ratio and the 0.2% proof stress. However, Moen et al. (1999)[15,16] and Mazzolani and Piluso (1997)[14] recognized that also, many other parameters influence the rotation capacity of aluminum alloy beams. In the next sections, more information about findings in the field of several parameters is given for the last two decades **[15,16]**.

3.2. Cross-sectional classification

To avoid premature local buckling, the geometrical properties of the cross-section have to guarantee the development of the plastic and ductile behavior of the structure. Therefore, a cross-sectional classification was developed, which has been introduced in EN-1993-1[2]. An analogous classification concept is used for aluminum alloy members in EN-1999-1[3]. According to the limit states, the bending behavior of an aluminum alloy beam can be classified into four different groups. Class 1 refers to ductile behavior and is characterized by the capability of developing an ultimate moment resistance above the full plastic moment and can obtain this moment resistance during sufficient plastic rotation. Sections of class 2 are also able to reach the full plastic moment resistance before local plastic buckling occurs accompanied by an appreciable deformation capacity. Structural members of class 3 can develop the elastic limit moment resistance but, due to premature occurring local buckling, plastic redistribution is not possible. When using class four members, the elastic limit cannot be reached due to premature elastic local buckling of the compressed parts of the section. These cross-sections in the fourth class are also referred to as slender sections **[13,14]**.

The classification system of EN-1999-1 is based on experimental test results and simulations. The width-to-thickness ratio b/t and the 0.2% proof stress are adopted as the critical parameters of the classification system. Unfortunately, the number of test results available for aluminum alloy beams regarding rotational capacity is minimal compared to the number of results available for steel. Nevertheless, a large number of experimental tests are needed because of the wide variety of aluminum alloy tempers and section shapes. Therefore, recent research focused onto the plastic rotation is done with means of FE simulations. The most recent studies in this area are those performed by Su et al. (2014)[17], Castaldo et al. (2016)[12,13], and Piluso et al. (2018)[18]. They all pointed out the lack of considering other parameters influencing the ultimate moment and deformation capacity of aluminum alloy members. For example, neither the $f_u/f_{0.2}$ ratio nor the longitudinal stress gradient due to shear is considered. Also, no attention is paid to the hardening of the material or the possibility of premature tensile failure due to reduced material ductility **[12, 13, 17, 18]**.

3.3. Slenderness parameter

Currently, the classification of a cross-section is based on the slenderness and the 0.2% proof stress. The majority of the studies consider this slenderness by the normalized parameter. This normalized parameter is defined as the local slenderness λ_f divided by the Eulerian slenderness λ_0

$$\lambda = \frac{\lambda_f}{\lambda_0} = \frac{\sqrt{\frac{12(1-v^2)}{k}} \cdot \frac{c_f}{t_f}}{\pi \cdot \sqrt{E/f_{0.2}}}, \tag{3.3}$$

where v is the poisons ratio, k the buckling factor, c_f the length of the element, t_f the thickness of the element, E the Young's modulus and $f_{0.2}$ the 0.2% proof stress **[11,18]**. The buckling factor k has different values for outer or inner elements since it depends upon the support conditions. For inner elements, this results in $k = 4{,}00$ (both edges simply-supported). For outer elements like flanges, which are considered as pin-free elements (one edge simply supported), the buckling factor can be substituted by $k = 0{,}425$ and $c_f = \frac{b}{2}$. This results in the following simplified equations

for inner elements [11]

$$\lambda = 0{,}52 \cdot \frac{b}{t}\sqrt{\frac{f_{0.2}}{E}}\ ; \tag{3.4}$$

for outer elements [18]

$$\lambda = 0{,}807 \cdot \frac{b}{t}\sqrt{\frac{f_{0.2}}{E}}\ . \tag{3.5}$$

In the standard EN-1999-1-1, the slenderness parameter is calculated by

$$\beta = b/t\ . \tag{3.6}$$

This parameter only considers the width-to-thickness ratio. However, the buckling factor is covered by the fact that some different slenderness limits are defined for inner or outer elements. The Young's modulus and the poisons ratio are considered independent of the alloy. The $f_{0.2}$ value is covered by the fact the slenderness limits are depending on $\varepsilon_{limit} = \sqrt{\left(\frac{250}{f_{0.2}}\right)}$.

The slenderness of a cross-section is calculated for the plates separately, as shown in Figure 3.2 and not considering the interrelation of the slenderness parameters between the different plates composing the cross-section **[3, 11, 18]**.

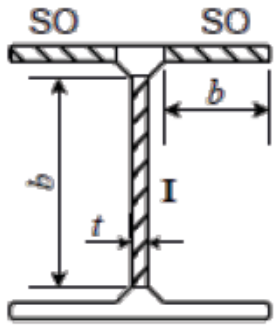

Figure 3.2: definition of b and t values for the slenderness parameter [3].

The studies of Mazzolani and Piluso (1997)[14], De Matteis et al. (2001,2004)[11,19], Castaldo et al. (2016)[12], and Piluso et al. (2019)[18] recognize a significant effect of the slenderness parameter on the rotational capacity. They all mentioned that an increasing ratio of the slenderness leads to a decrease of both moment and rotational capacity. The rotation capacity of low slenderness ($\lambda = 0.24$) sections

was, in some cases, almost 15 times as higher than high slenderness ($\lambda = 0.50$) sections. Also, all the studies noticed a small influence on the rotational capacity by the shear length, flange to web interaction, and the strain hardening. From the results of these studies, the researchers concluded that the slenderness parameter is the most governing factor regarding the moment and rotational capacity. However, taking in mind that also some other parameters influence the rotational capacity, it seems that considering only the slenderness and the 0.2% proof stress is still very conservative.

3.4. Shear length and stress gradient

The studies of De Matteis et al. (2001,2004)[11,19], Castaldo et al. (2016)[12], and Piluso et al. (2019)[18], mentioned that the ratio between shear length and flange width has a significant influence on the available rotation capacity. This ratio, also known as the moment gradient steepness or the compactness ratio, can be calculated by

$$compactness\ ratio = \frac{L_s}{b_f}, \tag{3.7}$$

where, L_s is the shear length, defined as the length between the zero-moment point and the plastic hinge location. For a 3-point bending test L_s is equal to half the span of the beam **[18]**.

The studies of De Matteis et al. (2001) and Castaldo et al. (2016) mentioned both that the compactness ratio strongly affects the post-buckling behavior. For example, Castaldo et al. showed that the rotation capacity halved when the compactness ratio doubled. However, the researchers stated that moment resistance and stable part of the rotation capacity were barely affected. In contrast with these studies, Piluso et al. (2019) recently mentioned there is an influence of the compactness ratio on both the ultimate moment resistance and the stable rotation capacity. For low slenderness values, they noticed a significant decrease in the stable rotational capacity in conjunction with a small decrease of the moment resistance for increasing values of L/b. The increase in stable rotational capacity was also in these cases, roughly equal to the rate of decrease in the compactness ratio.

3.5. Web and flange interaction

Currently, the cross-sectional classification system of the EN-1999-1-1 not considers the interaction between the web and flange slenderness. However, Mazzolani and Piluso (1997)[14] mentioned in their study the importance of this interaction as it is likely that web slenderness influences the buckling behavior of the compressed parts. De Matteis et al. (2001)[11] noticed a negligible influence in the case of rectangular hollow sections. However, in a follow-up study of De Matteis et al. (2004)[19], they concluded that the interaction could substantially influence the inelastic behavior of I-shaped beams. Also, Castaldo et al. (2016)[12] and Piluso et al. (2019)[18] recognized this, especially in the case of low flange slenderness.

3.6. Ratio ultimate strength to 0.2% proof stress and strain hardening

Many studies frequently mentioned the dominant influence of the strain hardening on the rotational capacity of aluminum alloy beams. The strain hardening is related to the $f_u/f_{0.2}$ ratio and depends on the temper used. Non-heat-treated alloys exhibit a characteristic high strain hardening behavior and a corresponding large $f_u/f_{0.2}$ ratio. Heat-treated alloys show a weaker hardening and, therefore, usually also with a lower $f_u/f_{0.2}$ ratio.

The importance of the f_u/f_y ratio in steel structures, and hence the strain hardening, was already pointed out by Steenbergen et al. (1996)[20] using a specially developed numerical model. They investigated several parameters for a three-point bending model, including the f_u/f_y ratio. Varying the f_u/f_y ratio from 1.0 to 1.5 led to an increase of the ultimate moment to elastic moment ratio (M_u/M_e) of about 40%, where the available rotational capacity increased from a value of 1 up to 15.

Also, the results showed that values lower than 1.05 for the f_u/f_y ratio led to unsafe situations by a lack of rotation capacity. Although the research focused on structural steels, it shows the importance of the f_u/f_y ratio and the corresponding strain hardening.

Moen et al. (1999)[16] further investigated the influence of the strain hardening on the rotation capacity for aluminum alloy structures. With the help of a numerical study, they stated that the rotational capacity directly depends on the strain hardening behavior. Materials with much hardening will have more rotational capacity compared to a material with little hardening. This increase in rotational capacity holds even for the same values of ultimate curvature, which is explained in Figure 3.3. The beam with much hardening (at plots d) extends the plastic hinge over a broader region of the beam length compared to the cases as can be seen for steel (b.) or low hardening aluminum (c). The more rounded curvature gradient for the high hardening material leads to this broader region. Therefore, more curvature and deformation are obtained until failure.

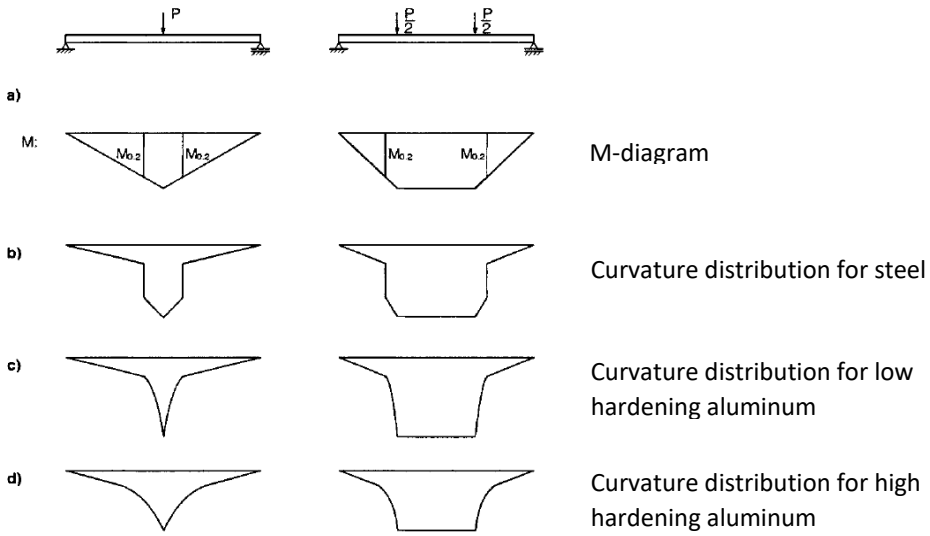

Figure 3.3: schematized Moment-Curvature behavior of Beams. a): Static system, b): Curvature distribution of steel beam, c): curvature distribution of Aluminum low strain hardening, d): Curvature distribution Aluminum high strain hardening [15].

Based on the findings of Figure 3.3, Moen et al. (1999)[15] concluded that the first proposed slenderness limits in EN-1999-1-1 were too conservative. Since the standard was unable to account for the increased rotational capacity due to material strain hardening. After the study was conducted, the standard was adjusted. Also, De Matteis et al. (2001, 2004)[11,19] and Manganiello et al. (2005)[21] pointed out the significant influence of strain hardening on the rotational capacity and ultimate load. Manganiello et al. (2005) mentioned that the extension of the plastic zone depends heavily on the hardening properties of the material. Consequently, it led to the conclusion that the plastic hinge method could be too conservative for strong hardening alloys and unsafe in the case of weak hardening alloys. Manganiello et al. tested two continuous beams with the same conditions but different material properties to examine the significance of the hardening properties. For a continuous class 4 cross-section beam with aluminum alloy 5083-O (n=7) and a span of 1 meter, the ultimate load, calculated using the plastic hinge method and EN-1999-1-1, underestimated the results by approximately 25%. For the same setup and cross-section, but with low hardening aluminum alloy 6082-T6 (n=35), the results were overestimated by approximately 15% **[21]**.

In the last decade also, more research was done to the impact of the f_u/f_y ratio at steel materials. Especially due to the increased use of high strength steels. In these high strength steel materials, the ratio f_u/f_y will reach 1.0 closer as known for mild steels. Even though these studies did not consider

aluminum alloys, it emphasizes the importance of the ratio, especially for low values of f_u/f_y. Also, Van Es et al. (2018)[23] raised some questions regarding the impact of the f_u/f_y ratio. They stated, as in the study of Steenbergen et al., that the f_u/f_y ratio influences the ability to form a plastic hinge in steel members. Also, Van Es et al. pointed out the relevance of the ratio at elements containing a change in geometry or near welds and bolts since the f_u/f_y ratio influence the ability of a structure to redistribute stresses where stress concentrations can occur. For good engineering practice for bolted connections, it is recommended to ensure that plastic deformation occurs before the ultimate load of the net cross-section is reached. Therefore the following condition is introduced: $N_{pl,Rd} < N_{net,Rd}$. To satisfy this condition and to allow the net section to be smaller than the gross section, the f_u/f_y ratio needs to be larger than 1.38. Mild steels clearly have a value higher than this ratio. However, for steel grades S420 and higher, this is not the case considering the values mentioned in-EN-1993-1 (3.2). Also, heat-treated aluminum alloys barely reach a minimum value of 1.38 for the $f_u/f_{0.2}$ ratio. Therefore, it can be questioned if small $f_u/f_{0.2}$ ratios can lead to brittle and unsafe behavior of aluminum alloy elements.

3.7. Influence of welding

By welding of aluminum alloy members, the material properties near the weld are significantly affected. This results in a noticeable reduction of material strength, especially with heat-treated or cold worked aluminum alloys. This reduction can influence the resistance and ductility of a structure. Matusiak and Larssen (1999)[24] mentioned that still, limited experimental information is available relating to the structural response of aluminum alloy members containing transverse welds. They addressed that Robertson (1985) already stated that welding primarily caused a change in failure mode for aluminum alloy beams. By applying transverse welds, the failure mode of local buckling changed to tensile failure in the flange. Matusiak et al. (1999) performed in their study four-point bending tests on class 2 cross-section aluminum beams with different welding configurations. The welded stiffeners showed the most detrimental effect and poor structural behavior, as shown in Figure 3.4. Also, the study noticed that both the ultimate moment resistance and especially the ductility reduced significantly due to material softening. Also, the other specimens containing a weld in the tension flange showed a ductility reduction. Both specimens with a butt weld or a bracket (fillet) weld in the tension flange showed a similar behavior as the welded stiffener. However, with less reduction of the ultimate moment resistance compared to the welded stiffener specimen.

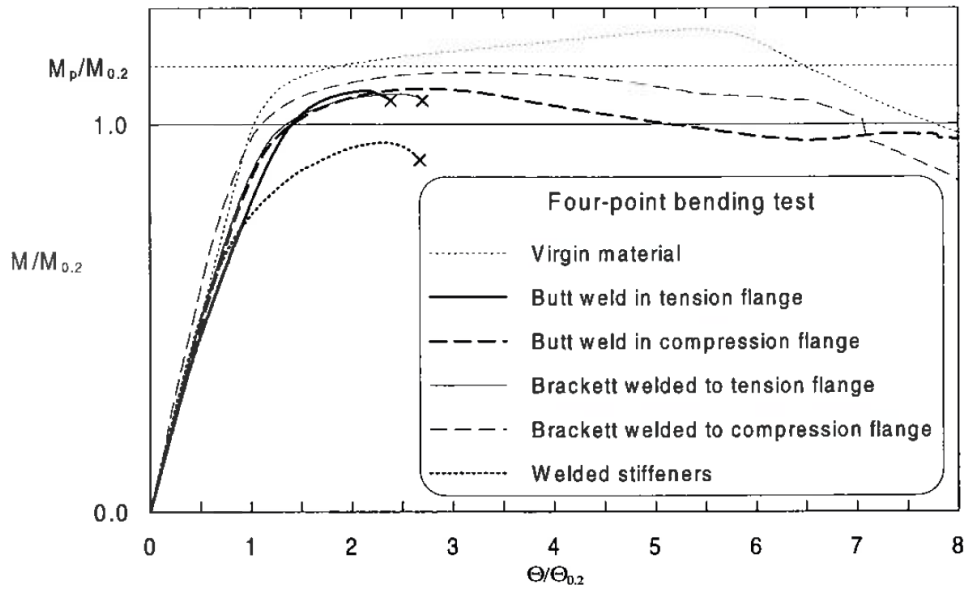

Figure 3.4: Normalized moment – rotation diagram for different test specimens [24].

Also, Moen et al. (1999)[15] investigated the behavior of welded aluminum alloy beams. They carried out both bending tests as some tensile specimen experiments and noticed that the local response of the members near the welds was ductile. However, since the extent of the HAZ was very small related to the beam length, the member failed abruptly due to stress and strain concentrations in the HAZ. The bending tests showed that all the specimens failed in the HAZ of the tensile flange with an ultimate moment reduction of about 25%. This failure occurred without any development of other instability modes. Tensile flange failure is a deformation mode, which is not considered in the cross-sectional classification system. Therefore, it was concluded that welded stiffeners must be avoided since both strength and ductility are severely reduced. Avoiding welded stiffeners is especially crucial for class 1 cross-sections since these require extensive rotation capacity.

Chan and Porter Goff (2000) [44] also addressed the negative effect of the use of transverse welds perpendicular to the load path. The study suggested that transverse welds significantly reduce the load-carrying capacity and the ductility of members. They stated in their study that a more efficient connection might be created by longitudinal welds parallel to the loading direction, carrying the forces through shear. In this study, the researchers investigated several longitudinally welded joints and the corresponding effect on the load-carrying capacity, ductile behavior, and the mode of failure.

Chan et al. (2000)[44] carried out two series of tests in total. They designed the first series to investigate the behavior of different welding configurations and the corresponding failure load. The second series was to evaluate three different finger profiles and their corresponding failure load. In Figure 3.5 a schematization of the designed longitudinally welded specimen is shown. The main concern in all the experiments was the ultimate load-carrying capacity. Therefore, the experiments were performed using a load-controlled method. The experiments showed that all specimens failed with a crack at the end of the finger, beginning near the weld toe. It was noticed that the narrower specimens of 100 mm wide are more efficient as the wider cruciform specimens of 200 mm wide. The narrower specimens better utilized the cross-section with a higher average stress value. Trimming of the rectangular finger to a triangular or parabolic shape reduced the ultimate load capacity by about 2.5% to 10%. However, applying a parabolic or triangular-shaped finger enlarged the ductility of the joints with about 1.4 and 2.7 times more plastic deformation, respectively. The initial stiffness was similar for all specimens but yielding occurred at lower loads for the parabolic and triangular-shaped finger specimens.

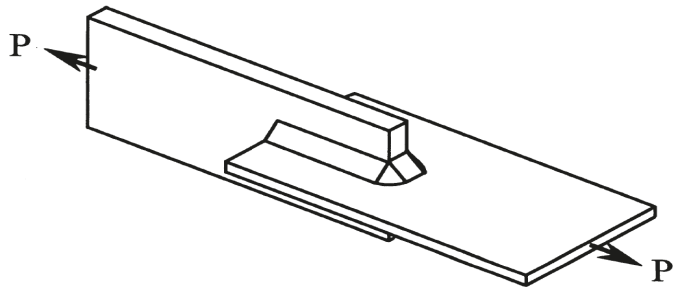

Figure 3.5: Schematization of the longitudinally welded specimen from the study of Chan et al. [44].

Next to the experimental tests, Chan et al. also performed some numerical analyses. These numerical analyses approached the experimental results with an overestimation of about 10% of the ultimate load capacity and the yield point of the specimens. This overestimation indicates that the actual specimens were less stiff in the plastic load region as compared to the numerical models.

Tin Wang (2006)[25] conducted an extensive study into welded thin-walled aluminum structures to develop a comprehensive capacity prediction of welded aluminum structures. Wang mentioned that, besides the loss of strength, the HAZ leads to a reduced ductility compared to an unwelded situation.

It was mentioned that the reduced ductility was caused by strain localization in the softest part of the HAZ and, consequently, premature failure of the welded component. Wang indicated that the common design codes provide reasonable estimations of the locally reduced strength of welded aluminum alloy members. However, no information and guidelines are available for the prediction of its ductility. This lack is present despite the importance of the loss of ductility over the loss of strength in some cases. Therefore, it was useful to investigate a method to predict the loss of ductility.

Wang (2006) performed experimental tests to assess the accuracy and robustness of the numerical model. Next to the validation purpose, also some interesting findings could be noticed from the experimental results. Based on the results of the experiments of the welded connections in tension, Wang noticed that failure occurred as expected in the HAZ, in conjunction with small deformations. The small deformations happened due to strong strain localization in this weaker part of the structure. Wang tested three types of different weld configurations with shifting weld orientations. The geometry of the tested specimens is shown in Figure 3.6 and the angle θ was varied from 0 to 45 degrees. From the results, they concluded that the strength and ductility are dependent on the weld configuration. A weld orientation of $\theta = 45°$ leads to an increase in strength of about 10% and 80% more deformation compared to a transversely welded ($\theta = 0°$) situation. For the $\theta = 30°$ weld orientation also an increase in strength of about 10% was observed. However, no significant change in ductility occurred.

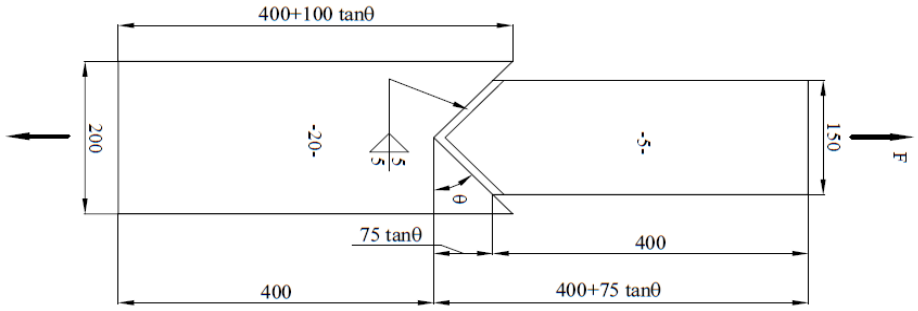

Figure 3.6: Geometry of the tested specimens by Wang [25].

As mentioned earlier, the main objective of the study was to assess the accuracy of a numerical model to predict the capacity of welded members. With the help of parametric studies, Wang investigated the influence of several parameters on the results of the models. This parametric study also included the effect of dividing the HAZ into several sub HAZ zones. By subdividing the HAZ into zones, the development of varying material strength over the HAZ length can be better represented. By comparing the results of the numerical analyses, it was found that the estimated ductility was dependent on the length of the sub-HAZ's. Especially, the length of the weakest sub-HAZ and the total HAZ length influenced the structural ductility the most. From an analytical study into strain localization, Wang noticed that subdividing the HAZ into six zones could lead to a decrease in the ultimate deformation of about six times compared to the situation with one homogeneous HAZ. By these findings, it is concluded that a detailed representation of varying material in the HAZ needs a different approach to accurately estimate the structural ductility. A small weak subpart of the HAZ will lead to strain localization in this zone. As a consequence, a small length of the specific zone will lead to a small deformation of the entire structure. Therefore, Wang recommended a minimal length of the sub-HAZ equal to the thickness of the member to obtain an accurate representation of the ductility **[25]**.

3.8. Conclusions from the literature review

From the literature study, one can conclude that regarding the rotation capacity of bending members, the slenderness of the member is the most influential parameter. Next to that, it was pointed out that the $f_u/f_{0.2}$ ratio and the strain hardening behavior of the used aluminum alloy has a significant impact. It appeared that strong hardening materials experienced a larger rotation capacity. Also, the web-flange interaction and the shear length showed some influence on the rotational capacity and hence the ductility, but to a much smaller extent.

Something that does immensely affects the ductility behavior of a structure is welding. It was already showed in Section 2.4.1 that the heat-affected material near welds can be more ductile than the base material by means of a higher $f_u/f_{0.2}$ ratio and additionally in some cases a higher strain at rupture. This was also outlined in the studies of Wang (2006)[25] and Woelke et al. (2017)[39]. However, Woelke et al. also noticed that the low strength and the limited size of the HAZ lead to a limited extent of plastic deformation near the weld. This results in a decrease in the overall ductility of the structure. Therefore, it was outlined in several studies that welding in the tensile zone of a structure must be avoided. Primarily for transversely welded structures a drastic reduction in ductility was noticed since transverse welds often results in a HAZ over the complete critical cross-section.

For aluminum alloy structures containing longitudinal welds, probably more ductility can be achieved. Wang (2006) already showed some promising results by rotating the weld from a transverse orientation to a diagonal orientation. However, comprehensive studies into the ductility of longitudinally orientated welds are still lacking.

4. Experimental research

An experimental research is conducted to examine the influence of welding on the ductility of aluminum alloys. By performing the experiments, more knowledge in this field is gathered where extensive previous research is still lacking. In order to be able to construct an accurate representation of the experimental results by a numerical FEM model, also material specimen tests were performed. Firstly, the material properties are obtained by testing dogbone specimens of both welded and unwelded samples. With the help of the dogbone results, the materials in the numerical model can be calibrated. Secondly, to determine the size of the HAZ caused by welding, hardness tests have been carried out. Thirdly, the welded cruciform specimens were tested. The results of these welded specimens were used for validation of the numerical cruciform model. Finally, experiments were conducted on bolted connections. The results of these bolted connections were used to compare the deformation capacity of the welded specimens.

4.1. Dogbone experiments

4.1.1. Introduction

Dogbone material experiments were performed in order to obtain the actual mechanical material properties. The obtained experimental results will be used for calibrating the material properties in the numerical model. The dogbone specimens were constructed from the same material batch as been used for the welded cruciform and bolted joint specimens. Hence, both aluminum alloy 6082T6 and 5083H111 material were examined. Also, both types of aluminum alloys were tested in welded and unwelded conditions. The welded dogbones consist out of a transversely welded and a longitudinally welded situation, representing correspondently local heat-affected material and fully heat-affected material. The unwelded dogbones tests were conducted to retrieve the base material properties.

4.1.2. Dogbone test specimens

As mentioned, three different kinds of dogbone specimens per aluminum alloy type were tested. Table 4.1 shows the different kinds of tested specimens.

Table 4.1: Dogbone specimen types for material properties testing.

Aluminum alloy	Type of weld	Specimen code	# of tests
6082T6	Unwelded / Base material	BM.6.1- BM.6.4	4
	Longitudinally welded	LW.6.1 - LW.6.4	4
	Transversely welded	TW.6.1 - TW.6.4	4
5083H111	Unwelded / Base material	BM.5.1 - BM.5.4	4
	Longitudinally welded	LW.5.1 - LW.5.3	3
	Longitudinally welded, 30mm away	LW.5.4 - LW.5.5	2
	Longitudinally welded, 100mm away	LW.5.6 - LW.5.9	4
	Transversely welded	TW.5.1 - TW.5.3	3

All the dogbone specimens are produced with the same dimensions. The dimensions were based on the guidelines regarding the standard ISO-6892-1[51], resulting in the dimensions listed in Table 4.2, corresponding to the indicated measures in Figure 4.1.

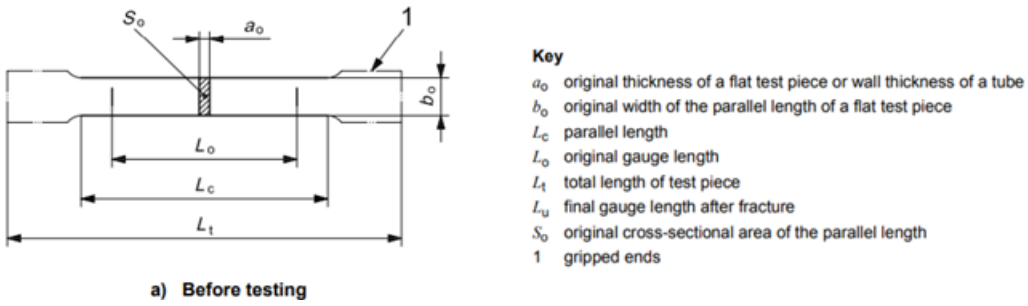

Figure 4.1: Coupon test dimensions [51].

Table 4.2: Applied dimensions for the tensile specimens.

	Applied [mm]
t	8
Width	12
Radius	12
L_0	60
L_c	75
L_t	300

4.1.3. Test set-up

Quasi-static tensile tests were carried out on the dogbone specimens at ambient temperature with the help of an Instron 250 kN testing machine. The specimens were loaded with a testing speed of 0.6 mm/min. The applied force and the crosshead displacement were recorded using a 250 kN load cell at the top of the testing machine. Next to the crosshead displacement, the deformation of the specimens was measured locally using Digital Image Correlation. The displacement of two marked dots placed 60 mm away from each other was measured. With the help of the measured displacement of these two points, the occurring strains were calculated as well as the strain at rupture A_{60}. Figure 4.2 shows a picture of the test set up in practice with the marked dots. For the transversely welded 6082T6 specimens also strain gauges were applied adjacent to the weld. This in order to measure the strains locally near the weld.

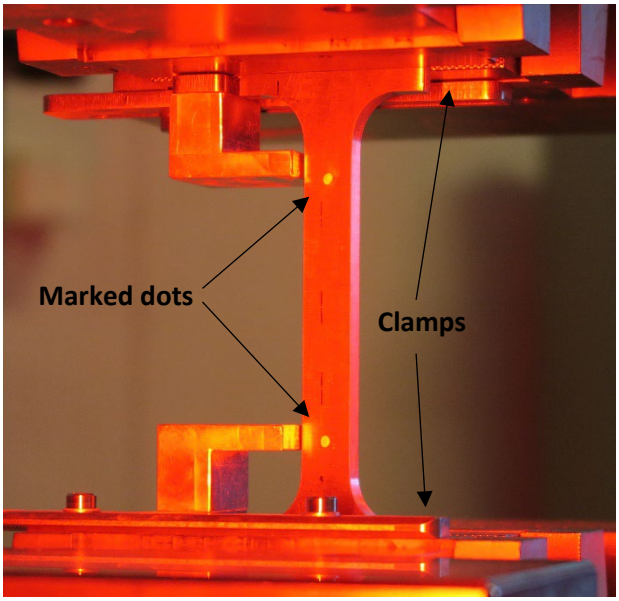

Figure 4.2: Test set-up in practice.

4.1.4. AA6082T6 dogbone results

In total, 12 dogbone specimens of aluminum alloy 6082T6 were tested. Four times the base material specimens, four times the longitudinally welded specimens, and four times the transversely welded specimens. The results of these tests are discussed in the next sections.

4.1.4.1. Base material

The unwelded dogbones are representing unaffected aluminum alloy 6082T6 material. As mentioned earlier, four specimens were tested. The results are plotted in Figure 4.3, and the key results are given in Table 4.3. These key results include the 0.2% proof stress $f_{0.2}$, the ultimate strength f_u, the elastic modulus E, and the strain at rupture A_{60} measured over $5.65\sqrt{A_o} \approx 60\ mm$. Next to the average of the specimens, also the standard deviaton (St. dev) and the Coefficient of Variation (CV) is given.

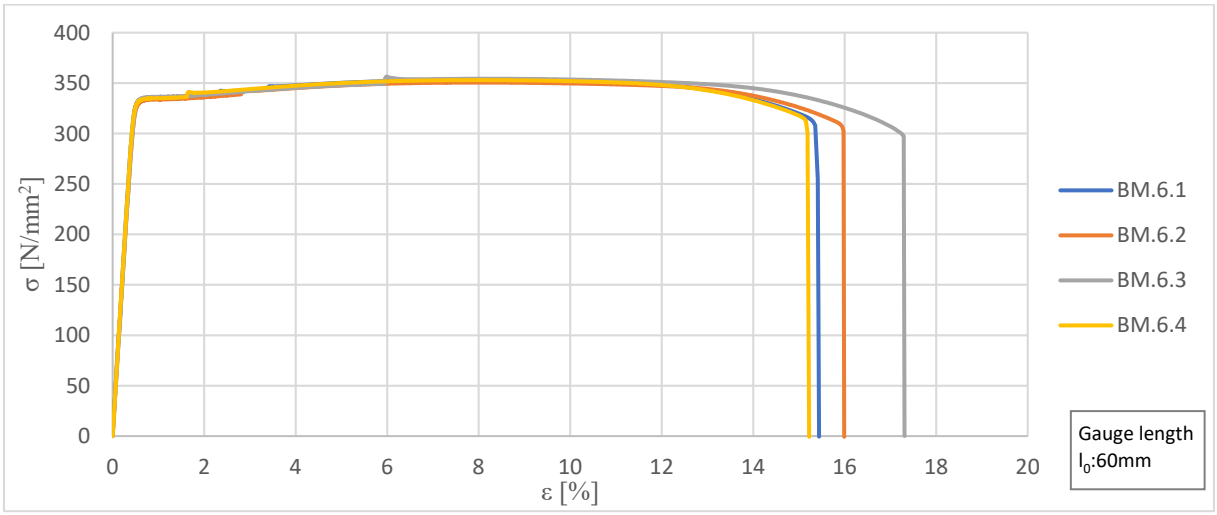

Figure 4.3: Stress-strain diagram of the AA6082T6 base material dogbones.

Table 4.3: Key results of the AA6082T6 base material dogbone coupons.

	Base material								
	Coupon 1	Coupon 2	Coupon 3	Coupon 4	**Average**	**St. dev.**	**CV**	**Certificate**	Dimension
$f_{0.2}$	334.5	332.4	335.5	333.9	334.0	1.12	0.34%	321	N/mm²
f_u	353.1	350.6	356.6	353.0	353.3	2.14	0.61%	352	N/mm²
E	74476.5	71979.1	71412.8	74244.0	73028.1	1349.6	1.85%	-	N/mm²
A_{60}	15.44	15.99	17.31	15.22	15.99	0.81	5.07%	16	%

The results show that the different specimens exhibited somewhat similar behavior with a minimal deviation in strength. The largest deviation is experienced for the strain at rupture of about 5%. Also, the given values by the certificate were matched close, except for the 0.2% proof strength.

4.1.4.2. Longitudinally welded

The results for the longitudinally welded AA6082T6 dogbone specimens are plotted in Figure 4.4 and listed in Table 4.4. These dogbones are representing fully heat-affected material.

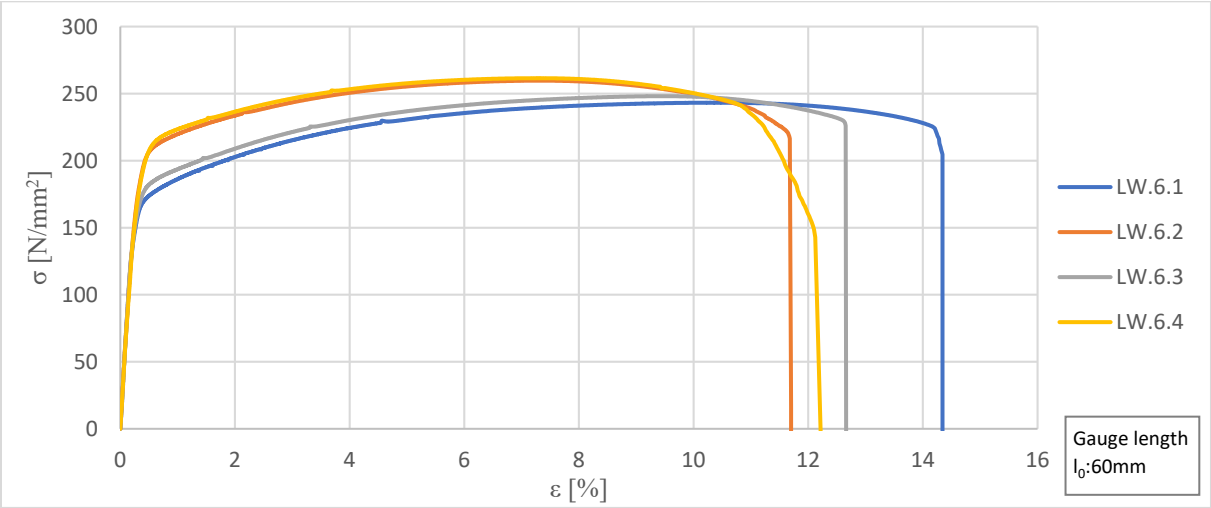

Figure 4.4: Stress-strain diagram of the fully heat-affected AA6082T6 dogbones.

Table 4.4: Key results of the longitudinally welded AA6082T6 dogbones.

	Fully heat-affected							
	Coupon 1	Coupon 2	Coupon 3	Coupon 4	**Average**	**St. dev.**	**CV**	Dimension
$f_{0.2}$	171.5	205.9	180.0	207.9	191.3	15.88	8.30%	N/mm²
f_u	243.3	259.7	248.1	261.5	253.2	7.69	3.04%	N/mm²
E	70477.5	70865.9	70959.8	68090.2	70098.4	1173.4	1.67%	N/mm²
A_{60}	14.34	11.70	12.66	12.22	12.73	0.99	7.78%	%

From Figure 4.4 and Table 4.4, it is noticed that the results can be divided into two different cases. Coupon 1 and 3 showed somewhat similar behavior. The same applies to coupon 2 and 4. Figure 4.5 shows the welded strip wherefrom the specimens were retrieved. Specimens LW.6.1 and LW.6.3 were positioned both at the lower half of the welded strip. The other specimen series were placed parallel to this at the upper half of the fabricated strip. By that fact, one can conclude that the LW.6.1 and LW.6.3 dogbones were more heat-affected as the LW.6.2 and LW.6.4 dogbones. This may be caused by a closer placement of the welds to the boundaries of the dogbone specimen or less spacing between the welds.

Figure 4.5: Picture of the longitudinally welded plate produced for dogbone specimens.

4.1.4.3. Transversely welded

Next to the longitudinally welded specimens, also transversely welded dogbones were tested. In this situation, the material is only locally heat-affected. In Figure 4.6, the results of these transversely welded specimens are plotted. In Table 4.5, the key results of these dogbones are listed.

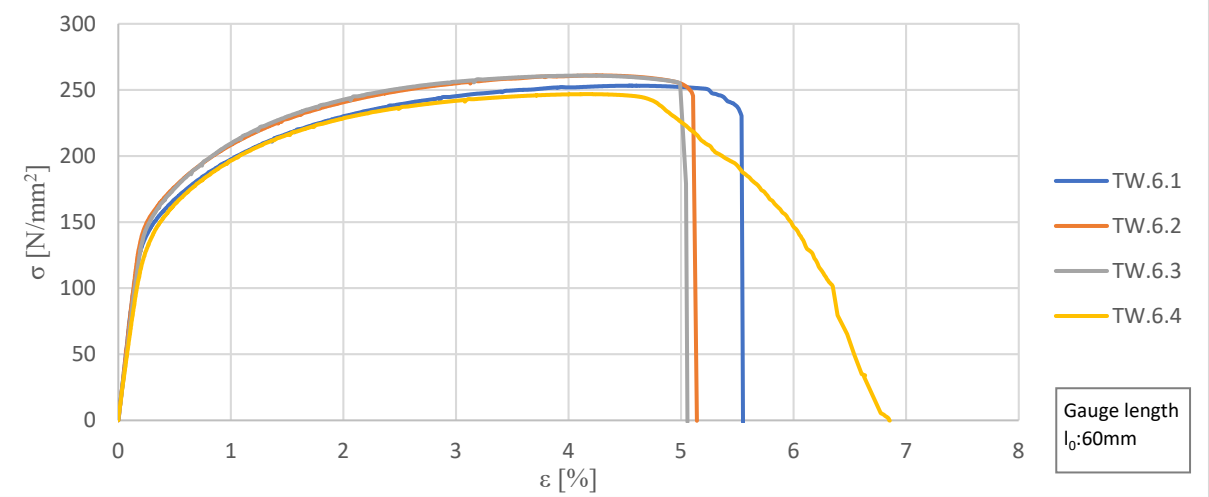

Figure 4.6: Stress-strain diagram of the transversely welded AA6082T6 dogbones.

Table 4.5: Key results of the transversely welded AA6082T6 dogbones.

	Transversely welded coupons							
	Coupon 1	Coupon 2	Coupon 3	Coupon 4	**Average**	**St. dev.**	**CV**	Dimension
$f_{0.2}$	160.0	170.4	170.6	158.4	164.8	5.66	3.44%	N/mm²
f_u	253.2	260.9	260.8	246.8	255.4	5.90	2.31%	N/mm²
E	74159.9	74388.0	68862.4	63818.1	70307.1	4350.1	6.19%	N/mm²
A_{60}	5.55	5.14	5.06	6.85	5.65	0.72	12.73%	%

The results clearly show that the deformations up to failure are much lower in the transversely welded specimens compared to the longitudinally welded specimens. The ultimate stress is, with an average value of 255 N/mm², roughly at the same level as the longitudinally welded specimens. The most notable fact is that there is a big difference between the welded and base material specimens. As known, the welded and, therefore, heat-affected specimens exhibited much lower mechanical strength values. This fact can be seen in the combined graph, plotted in Figure 4.7.

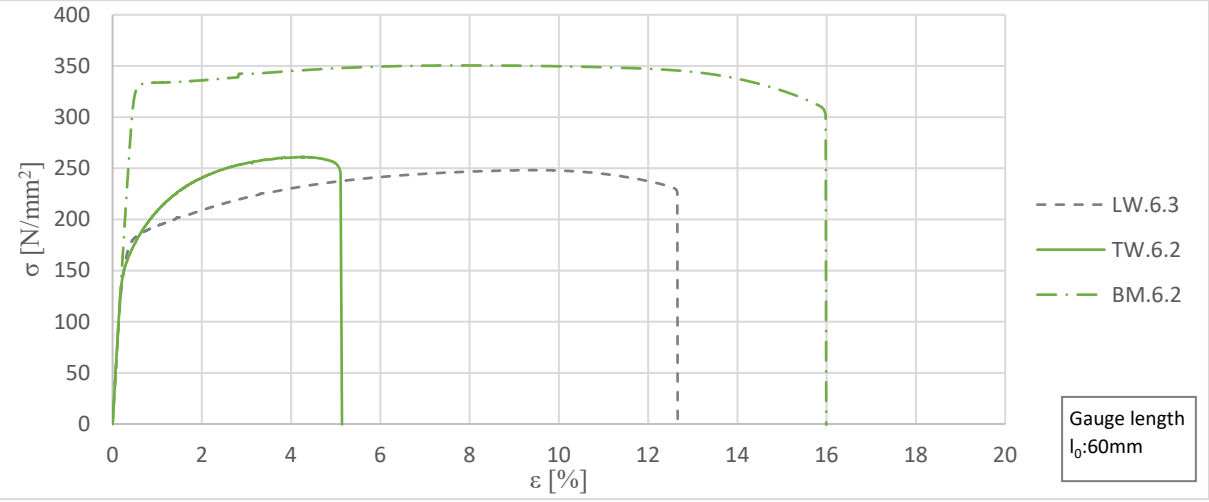

Figure 4.7: Combined stress-strain diagram of the three different AA6082T6 specimen types.

4.1.5. AA5083H111 dogbone results

As discussed, in total, 16 dogbone specimens of aluminum alloy 5083H111 were tested. Also, for this kind of aluminum alloy, both welded and unwelded specimens were tested.

4.1.5.1. Base material

The base material properties were tested using four dogbone specimens obtained from an AA5083H111 plate. The results of these specimens are plotted in Figure 4.8 and listed in Table 4.6. It is noted that there are quite some differences between the results and the certified values. All the specimens showed somewhat similar results, except for the strain at rupture where the highest Coefficient of Variation (CV) is noticed of about 5.3%.

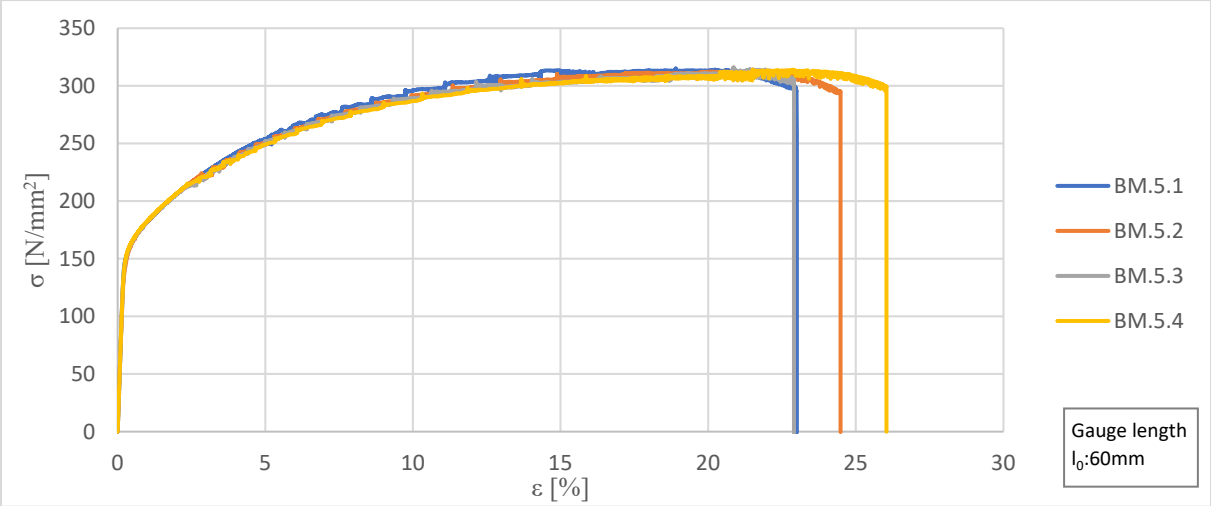

Figure 4.8: Stress-strain diagram of the AA5083H111 base material dogbones.

Table 4.6: Key results of the AA5083H111 base material dogbone coupons.

	Base material								
	Coupon 1	Coupon 2	Coupon 3	Coupon 4	**Average**	**St. dev.**	**CV**	**Certificate**	Dimension
$f_{0.2}$	161.3	159.7	160.9	161.9	160.9	0.80	0.50%	178.0	N/mm²
f_u	315.2	312.8	315.9	314.1	314.5	1.20	0.38%	300.7	N/mm²
E	73166.1	72598.9	75637.7	73795.8	73799.6	1142.6	1.55%	-	N/mm²
A_{60}	23.00	24.49	22.91	26.04	24.11	1.28	5.30%	24.67	%

4.1.5.2. Longitudinally welded

For the longitudinally welded specimens, several experiments were executed. The longitudinally welded dogbones were constructed with help of a 500x500x8 mm AA5083H111 plate. Due to lay out of the welds and dogbone placement, as shown in Figure 4.9, a large number of specimens was retrieved. However, in these series, only the dogbones LW.5.1 to LW.5.3 represent completely heat-affected material. Dogbones LW.5.4 and LW.5.5 represent partly or less heat-affected material due to a welded distance of minimal 30 mm away. Test specimens LW.5.6 to LW.5.9 represent base material due to the considerable distance to the weld of at least 100 mm. The results of the longitudinally welded plate series will be first treated per group as defined above. The results for the fully heat-affected dogbone specimens are shown in Figure 4.10. It can be noticed that specimens showed an almost similar behavior. This is also concluded for the specimen series LW.5.4 and LW.5.5 and series LW.5.6 to LW.5.9, as plotted in corresponding Figure 4.11 and Figure 4.12.

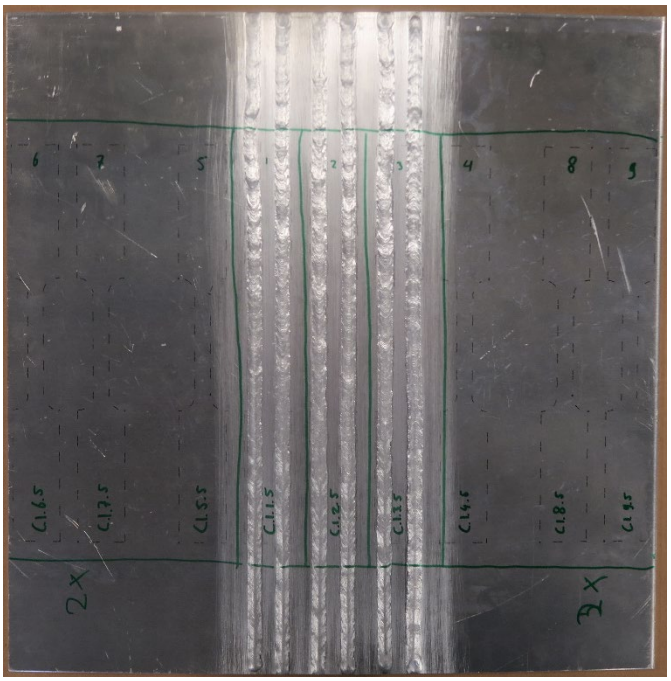

Figure 4.9: Overview of the welded coupon plate.

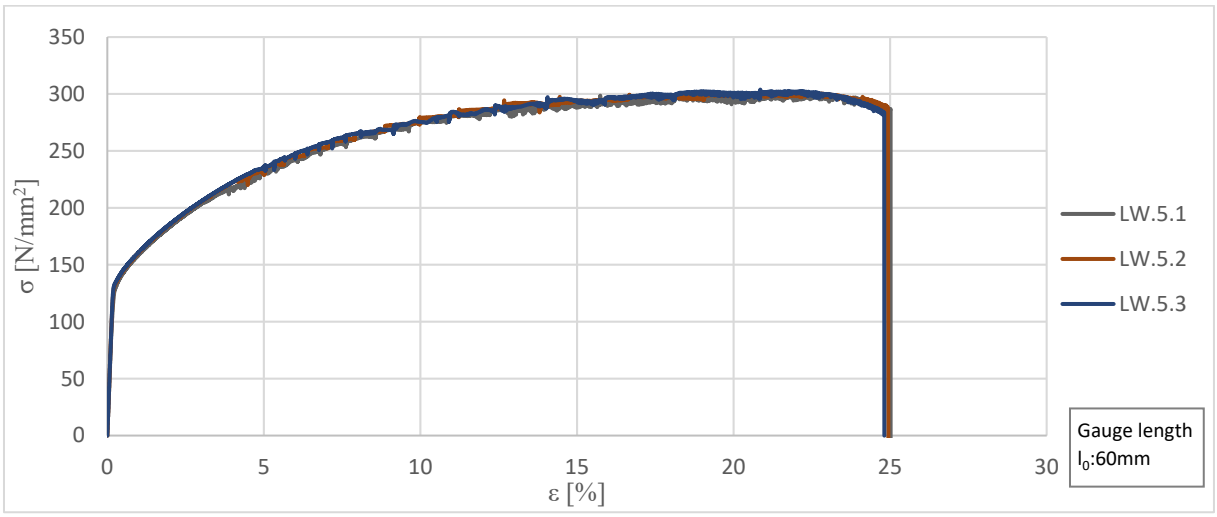

Figure 4.10: Stress-strain diagram of the fully heat-affected AA5083H111 dogbones.

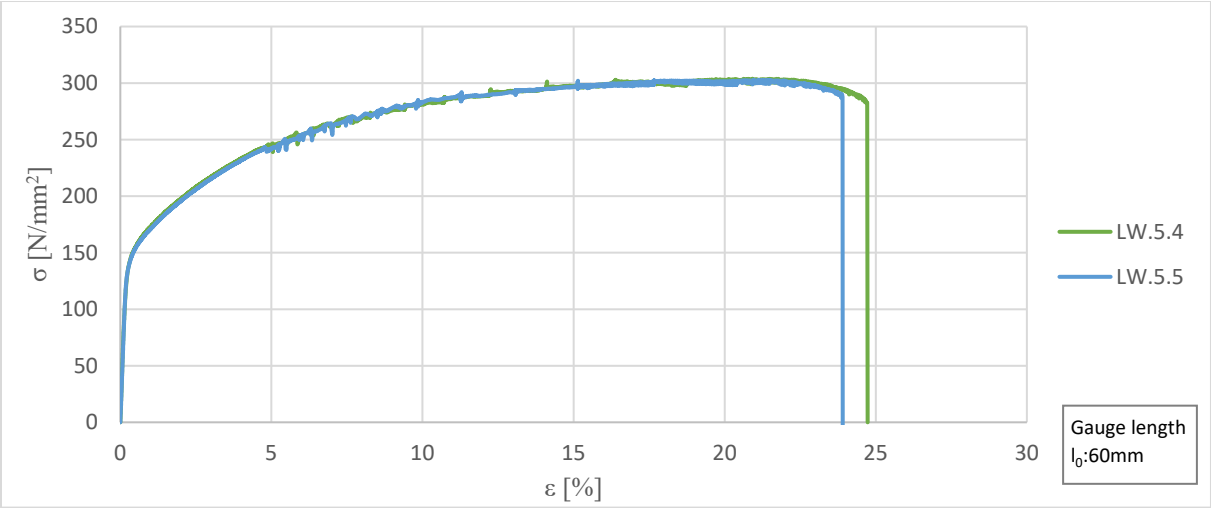

Figure 4.11: Stress-strain diagram of the AA5083H111 dogbones positioned 30 mm away from the welds.

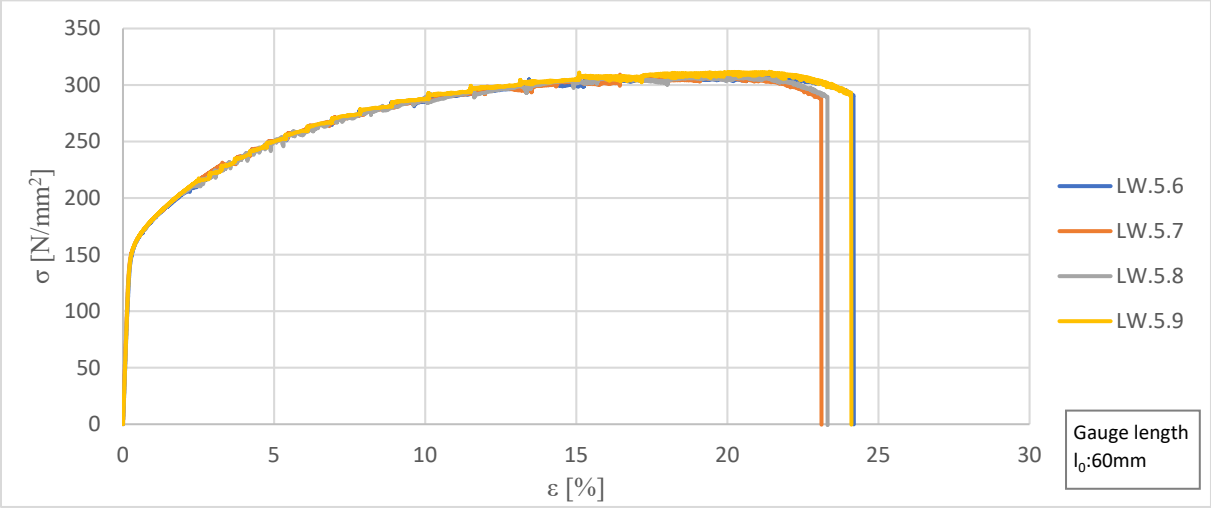

Figure 4.12: Stress-strain diagram of the AA5083H111 dogbones positioned 100 mm away from the welds.

From the results shown in Figure 4.10, Figure 4.11, and Figure 4.12, one is not yet able to see clear differences between a welded and unwelded specimen. However, by plotting the results of the specimens representing the average results of the corresponding series in one graph in Figure 4.13, small differences are noticed. It is concluded that a fully heat-affected specimen experienced both a lower 0.2% proof stress as a lower ultimate strength. This degrading effect can also be found in Table 4.7, where the most relevant results of all samples are shown. From the results, it is also observed that the LW.5.6 to LW.5.9 specimens experienced a somewhat similar outcome as the base material specimens BM.5.1 up to BM.5.4.

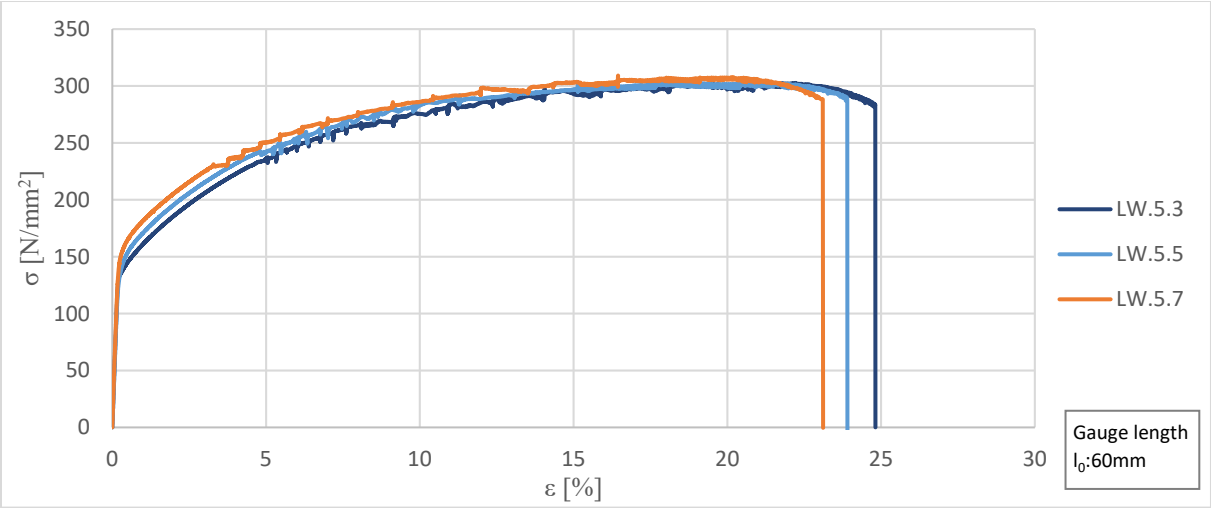

Figure 4.13: Combined stress-strain diagram of the three different types of AA5083H111 dogbones.

Table 4.7: Key results of the longitudinally welded AA5083H111 dogbones.

	Fully HAZ						**25-40mm away from the weld**			
	Coupon 1	Coupon 2	Coupon 3	**Average**	**St. dev.**	**CV**	Coupon 4	Coupon 5	**Average**	Dimension
$f_{0.2}$	137.9	140.0	140.7	139.5	1.20	0.86%	149.9	148.8	149.4	N/mm^2
f_u	299.7	301.1	303.8	301.5	1.70	0.56%	303.9	303.1	303.5	N/mm^2
E	70225.8	74270.3	73099.9	72532.0	1699	2.34%	73390.2	71214.8	72302.5	N/mm^2
A_{60}	25.01	24.94	24.82	24.92	0.08	0.33%	24.73	23.91	24.32	%

	Min. 100mm away from the weld (base material)								
	Coupon 6	Coupon 7	Coupon 8	Coupon 9	**Average**	**St. dev.**	**CV**	**Certificate**	Dimension
$f_{0.2}$	160.6	160.5	160.2	161.0	160.6	0.27	0.17%	178.0	N/mm^2
f_u	308.0	309.2	308.1	311.7	309.2	1.51	0.49%	300.7	N/mm^2
E	70922.2	77515.1	75024.5	73230.9	74173.2	2416	3.26%	-	N/mm^2
A_{60}	24.18	23.11	23.32	24.11	23.68	0.47	1.99%	24.67	%

4.1.5.3. Transversely welded

Next to the longitudinally welded specimens, also transversely welded specimens were produced and tested. The results of these tested specimens are plotted in Figure 4.14 and listed in Table 4.8. From the results, it is noticed that the 0.2% proof stress is decreased compared to the base material properties. Also, the elastic modulus and the strain at rupture is influenced a bit. However, the ultimate strength remained quite constant. For the small deviations are experienced between the specimens with a maximum of about 3.2% for the strain at rupture.

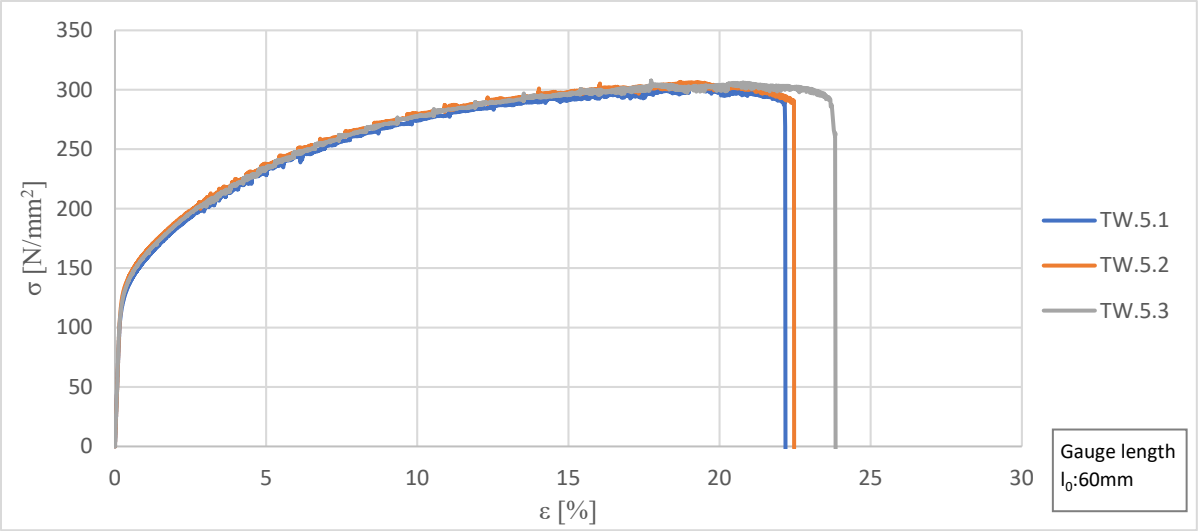

Figure 4.14: Stress-strain diagram of the transversely welded AA5083H111 dogbones.

Table 4.8: Key results of the transversely welded AA5083H111 dogbones.

Transversely welded coupons							
	Coupon 1	Coupon 2	Coupon 3	**Average**	**St. dev.**	**CV**	Dimension
$f_{0.2}$	131.8	139.3	135.3	135.5	3.03	2.24%	N/mm²
f_u	303.2	306.7	307.8	305.9	1.94	0.64%	N/mm²
E	68781.3	70571.6	73555.9	70969.6	1969.5	2.78%	N/mm²
A_{60}	22.18	22.47	23.84	22.83	0.72	3.17%	%

4.1.6. Conclusions from the dogbone experiments

From the results, as discussed in the previous sections, some conclusions can be drawn. Firstly, as expected, a big difference between the welded and unwelded specimens is experienced for AA6082T6. The heat input led to a decrease in both 0.2% proof stress and the ultimate strength in the Heat Affected Zone. The heat-affected specimens of the longitudinally welded series also showed a reduction in the strain at rupture of about 20%. In the case of the transversely welded specimens, the reduction of the strain at rupture was almost 70%. However, this can be dedicated to the stress and strain localization in the locally affected area. Also, it must be noted that the measured strain is dependent on the gauge length. A larger gauge length will result in a lower measured overall strain.

The aluminum alloy 5083H111 show very few differences between the welded and unwelded specimens, in contrast to the 6082T6 alloy. This is also in line with the expectations as it is generally assumed that the heat input of welding not reduced the mechanical properties for this kind of alloy. This because this alloy is not produced by the use of heat treatments. Nevertheless, a small reduction in the 0.2% proof stress by the application of welding is noticed. Both ultimate stress, elastic modulus, and the strain at rupture remained rather stable.

In Figure 4.15, the stress-strain diagrams of the AA6082T6-HAZ material, the AA6082T6 base material, and the AA5083H111 base material are plotted. AA6082T6-HAZ material is represented by the longitudinally welded dogbones since these specimens were fully heat-affected. The graph clearly shows the differences between the different materials.

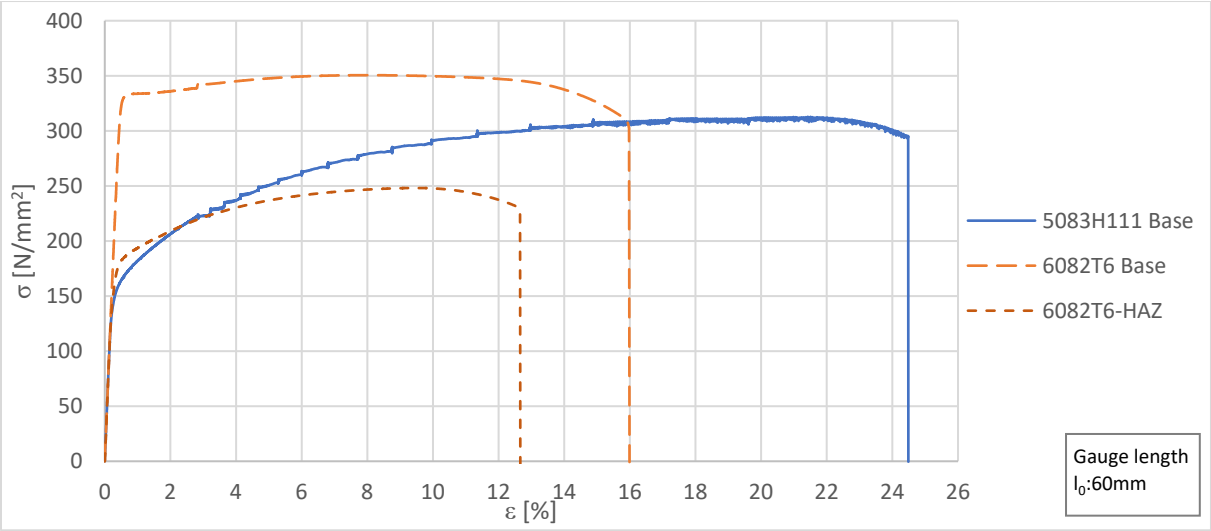

Figure 4.15: Combined stress-strain diagrams of the dogbone specimens.

4.2. Vickers hardness measurements

4.2.1. Introduction

In order to determine the extent of the Heat Affected Zone near the welds, Vickers Hardness tests are performed. These tests were carried out at the Multi-Scale Lab of the department of mechanical engineering at the Eindhoven University of Technology. With the help of a Vickers indenter, in the form of a square-based pyramid made out of diamond, an indentation will be made in the material. The indentation was viewed and measured using an optical microscope and computer software. The principle of the test is to observe the material's ability to resist plastic deformation when applying a specific load. The larger the indentation, the lower the hardness number of the material. The Vickers Hardness number is calculated by

$$HV = F/A\,, \tag{4.1}$$

where F is the force applied by the diamond pyramid in kilograms-force and A the surface of the resulting indentation in square millimeters [52]. The surface A can be determined by

$$A = \frac{d^2}{2\sin\left(\frac{136°}{2}\right)}, \tag{4.2}$$

where d is the average length of the diagonals of the indentation in millimeters. The angle of the pyramidal diamond typically corresponds to a value of 136 degrees. The indenter machine is shown in Figure 4.16. During the experiments, a 200-gram weight was placed in the device. After focusing on the target using the microscope, the indenter was lowered and pressed on the material for about 30 seconds. After this, the indenter will be lifted up, and the indentation can be measured, or another indentation can be made. In Figure 4.17, the optical microscope connected to the computer is shown, which will be used to measure the indentation left by the indenter.

Figure 4.16: Leitz micro Vickers Hardness tester.

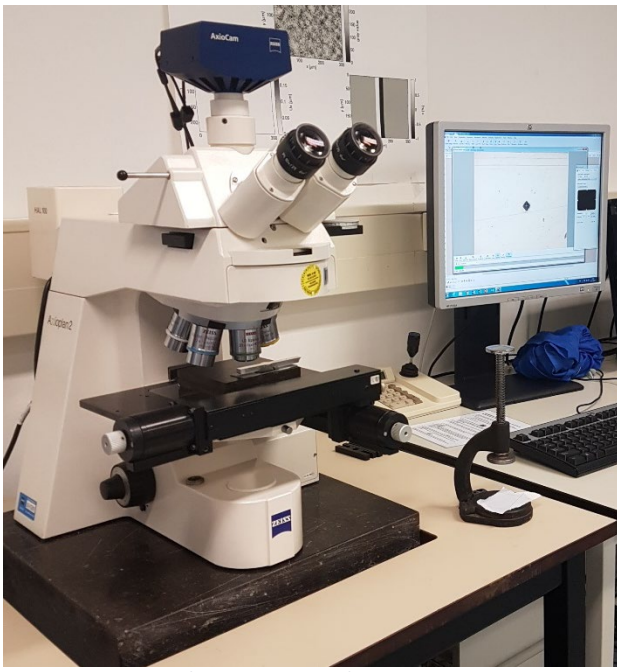

Figure 4.17: Optical microscope and computer.

4.2.2. Hardness specimens

For testing and measuring the Vickers hardness, some limitations were present regarding the dimensions of the specimens. Since the specimens must be able to be placed beneath the indenter and the microscope, the thickness and the width are limited. In addition, there are more requirements. For example, the specimen must have a perfectly flat surface at both sides, in order to guarantee the specimen can be placed stable, which is required for the indentation. The surface to be tested must also be in a perfect mirroring condition, to make sure that there are no more irregularities and to perceive the identification clearly.

The specimens used, consisted of remains after cutting the dog bones and are indicated in Figure 4.18. In total, six specimens were tested. Regarding the 6082T6 alloy, three times a specimen from the transversely welded dogbone was tested and one time a specimen from the longitudinally welded plate representing full HAZ material. Also, an AA6082T6 unwelded specimen was tested for reasons of comparison. For the AA5083H111 material, only one specimen was tested, which was obtained from the transversely welded dogbone. Since the hardness profile was almost constant and the well-known fact that the influence is minimal, no more specimens were tested. Before starting the tests, the specimens were marked first. On each specimen, a grid was drawn from the middle of the weld. On a horizontal line just 1mm below the surface, a point was marked every 5 mm away from the weld. In the tests, the hardness was measured at each of these points. In addition, in the vicinity of the weld, an extra point was measured. Resulting in a hardness measuring point spacing of 2.5 mm for the first 20 mm and subsequently a spacing of 5 mm.

Figure 4.18: Cut out dogbones and indicated hardness specimens.

4.2.3. Vickers hardness results

4.2.3.1. AA6082T6 Base material specimens

To determine when the hardness value of a specimen is back to its 'normal' base material level, a piece of the base material was tested. Five points were tested around the cross-section centerline of this specimen, corresponding to a depth of about 4 mm below the material surface. The points were separated 10 mm from each other. From the results, an average value for the Vickers hardness number of about 110 HV was found. For the upcoming experiments of the AA6082T6 samples, it is assumed that when a value of 110 HV is reached, the material is back at its base material level, and so on, no HAZ is present at this measured point.

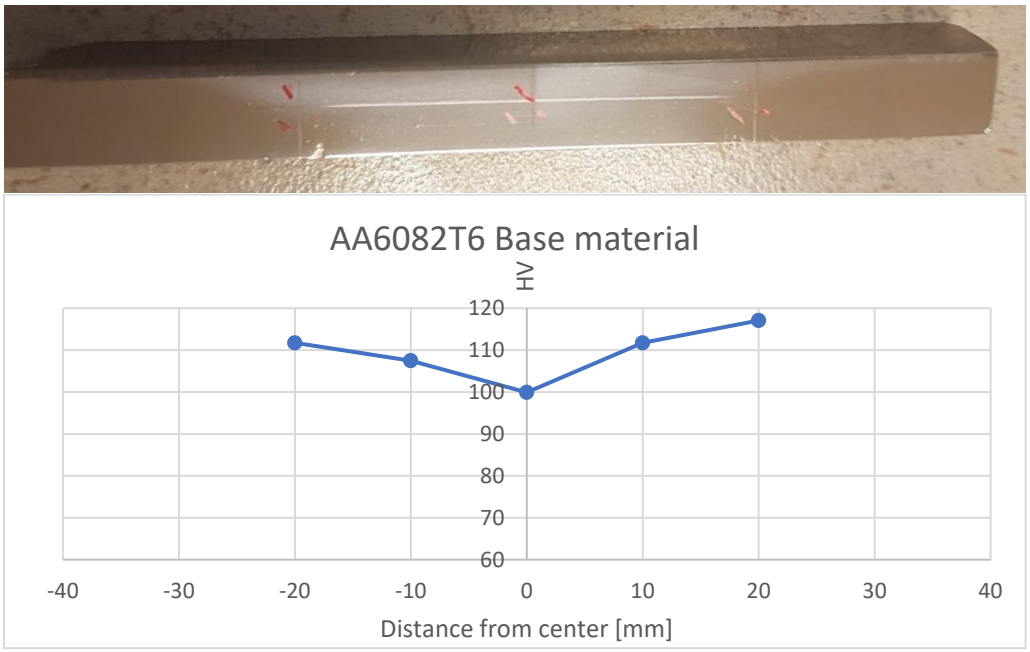

Figure 4.19: Vickers Hardness profile and a picture of the tested base material specimen.

Table 4.9: Vickers Hardness measurement results of the base material.

Distance from center [mm]	d_1 [µm]	d_2 [µm]	$d_{,avg}$ [mm]	A	HV
-20	57.08	58.14	0.057610	0.001790	111.7
-10	57.79	59.69	0.058740	0.001861	107.5
0	60.59	61.26	0.060925	0.002002	99.9
10	56.55	58.67	0.057610	0.001790	111.7
20	56.02	56.55	0.056285	0.001708	117.1
				Average	109.6
				Standard deviation	6.39

4.2.3.2. AA6082T6 Transversely Welded specimens

Two cutting leftovers of the transversely welded dogbone specimens were prepared and tested. One specimen of the TW.6.3 dogbone and one of the TW.6.4 dogbone. In total, 49 indention points were made and measured on the TW.6.3 specimen and 57 points on the TW.6.4 specimen. An example of a hardness specimen is shown in Figure 4.20. Figure 4.21 shows a schematization of a specimen with the indentation locations. The measured values of the Vickers Hardness test are visualized in a plot in Figure 4.22 and Figure 4.23. The hardness profiles show that the material was heat-affected to about 15 mm from the center of the welds. At a distance of more than 15 mm from the center, the hardness returned to its original value. Based on these observations, it is concluded that the size of the HAZ is limited to about 15 mm.

Figure 4.20: Prepared TW.6.3 specimen for measuring hardness.

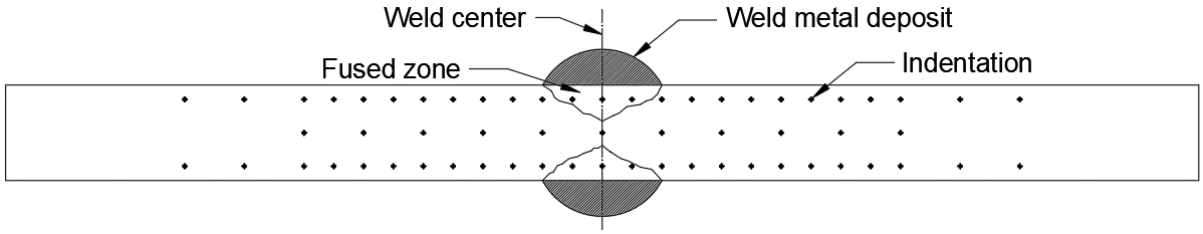

Figure 4.21: Schematization of an indented hardness specimen.

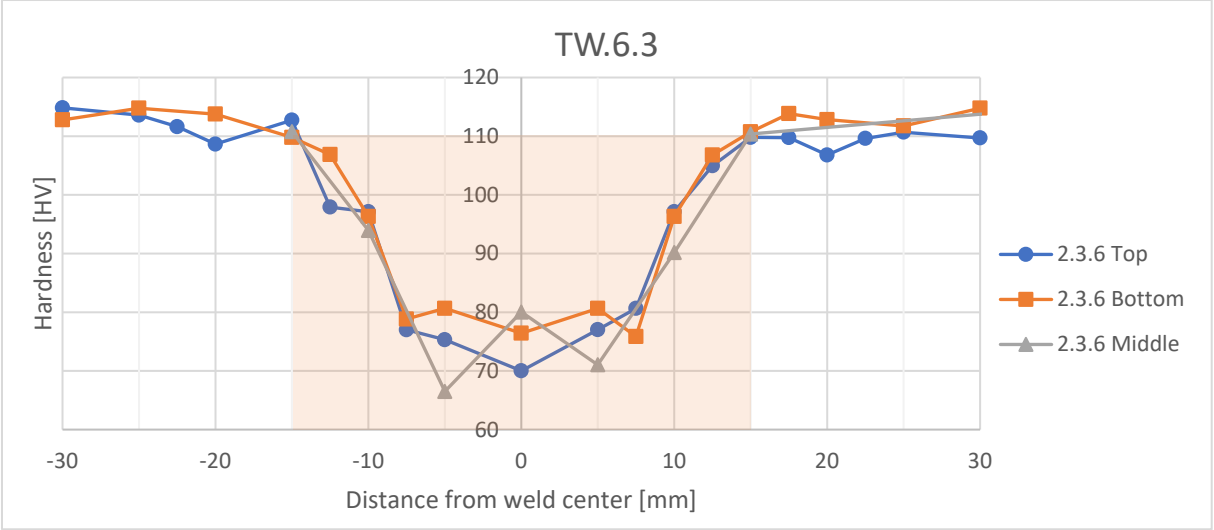

Figure 4.22: Hardness profile of the TW.6.3 specimen.

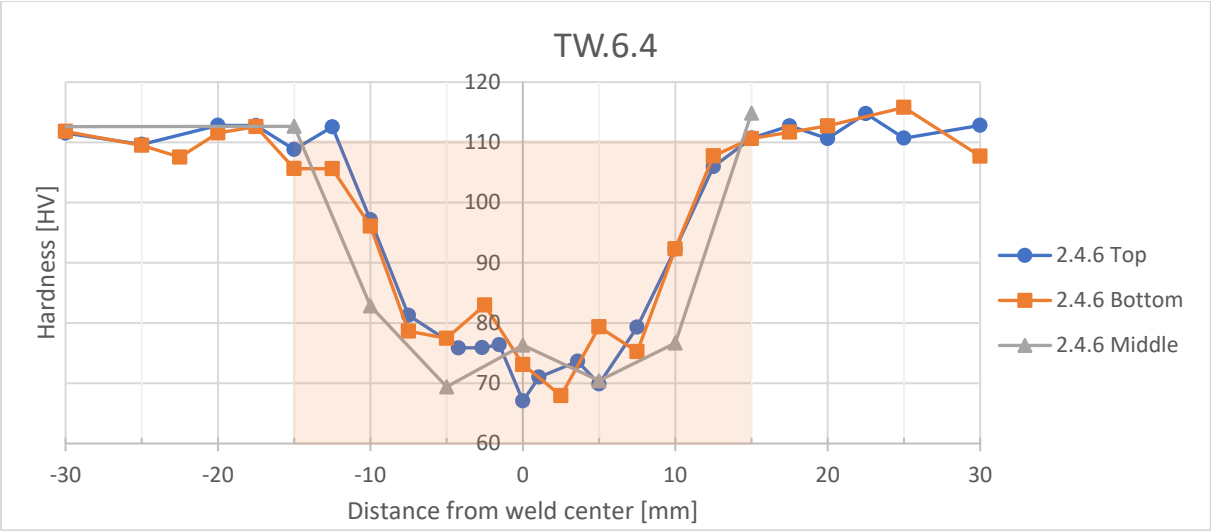

Figure 4.23: Hardness profile of the TW.6.4 specimen.

4.2.3.3. AA6082T6 Longitudinally Welded specimens

As mentioned earlier, a specimen of the longitudinally welded AA6082T6 dogbone is also tested. This specimen represents fully heat-affected material. From the hardness profile shown in Figure 4.24, it is concluded that the material indeed experiences a low hardness number. At the right-hand side, where dogbone LW.6.2 is located, the hardness number is about 70 to 80 HV, which also corresponds to the hardness values near the weld at the transversely welded specimens. For the left-hand side, representing dogbone LW.6.1, this is even lower and about 65 to 70 HV. This lower value matches with the tensile test results, where a lower value for both 0.2% proof stress and the ultimate strength was noted.

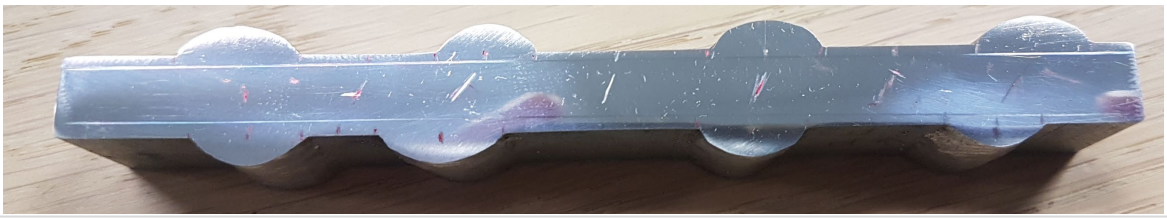

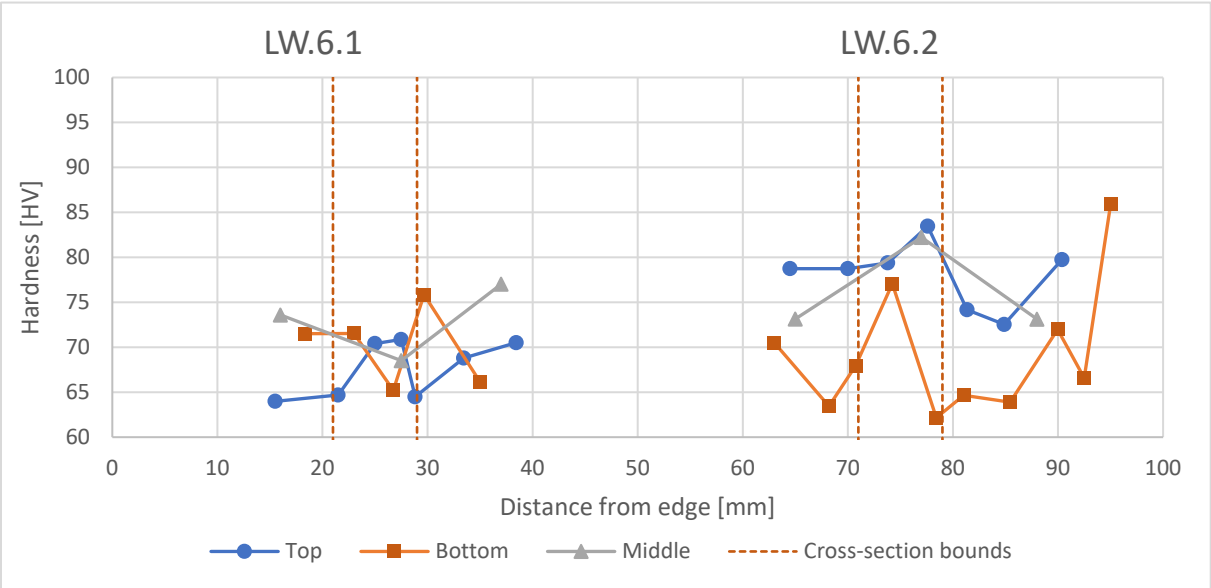

Figure 4.24: Hardness profile and picture of the cross-section of the longitudinally welded specimen.

4.2.3.4. *AA5083H111* Transversely *Welded specimens*

Additionally, to the aluminum alloy 6082T6 dogbones, also a specimen of alloy 5083H111 was tested. A leftover from cutting the transversely welded TW.5.2 specimen was used. After preparing the surface, in total, 42 indentations were made on this specimen following the same procedure as schematized in Figure 4.21. It is well known that non-heat-treated aluminum alloys like AA5083H111 are hardly affected by welding. However, in the results shown in Figure 4.25, some small deviations were found between the hardness measured near the weld and some distance away. Since there were often significant discrepancies at closely spaced points, the outliers were removed from the graph. Assuming that just a local weak spot was indented, which led to low values that do not appropriately represent the material.

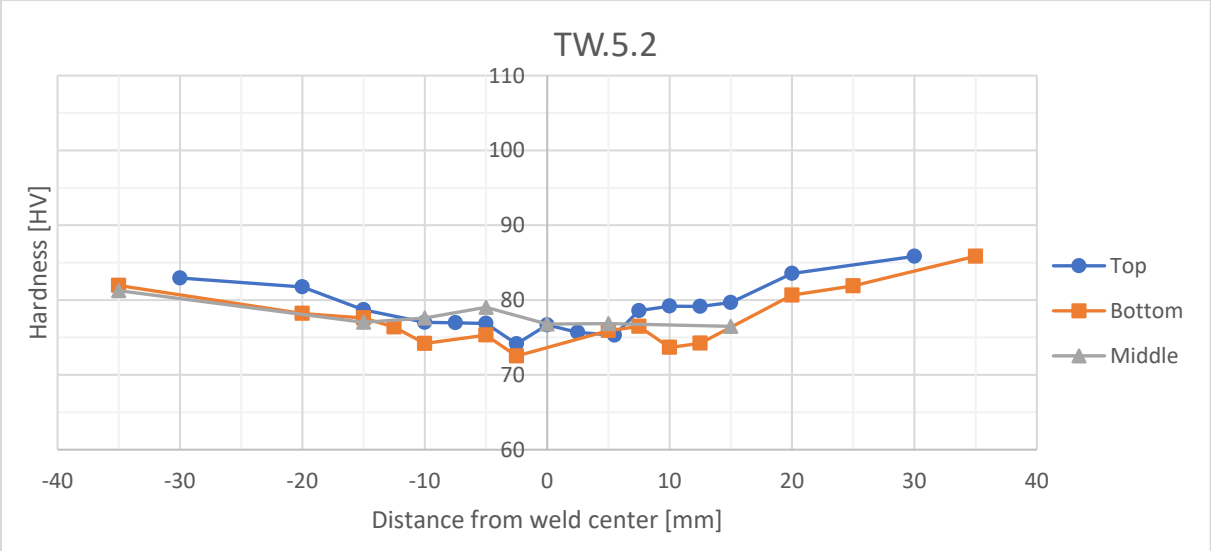

Figure 4.25: Hardness profile of the transversely welded AA5083H111 specimen.

4.2.4. Conclusions from the hardness experiments

The results in the previous sections show a significant difference in the hardness of the AA6082T6 specimens in the vicinity of the weld. From these results it is concluded that the AA6082T6 material is strongly influenced by the application of a weld. At about 15 mm away from the center of the weld, it seems that the hardness has returned to its original value corresponding to the hardness of the base material. Given that fact, it can be concluded that the Heat Affected Zone for AA6082T6 material with a thickness of 8 mm is limited to about 10 mm from the end of the weld. The original (maximum) hardness number of the AA6082T6 welded plate is about 110 HV. The minimum value for the transversely welded specimens was measured at about 70 HV. For the longitudinally welded AA6082T6 specimens, this was even lower at the LW.6.1 dogbone location, which is also noticed in the tensile experiments where the LW.6.1 dogbone showed a lower strength.

Based on the measured hardness values of the different AA6082T6 specimens, the relation between the Vickers hardness and the material strength properties was examined. By plotting the 0.2% proof stress and ultimate strength against the hardness numbers of the different measured specimens, a reasonable relationship is noticeable. Figure 4.26 shows a plot of the measured points, including a linear regression line. From the regression line the following equations were obtained from which the material strength properties could be estimated for the 6082T6 alloy:

$$f_u = 2.738 \cdot HV + 51.94$$

$$f_{0.2} = 4.239 \cdot HV - 133.81$$

The results of the AA5083H111 specimen were also included in the strength to hardness relation plot. However, for this material only one HAZ point and one base material point were measured. The minimal hardness value for the transversely welded AA5083H111 specimens was measured at about 75 HV. The hardness value of the base material was measured with a slightly higher value of about 85 HV. This small difference indicates a minor influence of the heat input on the AA5083H111 material. This small influence is also observed in the tensile experiments, where the longitudinally welded coupons showed a slightly lower strength as the base material coupons.

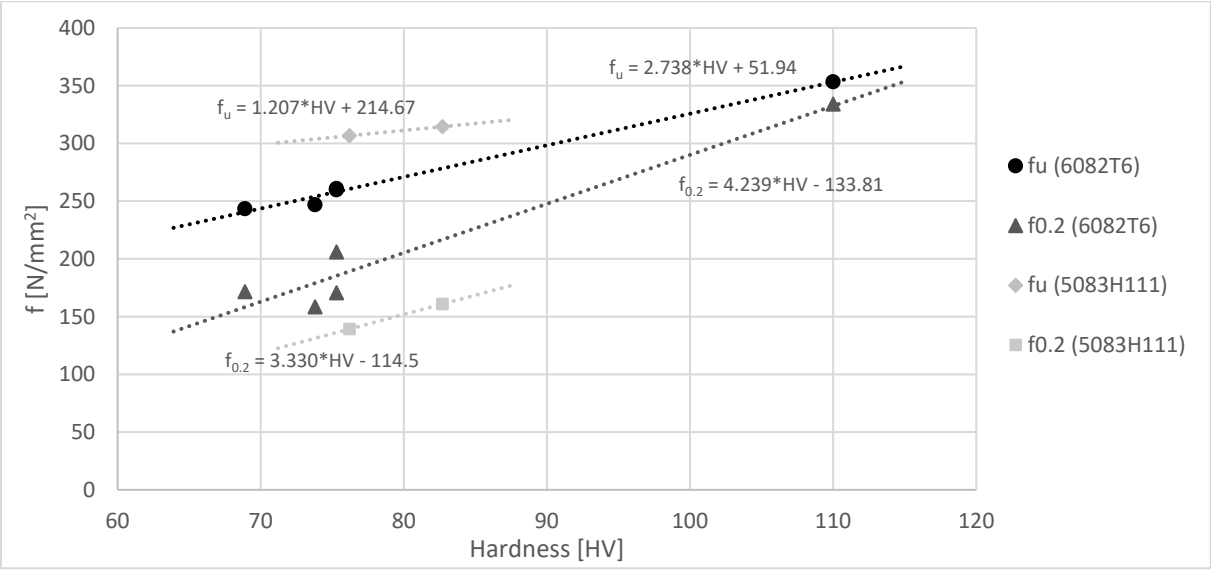

Figure 4.26: Relation material strength to Vickers Hardness of the AA6082T6 alloy.

4.3. Welded cruciform experiments

4.3.1. Introduction

Experimental tests on welded cruciform specimens were conducted in order to analyze the ductility of longitudinally welded connections. Four different welded cruciforms were designed, and each variant was tested four times resulting in a total of 16 experiments. With the help of the experimental tests of the welded cruciforms, the structural behavior of longitudinal welds can be assessed. Besides, the numerical model can be validated based on the experimental results.

In Figure 4.27, a schematization is given of the welded cruciform specimen with sloped edges. On the left-hand side, the member plate is situated, which is constructed of aluminum alloy 6082T6. On the right-hand side, the finger plate is situated, which is made out of aluminum alloy 5083H111. This finger plate contains a slot where the member plate is inserted. Sloped edges of the plates are used since this is also usually applied in practice to optimize fatigue performance.

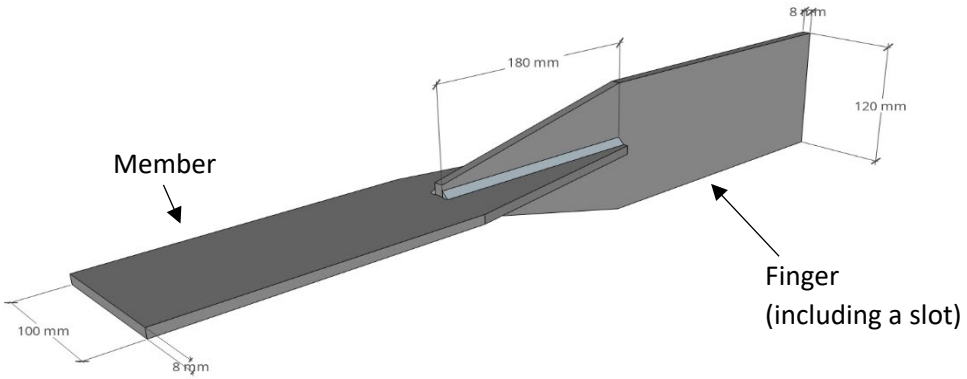

Figure 4.27: 3D schematization of the cruciform specimen.

4.3.2. Design considerations and fabrication

Four variants were designed for experimental testing. These variants were dimensioned based on the given boundaries of the testing machine and four different design considerations. With these four different design ideas, the aim was to experience different deformation capacity results. The primary design considerations and principles are outlined in this subsection. The applied dimensions are presented in the up-following subsections of the corresponding variant.

The first variant was dimensioned based on the assumption that failure will occur in the AA6082T6 member plate with a limited HAZ extension present. The idea is that the HAZ is not present over the full cross-section. In this case, unaffected base material is present around the HAZ, which can contribute to the strength and deformation capacity. The AA5083H111 finger plate is designed with sufficient more ultimate strength than the member plate to ensure failure will occur in the partly heat-affected member plate. In addition, the finger plate was dimensioned to exhibit plastic deformations before failure occurs in the member plate. By this design, plastic deformations will occur in both the finger and member plate before failure.

The second variant is also designed based on failure in the AA602T6 member plate. However, in this case, by applying a minimal member width, it is assumed that the full critical cross-section is heat-affected. In this situation, no unaffected base material is present, which can contribute to the strength and deformation capacity. Also, due to the minimum width of the member plate, early failure will occur, and the elastic limit strength in the finger plate will not be reached. It is assumed that this variant fails with minimal deformation capacity and hence is the worst designed variant considering ductility.

The third and fourth variants are both designed with the approach that failure occurs in the AA5083H111 finger plate. Therefore, the complete strain hardening behavior of the aluminum alloy 5083H111, which is characteristically high, is utilized up to failure. This may result in a larger deformation capacity. By these designs, no plastic deformations will occur in the AA6082T6 member plate. The third and fourth variant differs from each other by the shape of the finger plate around the transition zone to the member plate. The slope of the fingerplate of the third variant will begin inside the transition zone to the member plate. Therefore, enough material width is present around the critical zone, ensuring enough space for stress redistribution. For variant 4, the slope will end after the transition zone, resulting in a critical section just after the end of the transition zone. In this last case, the critical section is narrowed compared to the original width. This last variant will probably exhibit a much lower deformation capacity compared to variant 3.

A brief overview of the variants and the corresponding width of the critical section of the plates is given in Table 4.10. Each plate was constructed out of an 8 mm thick aluminum alloy plate. Besides the width at the critical section, also the elastic limit and ultimate limit strength are listed in this table. These values are calculated by actual values obtained from the literature listed in Table 4.11 and no safety factors.

Table 4.10: Different welded specimens. The critical plate is indicated with an underscore.

Specimen	**Member plate (AA6082T6)**			**Finger plate (AA5083H111)**		
	Width	N_0	N_u	*Width*	N_0	N_u
W1-x	70 mm	136 kN	158 kN	100 mm	132 kN	236 kN
W2-x	40 mm	46 kN	67 kN	100 mm	132 kN	236 kN
W3-x	100 mm	159 kN	200 kN	70 mm	92 kN	165 kN
W4-x	100 mm	159 kN	200 kN	64 mm	85 kN	152 kN

With the help of CNC milling, the specimens were precisely cut out of an aluminum alloy strip or plate, corresponding to the designed dimensions. The member and finger plates were joined together by MIG-welding, using AA5183 filler material and a minimal weld throat thickness of 4 mm. After 40 to 50 days from the moment of welding, the specimens were tested.

4.3.3. Test set-up

Quasi-static tensile tests were carried out on the welded cruciform specimens at ambient temperature with the help of an Instron 250 kN testing machine. The specimens were loaded with a testing speed of 1.8 mm/min and 1.0 mm/min, which corresponds to a strain-rate of about 0.000 07 s^{-1} and 0.000 04 s^{-1}. The applied force and the crosshead displacement were recorded using a 250 kN load cell at the top of the testing machine. Besides the crosshead displacement, the deformation was also measured locally over the connecting region with the help of a Linear Variable Differential Transformer (LVDT). This measurement was performed since it will provide more reliable results while slip will occur in the crosshead clamps. For the first experiment of each variant, the LVDT was placed 30 mm away from both sides of the end of the weld region, corresponding to a gauge length of 240 mm. However, this length was adjusted to 260 mm for the subsequent experiments since one LVDT point was placed 50 mm from the end of the critical welding zone, instead of 30 mm. This adjusted distance was applied because the locations of the strain gauges overlapped with the LVDT attachment locations. Also, this brought the additional positive effect that a more extensive distance was measured, ensuring that the necking formation was covered between the LVDT attachment points. An overview of the test set-up and LVDT placement in practice is shown in Figure 4.28. At the beginning of the test, the distance between the clamps was about 500 mm.

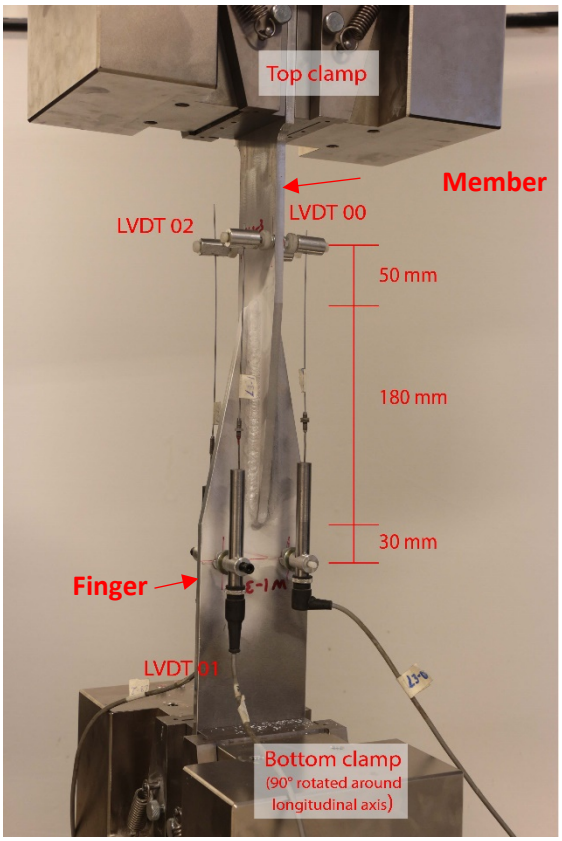

Figure 4.28: Test set-up of the welded cruciform (W1-3) in practice.

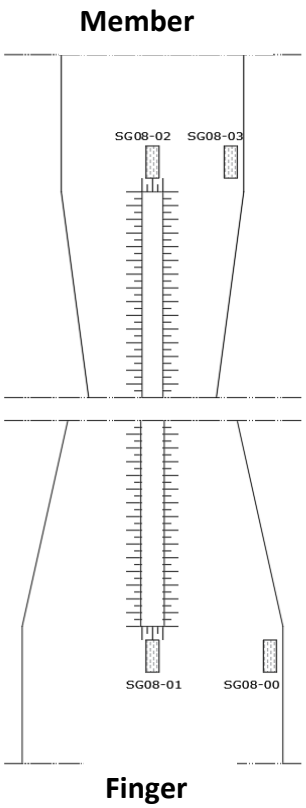

Figure 4.29: Strain gauge locations at the W1 specimen.

Next to the LVDT, also strain gauges were placed to measure the strains locally. These strain gauges were placed at only one specimen of each type. The locations of the placed strain gauges are shown in Figure 4.29. From this figure, it can be seen that strain gauge SG8-02 was placed in the middle of the critical section just after the end of the connecting plate. Strain gauge SG8-03 was placed at the same height but near the edge of the plate. SG8-00 and SG8-01 were placed at the bottom plate in the same way as gauge 2 and 3, as can be seen in Figure 4.29.

4.3.4. Cruciform with failure in partly heat-affected cross-section

4.3.4.1. Dimensions

The first variant is dimensioned in a way, that failure will occur in the heat-treated AA6082T6 member plate where a part of the cross-section is heat-affected by welding. This variant is further indicated as 'Variant 1' and coded by 'W1-#', where # is the specimen number. The dimensions of this variant are shown in Figure 4.30.

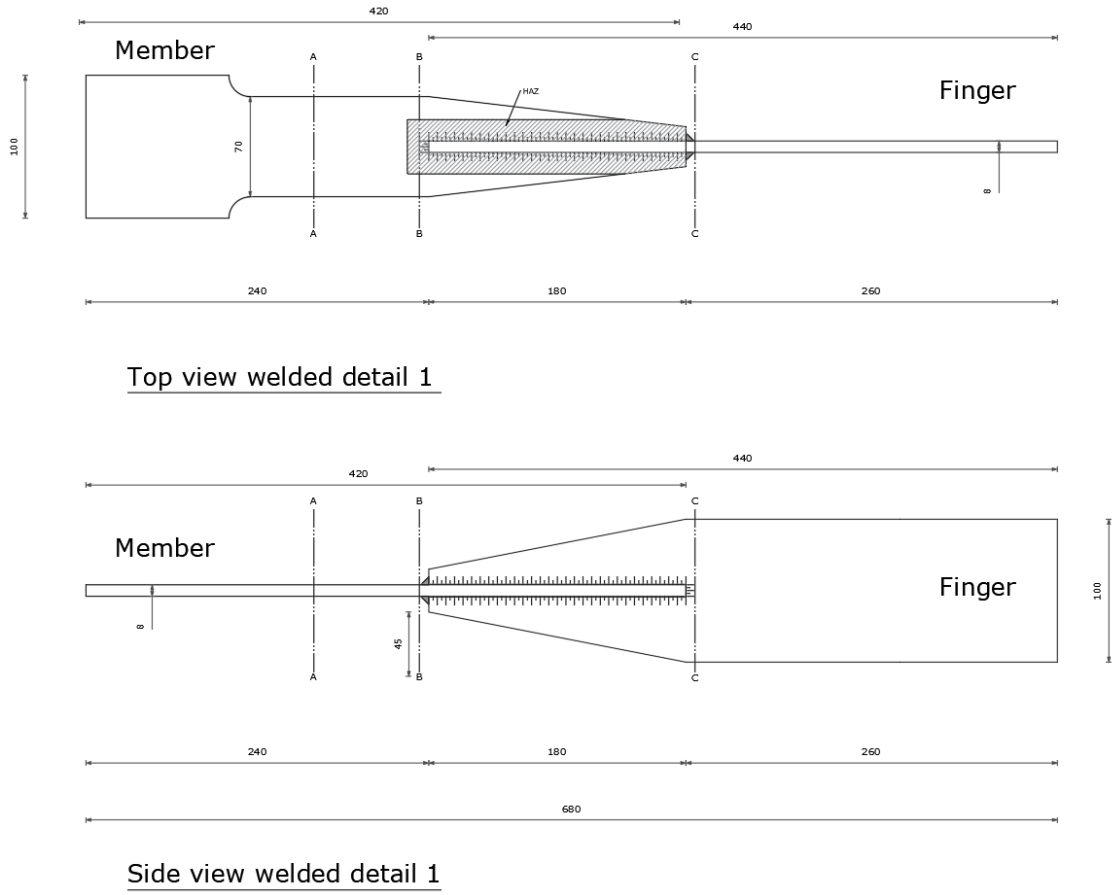

Figure 4.30: Dimensions of welded cruciform variant 1.

With the known dimensions as designed, the failure load at the critical section B in Figure 4.30, can be calculated. With the help of the measured HAZ extent obtained by the hardness tests and the known material properties retrieved from the dogbone experiments, the failure load can be accurately estimated by

$$F_{limit} = \left((2b_{haz} + t_{finger}) \cdot t_{member}\right) \cdot f_{u,HAZ} + \left(b_{member} - b_{haz,total}\right) \cdot t_{member} \cdot f_u =$$
$$F_{limit} = \left((2 \cdot 15 + 8) \cdot 7.87\right) \cdot 253 + (70 - 38) \cdot 7.87 \cdot 353 = 164.6 \cdot 10^3\ N.$$

Table 4.11: Actual and nominal values used for calculations (in N/mm²).

	AA6082-T6			**AA5083-H111**		
	Actual	Lit. **[1]**	EN-1999	Actual	Lit. **[2]**	EN-1999
$\mathbf{f_{0.2}}$	334	314	260	161	165	125
$\mathbf{f_u}$	353	335	310	315	295	275
$\mathbf{f_{0.2,HAZ}}$	191	145	125	140	165	125
$\mathbf{f_{u,HAZ}}$	253	210	185	302	295	275

4.3.4.2. Results

The results of the experiments of variant 1 are plotted in the load-displacement graph in Figure 4.31. The key results are listed in Table 4.12. From the results, it is concluded that a good correlation between the different experiments was obtained. Furthermore, the results closely approached the estimated maximal load, as calculated in the previous section.

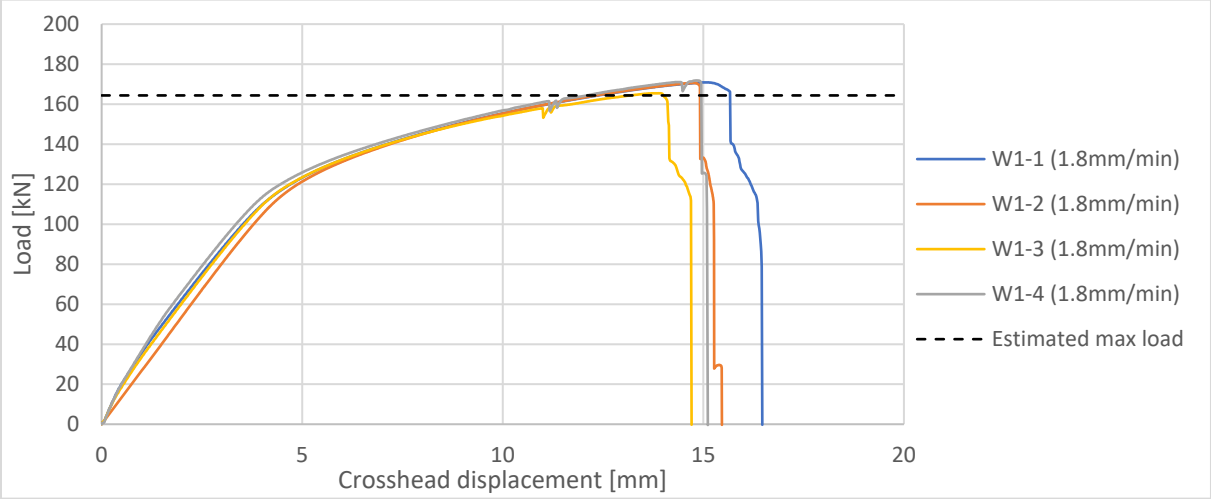

Figure 4.31: Load-displacement graph of the W1 experiments.

Next to the measured displacement of the clamps, also the displacement of a restricted zone near the weld region was measured using LVDT's. These LVDT's were placed 240 mm apart in the first test (W1-2) and 260 mm apart in the other experiments. The results of the four LVDT's at each experiment are averaged and plotted in Figure 4.32 and listed in Table 4.12. In this table also the average of the variant results, the standard deviation, and the Coefficient of Variation (CV) in percentage is given.

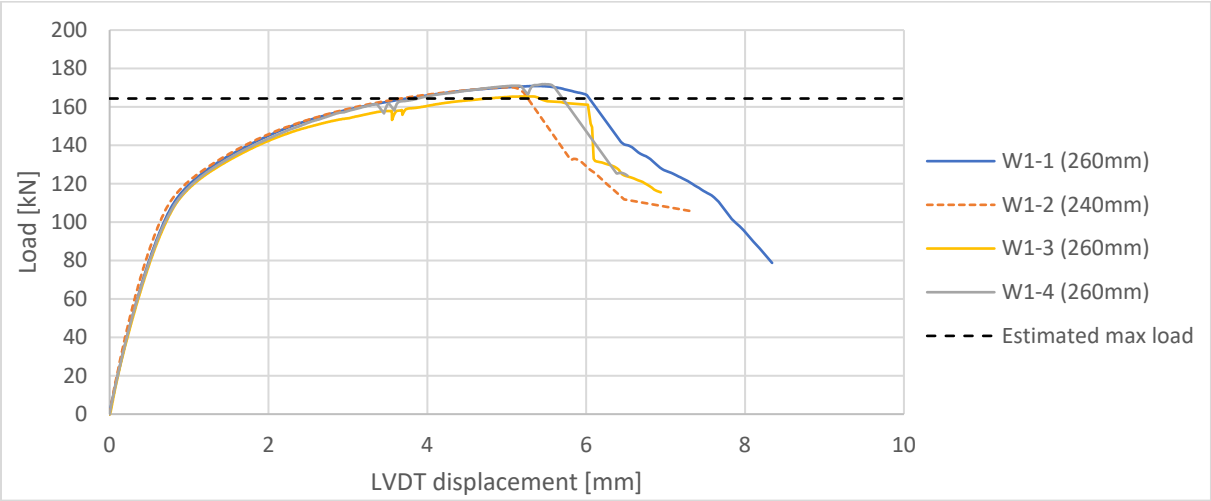

Figure 4.32: Load-displacement graph of the LVDT's of the W1 experiments.

Table 4.12: Key results of the W1 experiments.

	W1-1	W1-2	W1-3	W1-4	Average	St. dev.		CV
Maximal Force	170.89	170.59	165.45	171.84	169.69	2.49	kN	1.5%
Crosshead displ. at max F	15.12	14.77	13.89	14.84	14.65	0.46	mm	3.1%
Max crosshead displ.	16.47	15.46	14.71	15.11	15.44	0.65	mm	4.2%
LVDT displ. at max F	5.42	4.99	5.23	5.49	5.28	0.19	mm	3.6%
Max LVDT displ.	8.34	7.36	6.94	6.52	7.29	0.68	mm	9.3%

In addition to the displacement measurements by the LVDT, one experiment was executed using strain gauges near the end of the weld region. The applied load is plotted against the results of these strain gauges up to a strain of 4.5% in Figure 4.33. The placings of the SG8-02 and SG8-03 gauges are shown in Figure 4.34. The SG8-01 gauge was placed in the middle of the AA5083H111 fingerplate and the SG8-00 gauge near the edge of the fingerplate. From the results shown in Figure 4.33, it is concluded that strain and stress concentrations occurred in the middle of the finger and member plate. The most strain occurred in the middle of the finger plate since the plastic branch is reached earlier in the applied aluminum alloy 5083H111. At the point around 2.4% strain, the SG8-02 strain gauge got loose, causing the measurement of this gauge to stop. The measurements of the SG8-01 and -02 gauges stopped about 4.5% since the end of the measuring range was reached.

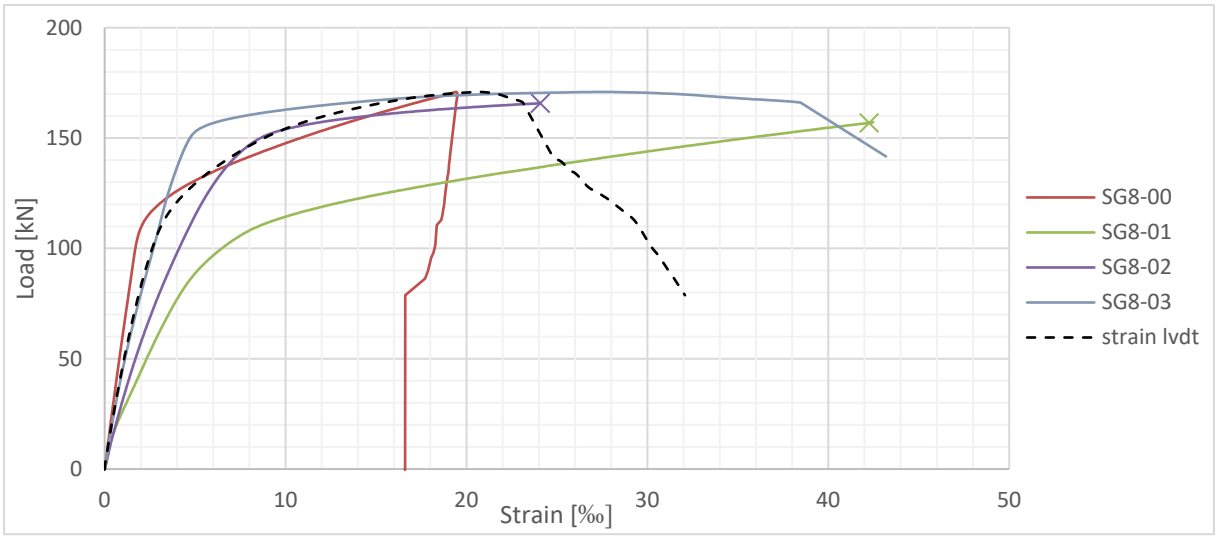

Figure 4.33: Load-strain graph of the strain gauges and LVDT of the W1-1 specimen.

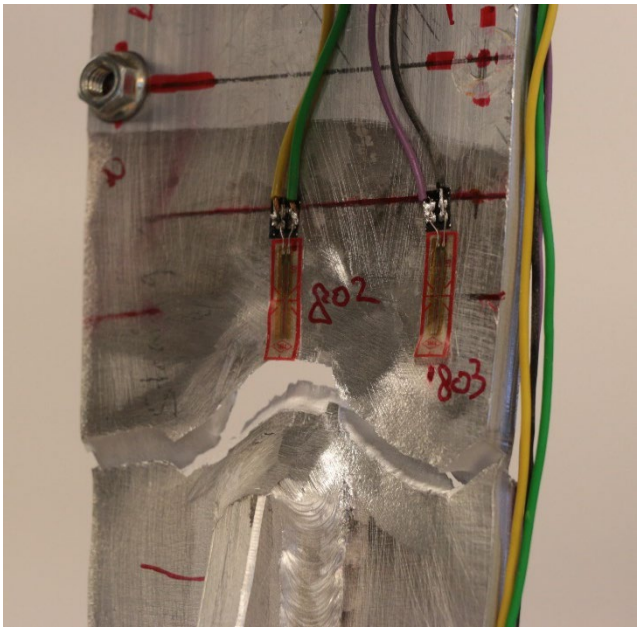

Figure 4.34: Cracked W1-1 specimen with placed strain gauges.

In order to be able to compare the ductility of the different cruciform variants, a deformation capacity measure is introduced. The rotation capacity usually defines the deformation capacity of bending beams. This dimension was described earlier in Section 3.1 and is related to the elastic limit moment values. The same ductility measurement principle could also be defined for axially loaded members. This can be done by relating the occurring forces and displacements to the elastic limit force and corresponding elastic limit displacement. For this current research, the total deformation capacity is defined by U_c and is calculated by the following equation

$$U_c = \frac{u_{el} - u_{0.2}}{u_{0.2}}. \tag{4.1}$$

The stable deformation capacity $U_{c,s}$, is defined by

$$U_{c,s} = \frac{u_{max} - u_{0.2}}{u_{0.2}}, \tag{4.2}$$

where $u_{0.2}$ corresponds to the displacement at the moment of reaching the elastic limit, and u_{el} corresponds to the measured displacement at the moment the applied force drops down below the elastic limit. The displacement measured at the point of maximal applied load is indicated by u_{max}. The elastic limit is calculated by

$$N_{0.2} = \left((2b_{haz} + t_{finger}) \cdot t_{member}\right) \cdot f_{0.2,HAZ} + \left(b_{member} - b_{haz,total}\right) \cdot t_{member} \cdot \ f_{0.2} =$$
$$N_{0.2} = \left((2 \cdot 15 + 8) \cdot 7.87\right) \cdot 191.3 + (69.9 - 38) \cdot 7.87 \cdot 334.0 = 141.1 \cdot 10^3 \ N.$$

Based on the results of variant 1, it is noticed that already some plastic deformations occurred in the material before the calculated elastic limit was reached. From the strain gauge measurements, it is shown that already plastic deformation occurred in the center of the welded specimen before plastic deformation was reached near the edge of the plate. It is also likely that the plastic deformations are concentrated in the HAZ as here, the 0.2% proof stress is reached earlier. Based on this, it is concluded that plastic deformations already occur when the cross-section reaches the 0.2% proof stress of the HAZ. Based on this conclusion, the elastic limit force is recalculated by

$$N_{0.2} = 69.9 \cdot 7.87 \cdot 191.3 = 105.2 \cdot 10^3 \ N.$$

Figure 4.35 shows the normalized load-displacement graphs from where the deformation capacity can be determined. In Table 4.13, the key values concerning the deformation capacity are listed.

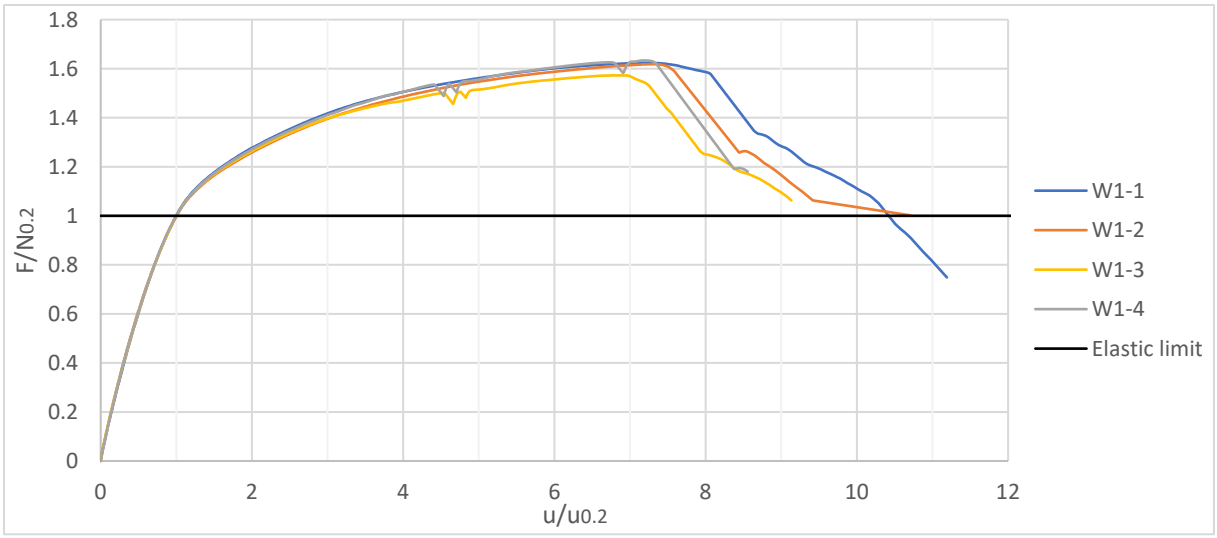

Figure 4.35: Normalized load-displacement graph of the variant 1 experiments.

Table 4.13: Key results concerning the deformation capacity of the variant 1 experiments.

	W1-1	W1-2	W1-3	W1-4	Average	St. dev.	
Max $F/N_{0.2}$	1.62	1.62	1.57	1.63	1.61	0.02	
$u_{0.2}$	0.75	0.69	0.76	0.76	0.74	0.03	mm
u_{max}	5.42	4.99	5.23	5.49	5.28	0.19	mm
u_{el}	7.83	6.48	6.94	6.52	6.94	0.55	mm
$U_{c,s}$	6.28	6.26	5.89	6.20	6.16	0.71	
U_c	9.51	8.42	8.13	7.56	8.41	0.16	

The results show that the variant 1 specimens exhibit a stable rotation capacity value of about 6.2. The total rotation capacity was slightly higher, with a value of about 8.4. The average maximal force of the experiments was 60% as high as the elastic limit, indicating that quite much plastic reserve was present.

4.3.5. Cruciform with failure in fully heat-affected cross-section

4.3.5.1. Dimensions

The second variant is dimensioned in a way that the entire cross-section is heat-affected. Regarding the dimensioned variant 2, failure will occur in the member plate before the yield strength in the finger plate is reached. Hence, no plastic deformation is present in the finger plate. The dimensions were based on a 15 mm wide HAZ from the center of the weld. Taking the thickness of the finger plate into mind the total heat-affected zone amounts:

$$b_{haz,total} = 2b_{haz} + t_{member} = 2 \cdot 15 + 8 = 38\,mm.$$

Therefore, the member plate was constructed with a width of 40 mm, assuming the entire width was heat-affected. The used dimensions are shown in Figure 4.36.

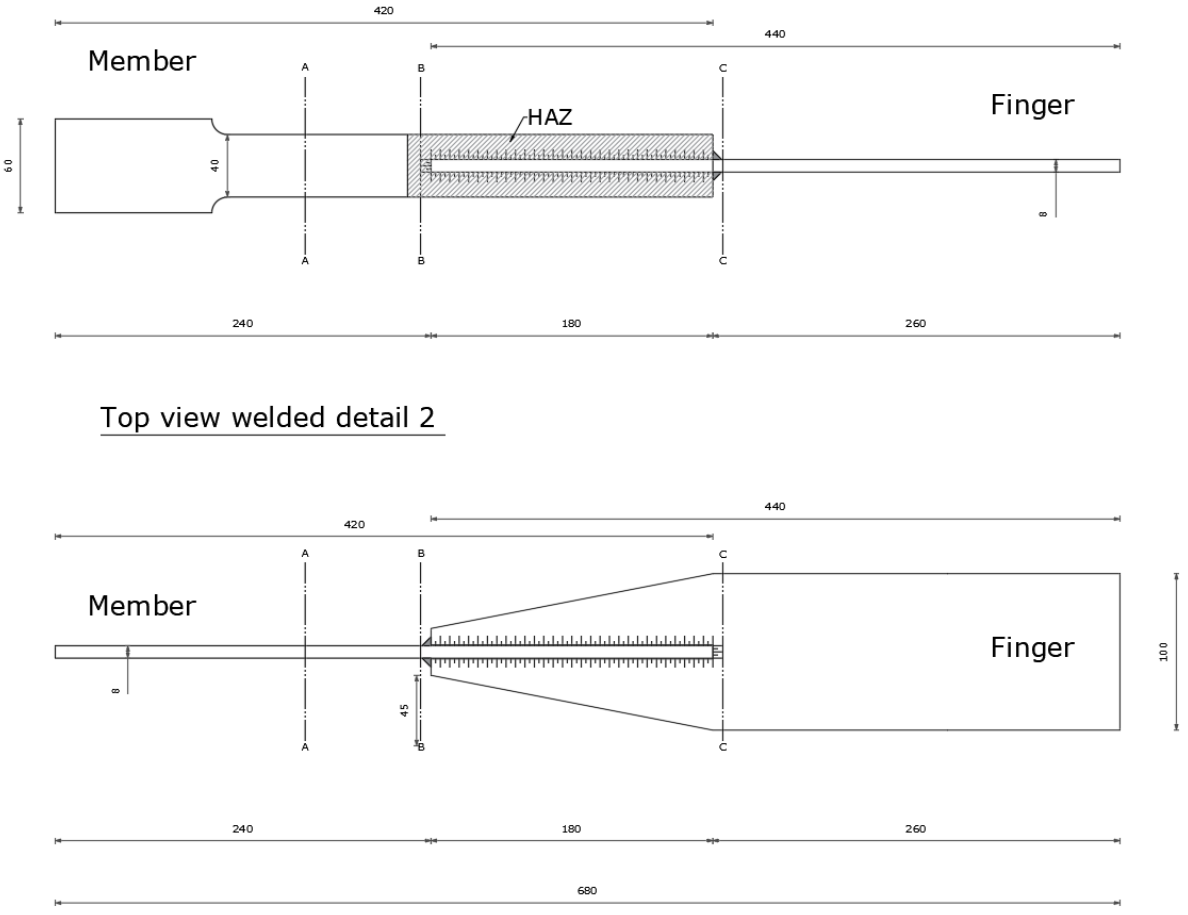

Figure 4.36: Dimensions of welded cruciform variant 2.

The failure load of the member plate at section B indicated in Figure 4.36, is calculated with the help of the actual material strength by

$$F_{limit} = (b_{haz} \cdot t_{member}) \cdot f_{u,HAZ} = (40.2 \cdot 7.74) \cdot 253 = 78.7 \cdot 10^3\ N.$$

4.3.5.2. Results

The load-displacement graphs of the four different experiments of variant 2 are plotted in Figure 4.37. The key results are listed in Table 4.14. Two specimens were tested using a crosshead displacement speed of 1.8 mm/min. The other two specimens were executed using a speed of 1.0 mm/min. From the results, it is shown that a different speed did not influence the results. Also, it is concluded that a good correlation was obtained between the four different tests. Only the W2-1 specimen experienced a somewhat higher failure load.

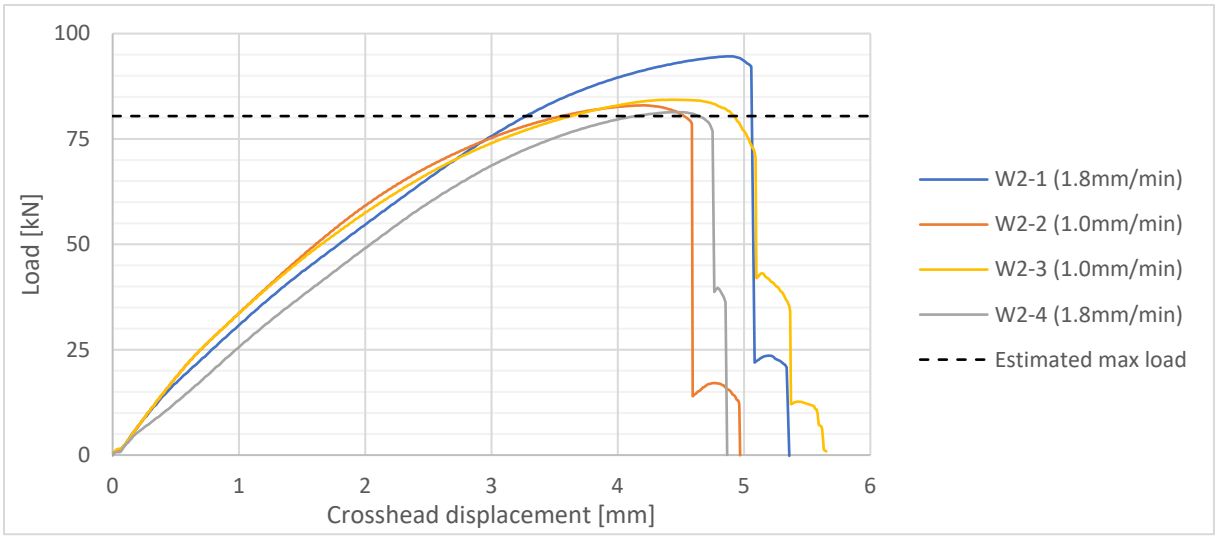

Figure 4.37: Load-displacement graph of the W2 experiments.

In order to exclude the effect of the slip of the clamps, the displacement was measured over the welded region using LVDT's, as mentioned earlier. The averaged results of the four LVDT's are plotted in Figure 4.38 and listed in Table 4.14. From the results, it is noticed that all the experiments showed a somewhat similar result except for the W2-1 specimen.

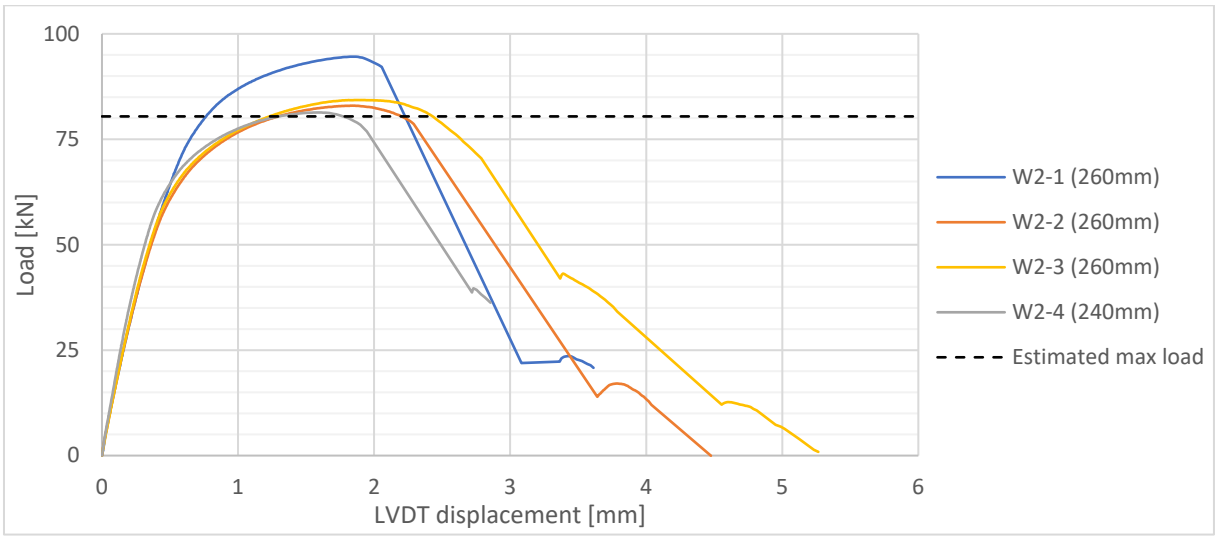

Figure 4.38: Load-displacement graph of the W2 experiments measured by the LVDT's.

Table 4.14: Key results of the W2 experiments.

	W2-1	W2-2	W2-3	W2-4	Average	St. dev.		CV
Maximal Force	94.59	82.97	84.30	81.36	85.80	5.18	kN	6.0%
Crosshead displ. at max F	4.87	4.21	4.47	4.49	4.51	0.24	mm	5.3%
Max crosshead displ.	5.36	4.97	5.65	4.87	5.21	0.31	mm	6.0%
LVDT displ. at max F	1.84	1.85	1.92	1.61	1.80	0.11	mm	6.1%
Max LVDT displ.	3.64	4.97	5.65	4.87	4.78	0.72	mm	15.1%

In Figure 4.39, the applied force is plotted against the strains measured by the strain gauges. These strain gauges were applied at specimen W2-1. From these results, it is noticed that the strains concentrate primarily at the center of the member plate cross-section. Also, it shows that at the locations of the finger plate, the strain gauges SG8-00 and -01 experienced a minimal plastic deformation.

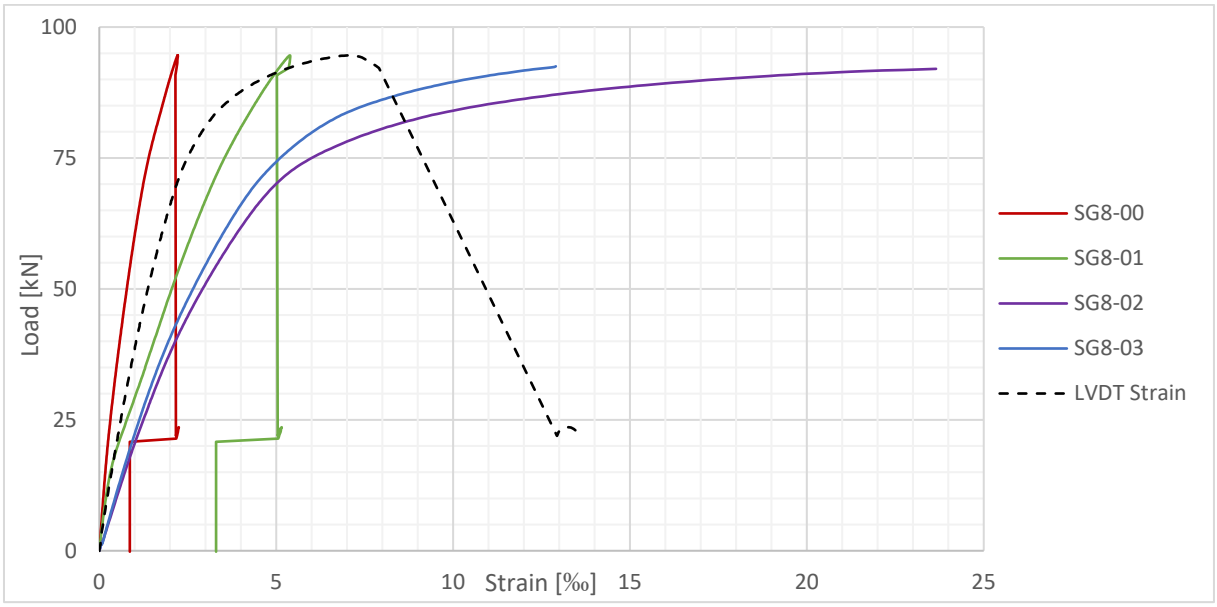

Figure 4.39: Load-strain graph of the strain gauges and LVDT of the W2-1 specimen.

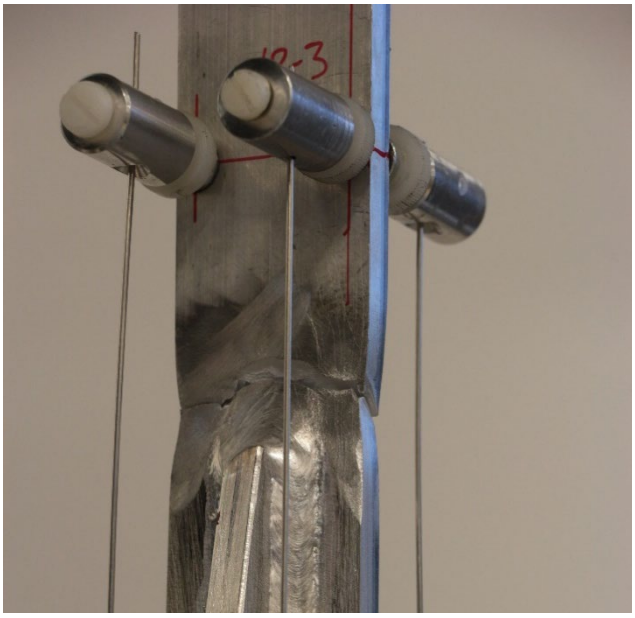

Figure 4.40: Failure of the W2-3 specimen.

Additionally, the deformation capacity was examined for the variant 2 experiments. The elastic limit force is calculated by

$$N_{0.2} = (b_{haz} \cdot t_{member}) \cdot f_{0.2,HAZ} = (40.2 \cdot 7.74) \cdot 191.3 = 59.5 \cdot 10^3\ N.$$

Figure 4.41 shows the normalized load-displacement graphs from where the deformation capacity can be determined. In Table 4.15, the key values concerning the deformation capacity for variant 2 are listed. From these findings, it is observed that the ultimate applied force was about 40% more as the elastic limit for three out of four cases. An averaged stable deformation capacity of 3.0 was reached for the variant 2 specimens. The total deformation capacity was somewhat higher with a value of 4.0

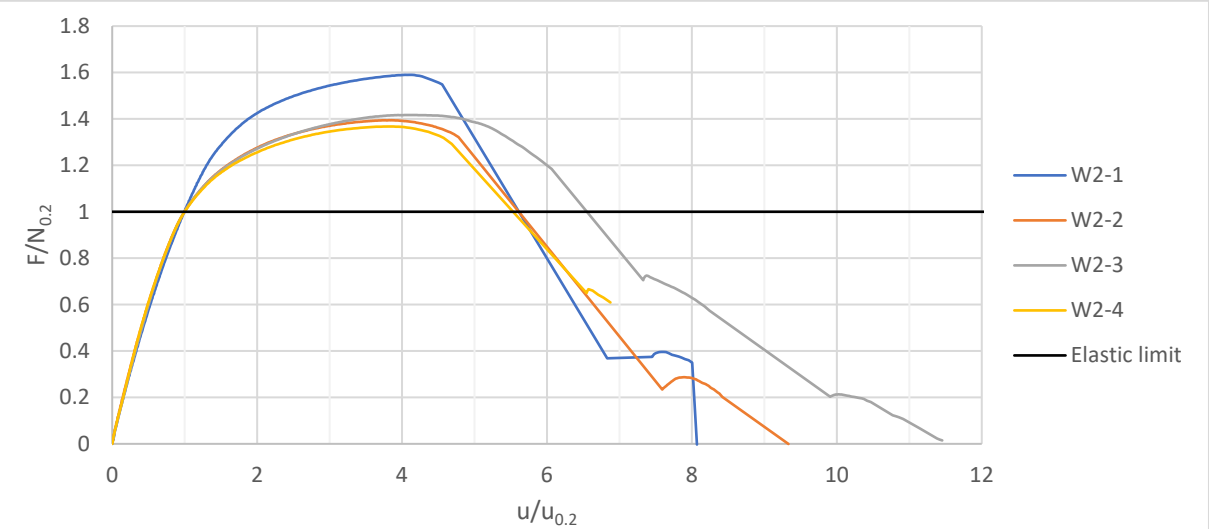

Figure 4.41: Normalized load-displacement graph of the variant 2 experiments.

Table 4.15: Key results concerning the deformation capacity of the variant 2 experiments.

	W2-1	W2-2	W2-3	W2-4	Average	St. dev.	
Max F/$N_{0.2}$	1.59	1.39	1.42	1.37	1.44	0.09	
$u_{0.2}$	0.45	0.48	0.46	0.42	0.45	0.02	mm
u_{max}	1.84	1.85	1.92	1.61	1.80	0.11	mm
u_{el}	2.06	2.29	2.79	1.95	2.27	0.32	mm
$U_{c,s}$	3.07	2.86	3.17	2.88	3.00	0.13	
U_c	3.55	3.78	5.06	3.69	4.02	0.61	

4.3.6. Cruciform with failure in cold worked finger plate

4.3.6.1. Dimensions

The specimens of the third and fourth variants are dimensioned in a way that failure will occur in the finger plate. Since this finger plate consists out of cold worked AA5083H111 material, the heat effect by welding is negligible. By providing failure in this finger plate, it is ensured that plastic deformation is present in this plate before the connection fails. The sloped edges in variant 3 are starting and ending at a certain distance inside the transition zone. The slope will end before the end of the weld length. Therefore, more material is present around the toe of the member plate, where stress concentrations will occur. The configuration and dimensions of the third variant are shown in Figure 4.42.

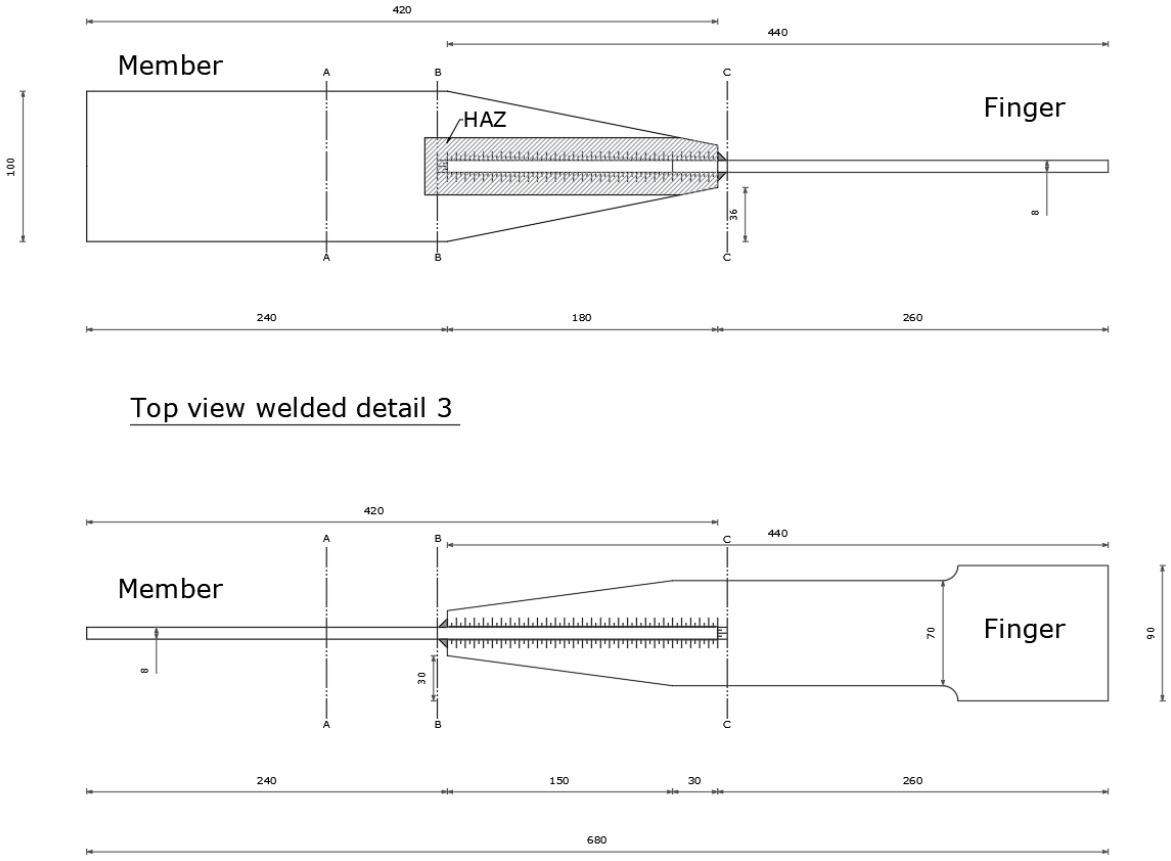

Figure 4.42: Dimensions of welded cruciform variant 3.

An estimation of the ultimate load of this finger plate (section C) using actual strength properties, is calculated by

$$F_{limit} = \left(b_{finger} - b_{slot}\right) \cdot t_{finger} \cdot f_u = (70 - 9) \cdot 7.92 \cdot 302 = 145.9 \cdot 10^3\ N.$$

4.3.6.2. Results

The results of the four experiments of variant 3 are plotted in the load-displacement graph shown in Figure 4.43 and are listed in Table 4.16. One of the most remarkable things observed from the results is the significant discrepancy between the four experiments. W3-2 and W3-4 showed quite a similar behavior. However, variant W3-3 and especially W3-3 seemed to fail prematurely. The calculated estimated load was not reached in any experiment.

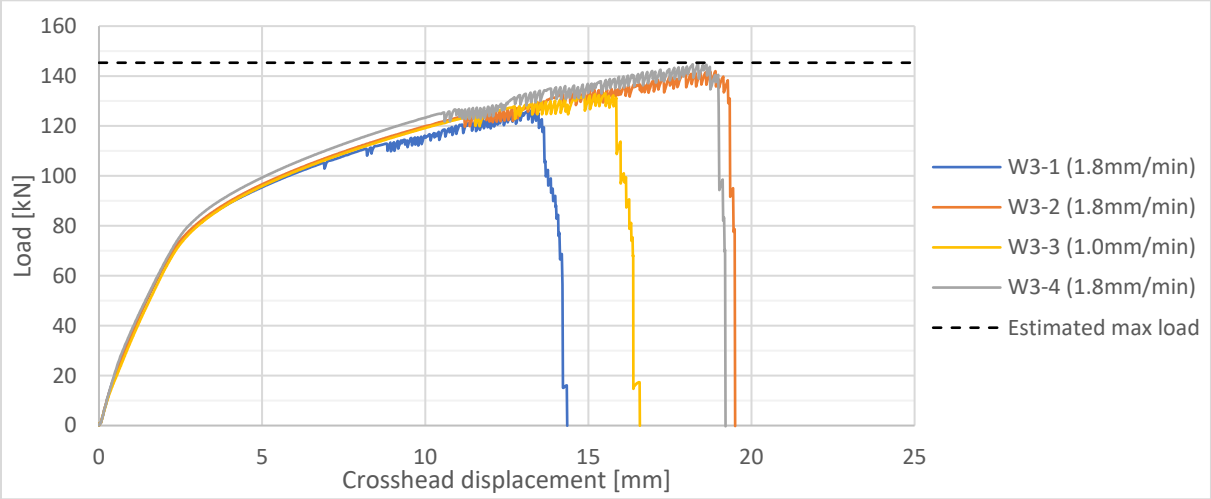

Figure 4.43: Load displacement graph of the variant 3 experiments.

In Figure 4.44, the load-displacement graph measured by the LVDT's is shown. In Table 4.16, the key results of these measurements are listed. From the LVDT results, it is noticed that it already better approached the results of the experiments. Only experiment W3-1 still experienced premature failure behavior.

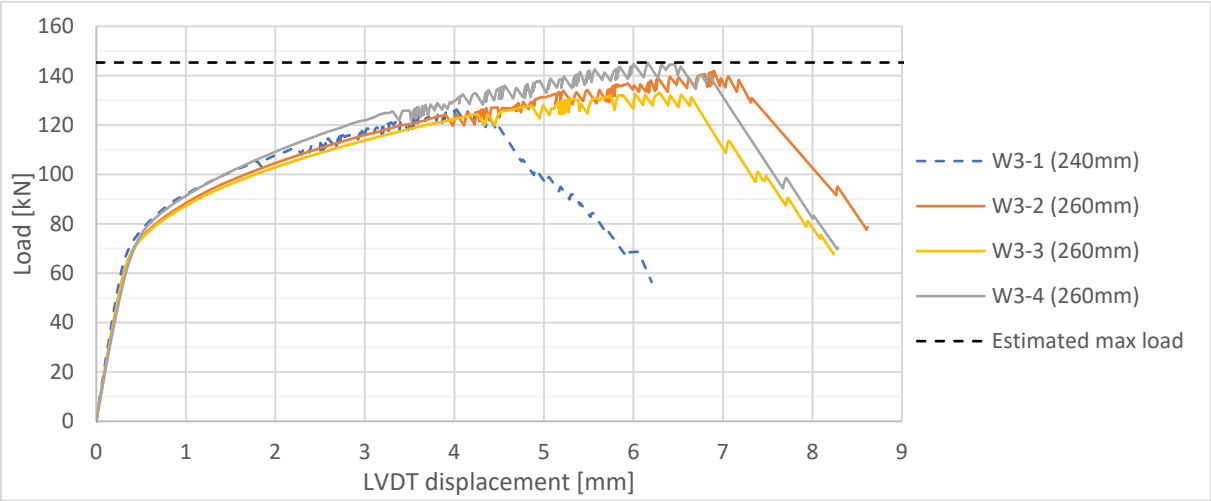

Figure 4.44: Load-displacement graph measured by the LVDT at variant 3 experiments.

Table 4.16: Key results of the W3 experiments.

	W3-1	W3-2	W3-3	W3-4	Average	St. dev.		CV
Maximal Force	126.29	141.98	133.07	145.12	136.61	7.42	kN	5.4%
Crosshead displ. at max F	13.26	18.90	15.53	18.36	13.08	2.27	mm	17.4%
Max crosshead displ.	14.35	19.50	16.58	19.21	17.41	2.10	mm	12.1%
LVDT displ. at max F	4.02	6.90	6.29	6.16	5.84	1.09	mm	18.7%
Max LVDT displ.	6.20	8.61	8.24	8.28	7.83	0.95	mm	12.1%

For specimen W3-2, strain gauges were applied in the same manner as earlier explained in Section 4.3.3 and Figure 4.29, where the gauges SG8-02 and -03 also were applied near the critical section. Therefore, in this case, these gauges are placed on the AA5083H111 finger plate instead of the AA6082T6 member plate. The results of the measurements by the strain gauges are plotted in Figure 4.45. A picture of the strain gauges locations at the W3-2 specimen in practice is shown in Figure 4.46.

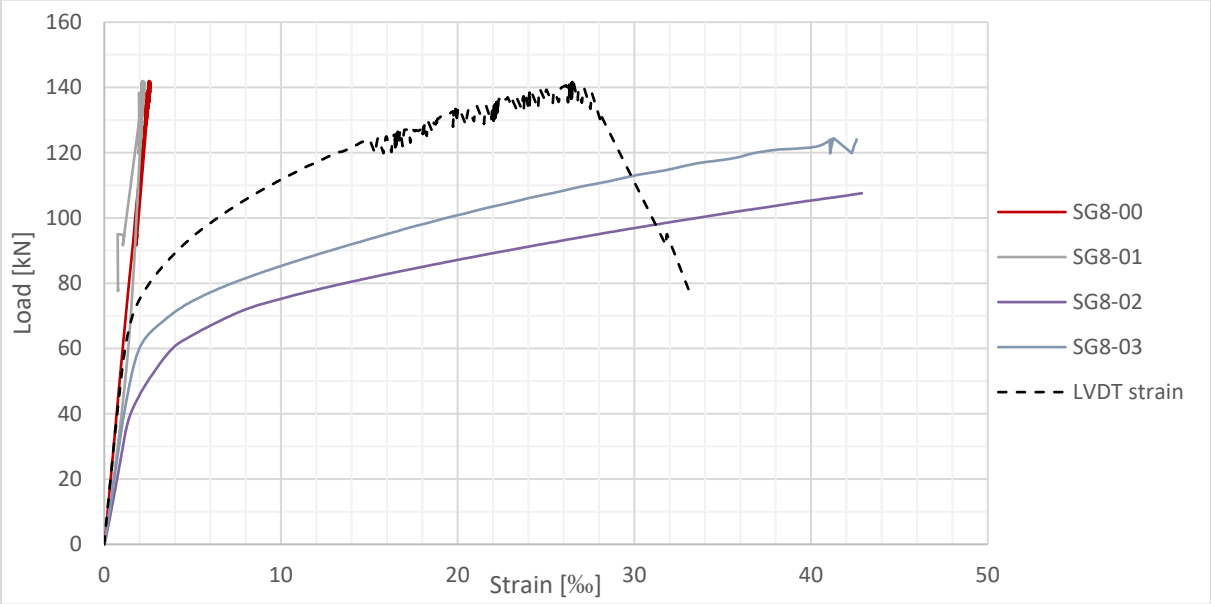

Figure 4.45: Load-strain graph of the strain gauges and the LVDT at the W3-2 specimen.

From the results in Figure 4.45, it is noticed that the strains concentrate at the AA5083H111 finger plate, especially in the middle. Also, a quite large plastic branch is experienced during loading. However, this was not the case for the AA6082T6 member plate, where the strain gauges never reached the plastic branch. The strain measured by these gauges was limited to about 0.26%.

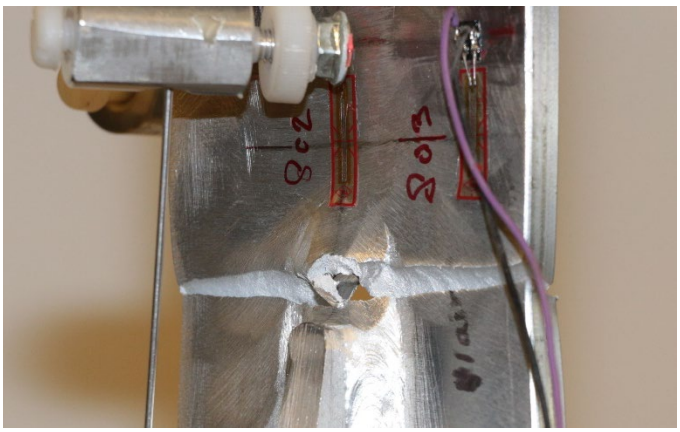

Figure 4.46: Failure of the W3-2 specimen.

The elastic limit force for variant 3 specimens is calculated by

$$N_{0.2} = \left(b_{finger} - b_{slot}\right) \cdot t_{finger} \cdot f_{0.2} = (69.9 - 9) \cdot 7.92 \cdot 160.9 = 77.6 \cdot 10^3\ N.$$

Figure 4.47 shows the normalized load-displacement graphs from where the deformation capacity can be determined. In Table 4.17, the key values concerning the deformation capacity for variant 3 are listed. From these findings, it is observed that the ultimate force significantly exceeds the elastic limit with almost 80%. Also, high values for the deformation capacity were experienced compared to variants 1 and 2.

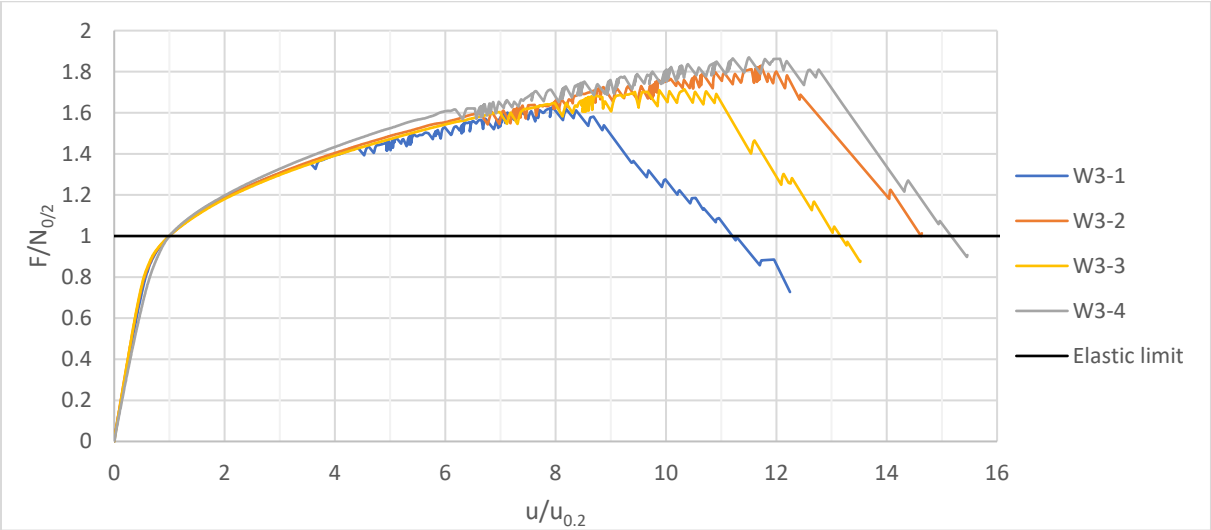

Figure 4.47: Normalized load-displacement graph of the variant 3 experiments.

Table 4.17: Key results considering the deformation capacity of the variant 3 experiments.

	W3-1	W3-2	W3-3	W3-4	Average	St. dev.	
Max F/$N_{0.2}$	1.63	1.83	1.71	1.87	1.76	0.10	
$u_{0.2}$	0.51	0.59	0.61	0.54	0.56	0.04	mm
u_{max}	4.02	6.90	6.29	6.16	5.84	1.09	mm
u_{el}	5.71	8.61	7.95	8.01	7.57	1.10	mm
$U_{c,s}$	6.94	10.72	9.33	10.50	9.38	1.50	
U_c	10.28	13.62	12.05	13.96	12.48	1.46	

4.3.7. Cruciform with failure in cold worked narrowed finger plate

4.3.7.1. Dimensions

The fourth and last variant is very similar to variant 3. Although, for this variant, the slope of the edges of the finger plate is extended. Therefore, the slope starts before the presence of the member plate, and the critical cross-section is narrowed. As a consequence, less material is present around the toe of the member plate, which will result in a lower resistance and deformation capacity. The measurements of this last variant are shown in Figure 4.48.

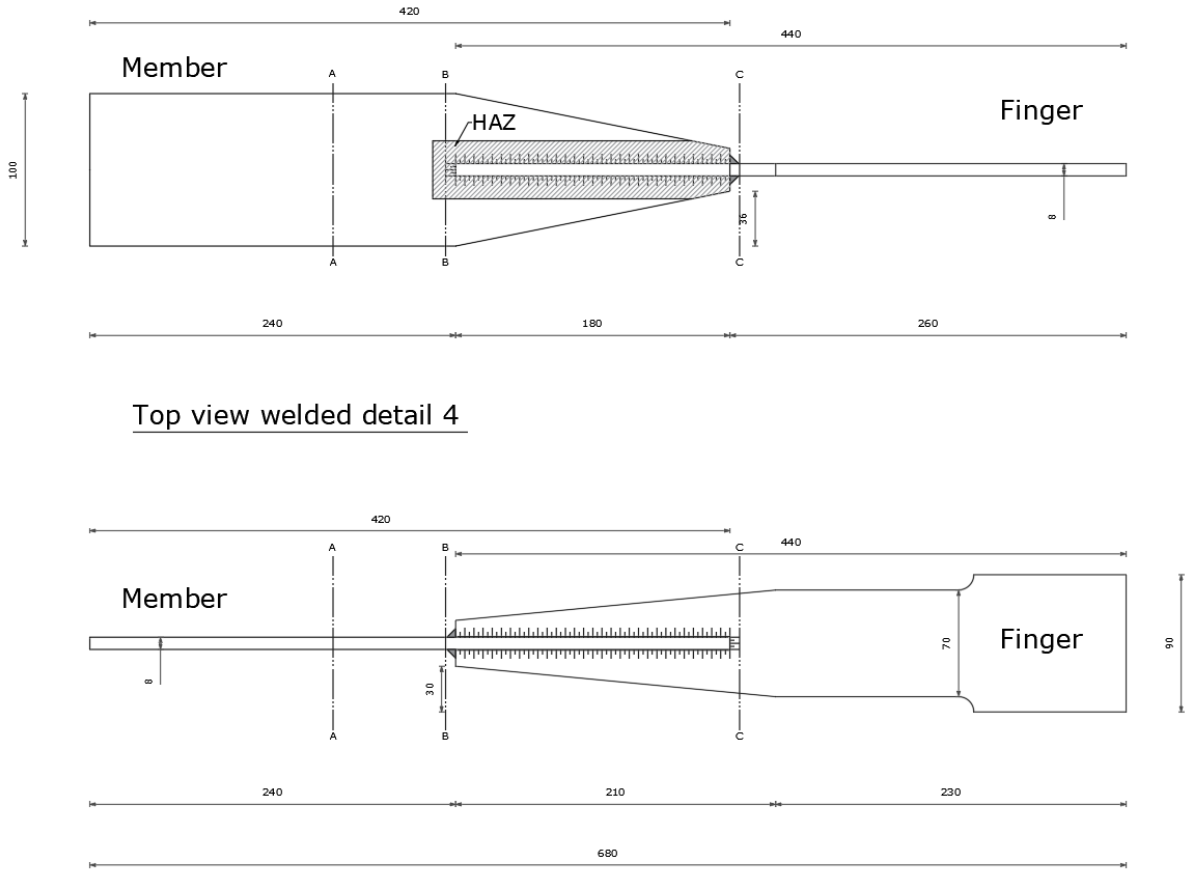

Figure 4.48: Dimensions of the welded cruciform variant 4.

The estimated ultimate strength of the finger plate near the toe of the member plate (section C) is calculated by

$$F_{limit} = (b_{finger} - b_{slot}) \cdot t_{finger} \cdot f_u = (64.3 - 9) \cdot 7.92 \cdot 302 = 132.3 \cdot 10^3\ N.$$

4.3.7.2. Results

The results of the variant 4 specimens are plotted in Figure 4.49 and listed in Table 4.18. From these results, it is concluded that the first three specimens exhibit the same tendency. However, the last specimen W4-4 failed prematurely compared to the other specimens. This premature failure is also noticed in the load-displacement graph measured by the LVDT's shown in Figure 4.50. Both the load and displacement are lower compared to the other specimens. The calculated estimated load of about 132 kN was not reached in any experiment.

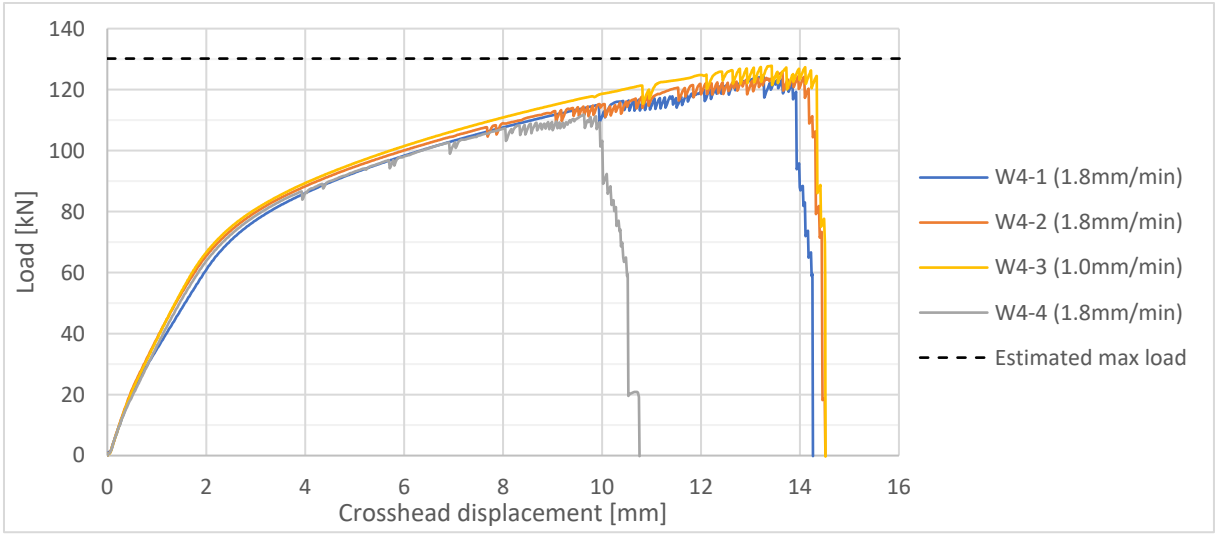

Figure 4.49: Load-displacement graph of the variant 4 experiments.

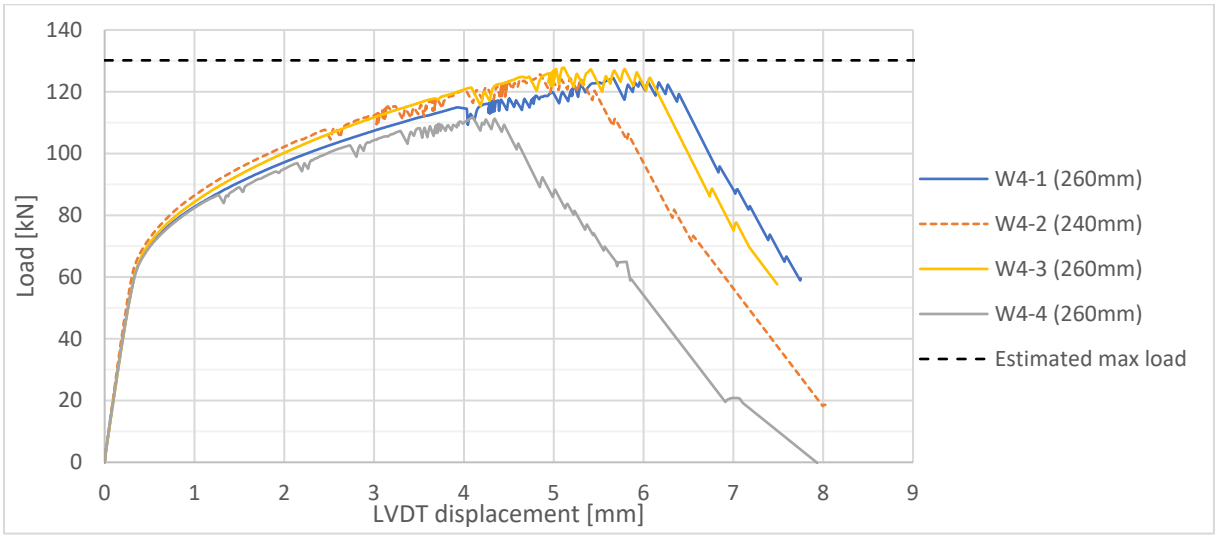

Figure 4.50: Load-displacement graph measured by the LVDT at variant 4 experiments.

Table 4.18: Key results of the W4 experiments.

	W4-1	W4-2	W4-3	W4-4	Average	St. dev		CV
Maximal Force	124.42	125.57	127.83	111.80	122.41	6.24	kN	5.1%
Crosshead displ. at max F	13.27	13.65	13.43	9.64	12.49	1.66	mm	13.3%
Max crosshead displ.	14.26	14.51	14.52	10.76	13.51	1.59	mm	11.8%
LVDT displ. at max F	5.66	4.85	5.11	4.10	4.93	0.56	mm	11.4%
Max LVDT displ.	7.75	8.02	7.49	7.93	7.80	0.20	mm	1.5%

Next to the deformation measured by the tensile machine and the LVDT's, also some strain gauges were placed to measure the strains locally. This measuring was executed for the W4-1 specimen, and the corresponding results are plotted in a load-strain graph shown in Figure 4.51. From this plot, it is noticed that the strains mostly concentrate on the AA5083H111 finger plate. Some more strains and stresses occurred in the AA6082T6 member plate compared to the variant 3 situation. However, the plastic deformation in this plate is almost negligible.

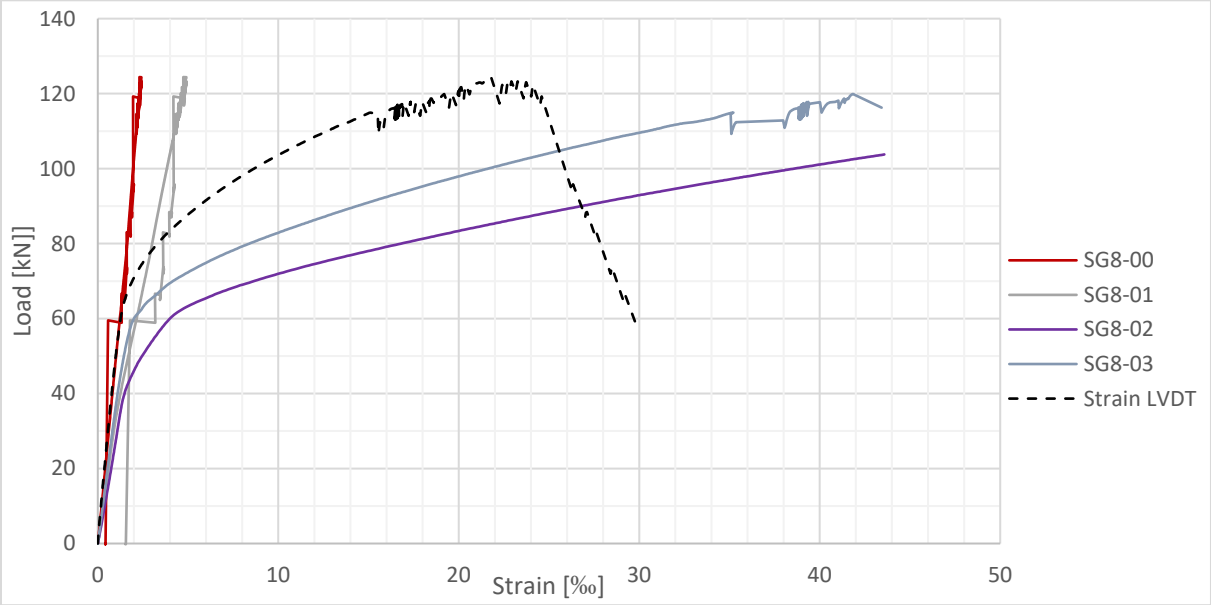

Figure 4.51: Load-strain graph measured by the strain gauges and the LVDT at the W4-1 specimen.

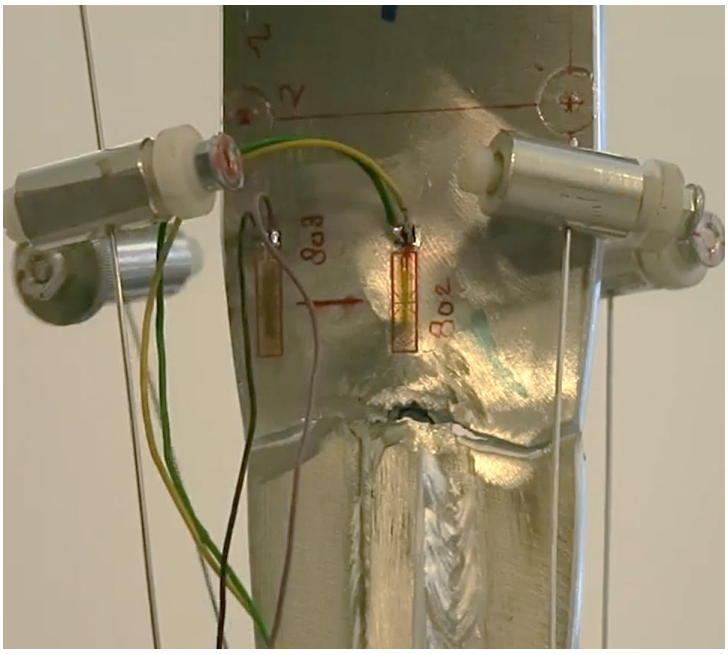

Figure 4.52: Failure of the W4-1 specimen.

The elastic limit force for the variant 4 specimens is calculated by

$$N_{0.2} = \left(b_{finger} - b_{slot}\right) \cdot t_{finger} \cdot f_{0.2} = (63.5 - 9) \cdot 7.92 \cdot 160.9 = 69.5 \cdot 10^3\ N.$$

Figure 4.53 shows the normalized load-displacement graphs of variant 4, from where the deformation capacity can be determined. In Table 4.19, the key values concerning the deformation capacity for

variant 4 are listed. From these findings, it is observed that also for this variant, the ultimate force was significantly larger as the elastic limit force with about the same ratio as shown for variant 3. The averaged measured displacements at ultimate load, and the plastic deformation were both lower for the variant 4 experiments compared to variant 3. However, since also the elastic limit force and displacement are defined lower due to a smaller critical cross-section, the deformation capacity turns out to be higher.

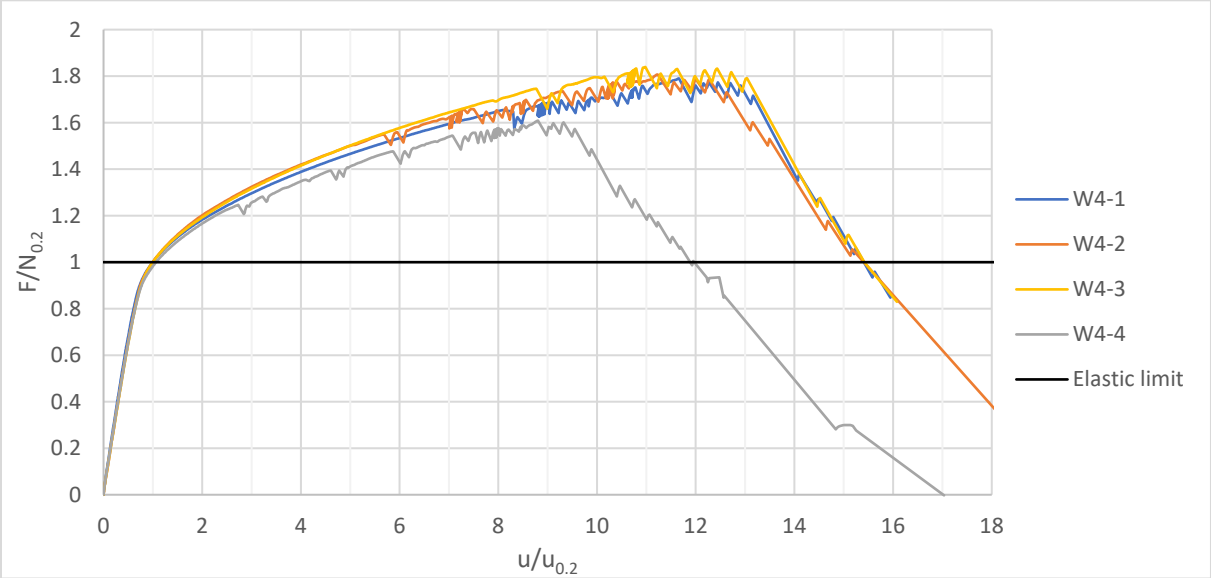

Figure 4.53: Normalized load-displacement graph of the variant 4 experiments.

Table 4.19: Key results considering the deformation capacity of the variant 4 experiments.

	W4-1	W4-2	W4-3	W4-4	Average	St. dev.	
Max $F/N_{0.2}$	1.79	1.81	1.84	1.61	1.76	0.09	
$u_{0.2}$	0.49	0.43	0.47	0.50	0.47	0.02	mm
u_{max}	5.66	4.85	5.11	4.10	4.93	0.56	mm
u_{el}	7.41	6.55	7.18	5.56	6.68	0.72	mm
$U_{c,s}$	10.66	10.23	9.98	7.24	9.53	1.35	
U_c	14.25	14.17	14.42	10.17	13.25	1.78	

4.3.8. Conclusions from the welded cruciform experiments

From the results of all tested specimens, some conclusions can be drawn. In order to compare the different variants, the experiment that showed the average results in terms of ductility of the corresponding specimen series is plotted in a graph in Figure 4.54. From this graph, it is concluded that the most substantial difference is present between variant 2 and the other variants. For the significant difference between the failure loads, a logical explanation can be found as the critical cross-section area is almost half the area of the other variants. However, the total displacement up to failure reduced significantly, with about 66% compared to variant 1. This significant difference was present even though the same materials were used for both variants. This phenomenon is probably because almost the entire cross-section of variant 2 was heat-affected. As a result, no base material was present that could lead to a strengthening effect.

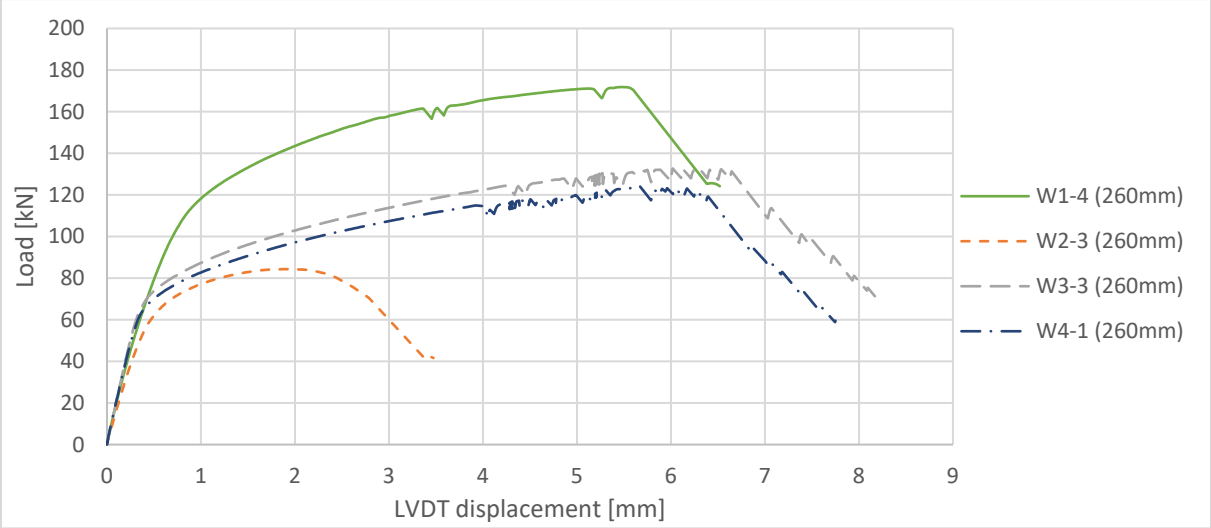

Figure 4.54: Load-displacement graph of the four different variants.

To be able to compare the different variants fairly, the deformation capacity is considered. By this definition, the results of the different variants are normalized to the elastic limit strength and displacement. In Figure 4.55, the experiment that showed the average results in terms of ductility of the corresponding specimen series is plotted.

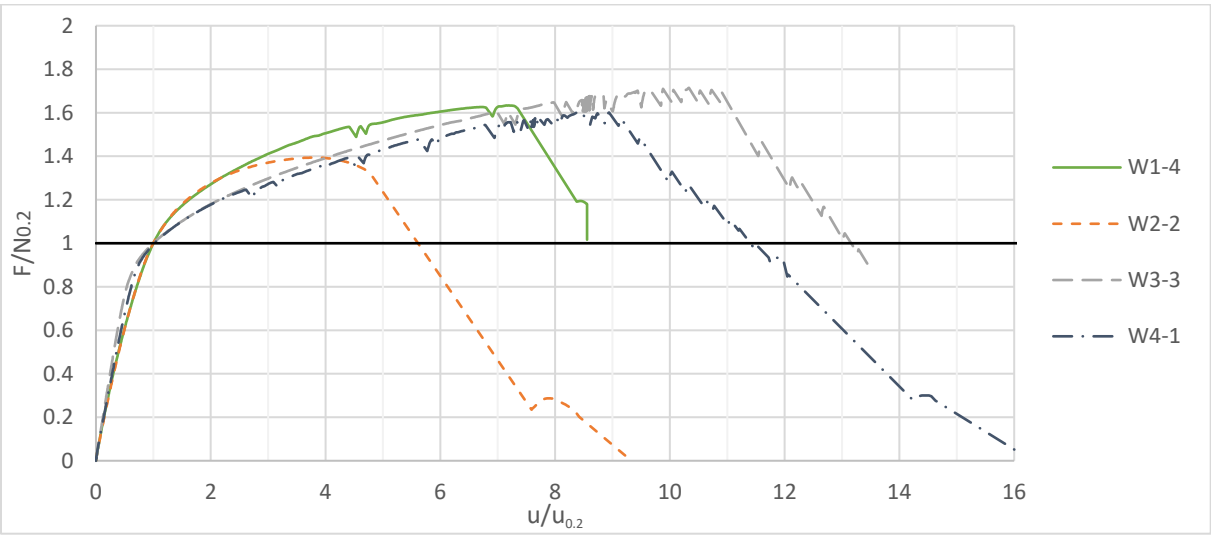

Figure 4.55: Normalized load-displacement graph of the four different variants.

From the graph shown in Figure 4.55, it is concluded that variant 2 showed the weakest performance, which was also already noticed in Figure 4.54. However, also the normalized force was significantly lower as experienced for the other variants. Furthermore, it turned out that the differences between the better-performing variants 1, 3, and 4 were higher, as observed in Figure 4.54. Variant 1 showed both a lower stable deformation capacity and total deformation capacity as variants 3 and 4. Based on this, it is concluded that the variants with failure in AA5083H111 material plate resulted in the best performing connections when one considers the deformation capacity.

Besides the differences in the deformations and applied loads between the variants also some remarkable things are noticed within a variant. For variants 1 and 2, it is shown that all specimens exceeded the estimated failure load with about 5%. However, for the variants 3 and 4, the estimated failure load was not achieved for any specimen. Furthermore, it is noticed that variants 1 and 2 showed consistent results between the different specimens with a maximal coefficient of variation around 6% for the measured displacements. For variants 3 and 4, more deviation is experienced with a corresponding maximal coefficient of variation around, respectively, 19% and 12% for the measured displacements. Especially for variant W3-1 and variant W4-4 a significant deviation between the other experiments is experienced. However, for variant W3-1, this is explained by the difference in the gauge length of the LVDT. For variant W4-4, no clear explanation could be found. The remarkable findings for the W3 and W4 specimens are probably due to the fact a slot is present in the finger plate, which is the critical plate in these variants. Therefore, failure is forced to occur around this gap. Since welds are located in this critical section, the weld quality probably significantly influences the results of the different samples.

4.4. Bolted joint experiments

4.4.1. Introduction

Next to a welded joint also experimental tests regarding a bolted joint and its deformation capacity were performed. These experiments were conducted to compare the results with the welded connection results. In the experiments, a simple bolted joint was tested using a heat-treated aluminum alloy 6082T6. This type of aluminum alloy was also used in the welded experiments. Since no welds were applied, obviously, no HAZ was present in this connection. Hence, the base material properties with a corresponding low $f_u/f_{0.2}$ ratio were still present in contrast to a welded connection. With this test, it is examined how much deformation capacity can be achieved using a bolted joint in combination with the base material properties of a heat-treated alloy.

4.4.2. Test set-up

Quasi-static tensile tests were carried out on the specimens at ambient temperature with the help of an Instron 250 kN testing machine. The specimens were loaded with a testing speed of 1.5 mm/min. The applied force and the crosshead displacement were recorded using a 250 kN load cell at the top of the testing machine. Next to the crosshead displacement, the deformation of the specimens was measured locally with the use of Digital Image Correlation. The displacements were measured by two marked dots placed 160 mm away from each other and centered in the middle of the specimen. Additionally, two LVDT's were placed on the back of the specimen as a backup. In Figure 4.56, an overview of the test set-up in practice is shown. For the experiments, two variants with bolts were tested and one variant without bolts. For each variant, three specimens were tested.

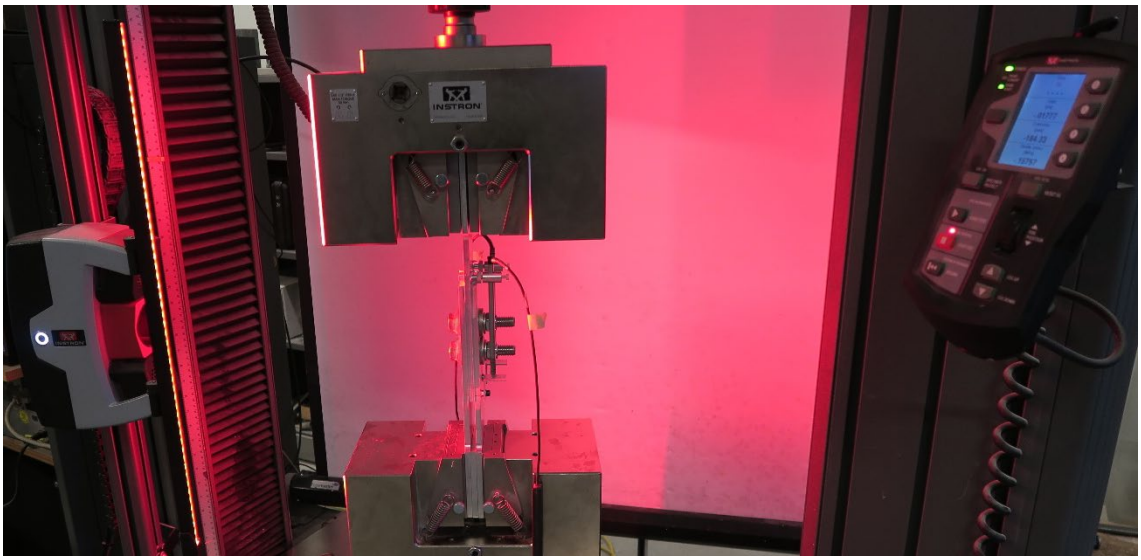

Figure 4.56: Test set-up overview.

4.4.3. Net cross-section failure

4.4.3.1. Dimensions

For the first variant, with the configuration shown in Figure 4.57, the dimensions are based on net cross-section failure. Following engineering guidelines, this failure mode is undesirable as it results in limited ductility. In the designed joint, the plates were connected by two bolts to ensure the bearing resistance was significantly higher as the net cross-section resistance. The joint was clamped into the tensile testing machine and pulled apart. Therefore, a shear force was present in the bolted connection. Two plates were connected to one single plate resulting in two shear planes, which prevented eccentricity in the connection.

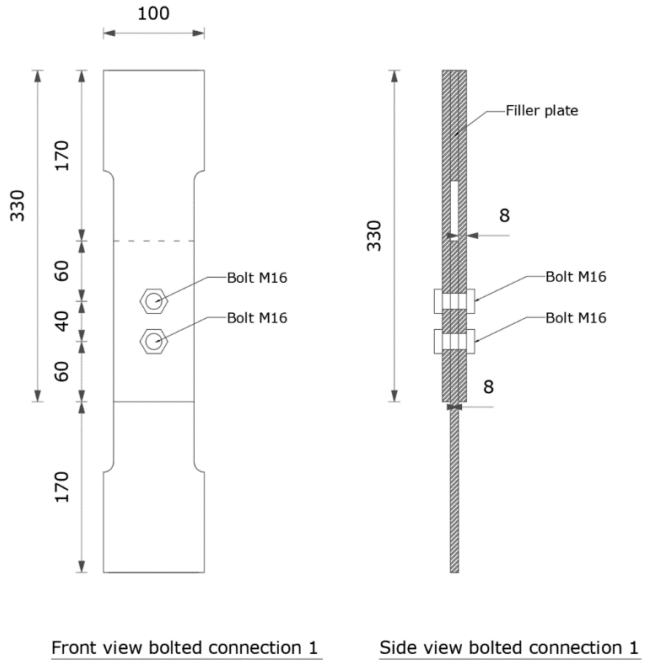

Figure 4.57: Dimensions of the bolted connection variant 1.

As mentioned, the variant 1 specimen will fail by net cross-section failure. The failure load is estimated using equation 8.6 of the standard NEN-EN-1999-1-1[3]. Using the actual material strength obtained from the base material dogbone experiments and no safety factors results in

$$N_{net} = 0.9A_{net} \cdot f_u = 0.9 \cdot (80 - 17.4) \cdot 7.9 \cdot 353 = 157.0 \cdot 10^3\ N.$$

Assuming the 0.9 factor is applied for additional safety measures, the failure load is better approximated by

$$N_{net} = A_{net} \cdot f_u = (80 - 17.4) \cdot 7.9 \cdot 353 = 174.4 \cdot 10^3\ N.$$

The elastic limit force, which is used for determining the deformation capacity, is calculated by

$$N_{0.2} = A_{net} \cdot f_{0.2} = (80 - 17.4) \cdot 7.9 \cdot 335 = 164.9 \cdot 10^3\ N.$$

4.4.3.2. Results

The results of the variant 1 specimens are shown in Figure 4.58, where the measured load is plotted against the displacement measured by the LVDT's. In Table 4.20, the key results of these specimens are listed. It can be noted that quite a similar tendency is experienced for the three specimens. Also, the estimated failure load was reached well in all cases. However, there appears to be a kind of shift between the curves. This shift can be explained by sliding of the plates until full contact between the plates and the bolt is reached.

Table 4.20: Key results of the bolted variant 1 specimens.

	B1-1	B1-2	B1-3	Average	Standard deviation		CV
Maximal load	178.69	178.64	177.96	178.43	0.4118	kN	0.23%
Displacement at max load	6.26	4.92	5.14	5.44	0.7217	mm	13.3%
Max displacement	7.25	5.88	6.11	6.41	0.7363	mm	11.5%
Displacement from 50 kN up to failure	5.52	5.41	5.49	5.47	0.0538	mm	0.98%

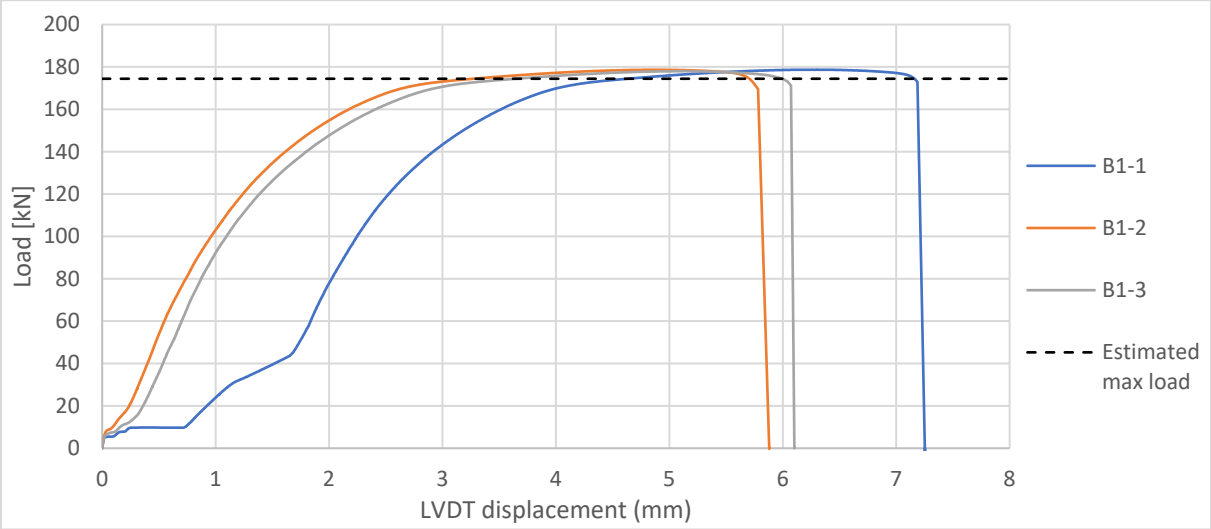

Figure 4.58: Load-displacement diagram of the B1 variant specimens.

In order to be able to compare the three different specimens, the curves are modified to ignore the sliding effects. The curves are shifted with a base point corresponding to the 50 kN point and have been moved until it matched the 50 kN point of the B1-2 specimen. This arbitrary point of 50 kN was chosen since no more sliding effects were experienced from this point on. From the shifted curves shown in Figure 4.59, it can be noted that an almost perfect correlation between the experiments was found. In Figure 4.60, it can be seen that the specimens indeed failed due to net cross-section failure.

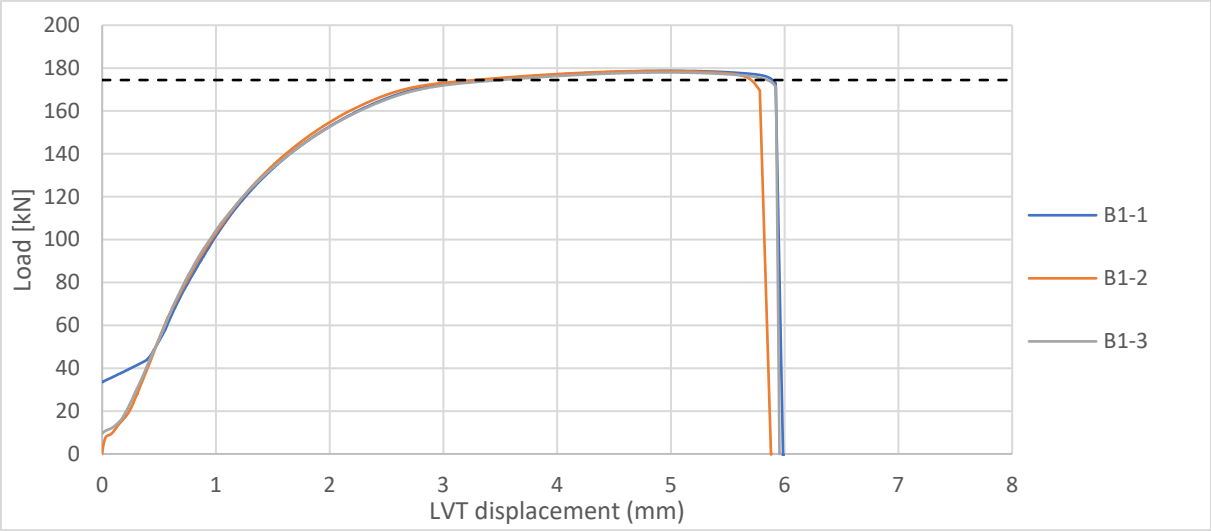

Figure 4.59: Shifted load-displacement graphs of the B1 variant specimens.

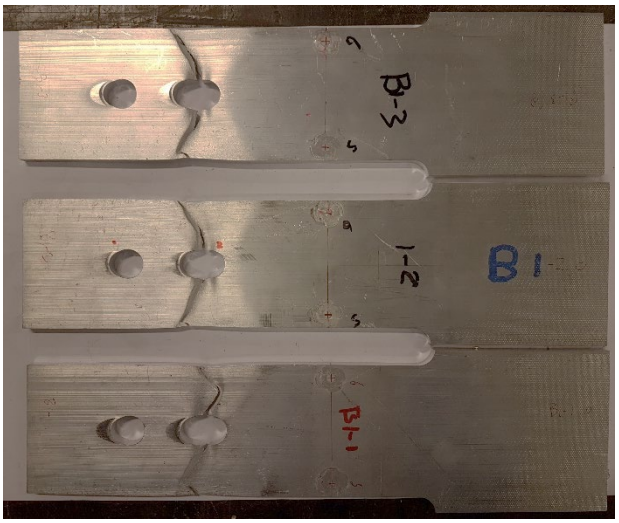

Figure 4.60: Failed B1 specimens.

To determine the deformation capacity of the bolted experiments, the load-displacement plot was normalized to the elastic limit strength and deformation. This plot is shown in Figure 4.61, and based on this graph, the deformation capacity was calculated. The procedure used for determining the deformation capacity is equivalent to the procedure, as demonstrated for the welded cruciforms in Section 3.1. The key results for the variant 1 experiments are listed in Table 4.21. From these results, it is noticed that the variants failed with limited plastic reserves and deformation. The stable deformation capacity value was just about 1.0. The total deformation capacity was slightly higher, with a value of 1.4.

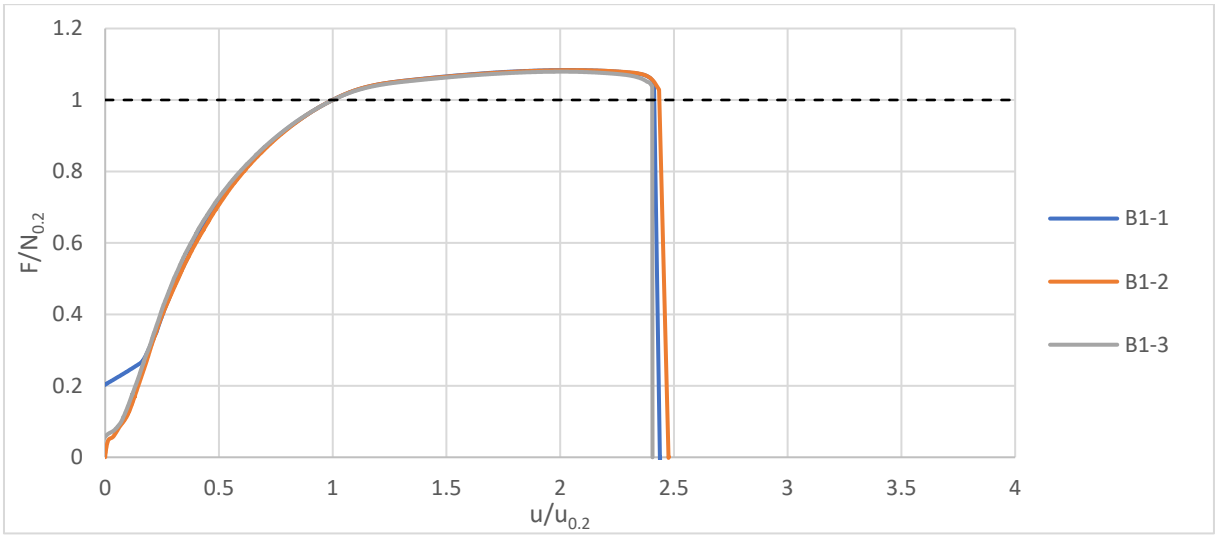

Figure 4.61: Normalized load-displacement graphs of the B1 experiments.

Table 4.21: Key results considering the deformation capacity of the B1 experiments.

	B1-1	B1-2	B1-3	Average	St. dev.	
Max $F/N_{0.2}$	1.08	1.08	1.08	1.08	0.0025	
$u_{0.2}$	2.45	2.37	2.48	2.44	0.0535	mm
u_{max}	5.00	4.92	4.99	4.97	0.0456	mm
u_{el}	5.92	5.78	5.92	5.88	0.0810	mm
$U_{c,s}$	1.04	1.07	1.02	1.04	0.0272	
U_c	1.41	1.44	1.39	1.41	0.0213	

4.4.4. Bearing failure

4.4.4.1. Dimensions

Variant 2 of the bolted connections is dimensioned based on failure due to bearing. For this case, a similar set-up and the same dimensions were applied as known for variant 1. However, only one bolt was used. The dimensions of this variant are shown in Figure 4.62.

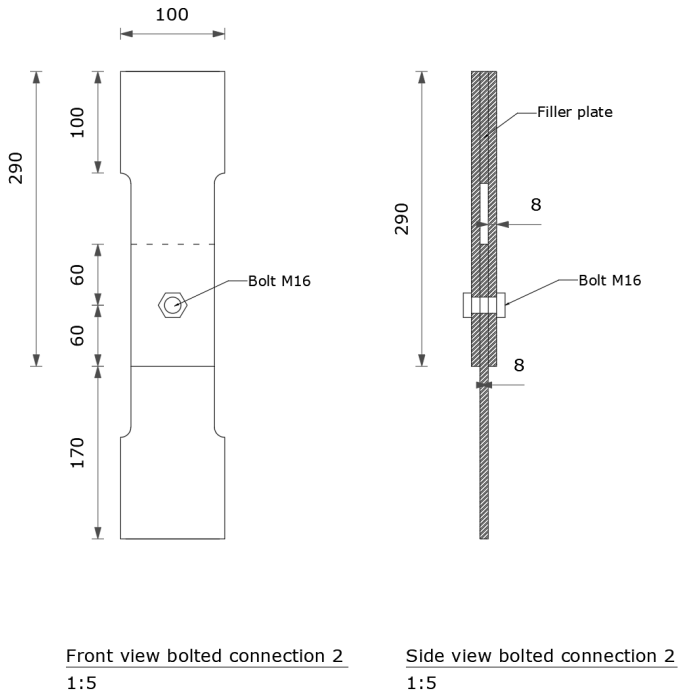

Figure 4.62: Dimensions of bolted connection variant 2.

The bearing resistance is estimated by

$$F_{b,R} = k_1 \alpha_b f_u dt = 2.5 \cdot 1 \cdot 353 \cdot 16 \cdot 7.9 = 111.5 \cdot 10^3\ N.$$

The elastic limit force is calculated by

$$N_{b,0.2} = k_1 \alpha_b f_{0.2} dt = 2.5 \cdot 1 \cdot 334 \cdot 16 \cdot 7.9 = 105.4 \cdot 10^3\ N.$$

4.4.4.2. Results

The results of the three tested specimens of variant 2 are plotted in Figure 4.63 and listed in Table 4.22. The displacements are measured by the LVDT's with a gauge length of 160 mm. From the results, it is noticed that some small sliding at the beginning of loading is experienced. Therefore, the curves are shifted in Figure 4.64 according to the 50 kN point, as similarly shown for variant 1. The specimens of variant 2 are showing quite a similar tendency. However, B2-1 failed slightly earlier. Furthermore, another failure pattern was shown for this specimen, as can be seen in Figure 4.65, where a picture of the three failed specimens is shown. The estimated failure load was far exceeded with each sample.

Table 4.22: Key results of the bolted variant 2 specimens.

	B2-1	B2-2	B2-3	Average	Standard deviation		CV
Maximal load	146.18	145.05	145.28	145.50	0.599	kN	0.41%
Displacement at max load	15.77	15.70	15.99	15.82	0.154	mm	0.97%
Max displacement	22.66	26.69	26.17	25.17	2.192	mm	8.71%
Displacement from 50 kN up to failure	15.15	14.81	15.28	15.08	0.242	mm	1.60%

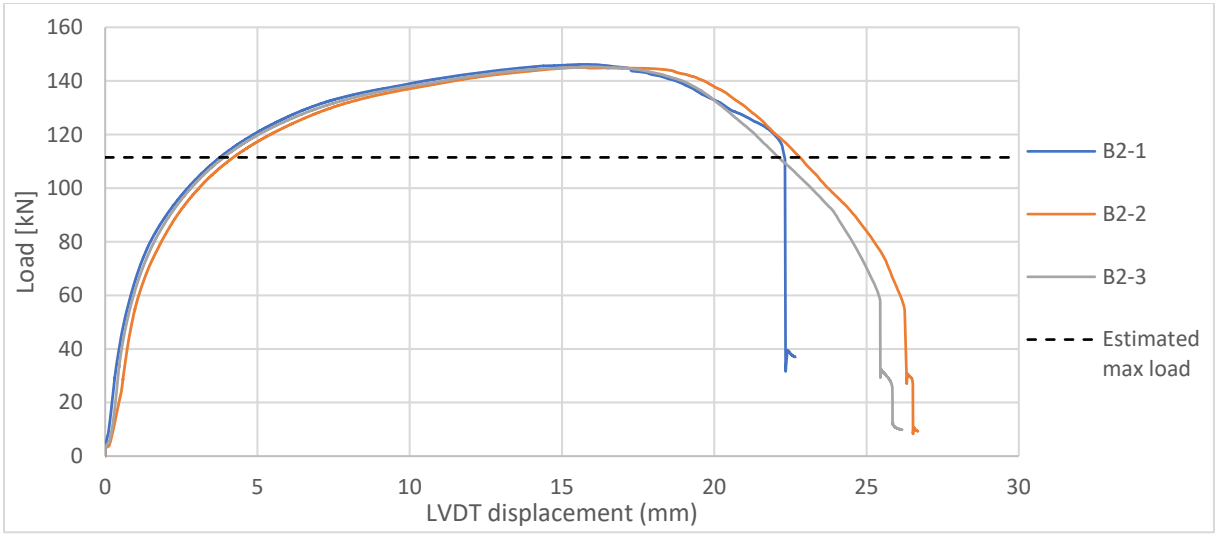

Figure 4.63: Load-displacement diagram of the B2 variant specimens.

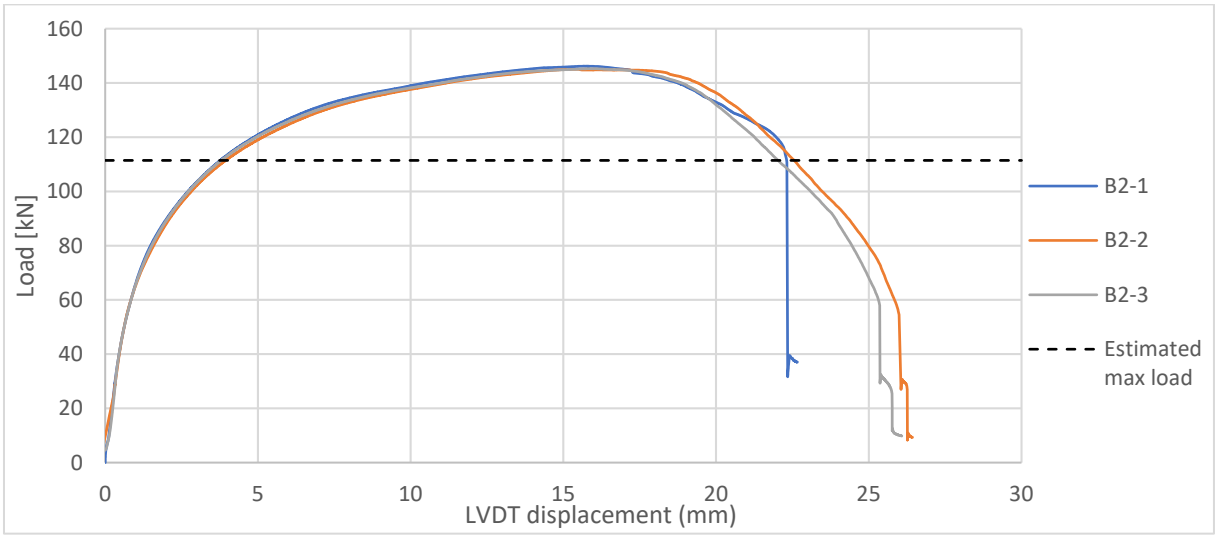

Figure 4.64: Shifted load-displacement graphs of the B2 variant specimens.

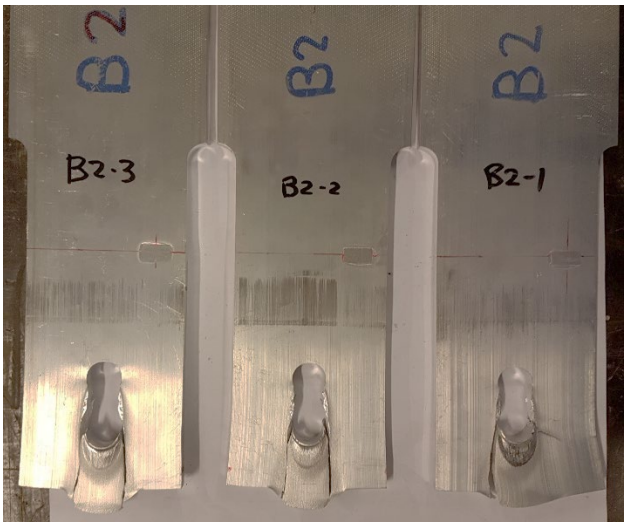

Figure 4.65: Failed B2 specimens.

The deformation capacity was evaluated for variant 2 as well. The normalized load-displacement graph is shown in Figure 4.66. The corresponding key values for determining the deformation capacity are listed in Table 4.23. From these results, it is shown that this bolted variant with bearing failure exhibits much more plastic reserves and deformation compared to the net section failure variant.

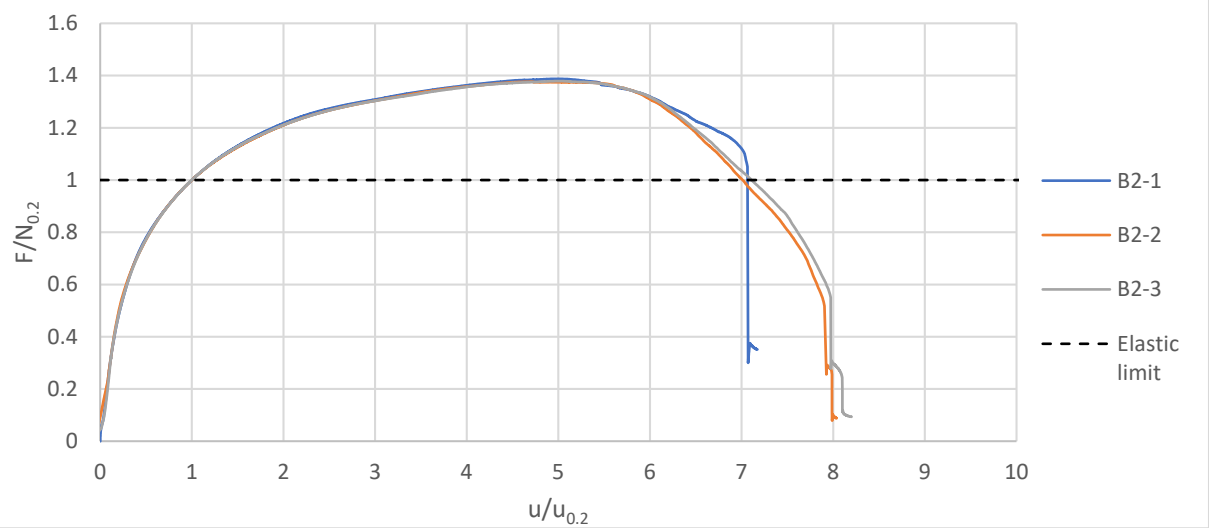

Figure 4.66: Normalized load-displacement graph of the bolted variant 2 experiments.

Table 4.23: Key results considering the deformation capacity of the bolted variant 2 experiments.

	B2-1	B2-2	B2-3	Average	St. dev.	
Max $F/N_{0.2}$	1.39	1.38	1.38	1.38	0.0057	
$u_{0.2}$	3.16	3.29	3.18	3.21	0.0687	mm
u_{max}	15.77	15.43	15.91	15.70	0.2420	mm
u_{el}	22.32	23.05	22.61	22.66	0.3699	mm
$U_{c,s}$	3.99	3.69	4.00	3.89	0.1738	
U_c	6.06	6.01	6.11	6.06	0.0475	

4.4.5. Net cross-section failure without bolts

4.4.5.1. Dimensions

The last variant that was designed for the experimental bolted joints program is, in fact, not a bolted connection. The specimen is based on variant 1 but does not contain any bolts. With the help of this specimen, the influence of the bolts on the net section resistance can be determined. Figure 4.67 shows the dimensions of the tested plate containing two bolt holes. This variant is further mentioned as “variant 3” or indicated by B3.

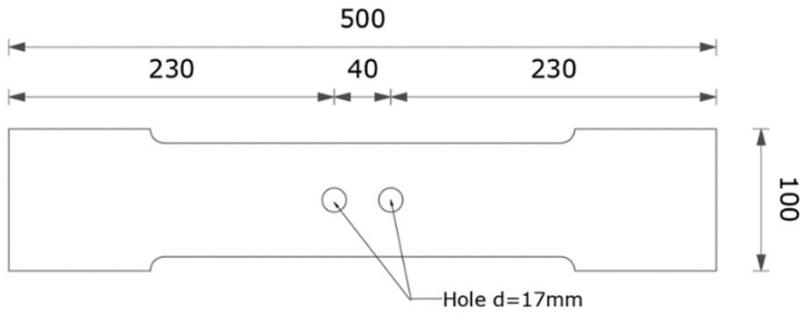

Figure 4.67: Dimensions of the plate of variant 3.

The failure load of variant 3 is equal to the net cross-section resistance, similar to variant 1. This holds that the failure load is estimated by

$$N_{net} = A_{net} \cdot f_u = (80 - 17.4) \cdot 7.9 \cdot 353 = 174.4 \cdot 10^3\ N.$$

The elastic limit force, which is used for determining the deformation capacity, is calculated by

$$N_{0.2} = A_{net} \cdot f_{0.2} = (80 - 17.4) \cdot 7.9 \cdot 335 = 164.9 \cdot 10^3\ N.$$

4.4.5.2. Results

The three tested specimens without bolts were tested and measured using LVDT’s at the backside of the specimen with a gauge length of 160 mm. The results are plotted in Figure 4.68 and listed in Table 4.24. It is noticed that the estimated failure load was reached quite near. In Figure 4.69, the results of variant 1, which also fails by net section failure, are plotted together with variant 3 results. From this diagram, it can be seen that some differences between the two situations are present. Figure 4.70 shows that the plate does fail as expected near the bolt hole due to net cross-section failure.

Table 4.24: Key results of variant 3 specimens.

	B3-1	B3-2	B3-3	Average	Standard deviation		CV
Maximal load	175.47	174.52	174.66	174.88	0.511	kN	0.29%
Displacement at max load	4.07	3.98	3.94	4.00	0.064	mm	1.60%
Max displacement	5.82	5.66	5.29	5.59	0.268	mm	4.80%
Displacement from 50 kN up to failure	5.63	5.47	5.11	5.40	0.268	mm	4.97%

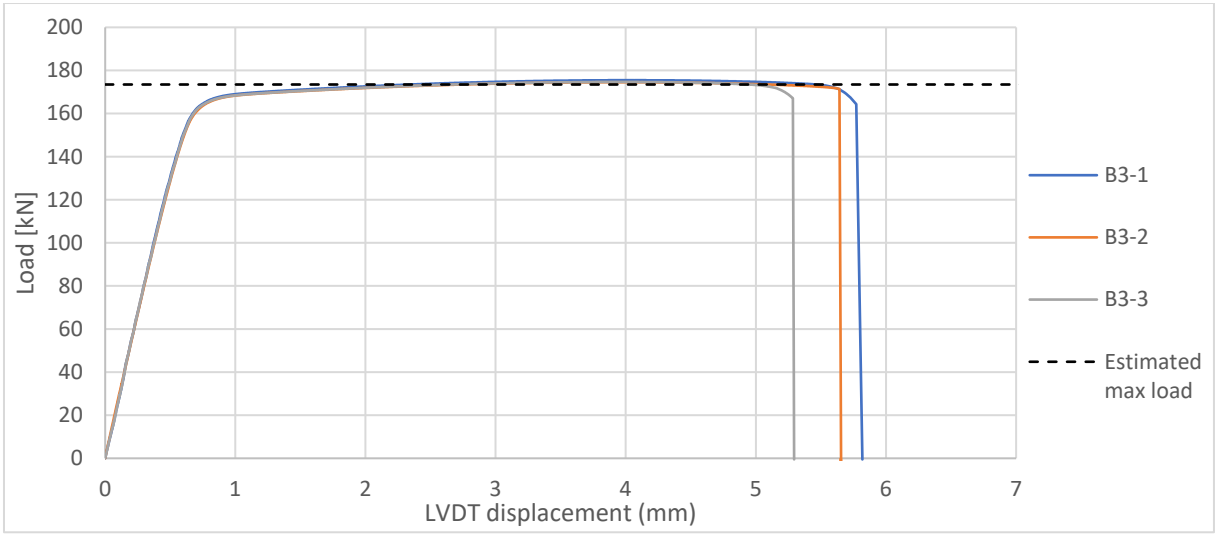

Figure 4.68: Load-displacement diagram of the B3 variant specimens.

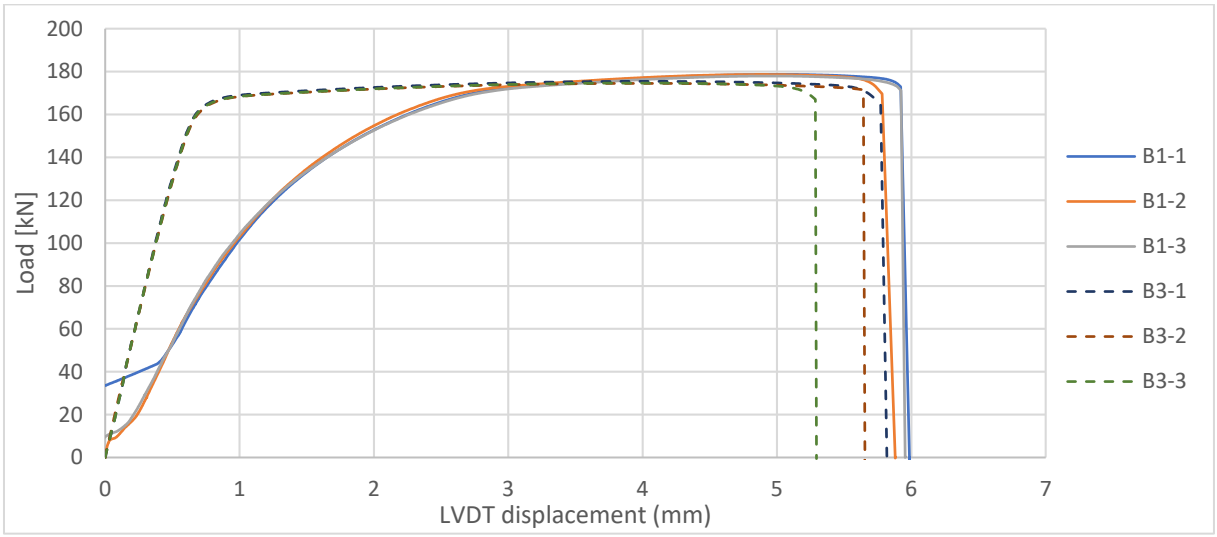

Figure 4.69: Combined load-displacement diagram of the B1 and B3 specimens.

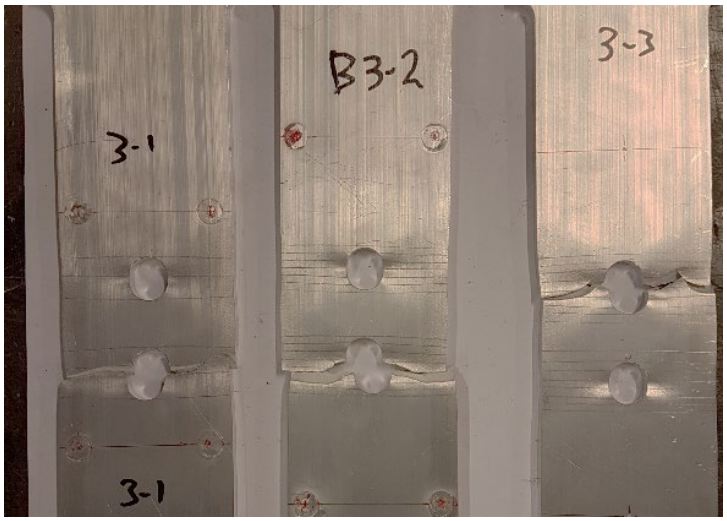

Figure 4.70: Failed B3 specimens.

The deformation capacity of variant 3 is determined by the same principle as described for the previous bolted variants. However, for this variant, the elastic limit is much more visible as experienced for the other variants. The normalized load-displacement graph is shown in Figure 4.71. The key results for determining the deformation capacity of variant 3 are listed in Table 4.25.

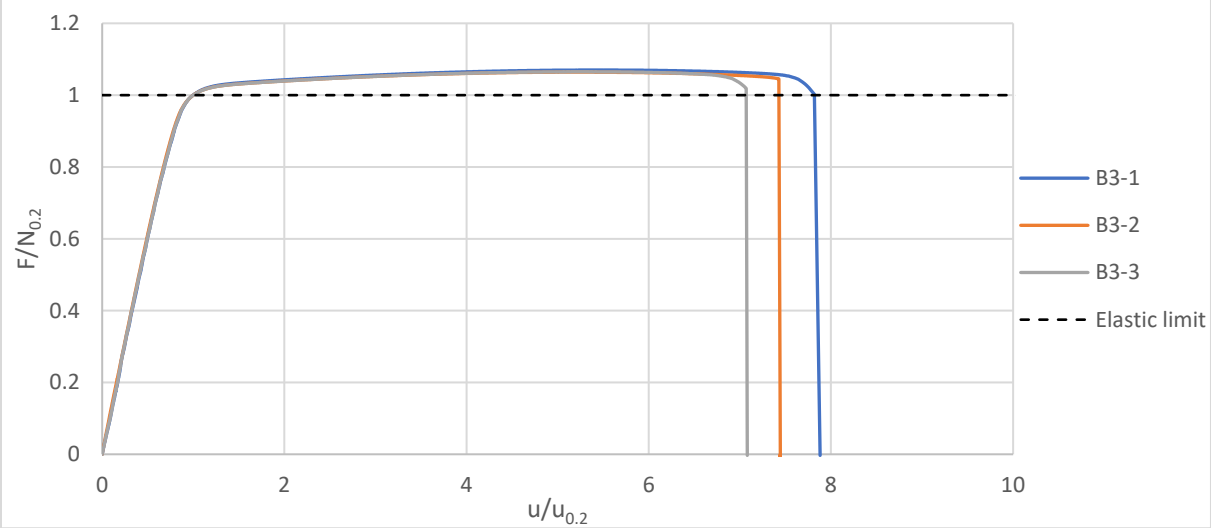

Figure 4.71: Normalized load-displacement graphs of the bolted variant 3 experiments.

Table 4.25: Key results considering the deformation capacity of the bolted variant 3 experiments.

	B3-1	B3-2	B3-3	Average	St. dev.	
Max $F/N_{0.2}$	1.07	1.06	1.07	1.07	0.0031	
$u_{0.2}$	0.74	0.76	0.75	0.75	0.0107	mm
u_{max}	4.10	4.01	3.98	4.03	0.0639	mm
u_{el}	5.77	5.64	5.29	5.57	0.2520	mm
$U_{c,s}$	4.55	4.28	4.32	4.39	0.1473	
U_c	6.82	6.43	6.07	6.44	0.3738	

From the results, it is noticed that quite a large deformation capacity was reached for the variant 3 specimens. This, in contrast to the earlier findings in the different load-displacement graphs. Based on this, it is concluded that the deformation capacity was not determined in the right way for each variant. Therefore, the deformation capacity was recalculated based on the average elastic limit deformation of the variant 3 specimens in order to compare the three different variants by a more equitable method. The key values for the recalculated deformation capacity of variants 1 and 2, are listed in Table 4.26.

Table 4.26: Key results considering the recalculated deformation capacity of variants 1 and 2.

	B1-1	B1-2	B1-3	Average	B2-1	B2-2	B2-3	Average	
Max $F/N_{0.2}$	1.08	1.08	1.08	1.08	1.39	1.38	1.38	1.38	
$u_{0.2}$	0.75	0.75	0.75	0.75	0.75	0.75	0.75	0.75	mm
u_{max}	5.00	4.92	4.99	4.97	15.77	15.43	15.91	15.70	mm
u_{el}	5.92	5.78	5.92	5.88	22.32	23.05	22.61	22.66	mm
$U_{c,s}$	5.66	5.55	5.66	5.62	20.03	19.58	20.21	19.94	
U_c	6.89	6.71	6.90	6.83	28.76	29.74	29.14	29.21	

4.4.6. Conclusions from the bolted experiments

From the results shown in the previous sections, it can be concluded that the intended failure modes and the estimated values from hand calculations were quite accurate. As expected, a tremendous difference in deformation between the net cross-section failure and the bearing failure variants is experienced. This can be clearly seen in Figure 4.72, where the three different variants are presented by a load-displacement graph. All the specimens were measured with a gauge length of 160 mm. For the B2 variant, it appeared that about four times as much displacement up to failure occurred as for the net cross-section failure variants. It must be kept in mind that, in both situations, almost all plastic deformation was obtained in the vicinity of the bolt holes since the 0.2% proof stress was not reached in the gross section of the specimens. A larger member length will therefore not result in more plastic deformations up to failure.

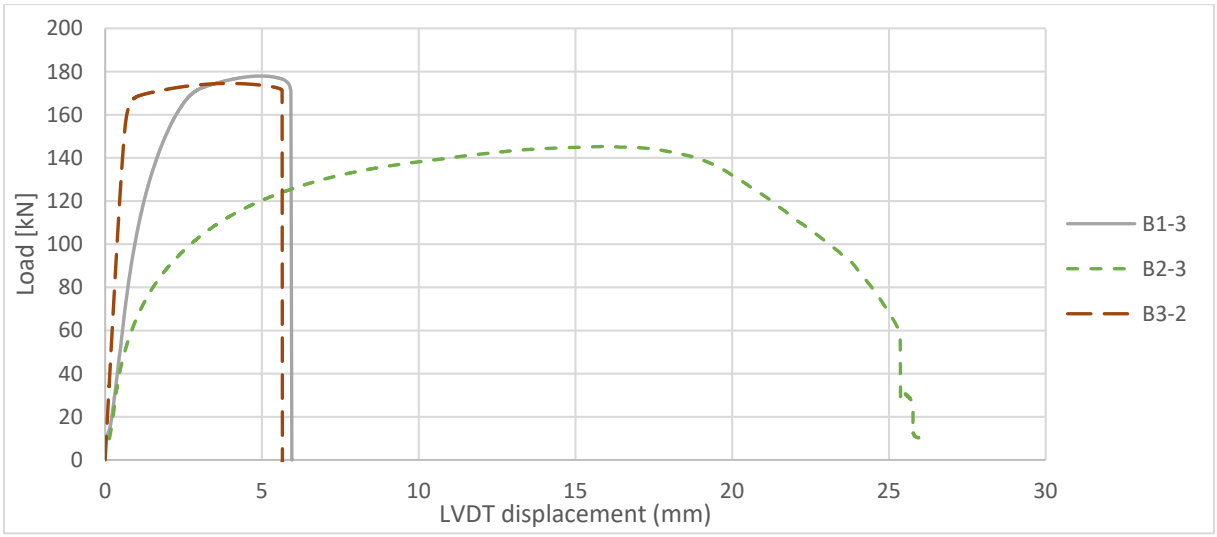

Figure 4.72: Combined load-displacement diagram of the three different bolted variants.

Furthermore, to compare the different specimens in an equal way, the load-displacmeent graph was normalized based on the elastic limit deformation of variant 3, as explained in the previous section. The combined normalized load-displacement plot of the specimens representing the average results within the corresponding specimen series, is presented in Figure 4.73.

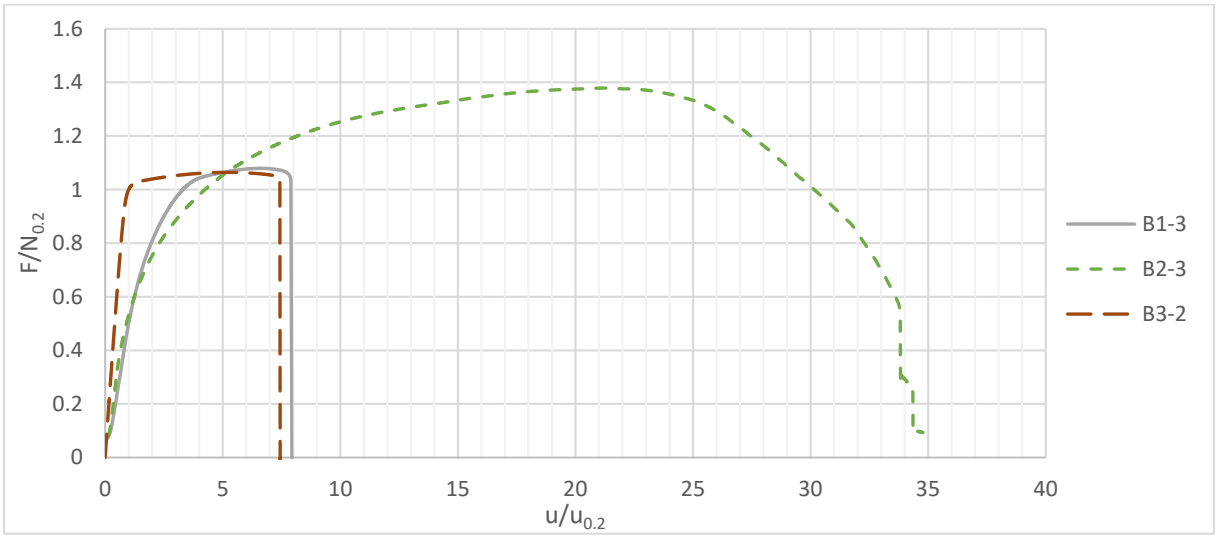

Figure 4.73: Normalized load-displacement graph of the representative bolted specimens.

From the normalized plot shown in in Figure 4.74, the stable and total deformation capacity values are determined. It is concluded that the botled variant 2 resulted in far the most deformation capacity compared to the net section failure variants 1 and 3. Furthermore, it is noticed that the variant 2 failed in conjunction with much more plastic reserves up to failure. For this variant 2, the ultimate strength was about 40% as high as the elastic limit strength.

Previously some differences were noted between the net section failure specimens with and wihtouth the application of bolts. The variant that contain bolts, variant 1, experienced some more deformation capacity and ultimate strength as the variant without bolts. The presence of the bolts can explain this difference, which is also visible in Figure 4.74, where a picture of the failed specimens B1-3 and B3-1 is shown. It can be noticed that for variant 1, shown in the figure at the left-hand side, the forces are transferred by both the bolts. This probably resulted in a different and better stress distribution around the bolt hole compared to variant 3 shown on the right-hand side.

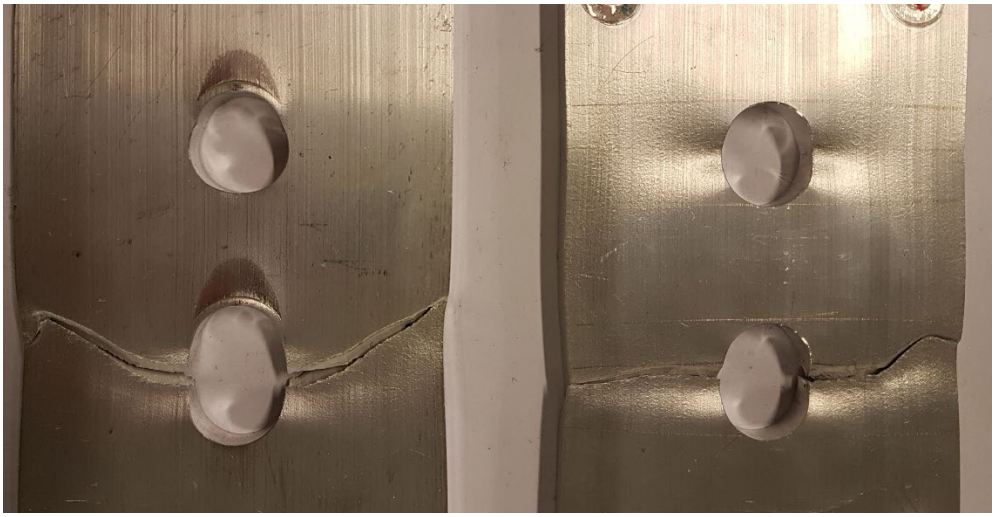

Figure 4.74: Failed specimens B1-3 (left) and B3-1 (right).

4.5. Experimental results discussion and relation to practice

Based on the findings of the different experiments that were conducted, some overall conclusions can be made. In addition, conclusions are drawn related to practice and the application of the European standard EN-1999-1-1.

From the dogbone experiments, it is noticed that a rather good correspondence with the material certificate values of $f_{0.2}$, f_u, and $A_{5.65\sqrt{A}}$ was obtained. However, as expected, the measured values did significantly exceed the values listed in the standard. An important finding that is observed by the experiments is the vast difference in deformation between the transversely welded dogbones and the longitudinally and unwelded dogbones for the aluminum alloy 6082T6. This difference clearly shows that the local weakening of the material due to the heat of welding led to an enormous decrease in the deformation capacity of the specimen. The total deformation up to failure decreased by about 65% compared to the unwelded situation. This tremendous decrease can be explained by the fact that the critical heat-affected zone was small compared to the complete structure in the transversely welded situation, and hence plastic deformations were limited by this zone. The results of the transversely welded dogbones support the recommendation to avoid transverse welds for heat-treated alloys if possible, which was earlier mentioned in the literature study in Section 3.7.

With the found results of the AA5083H111 dogbone experiments, it is confirmed that the welding of this material hardly leads to material strength degradation. The results of the Vickers hardness experiments support this conclusion. From the hardness profiles, it is noticed that the material around the welds was only marginally affected by a maximal decrease in Vickers hardness of about 10%. The hardness profiles of the welded AA6082T6 dogbones show a more significant influence of the heat input with a maximal decrease of the Vickers hardness of about 35%. From the hardness profile, a heat-affected zone of about 15 mm away from the weld center is observed. This value is significantly lower as the prescribed HAZ width of 30 mm by EN 1999-1-1 for MIG-welding of 8 mm thick aluminum alloys.

No significant differences between the different welded cruciform variants are discovered in the calculation process when taken the EN-1999-1-1 in mind. For all the four variants, it is prescribed to account for the entire cross-section to be heat-affected. This since the distance of the weld to the edge was lower than three times the prescribed HAZ width of 30mm in all cases by section 6.1.6.3(7) of EN-1999-1-1. Calculations were performed for the critical section for both the AA6082T6 and AA5083H111 plates to compare the experimental results with EN-1999-1-1. The member and finger plates were connected in all variants by longitudinal welds. For cross-sections containing longitudinal welds, EN-1999-1-1 indicates that for calculating the ultimate tensile force, $N_{0,Rd}$ must be used. Where the 0.2% proof stress and the reduction factor for the HAZ, must be accounted[3]. Also, for the bolted experiments, the design strength was calculated by the guidelines of the EN-1999-1-1 standard.

For reasons of comparison, the maximal force F, obtained from the experiments, is divided by the decisive design strength calculated by the standard for all the performed experiments. In Table 4.27, these values are listed for each experiment indicated by F/N_{EC9}. This table also includes other fundamental values, such as the maximal force F divided by the expected limit force F_{limit}, the maximal force divided by the elastic limit $N_{0.2}$, and the deformation capacity values. From these listed results, the ductility performance of all the different experiments is assessed.

Table 4.27: Summary of the results of the experimental program.

Experiment	F/N_{EC9}	$F/N_{0.2}$	F/F_{limit}	$U_{c,s}$	U_c	$U_{c,s,2}$*	$U_{c,2}$*
Dogbone experiments							
AA6082T6 Base material	*1.14*	*1.06*	*1.00*	*11.17*	*23.31*	*11.17*	*13.97*
AA6082T6 Transversely welded	*1.38*	*1.55*	*1.00*	*8.88*	*11.18*	*2.05*	*2.58*
AA6082T6 Longitudinally welded	*1.37*	*1.32*	*1.00*	*13.61*	*23.00*	*13.61*	*15.77*
AA5083H111 Base material	*1.14*	*1.95*	*1.00*	*50.10*	*56.62*	*50.10*	*51.60*
Cruciform experiments							
Partly HAZ failure	*2.67*	*1.61*	*1.03*	*6.16*	*8.41*		
Experiment W1-1	2.69	1.62	1.04	6.28	9.51		
Experiment W1-2	2.68	1.62	1.04	6.26	8.42		
Experiment W1-3	2.60	1.57	1.01	5.89	8.13		
Experiment W1-4	2.70	1.63	1.05	6.20	7.56		
Fully HAZ failure	*2.36*	*1.44*	*1.07*	*3.00*	*4.02*		
Experiment W2-1	2.60	1.59	1.18	3.07	3.55		
Experiment W2-2	2.28	1.39	1.03	2.86	3.78		
Experiment W2-3	2.32	1.42	1.05	3.17	5.06		
Experiment W2-4	2.24	1.37	1.01	2.88	3.69		
Cold worked plate failure	*2.15*	*1.76*	*0.90*	*9.38*	*12.48*		
Experiment W3-1	1.99	1.63	0.83	6.94	10.28		
Experiment W3-2	2.23	1.83	0.94	10.72	13.62		
Experiment W3-3	2.09	1.71	0.88	9.33	12.05		
Experiment W3-4	2.28	2.09	0.96	10.50	13.96		
Cold worked narrowed plate failure	*2.10*	*1.76*	*0.90*	*9.53*	*13.25*		
Experiment W4-1	2.14	1.79	0.92	10.66	14.25		
Experiment W4-2	2.16	1.81	0.92	10.23	14.17		
Experiment W4-3	2.20	1.84	0.94	9.98	14.42		
Experiment W4-4	1.92	1.61	0.82	7.24	10.17		
Bolted experiments							
Net section failure	*1.59*	*1.08*	*1.02*	*5.62*	*6.83*	*3.46*	*4.21*
Experiment B1-1	1.59	1.08	1.02	5.66	6.89		
Experiment B1-2	1.59	1.08	1.02	5.55	6.71		
Experiment B1-3	1.58	1.08	1.02	5.66	6.90		
Bearing failure	*1.83*	*1.38*	*1.31*	*19.94*	*29.21*	*12.27*	*17.98*
Experiment B2-1	1.84	1.39	1.31	20.03	28.76		
Experiment B2-2	1.83	1.38	1.30	19.58	29.74		
Experiment B2-3	1.83	1.38	1.30	20.21	29.14		
Net section failure without bolts	*1.55*	*1.07*	*1.01*	*4.39*	*6.44*	*2.70*	*3.96*
Experiment B3-1	1.56	1.07	1.01	4.55	6.82		
Experiment B3-2	1.55	1.06	1.01	4.28	6.43		
Experiment B3-3	1.55	1.06	1.01	4.32	6.07		

* New deformation capacity values were calculated since the values are dependent on the gauge length. The capacity values were recalculated by adjusting the elastic limit deformation to an elastic limit deformation for a 260 mm gauge length situation.

From the results in Table 4.27, it is concluded that all the experiments exceeded the calculated design strength, indicating a safe underestimation by the standard for all the experiments. Especially for the welded cruciform experiments, a significantly higher resistance than the design strength is experienced. Furthermore, large values of the ratio maximal to plastic force are experienced for the welded cruciform experiments. This high ratio indicates that much plastic reserve was present up to failure. It is concluded that all the connections performed well with extensive safety margins, considering the strength of the different specimens.

However, regarding the deformations, some critical issues appear in the performance of some experiments. The welded cruciform containing a fully heat-affected cross-section failed by a significantly lower deformation capacity. The stable deformation capacity with an averaged value of 3.00 for this variant is about two times smaller than the partly heat-affected cross-section and more than three times smaller than the welded cruciforms with failure in the cold worked plate.

Furthermore, the deformation capacity value of the fully heat-affected cruciform is in the same range of the 'badly engineered' bolted connection, which failed by net cross-section failure. Since, in practice, net cross-section failure is highly recommended to avoid, this fully heat-affected welded variant can be characterized as a poor performing connection.

The partly heat-affected welded cruciform showed some better performance regarding the ductility, compared to the fully heat-affected cruciforms. However, the cruciforms with failure in the cold worked AA5083H111 finger plate showed the best ductility results of the welded cruciform variants. The deformation capacity values for this variant, where the critical cross-section was unaffected by heat, were almost in the range of the 'ductile' bolted connection, which failed by bearing.

Based on the adjusted deformation capacity values for the transversely welded AA6082T6 dogbones, it can be concluded that the earlier statement to avoid welded connections in heat-treated alloys is justified. With values of only 2.05 and 2.58 for the stable and total deformation capacity, respectively, it is confirmed that this weld configuration results in a poor performance related to the ductility compared to the base and HAZ material.

In short, when considering the deformation capacity results of all the experiments, it is concluded that some connection details must be avoided in structural aluminum alloy applications. As previously concluded from the literature review, transverse welding of heat-treated aluminum alloys appears to result in early failure of structural elements in conjunction with very limited ductility. Premature failure and low ductility are also experienced for the fully heat-affected variant, and the bolted connection failed by net section failure. The bolted variant with bearing failure and the other welded cruciform variants show better performance regarding the ductility. Especially this bolted variant and the welded cruciforms with failure occurring in the unaffected AA5083H111 plate showed relatively high values for the deformation capacity.

5. Numerical research

With the help of a numerical model, the ductility behavior of aluminum alloy structures can be investigated quicker and less costly for a wide variety of materials, connection types and geometry changes. In this study a foundation for such a model is established. The calibration and validation process for this model is outlined in this chapter. Firstly, the material models required for the model are calibrated with the help of the experimental results in Section 5.1. Afterwards, a first validation was performed in Section 5.2, based on the experiment of the plate with 2 bolt holes. Finally, a complete welded cruciform model was created and validated with the help of the experimental results in Section 5.3. The overall conclusions based on the validation of the numerical models are presented in Section 5.4.

5.1. Numerical material model calibration by the dogbone specimens

5.1.1. Introduction

In order to reproduce the results of the welded cruciform experiments as accurately as possible, the material models were calibrated using the results of the dogbone experiments. Numerical models of the dogbone experiments have been created and evaluated using the finite element software Abaqus version 6.14-1/standard. The FEM dogbone models were constructed with the same dimensions as used in the experiments. A non-linear material model, in combination with a fracture model, was implemented based on the experimental results. More information about this material model, based on the Ramberg-Osgood (RO) equation and fracture modeling is given in Section 2.3 and 2.6. After performing the analysis, the result was compared with the experimental results. In the subsequent steps, the material parameters were adjusted step by step until a close match with the experiments was reached. The parameters that were varied in the calibration process are the strain at the onset of fracture ε_f, the fracture energy dissipation G_f and the stiffness of the plastic branch in the σ-ε diagram after reaching the ultimate stress. Calibrations were performed for three different materials, namely the AA6082T6 base material, the AA6082T6 HAZ material, and the AA5083H111 base material. The three different material models followed the same calibration process. First, analyses were carried out using starting values based on the experimental results and previous studies by others. In the subsequent steps, the fracture strain was calibrated by remaining the fracture energy and the stress-strain relation constant as the original. Additionally, the material models were calibrated based on the fracture energy and the stress-strain relationship.

The calibration process was first performed for the aluminum alloy 6082T6. Both base and heat-affected materials were calibrated. After that, both base material and heat-affected material models were implemented in one single model representing the transversely welded dogbone situation, also known as the local HAZ situation. Based on this model, the earlier calibrated models are validated and further improved. For the aluminum alloy 5083H111, only the base material was calibrated since the influence of the heat input by welding was almost negligible. Therefore, no validation step based on the dogbones was performed for this material. With the help of the results of the welded cruciform specimens, this aluminum alloy will eventually be validated.

5.1.2. Model layout

As mentioned, the numerical models of the dogbones are created with the same dimensions as used in the experimental tests. Only the clamped end parts are reduced in size to minimize the model complexity. The dimensions used are indicated in Figure 5.1. In the dogbone FEM models, some different mesh configurations and sizes are applied and evaluated. More details and the corresponding results are presented later on in this chapter. For all the dogbones, hexahedron C3D8R elements are used. This is a continuum 3D element with eight nodes and reduced integration.

For the transversely welded model, containing a local HAZ, a zone equal to the HAZ width was constructed. Within this zone, a refined mesh and the specific HAZ material properties were applied. In the rest of the model, the calibrated base material properties were assigned. An overview of the mesh and the refined mesh zone is illustrated in Figure 5.2.

The dogbone was restricted to move in all directions at the bottom by applying the boundary condition $x = y = z = 0$. At the top, the dogbone was restricted to move in the horizontal x and y directions. In the vertical direction z, an imposed displacement was applied parallel to the longitudinal axis of the dogbone. An overview of the boundary conditions and the applied displacement is shown in Figure 5.2. The imposed displacement was applied with static general load steps. Similar to the experiments, the displacements in the numerical model were measured between two points separated 60 mm from each other. These points were placed around the center of the dogbone.

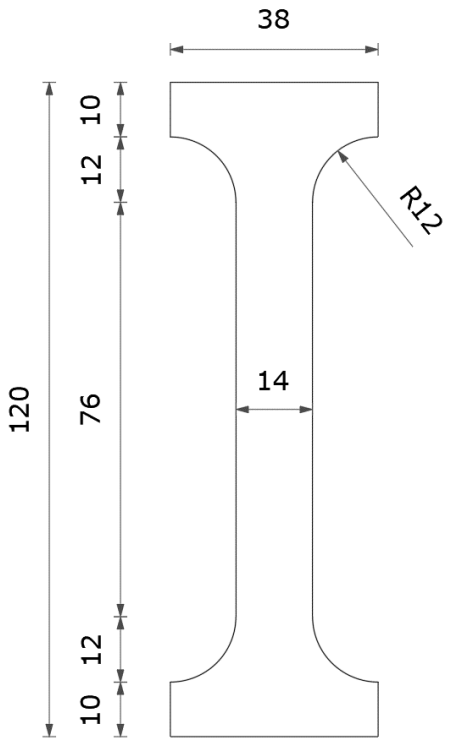

Figure 5.1: Dimensions of the modeled dogbone specimen (t=8mm).

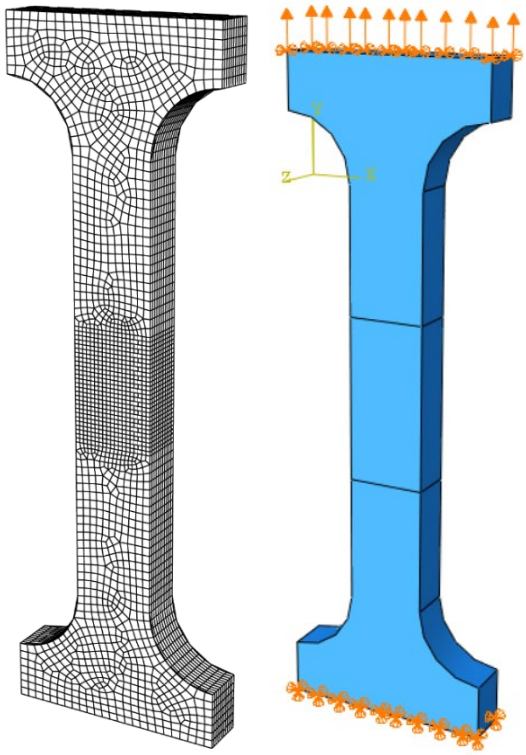

Figure 5.2: Overview of the mesh configuration and the applied boundary conditions in Abaqus.

5.1.3. Material models

As mentioned, the initial material models were implemented by using the experimental results. With the help of these results and the RO equation, mentioned in Section 2.3.2 by Equation 2.1, a non-linear stress-strain relation was constructed. In Table 5.1, the average values of the experimental results are listed. These values are the representative values for the specific alloy and the corresponding material state. The RO models for the materials were constructed with the help of the 0.2% proof stress $f_{0.2}$, the ultimate stress $f_{u,}$ the modulus of elasticity E, and the strain at the point of maximal stress ε_u. The value for A_{60} mentioned in Table 5.1 represents the strain at fracture measured with a gauge length of 60 mm. This value of A_{60} was used as the initial value for the strain at the onset of fracture ε_f.

With the help of the RO equation, the stress can be calculated for every arbitrary value of strain. By subdividing the maximal strain into 19 steps, 19 different points on the material curve were constructed. These values were converted to true stress-strain values and listed in Table 5.2. The value in the penultimate row was calculated using the maximal stress and the corresponding strain. The last

row was constructed to extend the material model. For this purpose, an arbitrary value for the strain was chosen, which is significantly larger than the second last point. The corresponding stress at this point was calculated with the Ramberg-Osgood relation and indicated with *fx. This value was varied later on in the calibration process to adjust the curve after reaching the maximal stress. The true σ-ε material models, as listed in Table 5.2, are plotted for each material by a solid grey line in Figure 5.3 up to Figure 5.5. In these figures also the true σ-ε relation obtained from the experiments is plotted by a dotted line. In addition, an example of an adjusted material model is plotted by a dashed grey line.

Table 5.1: Average of the experimental results.

	AA6082T6 (base material)	**AA6082T6HAZ** (longitudinally welded)	**AA5083H111** (base material)
$f_{0.2}$ [N/mm²]	334.0	206.9	160.0
f_u [N/mm²]	353.3	260.6	314.0
E [N/mm²]	73000	69500	74000
ε_u [-]	8%	7.3%	21%
A_{60} [-]	16%	12%	24%

Table 5.2: Ramberg-Osgood true stress-strain material models.

AA6082T6 Base material		**AA6082T6 HAZ**		**AA5083H111 Base material**	
Strain [-]	Stress [N/mm²]	Strain [-]	Stress [N/mm²]	Strain [-]	Stress [N/mm²]
0.0	0.0	0.0	0.0	0.0	0.0
0.0009	66.9	0.0006	41.4	0.0004	32.0
0.0018	133.8	0.0012	82.9	0.0009	64.1
0.0027	201.0	0.0018	124.4	0.0014	96.1
0.0037	268.2	0.0024	165.9	0.0022	128.3
0.0039	285.0	0.0027	176.3	0.0025	136.3
0.0041	301.8	0.0031	186.8	0.0029	144.4
0.0044	318.7	0.0037	197.3	0.0035	152.5
$^{*}\varepsilon_{0.2\%}$ 0.0066	336.2 $^{*}f_{0.2}$	$^{*}\varepsilon_{0.2\%}$ 0.0050	207.9 $^{*}f_{0.2}$	$^{*}\varepsilon_{0.2\%}$ 0.0042	160.7 $^{*}f_{0.2}$
0.0075	338.4	0.0060	213.5	0.0061	176.5
0.0088	340.8	0.0075	219.3	0.0092	192.6
0.0107	343.3	0.0095	225.1	0.0141	209.1
0.0133	346.2	0.0123	231.2	0.0215	226.4
0.0171	349.4	0.0163	237.6	0.0324	244.8
0.0225	353.3	0.0217	244.4	0.0481	264.8
0.0302	357.9	0.0291	251.7	0.0700	287.2
0.0409	363.8	0.0391	259.8	0.0999	312.9
0.0560	371.3	0.0526	269.0	0.1395	343.3
$^{*}\varepsilon_{u}$ 0.0770	381.2 $^{*}f_{u}$	$^{*}\varepsilon_{u}$ 0.0705	279.6 $^{*}f_{u}$	$^{*}\varepsilon_{u}$ 0.1906	379.9 $^{*}f_{u}$
0.2447	459.8 $^{*}f_{x}$	0.2452	364.2 $^{*}f_{x}$	0.3631	503.2 $^{*}f_{x}$

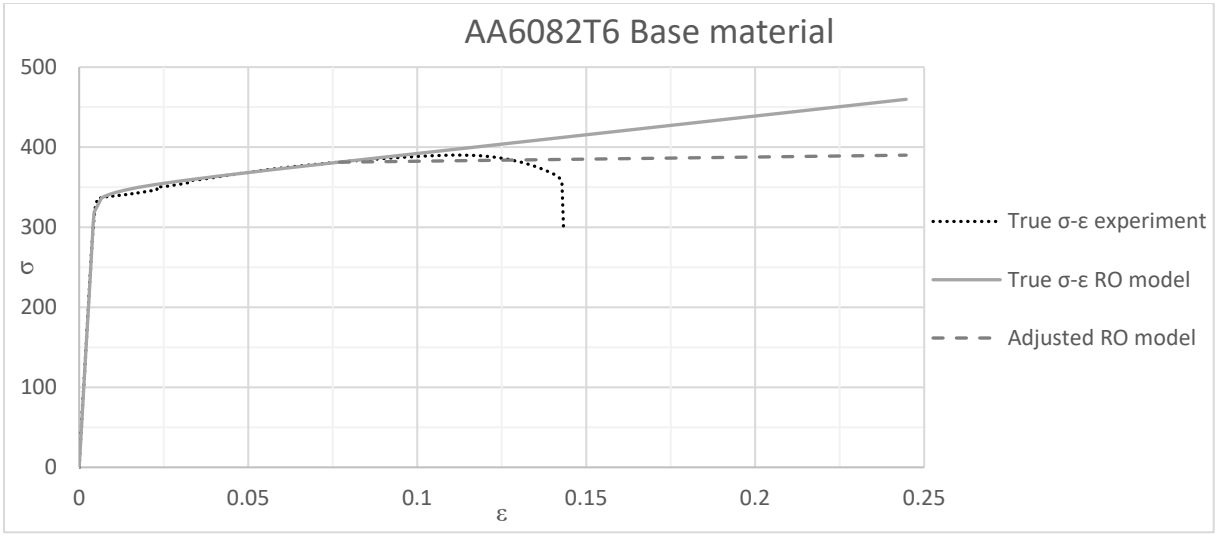

Figure 5.3: True stress-strain curves of the AA6082T6 Base material.

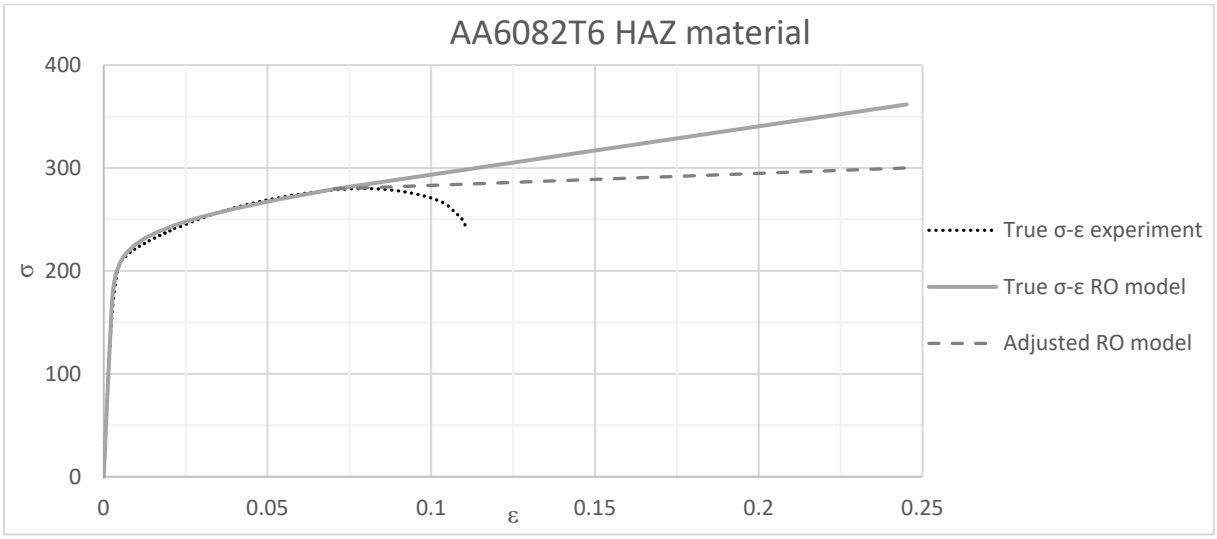

Figure 5.4: True stress-strain curves of the AA6082T6 HAZ material.

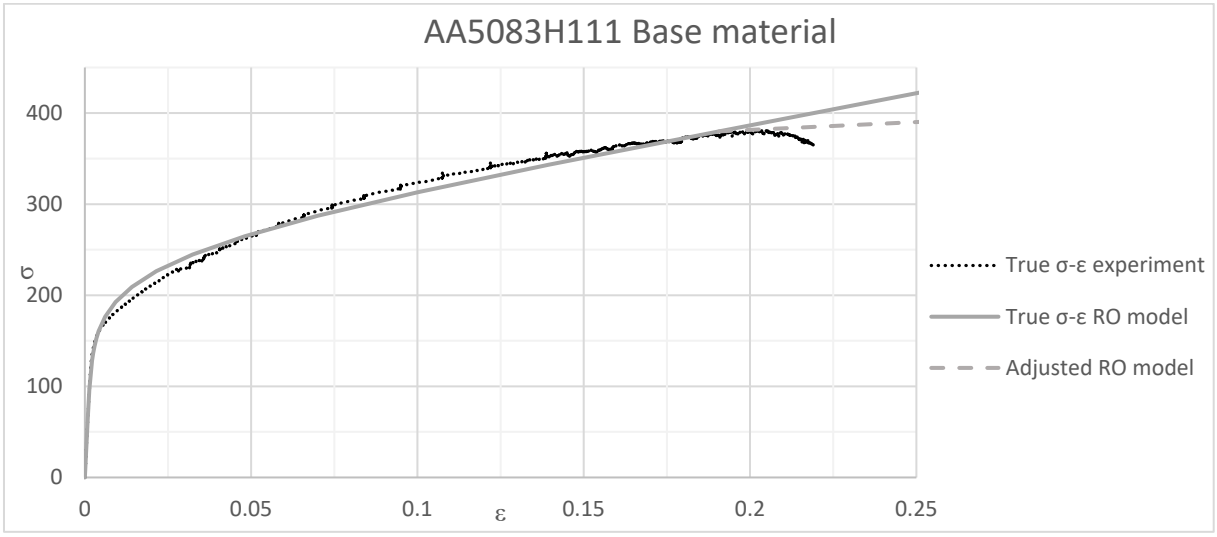

Figure 5.5: True stress-strain curves of the AA5083H111 material model.

5.1.4. AA6082T6 base material calibration

The first calibration run was performed for the AA6082T6 base material. As mentioned, the first analyses were carried out using the starting values. Next to stress-strain relation as obtained from the experiments and shown in the previous section, also input parameters for the fracture model were required. This ductile fracture model was earlier described in Section 2.6. For this fracture model, a starting value for the equivalent strain at the onset of damage was taken equal to the fracture strain of the experiments. The starting value for the fracture energy was not obtained from experiments but based on a previous study by Manders (2018). In this study, a value around 40 and 50 N/mm^2 was applied for the fracture energy using a mesh size of 1 mm[43]. Therefore, a starting value of 50 N/mm^2 is maintained. The starting values were used for the first four analyses. In these four analyses, the influence of the mesh size was examined. The first analysis was randomly meshed with an average mesh size of 2 mm. The second analysis was performed using a mesh size of 1.5 mm, resulting in about 130% more elements. Next, the mesh was further refined into mesh sizes of 1.0 mm and 0.75 mm, resulting in about 750% and 2000% more elements with respect to the 2 mm situation. In Figure 5.7, a visualization of the randomly applied mesh of 1 mm is shown. In all the four analyses, a fracture locus table was implemented, constructed based on a fracture strain of 0.16. The results of the four first analyses, together with the results of two experiments, are shown in Figure 5.6.

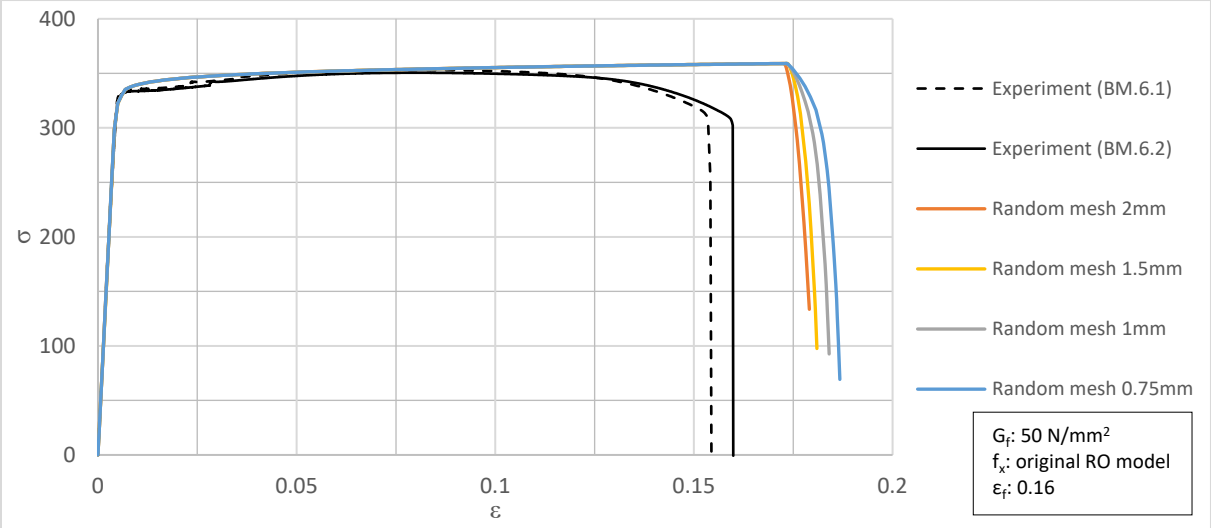

Figure 5.6: Results of the first analyses of the AA6082T6 base material.

Figure 5.6 shows that the curves of the numerical results already approached the experimental curves to some extent. In addition, the influence of the mesh size is noticed. For all the four analyses, it is observed that the curves were identical upon the point of onset of damage. From this point on, the damage behavior differed from each other. This difference indicates that the fracture energy is related to the used mesh size.

By applying locally a refined mesh restricted to the zone of interest, the numerical models can be simplified, which results in a reduction in the number of elements and calculation time. However, by this locally refined zone, a structured mesh is obtained, which can affect the results compared to a random mesh. An analysis was performed to investigate the effect of this locally structured mesh compared to a random mesh. In the local refined mesh model, a specific zone was meshed with 1 mm elements and the overall zone with 1.5 mm elements. With this local refinement, the total number of elements reduced from 21,256 to 11,920 compared to the overall 1 mm mesh. In Figure 5.7, the randomly meshed dogbone is shown, and in Figure 5.8, the applied local refined mesh.

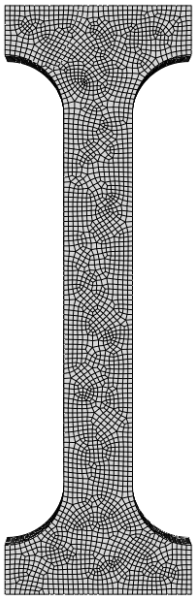

Figure 5.7: Visualization of the randomly meshed dogbone (element size=1.0 mm).

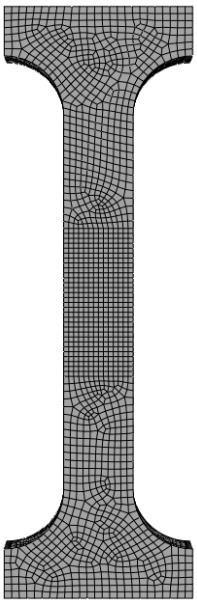

Figure 5.8: Visualization of the local refined meshed dogbone (element size in ref. zone=1.0 mm).

Furthermore, the effect of omitting the fracture locus was investigated for both random and local structured mesh. By applying a constant value for the fracture strain for all stress triaxialities, the fracture locus was omitted, and this locus did not have to be reconstructed every time. The results of the influence analyses of both structured mesh and the fracture locus are plotted in Figure 5.9.

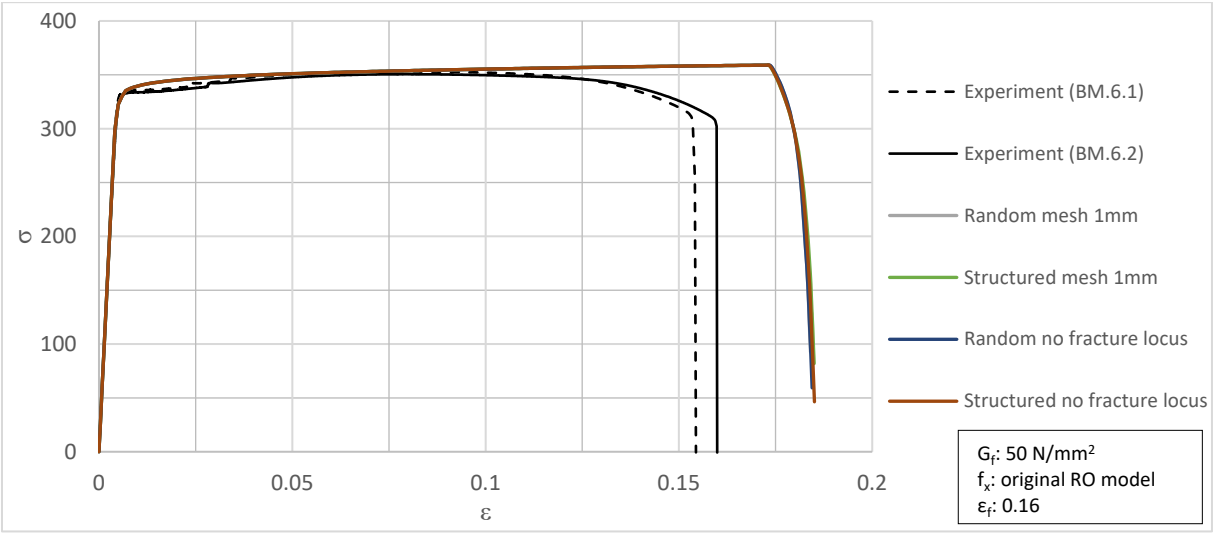

Figure 5.9: Results of the influence analyses of a structured mesh and a fracture locus.

From the results, it is concluded that there was not a significant difference influence of applying a structured mesh instead of a random mesh. Also, omitting the fracture locus resulted in similar results. The curves of the four different analyses show an almost identical shape. With these results in mind, a locally refined and structured mesh is used for the following analyses as well as omitting the fracture locus by taking a constant value for the fracture strain.

The next step in the calibration process was to examine the effect of the fracture energy parameter G_f. Therefore, the starting value of 50 N/mm^2 was once doubled and once halved. The results of these varied fracture energy analyses are shown in Figure 5.10.

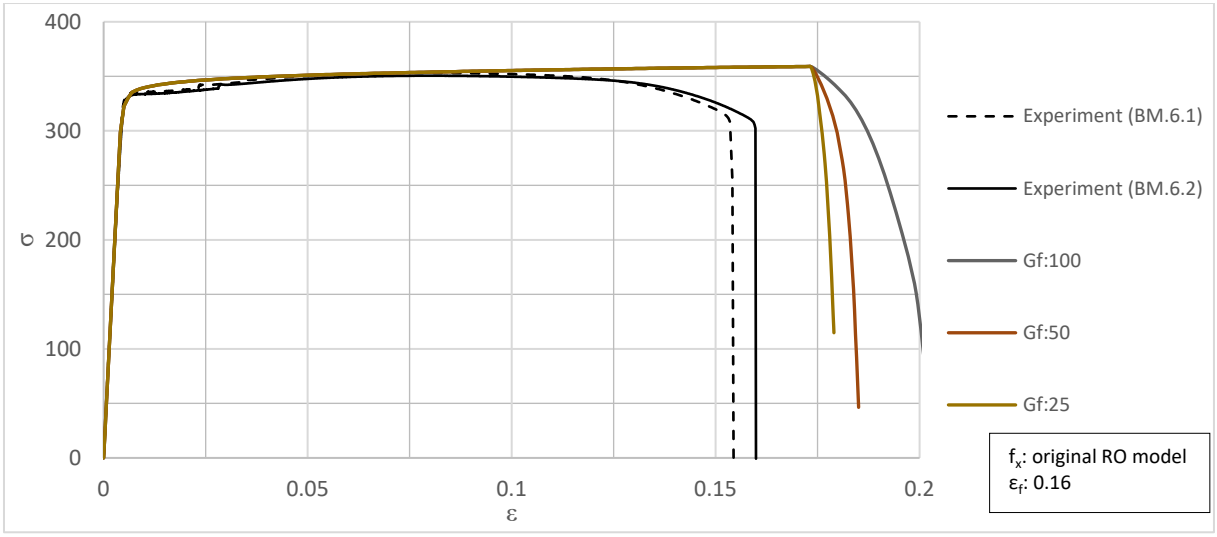

Figure 5.10: Results of the fracture energy influence analyses.

The influence of the fracture energy parameter is clearly observed from the results of the varied fracture energy analyses. Higher values for the fracture energy resulted directly in a more gradual damage process. However, since the fracture energy is based on a linear damage process, it only affects the steepness of the curve after the onset of damage. From the experimental results, a sudden drop in the curve is experienced after the necking process. Therefore, the kink in the curve between the necking process and failure cannot be modeled based on only the fracture energy parameter.

Besides the effect on the steepness of the curve after the onset of damage, also some remarkable things are experienced in the failure behavior of the test specimen. It is noticed that the analyses with a value of 100 N/mm^2 for G_f, resulted in a horizontal failure plane and a distinct necking behavior. A value for G_f of 50 and 25 N/mm^2 seemed to result in a diagonal shear failure plane. In all the experiments necking behavior is noticed, but all the specimens failed with a diagonal failure surface. In Figure 5.11 and Figure 5.12, the difference between the two failure patterns in the analyses is shown. In Figure 5.13 a picture of the failed dogbone specimen in practice is shown from where a diagonal failure plane is observed. However, in practice, this diagonal failure plane occurred over the thickness of the specimen instead of the width.

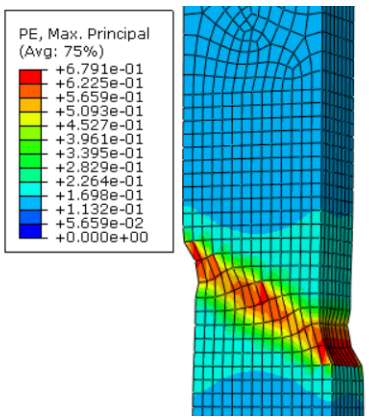

Figure 5.11: Unscaled plastic strains of the "Gf:50 εf:0.16" model at an imposed displacement of 13.5 mm.

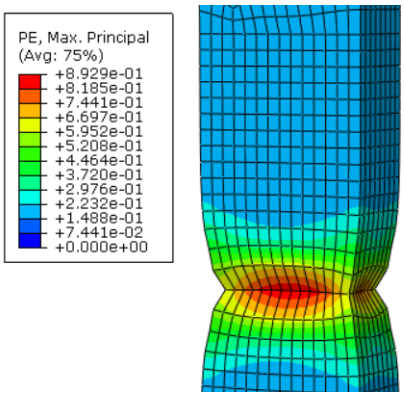

Figure 5.12: Unscaled plastic strains of the "Gf:100 εf:0.16" model at an imposed displacement of 14.3 mm.

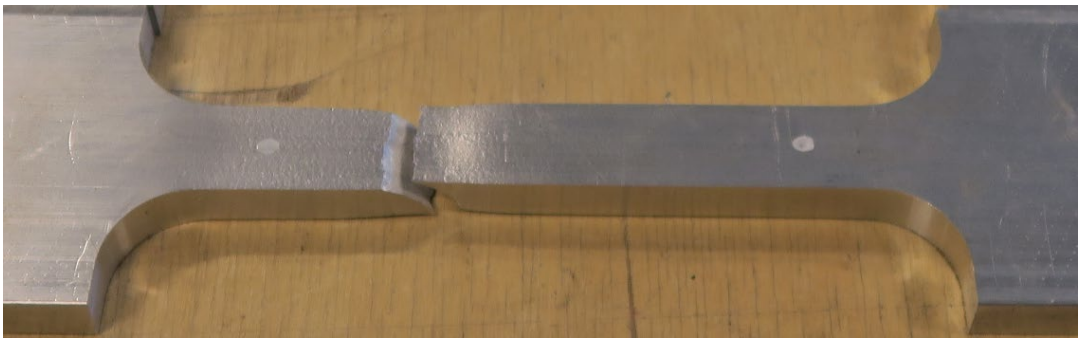

Figure 5.13: Failed base material specimen (BM.6.1).

In the Abaqus manual, it was stated that the fracture energy dissipation in linear cases could be calculated by rewriting Equation 2.20 resulting in the formula

$$G_f = \frac{u_f^{pl} \cdot f_u}{2}, \tag{5.1}$$

where u_f^{pl}, is the plastic failure displacement calculated by the plastic strain after fracture, multiplied with the element length[41]. f_u is equal to the ultimate strength of the material. From the equation, a value of 14 N/mm^2 was found for the fracture energy dissipation. This value was inserted in the subsequent models. Since only the fracture strain was left to calibrate in the following steps, this parameter was varied in order to calibrate the model. The result of this calibration step is shown in Figure 5.14.

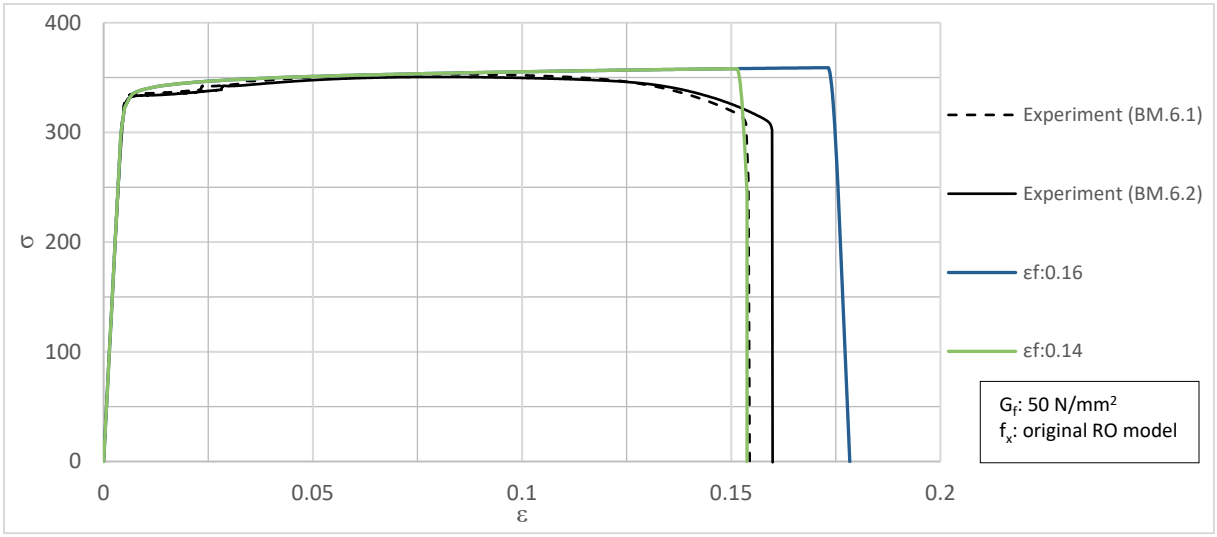

Figure 5.14: Results of the fracture strain calibration.

From the results shown in Figure 5.14, it is noticed that the experiment was approached well with already the first calibration step. Therefore, these parameters were maintained, and no further calibration steps were done for the calibration process based on the fracture strain. However, it is also observed that the decreasing trend in the stress-strain curves after reaching the ultimate stress was not taken into account correctly. Therefore, the branch of the implemented true stress-strain relationship was adjusted from the point of ultimate stress in order to enforce this downward curve. This by varying the value of the material stress in the last row of the constructed stress-strain relation shown in Table 5.2 and indicated with superscript *f_x. This original value of 459.8 N/mm^2 for f_x was changed to values of 450 and 440 N/mm^2. For this parameter study, the other parameters ε_f and G_f were maintained constant at values of 0.16 and 14 N/mm^2, respectively. The results are presented in Figure 5.15.

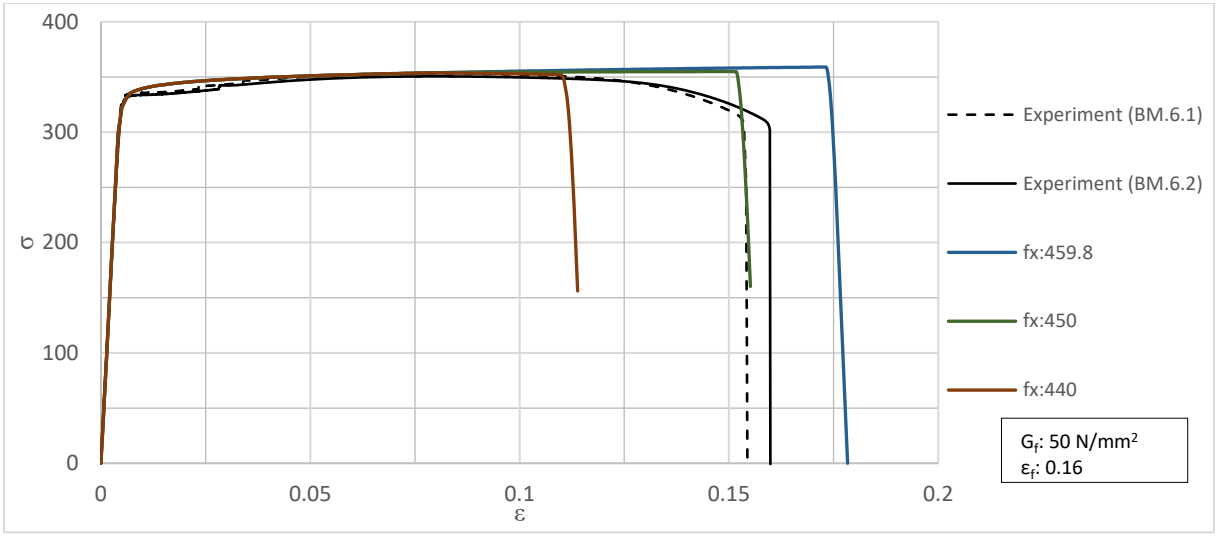

Figure 5.15: Results of the f_x calibration step.

As it can be noticed from the results, the analysis with a value of 450 N/mm^2 for f_x, shows the best result. However, the necking process by a descending curve after reaching the ultimate stress was not taken correctly into account. The analysis with a value of 440 N/mm^2 for f_x shows a better descending trend but shows less deformation. Therefore, the fracture strain was increased, and the value for f_x was further adjusted in the next calibration steps. The fracture energy value was maintained at 14 N/mm^2 for all the analyses. The results of this last calibrated model are shown in Figure 5.16.

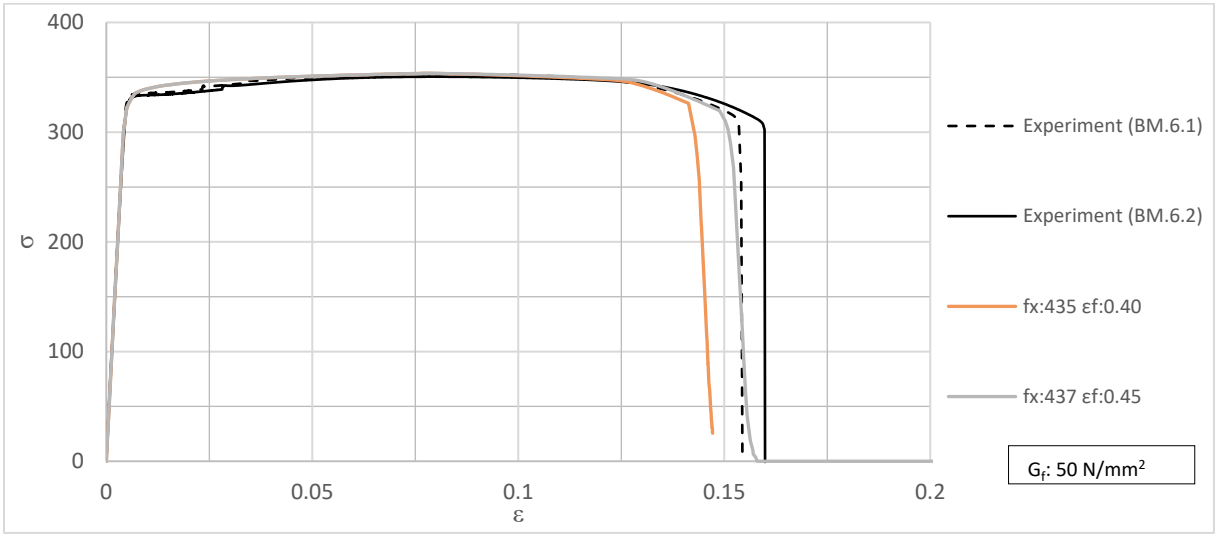

Figure 5.16: Results of the f_x and ε_f calibration steps.

From the results, it is shown that with the first calibration analysis already, a good result is achieved. By adjusting the value for f_x to 437 N/mm^2 and the value for ε_f to 0.45, the stress-strain curve was matched almost perfectly. However, from the deformation schematization output, it is shown that the specimen failed by a horizontal failure plane instead of a diagonal plane as previously. To assess if this was forced due to the mesh configuration, the same analysis was performed containing a random mesh. The stress-strain curves of both the structured and the random mesh analysis are plotted in Figure 5.17. The schematization of the test piece at the moment of failure is shown in Figure 5.18.

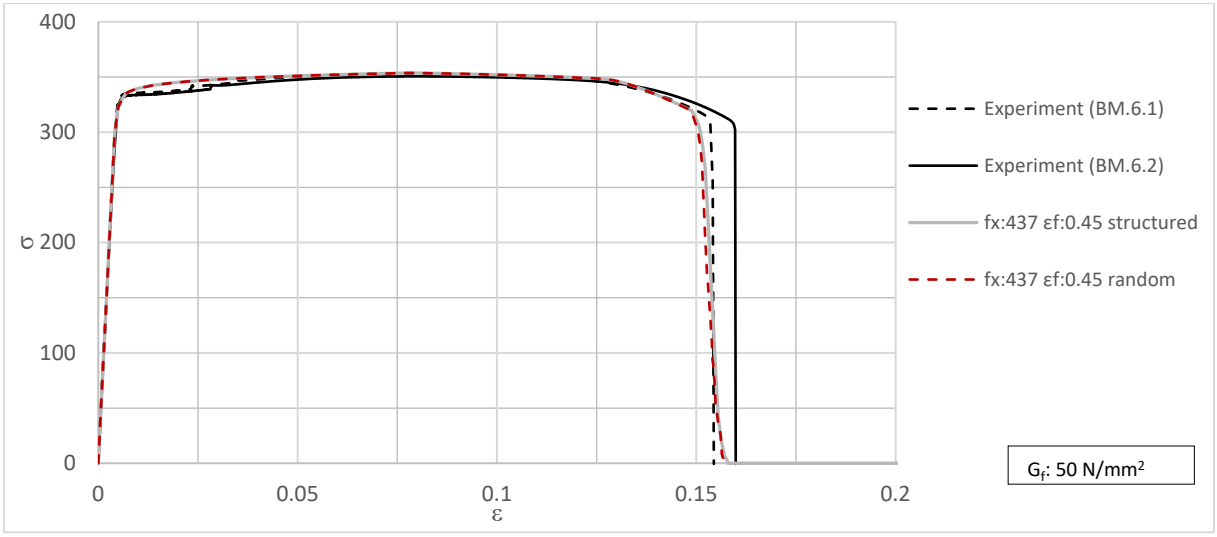

Figure 5.17: Results of the structured and arbitrary meshed calibrated analysis.

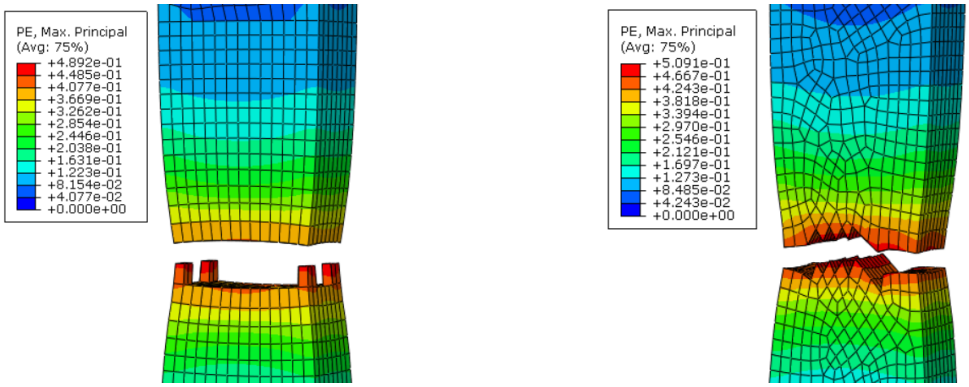

Figure 5.18: Visualization output of the structured (left) and arbitrary meshed (right) specimens at an imposed displacement of 10.1 mm.

It can be concluded that the influence of the random mesh is almost negligible. However, it does indicate that the exactly flat horizontal failure plane was changed for a horizontal failure plane over the edges of the elements resulting in a more notched failure plane. The question can be raised whether a diagonal shear failure plane was actually present in the tests or whether the specimen failed by necking but cracked over a diagonal plane forced by the material structure.

The AA6082T6 material was calibrated based on three different principles. The input parameters and the findings of these different material models are listed in Table 5.3.

Table 5.3: Calibrated AA6082T6 base material models.

Calibration approach	σ-ε model	ε_f	G_f	Findings
1. ε_f-calibrated	Original	0.14	14	A good approach and a diagonal shear failure pattern. Decreasing part of the curve after reaching the ultimate strength was not included.
2. f_x-calibrated	Adjusted f_x to 450	0.16	14	Fracture strain is equal to the experiments and a good approach to the experimental curve except for the decreasing part. Horizontal failure plane.
3. ε_f-f_x combined calibrated	Adjusted f_x to 437	0.45	14	A good approach of the experimental curve including the decreasing part after ultimate strength was reached. Horizontal failure plane.

5.1.5. AA6082T6 HAZ material calibration

Similarly, as demonstrated for the AA6082T6 base material, also the heat-affected material was calibrated. This calibration was based on the longitudinally welded dogbone test pieces, also known as the fully Heat Affected Zone dogbones. The first model of the HAZ material was analyzed with a value for the fracture energy obtained from Equation 5.1. From this equation, a value of 5 N/mm^2 was found for G_f. For the analysis, the original RO stress-strain relation, as presented in Table 5.2, was used. The fracture strain at the onset of damage was taken equal to A_{60} of the experiment, and a locally refined meshed zone was applied as also shown for the previous base material models. The results of the first analysis and the experiment are presented by a stress-strain diagram shown in Figure 5.19.

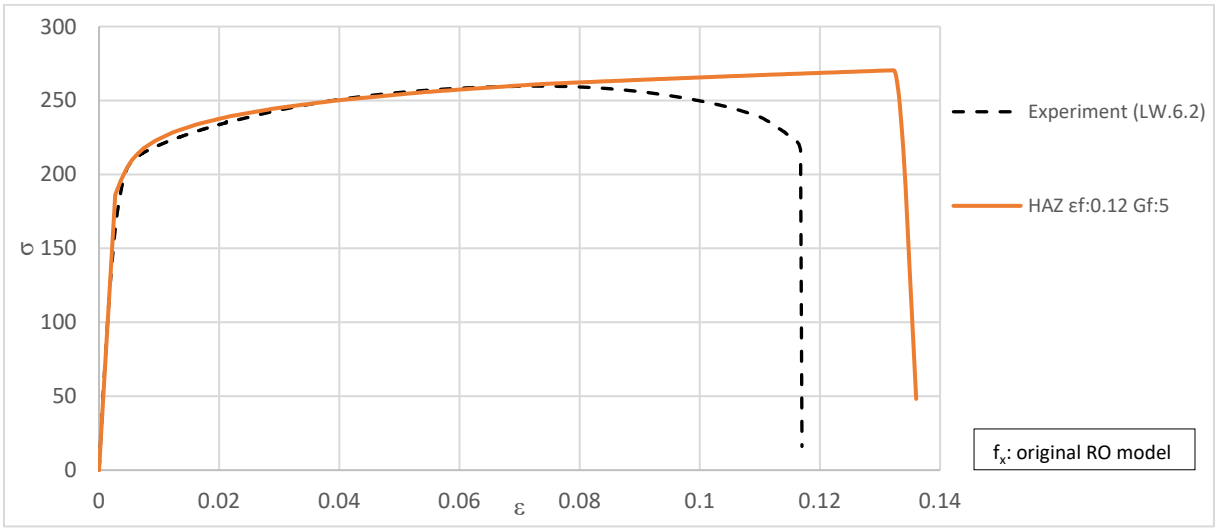

Figure 5.19: First analysis of the AA6082T6 HAZ material.

From Figure 5.19, it is noticed that the first analysis achieved a reasonably good first approximation. However, from the output visualization shown in Figure 5.20, it is observed that two diagonal failure surfaces occurred, both started at the edge of the refinement zone. An adjustment was made to ensure failure will not occur outside the measuring range or near the edge of the HAZ transition. By reducing locally, the width by 0.05 mm in the middle of the dogbone model, a minimal imperfection was applied. With this imperfection model, new analyses were performed. Next to the calculated value of 5 N/mm^2 for G_f, also values of 1, 10, and 25 N/mm^2 for G_f were applied in order to consider the influence. The results of these four different analyses are shown in Figure 5.21.

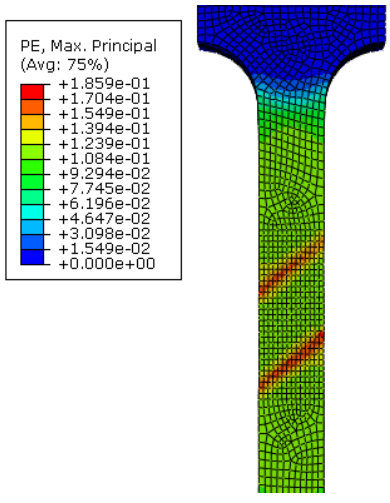

Figure 5.20: Contour plot of the occurring plastic strains just before failure.

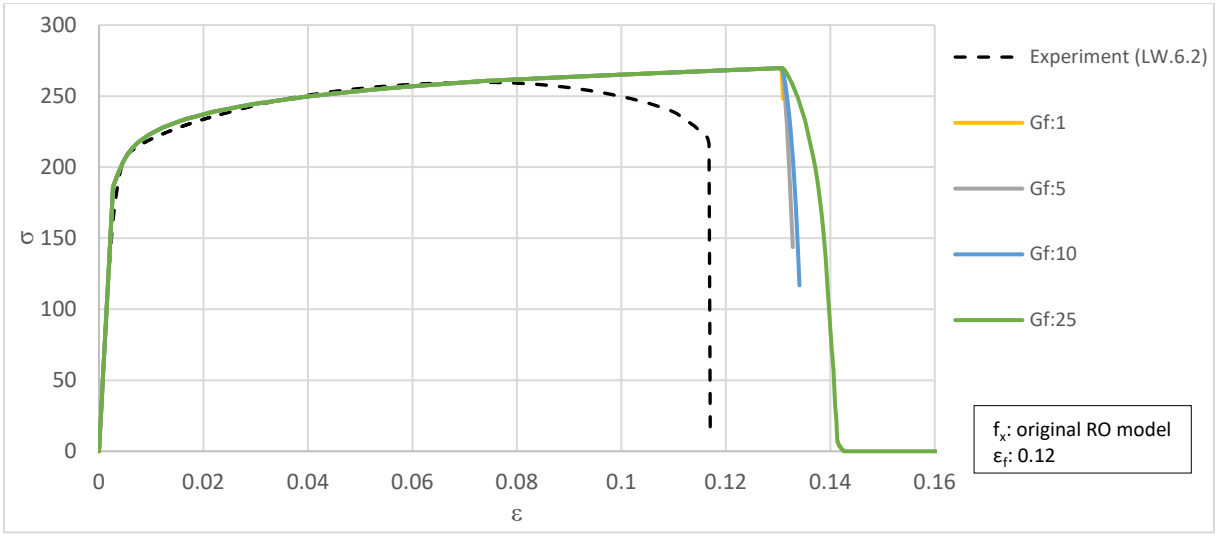

Figure 5.21: Results of the fracture energy influence analyses of the AA6082T6 HAZ material.

From the results of the four G_f influence analyses, it is observed that values for G_f of 10 N/mm^2 and lower, resulted in a quite steep decreasing curve after reaching the onset of damage. A value of 25 N/mm^2 for G_f, resulted in a more curved line after reaching the onset of damage point. For a value of 1 N/mm^2, no clear failure pattern is observed in the output visualization shown in Figure 5.22. For 10 and 25 N/mm^{2,} a clear diagonal failure pattern is shown. A value of 5 N/mm^2 showed a failure pattern in between the 1 N/mm^2 and 10 N/mm^2 variant. Since the 10 N/mm^2 variant showed a better and more gradual failure pattern as experienced for values of 5 N/mm^{2,} this value was maintained for further analyses.

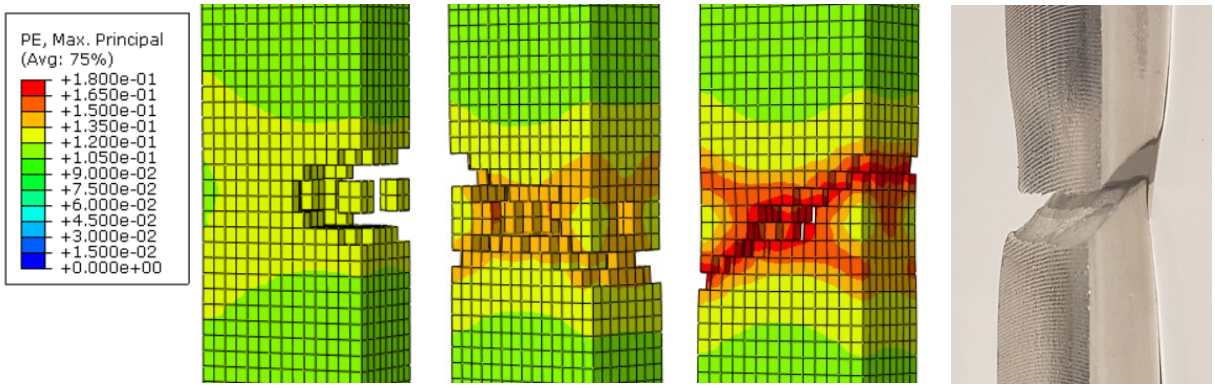

Figure 5.22: Plastic strain contour plot of the analyses with varying values of Gf (1, 5 and 10 N/mm^2 from left to right) and picture of a failed dogbone specimen.

After the fracture energy was determined, the next step was to calibrate the material by varying the fracture strain. The original material model and mesh configuration were maintained in these analyses. The results of this calibration step are shown in Figure 5.23.

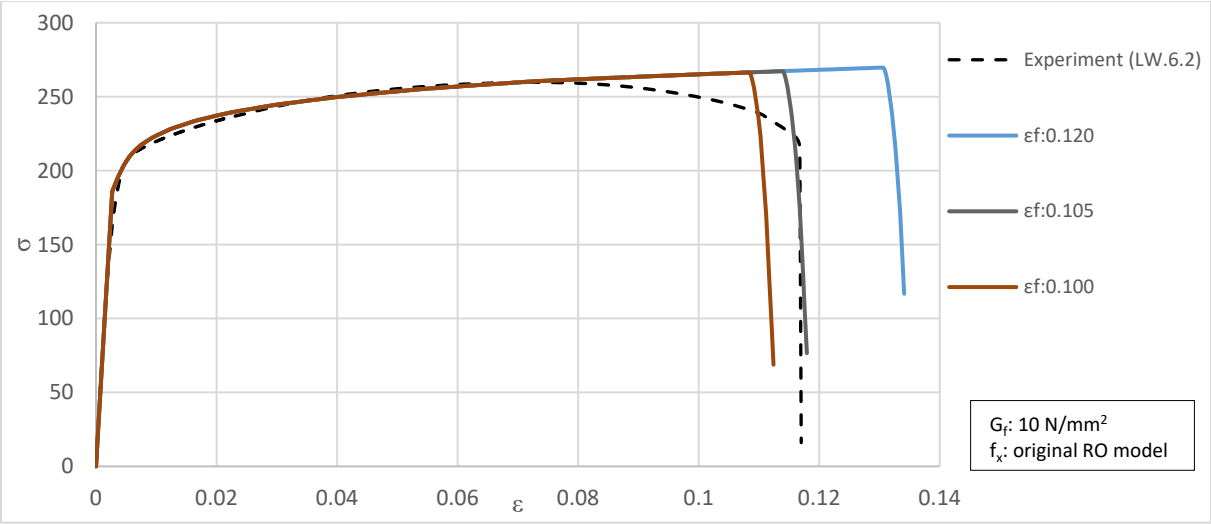

Figure 5.23: Fracture strain calibrated AA6082T6 HAZ model.

The results of the analyses showed that with an original RO stress-strain relation, in combination with a fracture strain of 0.105, an appropriate approach of the experimental results is obtained. Furthermore, the desired diagonal shear failure pattern is observed. However, only the descending trend of the curve after reaching the ultimate strength was not present.

In addition to the previous steps, a calibration sequence was done based on the stress-strain relation. Again, the last point in the σ-ε relation was varied by adjusting the value for f_x. In Figure 5.24, the results of the analyses with the original value of 364.2 N/mm^2 and the changed values of 330, 335, and 340 N/mm^2 are shown.

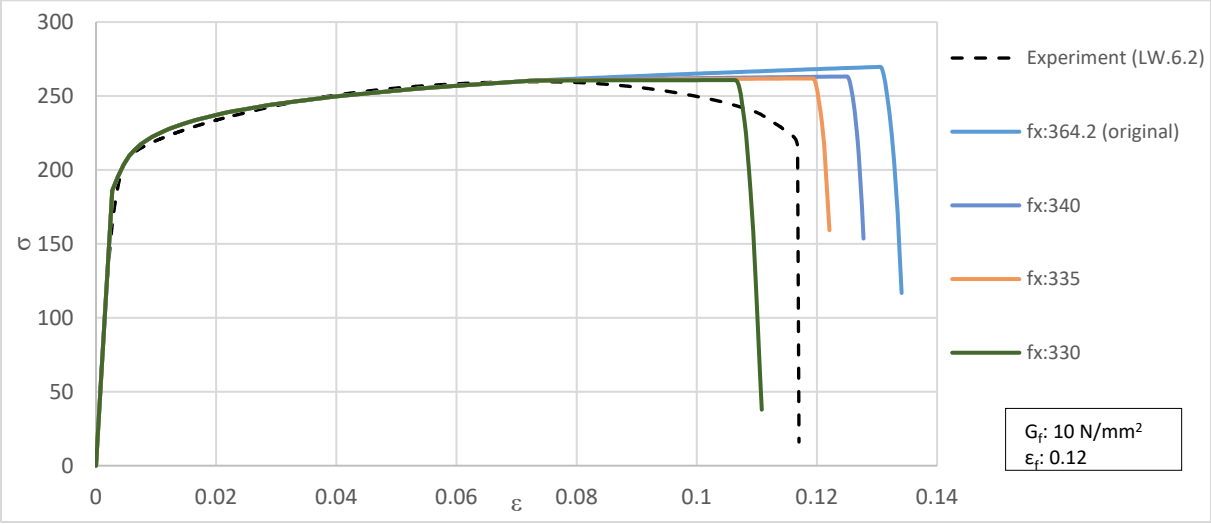

Figure 5.24: Stress-strain model calibrated AA6082T6 HAZ material.

From the results, it is observed that lowering the value for f_x directly leads to bringing forward the moment of failure. Also, it is shown that the steepness of the curve between ε=0.07 and the moment of failure was lowered. It is observed that with a value of 335 N/mm^2 for f_x, the closest match with the experiment was achieved. Also, it is noticed that the deviation between the three analyses was not linear. From the output visualizations in Figure 5.25 and Figure 5.26, it is observed that a shift in failure pattern occurred from a diagonal failure pattern to a horizontal one, for values of f_x of 335 and 330 N/mm^2, respectively. Since a value of 335 N/mm^2 for f_x, resulted in the closest match with the experiment and it matches the average fracture strain of 0.12, this value was maintained.

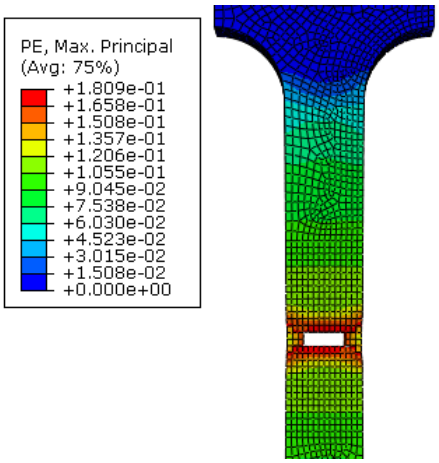

Figure 5.25: Contour plot of the plastic strains at moment of failure of the f_x:330 N/mm^2 specimen.

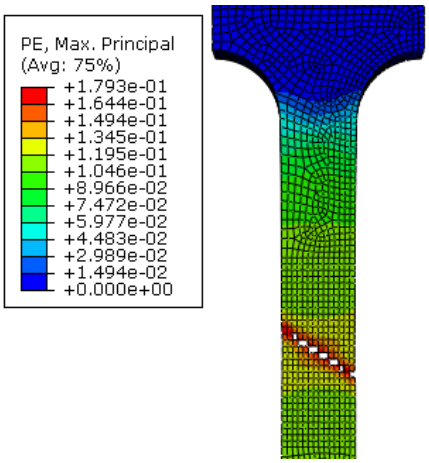

Figure 5.26: Contour plot of the plastic strains at moment of failure of the f_x:335 N/mm^2 specimen.

Additionally, for this kind of material, the stress-strain model was calibrated further by lowering the value for f_x and adjusting the value for ε_f. This calibration step was executed to obtain an even better match with the experimental curve. The results of these analyses are shown in Figure 5.27. The analyses were all performed with a value of 10 N/mm^2 for G_f.

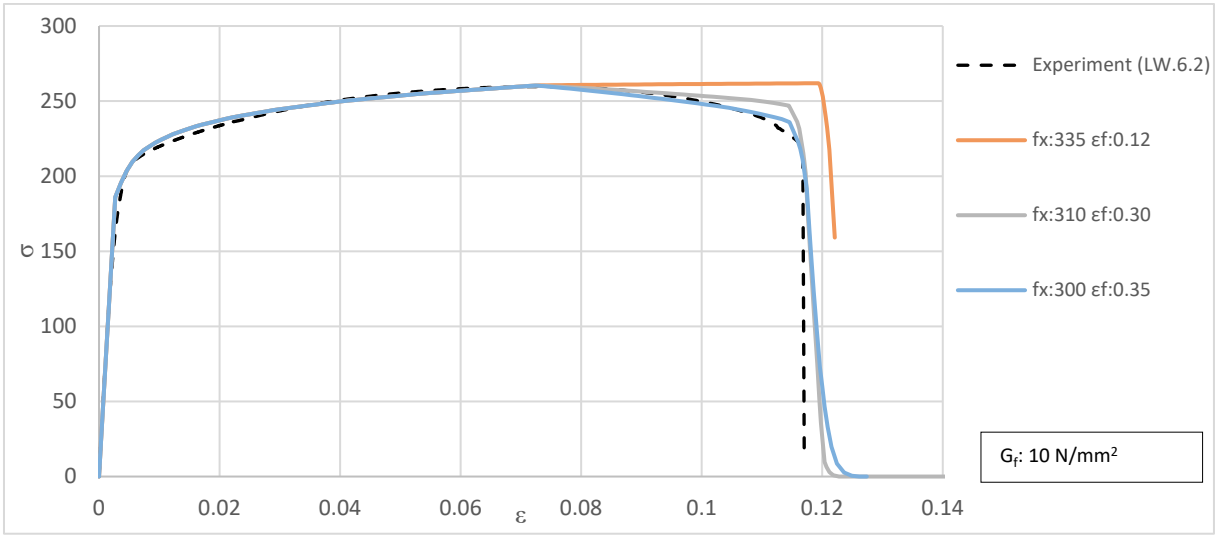

Figure 5.27: Results of the last calibration steps for the stress-strain model and ε_f.

In Table 5.4, a summary of the calibrated AA6082T6 HAZ material models is listed, which is used for the validation steps in the next sections.

Table 5.4: Calibrated AA6082T6 HAZ material models.

Calibration approach	σ-ε model	ε_f	G_f	Findings
1. ε_f-calibrated	Original	0.10	10	A good first approach of the experimental curve except for the decreasing trend. Diagonal failure plane present.
2. f_x-calibrated	f_x adjusted to 335	0.12	10	ε_f is equal to A_{60} of the experiments and a good approach to the curve and failure pattern. A decreasing trend of the curve was not present.
3. ε_f-f_x combined calibrated	f_x adjusted to 300	0.35	10	Accurate match with the experimental curve. However, failure occurred over a horizontal surface.

5.1.6. Local HAZ validation

After calibration of the base and the heat-affected material, the following step was to validate these material models based on a combined base and HAZ material FEM model. This model was set up and validated with the help of the experiments of the transversely welded dogbones containing locally a Heat Affected Zone.

The calibrated material models are divided into three different approaches, namely the ε_f parameter calibration, the f_x parameter calibration, and the coupled ε_f-f_x parameters calibration. The base and heat-affected material were combined for the same type of approach resulting in three different analyses. The analyses were performed with a similar mesh configuration as previously presented with both a refined zone and an imperfection. The heat-affected zone was constructed with b_{haz} =15 mm resulting in a total HAZ length of 30 mm centered in the middle. The results of the three analyses are shown in Figure 5.28.

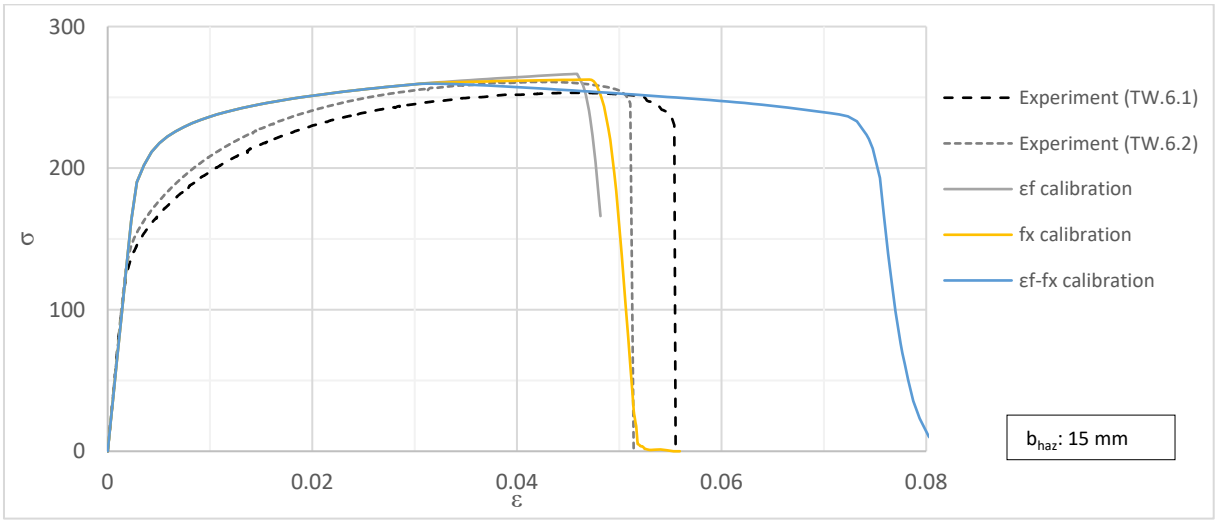

Figure 5.28: Results of the local HAZ model analyses.

Except for the transition area between the elastic and plastic regions, the models already gave a good approximation of the test results. The ε_f calibrated model and the f_x calibrated model even turned out to match quite closely with the curve of the experiments, certainly in relation to the moment of failure. The combined ε_f-f_x parameter calibration seems to produce the worst results for the selected HAZ size. Based on the results as presented in Figure 5.28, it is concluded that the f_x-calibration model resulted in the closest match with the experiments and is validated as the correct material model. However, it should be noted that an assumed HAZ width of 15 mm in both directions is used.

5.1.6.1. *Adjusting and* dividing *HAZ zones*

In reality, the material properties inside the heat-affected zone will gradually change from heat-affected to the base material properties. In the previous numerical models, the change of material properties was quite abrupt. Inside the specific zone, the material was assigned the heat-affected properties, and right after passing the zone, the material properties turned to the base material state. Since, in reality, this will change very smoothly, an investigation was done to examine the effect of reducing the size of the HAZ or dividing the HAZ into multiple zones. An analysis was performed using half the width of the HAZ compared to the previous models. In addition, an analysis was performed using a subdivided HAZ. By dividing the HAZ into multiple zones, the material properties will change more gradually. A start was made to divide the HAZ into two zones. One zone was assigned the fully heat-affected material properties. The other zone was assigned the material properties obtained by interpolating the base and HAZ material. The material properties of the two different HAZ regions and the base material are listed in Table 5.5.

Table 5.5: Mechanical properties of the base, HAZ, and semi-HAZ materials.

	6082T6	**6082T6HAZ**	**Semi-HAZ**
$f_{0.2}$ [N/mm^2]	334.0	206.9	270.5
f_u [N/mm^2]	353.3	260.6	307.0
E [N/mm^2]	73000	69500	71250
ε_u [-]	8%	7.3%	7.7%
A_{60} [-]	16%	12%	14%

Also, for obtaining the fracture strain of the semi-HAZ, an averaged value of the HAZ and base material was taken. The HAZ was divided equally into a fully HAZ of two times 7.5 mm and a semi-HAZ region of each 7.5 mm. A schematization of the constructed zones in Abaqus is shown in Figure 5.29, where the fully HAZ region is indicated by red and the semi-HAZ region by orange. The welds were not modeled, since in practice these were milled off before testing.

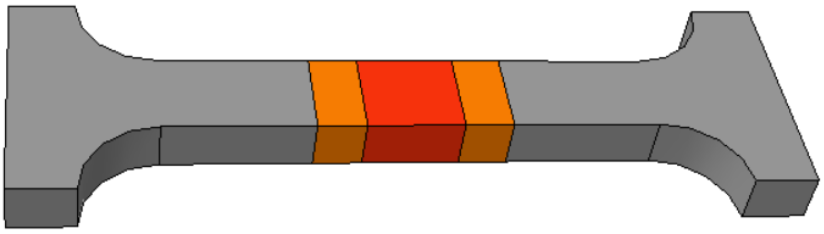

Figure 5.29: Schematization of the dogbone specimen with the specified HAZ sub-zones.

The ε_f-f_x calibrated models were used in both the narrowed HAZ and the sub-divided HAZ analyses. The results are presented in Figure 5.30, together with the previous local HAZ models. For the analyses, a constant value for the fracture strain was used.

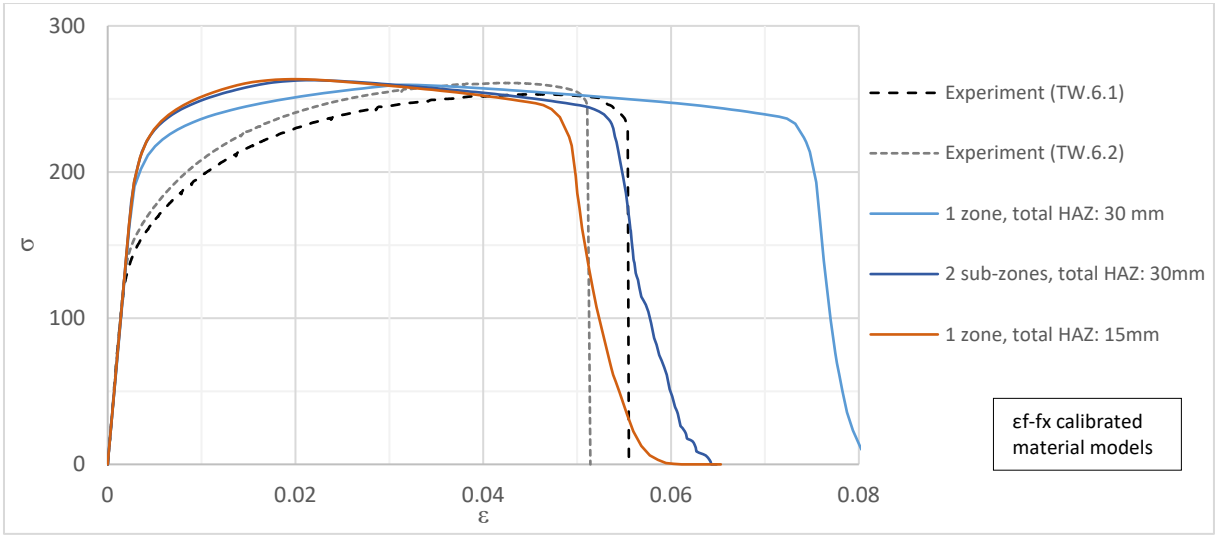

Figure 5.30: Results of the analyses using a subdivided and smaller HAZ.

From the results, it is concluded that dividing the HAZ into multiple zones leads to a more concentrated deformation in the smaller critical zone. In the halved HAZ width analyses less deformation is noticed compared to the sub-zones analysis, while the critical HAZ zone width was equal in both analyses. The difference in deformation between the halved and subdivided HAZ analyses shows that there is some influence of the semi-HAZ zone. For both analyses, the moment of fracture of the experiments was better approached, compared to the original HAZ analyses. However, a larger deviation to the experiments is noticed for the first part of the curve. When ignoring this deviation, it can be said that both a subdivided HAZ and a narrowed HAZ of two times 7.5 mm, leads to a decent approximation of the ultimate strength and displacements up to failure. Therefore, the ε_f-f_x calibrated model is also used in further analyses of the welded cruciforms.

5.1.7. AA5083H111 material calibration

Next to the aluminum alloy 6082T6, also the material model for AA5083H111 was calibrated based on the experimental test results. The results of the tests showed that the influence of the heat input by welding was practically negligible. Therefore, only the base material was calibrated. Due to the experiences from the calibrations of the previous material models, an imperfection was applied, and the AA503H111 material model was only calibrated based on the ε_f-f_x parameter calibration. However, similar to the previous calibrations first the influence of the fracture energy parameter G_f was examined for this material. In total, four different analyses were performed using varying values for G_f from 1 up to 100 N/mm^2. The value of 5 N/mm^2 was calculated by Equation 5.1. The results of these first analyses are shown in Figure 5.31.

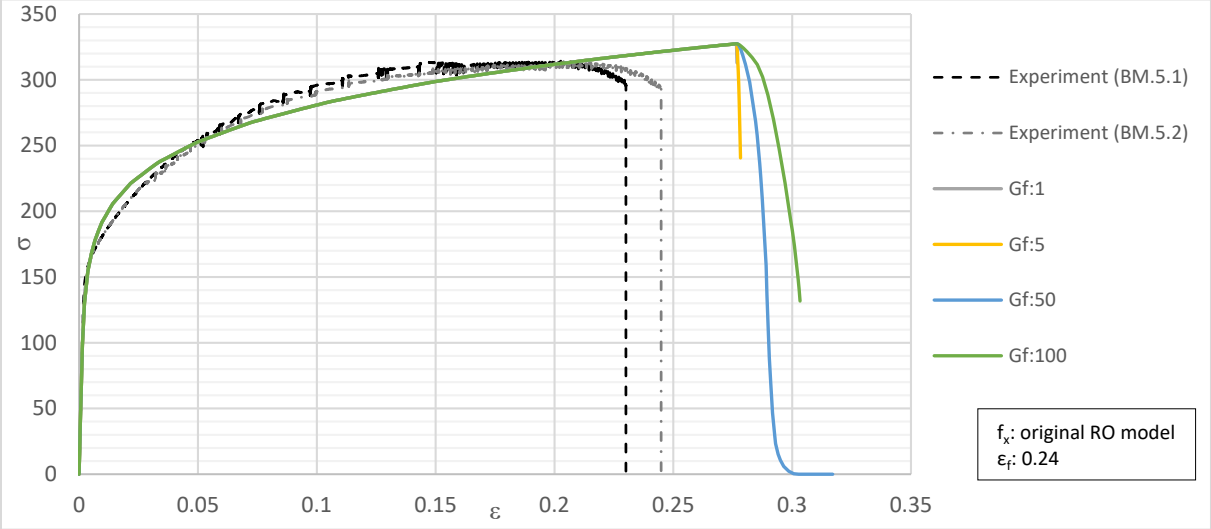

Figure 5.31: Results of the fracture energy influence analyses of the AA5083H111 material models.

From the results shown in Figure 5.31, it is concluded that values of 1 and 5 N/mm^2 for G_f resulted in a quite abrupt failure. For values of 50 and 100 N/mm^2, the curve after fracture is somewhat more curved. However, not the desired diagonal shear failure pattern is observed from the output visualization results. From the visualizations shown in Figure 5.32 and Figure 5.33, it is noticed that the 5N/mm^2 analyses shows a more diagonal failure pattern. Despite the quite abrupt failure, the calculated value of 5 N/mm^2 was obtained for further analyses. In the next analyses, the value for f_x was varied with 450, 420, and 400 N/mm^2. The results of these analyses are presented in Figure 5.34.

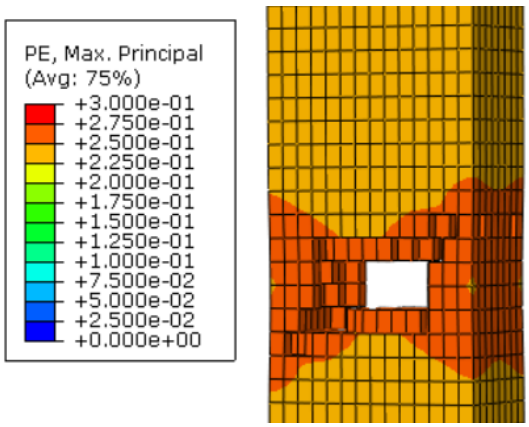

Figure 5.32: Plastic strain contour plot of analysis with G_f:5N/mm^2.

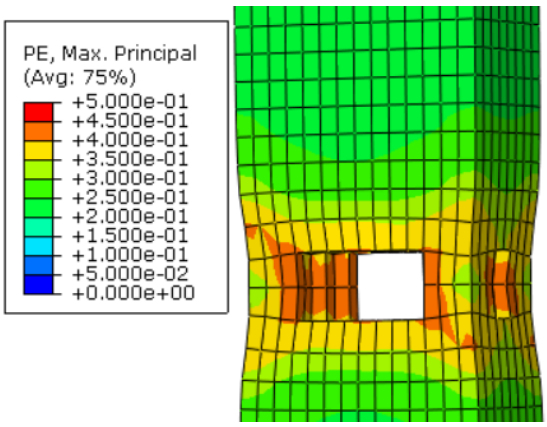

Figure 5.33: Plastic strain contour plot of analysis with G_f:50N/mm^2.

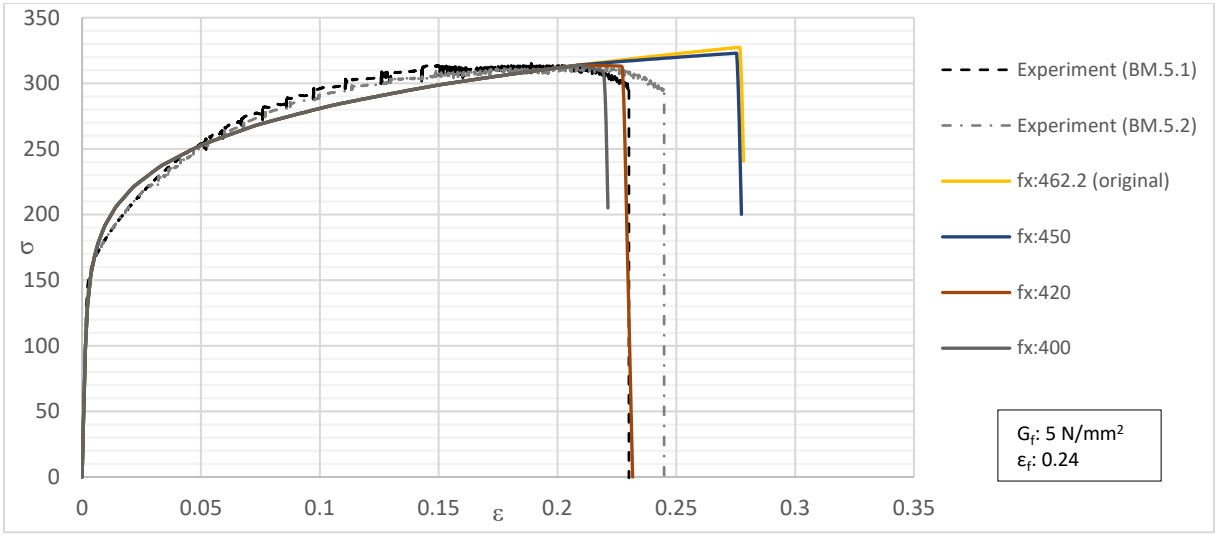

Figure 5.34: Results of the f_x influence analyses.

The analysis with a value of 400 N/mm^2 for f_x seems to result in an accurate approach of the decreasing part of the curve after reaching the ultimate strength. Therefore, this value was maintained and the value for ε_f was calibrated. This calibration resulted in the corresponding analyses results shown in Figure 5.35.

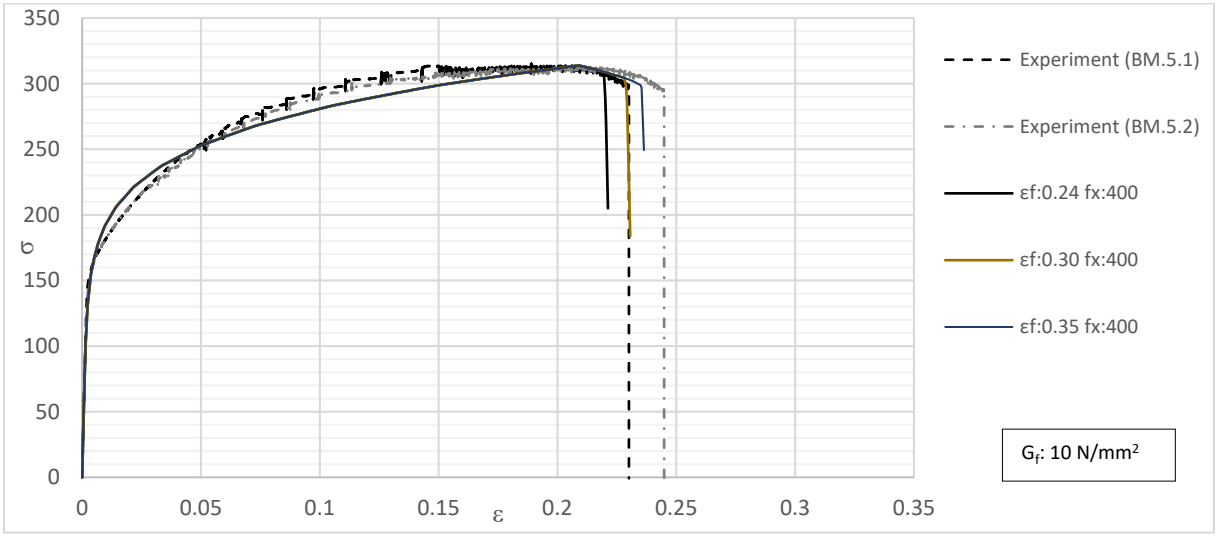

Figure 5.35: Results of the ε_f-f_x calibration analyses.

From the results, it is observed that the analyses with ε_f=0.30 already resulted in an exact match with the fracture strain of experiment BM.5.1. However, the average fracture strain of the experiments was somewhat higher. Therefore, the fracture strain in the model was enlarged to 0.35. This value resulted in a proper match since the curve was located in between the two experiments. In the subsequent analyses of the welded cruciforms, this ε_f-f_x calibrated model is used.

5.1.8. Calibration conclusions

The discussed calibration process finally led to three different calibrated materials. Namely, the aluminum alloys 6082T6, 6082T6-HAZ, and 5083H111. These three material models are eventually calibrated on both the ε_f and f_x parameters in a combined calibration. This calibration approach proved to give the best results according to the local HAZ validation. The calibrated material parameters for the three material models are listed in Table 5.6. These material models are used in the further analyses of the welded cruciforms and bolted joints.

Table 5.6: Calibrated materials and the corresponding key parameters.

	$f_{0.2}$ [N/mm²]	f_u [N/mm²]	f_x [N/mm²]	ε_u [-]	ε_f [-]	E [N/mm²]	G_f [N/mm²]
AA6082T6	334.0	353.0	437.0	0.08	0.45	73,000	14
AA6082T6-HAZ	206.9	260.6	300.0	0.073	0.35	69,500	10
AA5083H111	160.0	314.0	400.0	0.21	0.35	74,000	5

It is proved that the assumed width for the HAZ of 15 mm in both directions is too conservative. The material strength properties will gradually increase up to the base material state, and therefore, a full HAZ of 15 mm will not represent the actual situation. The analyses with a narrowed and sub-divided HAZ also showed a better approach to the experiments. For the further analyses of the welded cruciforms, it can be questioned if a narrowed HAZ of 7.5 mm must be maintained. This because for in the case of the welded cruciforms, more weld runs were applied, resulting in possibly more heat input.

5.2. Numerical modeling of the bolted experiments

In the experimental part of this study, also experimental tests on bolted specimens were performed. In total, three different bolted variants made out of aluminum alloy 6082T6 were tested. The first variant was dimensioned on net cross-section failure and the second on failure due to bearing. The last variant was also dimensioned on net cross-section failure. However, without the use of bolts. This variant was a simple tensile test on a plate with two holes. Therefore, the results of this variant were suitable to validate the AA6082T6 material model since no advanced contact modeling of the bolts is needed. With the help of a numerical model, based on the actual dimensions of the experimental test samples, several analyses were executed using the earlier calibrated material models, as presented in Section 5.1.4. By comparing the numerical results and the experimental results, the accuracy of the model was assessed.

5.2.1. Model layout

As mentioned, the numerical models of the dogbones were created with the same dimensions as used in the experimental tests. Only the clamped end parts are reduced in size to minimize the model complexity. Figure 5.36 presents an overview of the used dimensions. The mesh size was about 1.0 mm around the bolt holes and the middle of the plate. Towards the ends of the plate, the mesh size evenly increased up to 4.0 mm. Over the entire thickness of the sample, eight elements were applied, resulting in an element size of 1.0 mm over the thickness. An overview of the mesh configuration is presented in Figure 5.37.

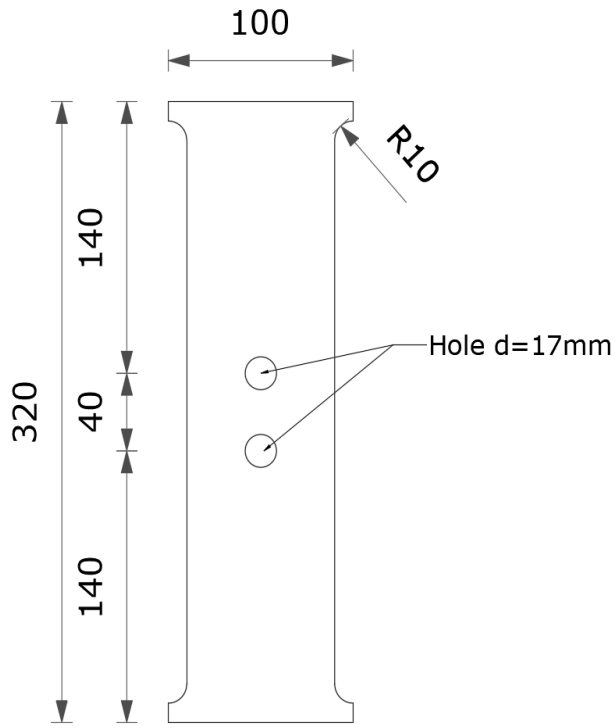

Figure 5.36: Dimensions of the modeled specimen.

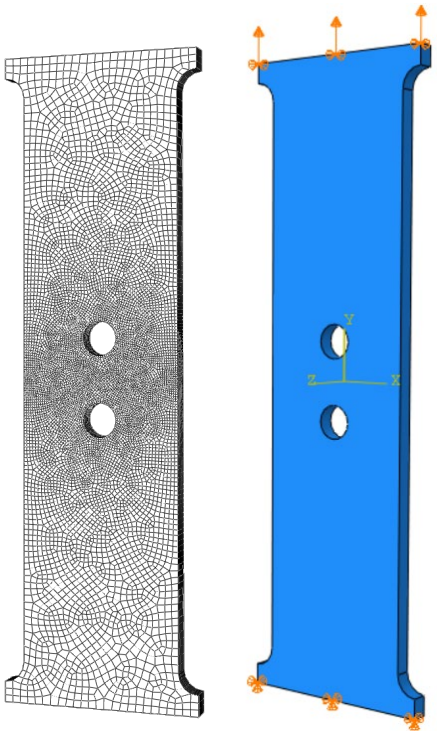

Figure 5.37: Overview of the mesh configuration and applied boundary conditions.

The plate was restricted to move in all directions at the bottom by applying the boundary condition $x = y = z = 0$. At the top, the nodes were restricted from moving in the horizontal x and z axes, representing the moveable clamp. In the vertical y-direction, parallel to the longitudinal axis of the specimen, an imposed displacement was applied. Figure 5.37 shows an overview of the applied boundary conditions and imposed displacement. The imposed displacement was applied with static general load steps. Similar to the experiments, the displacements in the numerical model were

measured over a distance of 160 mm by measuring two points located both 80 mm from the specimen center.

For the numerical analyses, the calibrated models of the aluminum alloy 6082T6 base material were implemented. Since three different calibration approaches were performed, the different models were implemented and individually analyzed. The implemented parameters correspond to the calibrated values listed in Table 5.3. In addition, an analysis was performed using the original RO stress-strain model but without the use of a damage model. This analysis was performed in order to examine the influence of the damage model.

5.2.2. Results

First, the three different calibrated models were implemented in the constructed FEM model. As previously mentioned, also an analysis without damage modeling was performed. For the three calibrated material models, a constant value for the fracture strain was applied. Figure 5.38 presents the results of the four analyses and the result of the experiment B3-3 by a load-displacement graph.

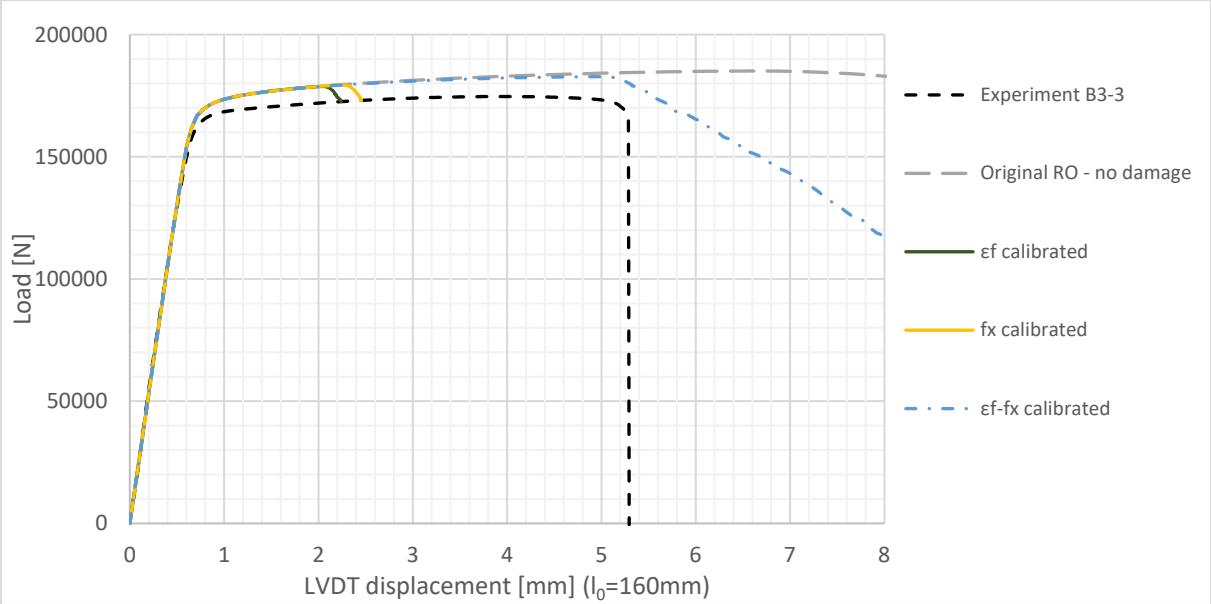

Figure 5.38: Results of the first analyses of the plate with two bolt holes.

From the results, it is observed that the analyses slightly overestimated the ultimate load by about 5%. This minimal deviation may be due to the variance in actual and modeled dimensions. Also, the displacements at the moment of failure of the calibrated ε_f-f_x model shows promising results. This calibrated model started with the onset of damage around 5.1 mm displacement. In the experiments, the LVDT's measured 5.2 mm displacement at the moment of failure. The small difference of 0.1 mm shows that the numerical model reaches an accurate match with the experiments. The ε_f and f_x calibrated models resulted in premature failure behavior. This premature failure indicates that these models appeared to be unsuitable. The results lead to the promising fact that the ε_f-f_x calibrated model appeared to be the best applicable model.

In Figure 5.39 and Figure 5.40, the von Mises stresses are presented using a stress contour plot. Figure 5.39 shows the stresses just before damage initiation, and Figure 5.40 presents the last calculated step. At this last calculated step, a significant loss in resistance of about 40% was noticed. Figure 5.41 shows a plastic strain contour plot of the same last step. It is noticed that plastic deformations occur around the bolt holes up to the edge of the plate. These plastic deformations were also experienced in the experimental tests. The experimental specimens failed over a nearly horizontal line from one of the

bolt holes up to the edge, as shown in Figure 5.42. A beginning of this failure pattern is also observed in the numerical model.

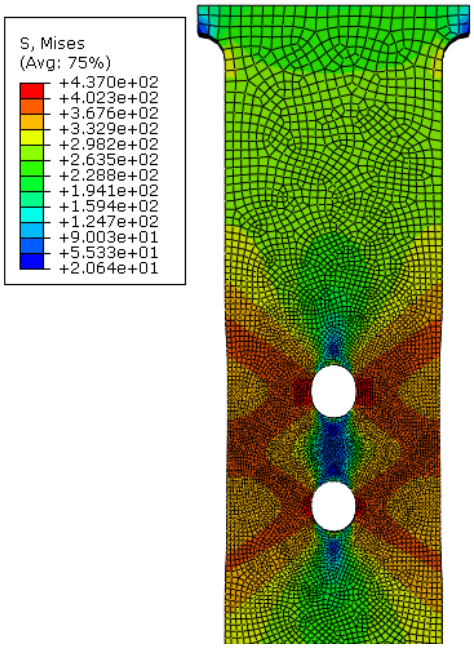

Figure 5.39: Stress contour plot at the moment of damage initiation.

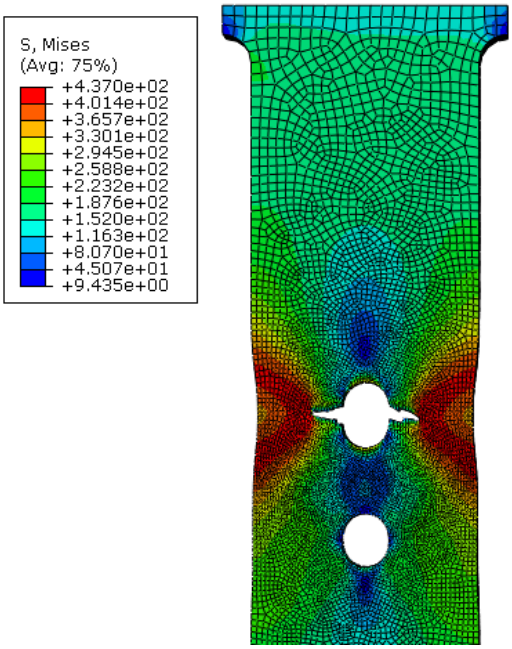

Figure 5.40: Stress contour plot at the moment of failure.

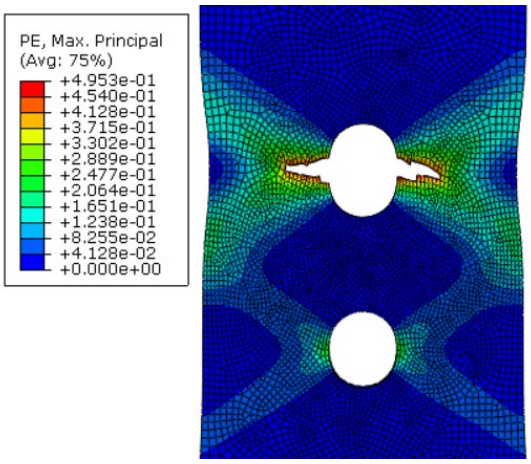

Figure 5.41: Plastic strain contour plot of the plate with two bolt holes during failure (u_{LVDT}=8.1mm).

Figure 5.42: Picture of failed B3-1 specimen.

In the earlier stage of calibrating the material models, it was concluded that the fracture locus did not affect the results of the dogbone specimens. To examine if applying this fracture locus model still results in a good representation of the experiments, this fracture model was implemented and analyzed. This shear fracture locus model was constructed using the calibrated fracture strain ε_f and the strain at ultimate stress ε_u. The constructed fracture locus is dependent on the stress triaxiality and is plotted in Figure 5.43. The result of the analysis of the ε_f-f_x calibrated model in combination with the fracture locus is presented in Figure 5.44, indicated by 'ε_f-f_x calibrated + FT'.

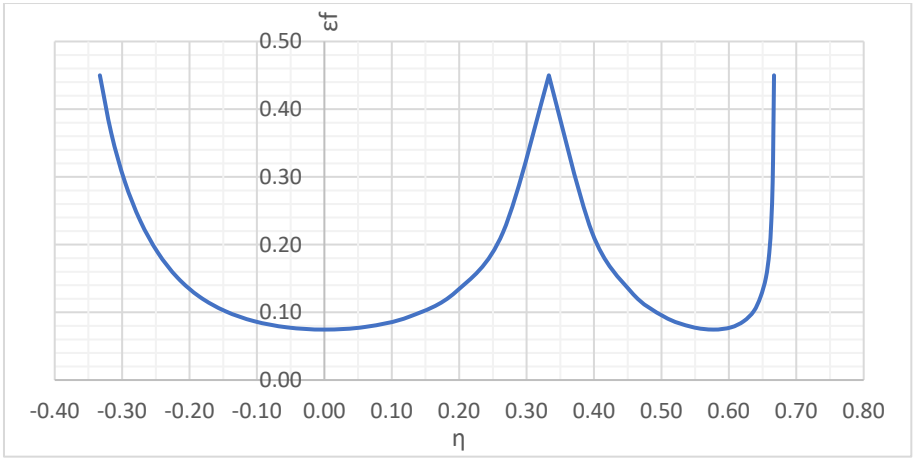

Figure 5.43: Shear fracture locus constructed for ε_f-f_x calibrated AA6082T6 material.

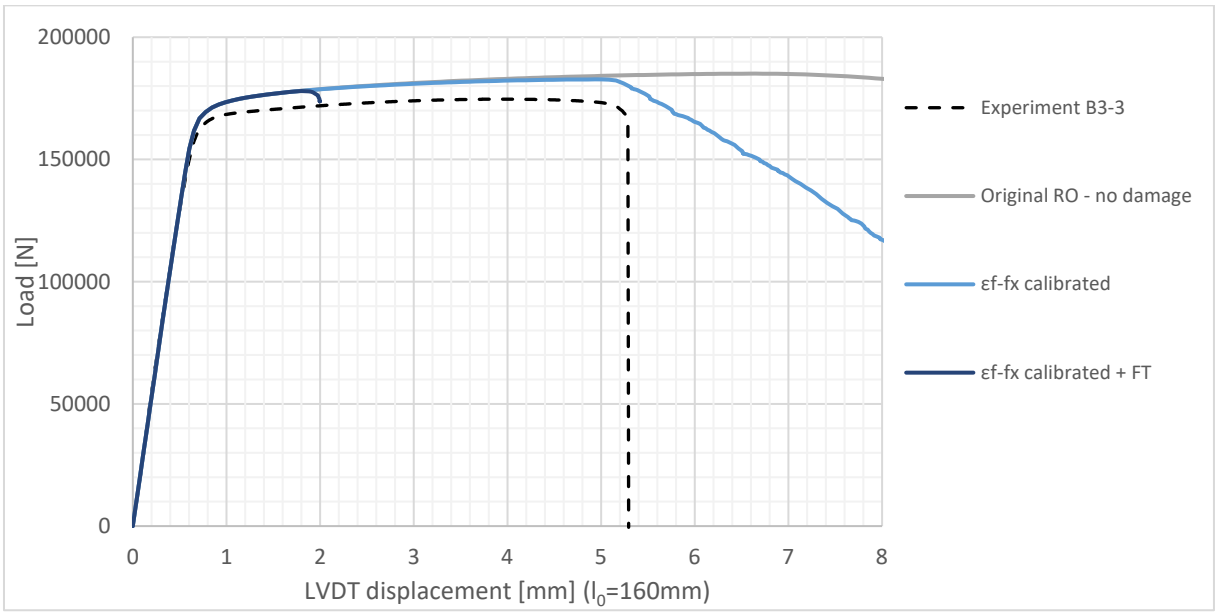

Figure 5.44: Results of the fracture locus implemented analyses.

From the results presented in Figure 5.44, it is observed that applying a fracture locus results in earlier failure compared to the model with a constant fracture strain. From the results, it is concluded that the constructed fracture locus was not suitable for representing the experiments. This is probably caused by the fact that the fracture strain was calibrated based on a specific stress triaxiality value. However, different values of stress triaxialities were found in these two different models. A contour plot of the stress triaxialities at the moment just before failure is shown in Figure 5.45 for the bolt hole plate, and in Figure 5.46 for the dogbone specimen. For the bolt holes experiment, a value of about 0.60 was found for the stress triaxialities. In the case of the dogbone experiments, values just around 0.30 to 0.40 were found.

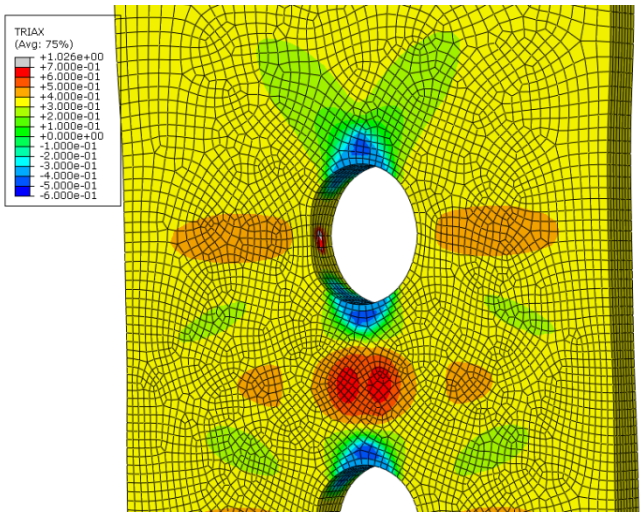

Figure 5.45: Stress triaxialities contour plot at the moment of damage initiation of the AA6082T6 plate containing two bolt holes specimen.

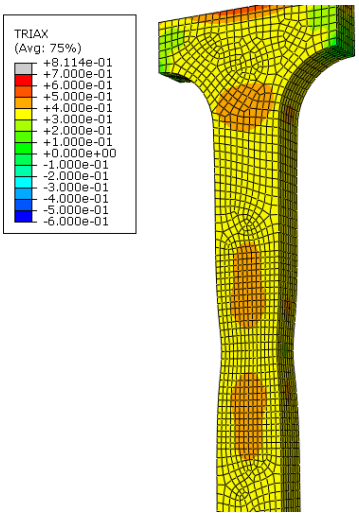

Figure 5.46: Stress triaxialities contour plot at the moment of damage initiation of the AA6082T6 BM dogbone specimen.

5.3. Numerical modeling of the cruciform specimens

After the dogbone specimens were calibrated, the material models of the aluminum alloys were implemented in the welded cruciform specimens. These welded cruciform specimens were consisting of four distinct variants that were already experimentally tested. The numerical models of the cruciforms were based on these tested specimens. With the help of the test results, the numerical models were validated. In the following sections, more information about the model is presented.

5.3.1. General model layout

The finite element models were created with the help of the Finite Element software Abaqus version 6.14-1/standard. The dimensions of the models correspond to the dimensions as tested. Since every variant was produced with different measurements, each variant has a unique layout. The actual dimensions are discussed in the specific sections.

Except for the dimensions, the variants were modeled all in a similar way. For each variant, the member plate and finger plate were separately modeled into two different parts. After that, the member plate was inserted into the finger plate. The welds were modeled with a throat of 4 mm. These welds were constructed in four pieces and placed around the interface of the member and finger plate. Finally, all the separate parts were assembled to model, the welds were connected to the plates using tie constraints. By this, the welds connected the two separate plates.

The member plate consisted out of a heat-treated alloy since welding will result in a heat-affected zone at heat-treated alloys. Furthermore, a HAZ region was modeled in the member plate. Inside this defined region, the HAZ material parameters were assigned. Outside the region, the base material properties were assigned. For the weld filler metal AA5183, a material model was assumed. For this material model, an elastic modulus of 67,000 N/mm^2, a 0.2% proof stress of 150 N/mm^2, and an ultimate strength of 210 N/mm^2 were assumed. These values were based on experimental results found by Leoni et al. (2019)[49]. The other material models were obtained from the calibrated material models listed in Table 5.6. The material models consisted of an elastic-plastic model in combination with a damage model to model the failure process. For this damage model, ductile damage was implemented with the help of a constant fracture strain equal to the calibrated fracture strain of Section 5.1.

The mesh size was varied over the length of the models. Around the interfaces, the mesh was downsized. In the direction of the end of the plate, the mesh size was enlarged. This with the assumption that around the intersections, more elements were needed for an accurate model. Also, in the critical region where failure was likely to occur, a smaller mesh distribution was applied. The plates were meshed using C3D8R linear brick elements with reduced integration. The welds were modeled using C3D10 quadratic tetrahedron elements due to the triangular shape of the welds. For all the weld parts, three elements were applied over the thickness of the weld. An example of the applied mesh configuration is visualized in Figure 5.47.

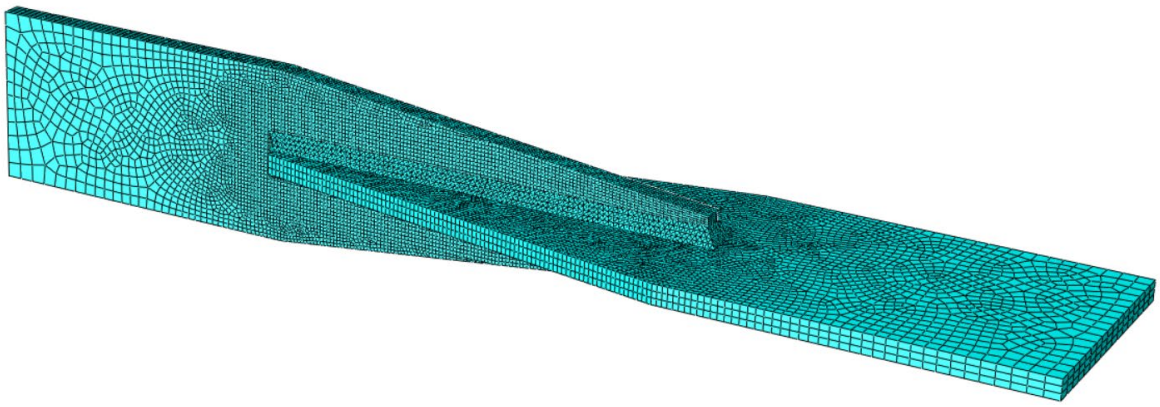

Figure 5.47: 3D visualization of the mesh configuration of the variant 1 specimen.

At the end of the member plate, the plate was fully clamped by applying boundary conditions over the full surface. Both displacement and rotations of the nodes in this area were restrained in all directions to be zero. At the end of the finger plate, the nodes were restrained from moving in both the parallel directions. In the longitudinal direction, an imposed displacement was applied. Figure 5.48 shows an overview of the applied boundary conditions and loads for variant 1.

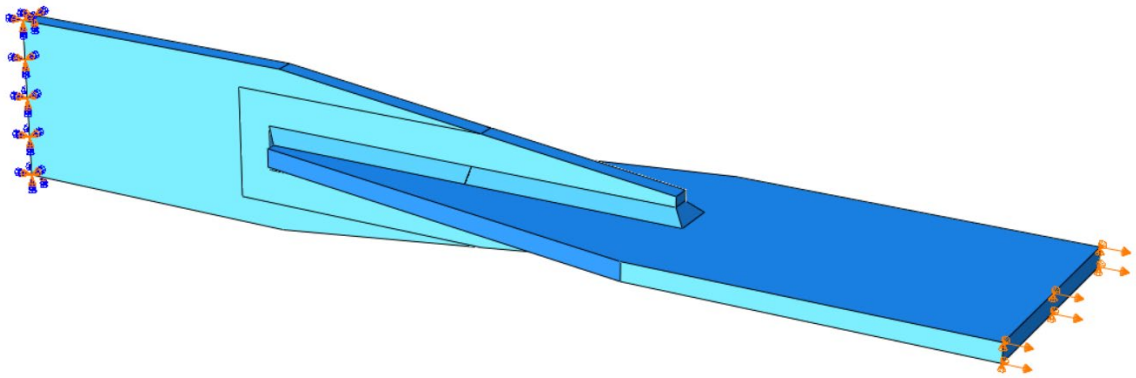

Figure 5.48: Overview of the applied boundary conditions and loads at the variant 1 specimen.

5.3.2. Cruciform with failure in partly heat-affected cross-section

The cruciform variant with failure in the partly heat-affected cross-section, also indicated by variant 1, was the first welded cruciform that was modeled and analyzed. In the case of variant 1, failure will occur in the member plate made of a heat-treated aluminum alloy 6082T6. As mentioned, the same dimensions as used for the specimens for the experiments were applied. These will be discussed in the following section.

5.3.2.1. Dimensions and layout

The applied dimensions in the numerical model are shown in Figure 5.49. The thickness of both plates was equal to 8 mm. The elements in the member plate are constructed with a minimum size of 1.0 mm around the critical points and a maximum of 6 mm around the end of the plate. A total of six elements was applied over the thickness. For the finger plate, which was considered to be uncritical, a minimum mesh size of 2 mm was applied around the welds and a maximum of 6 mm around the end of the plate. A total of three elements was applied over the thickness.

The HAZ width was varied in the analyses since the exact size was unknown for the welded cruciform specimens. Four different HAZ width values were implemented, based on the Vickers Hardness results of the dogbone specimens. From these values an average extent of 15 mm was found, by varying the HAZ width around this value, the influence was observed.

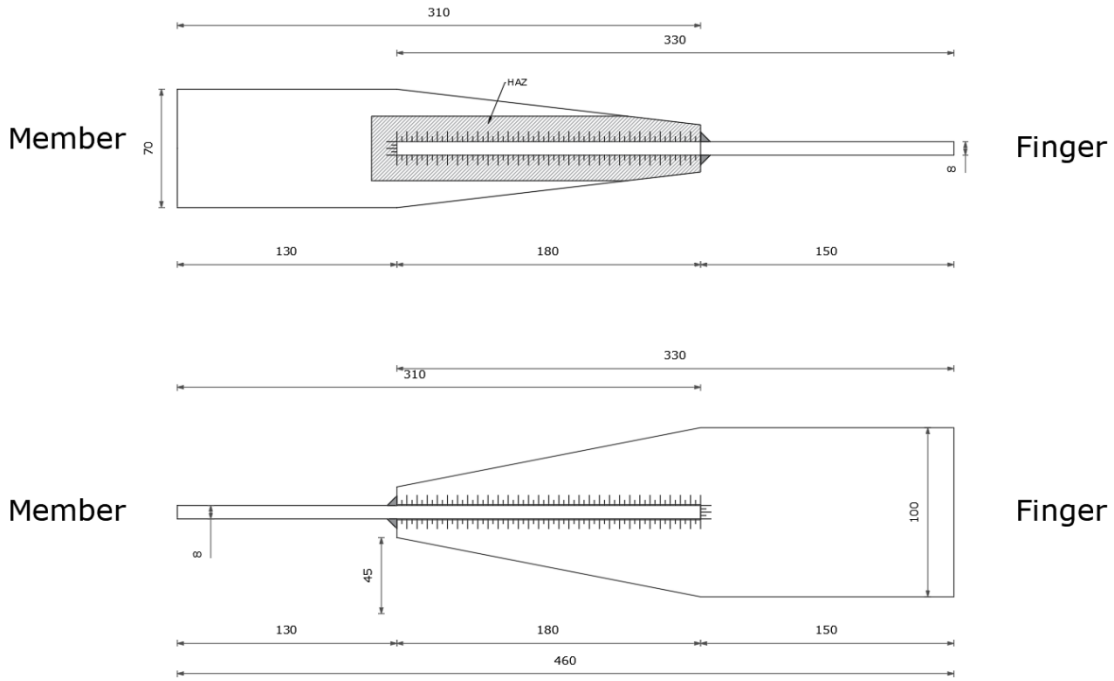

Figure 5.49: Applied dimensions in the numerical model for the variant 1 cruciform.

5.3.2.2. Results

The results of the analyses were compared with the results of the experimental tests. For the validation, only the results of the LVDT measurement could be used since the displacement measurement of the load cell did also encounter slip deformation. This last kind of deformation will not be present in the numerical model. In the numerical model the displacements were measured at the same locations as measured in the experiments corresponding to a total gauge length of 260 mm. The first step in the modeling process was to investigate the influence of the mesh sizes. In total, four different mesh configurations for the member plate were analyzed, varying with a minimum mesh size from 0.5 mm up to 2.0 mm. The analyzed mesh configurations for the member plate are shown in

Figure 5.50. Since the fracture energy is dependent on the element size, the fracture energy was adjusted corresponding the Equation 5.1 presented in Section 5.1.4. All the models were implemented with the ε_f-f_x calibrated material models and a HAZ width of 15 mm. The results of the mesh sensitivity study are shown in Figure 5.51.

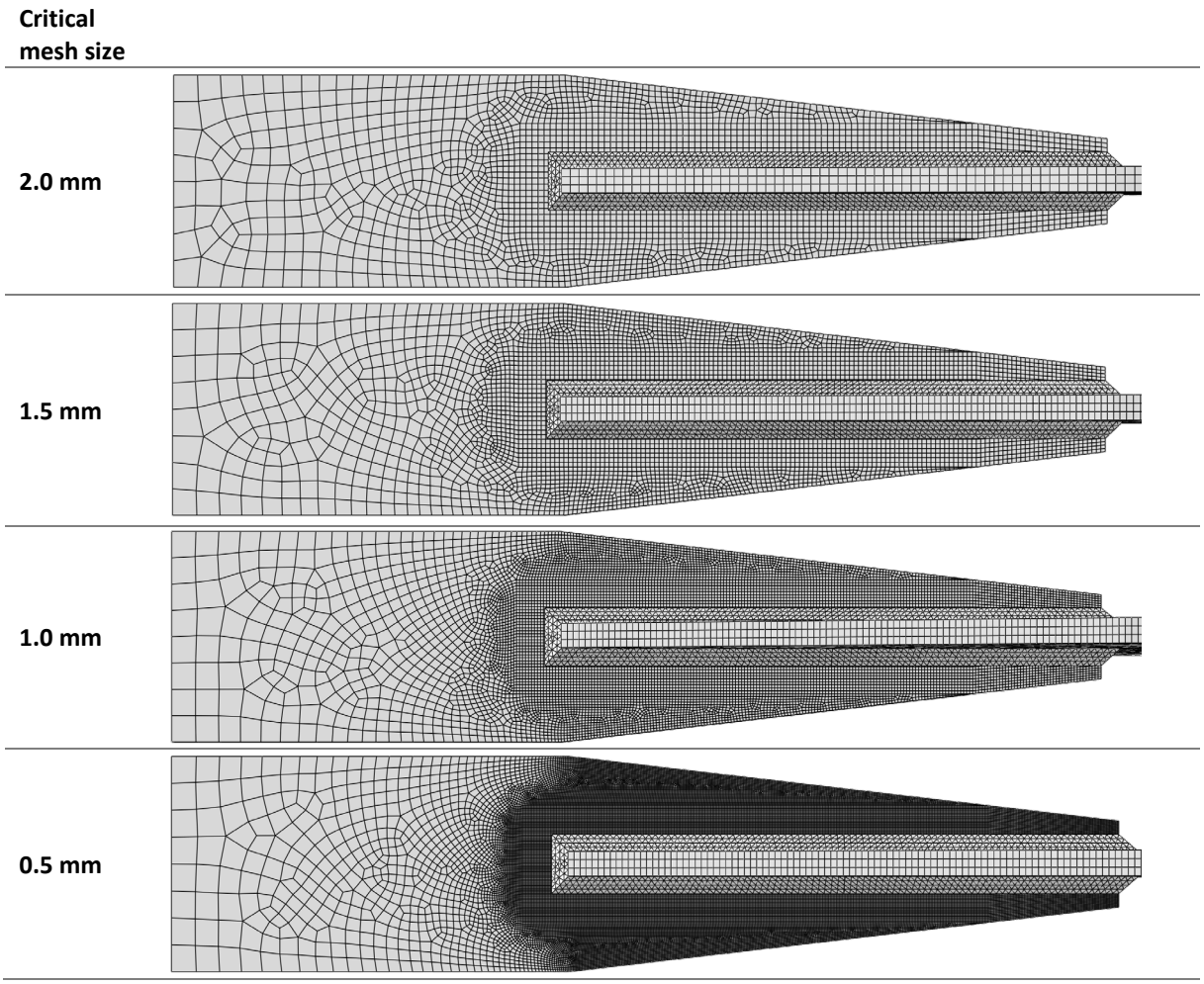

Figure 5.50: Different mesh configurations.

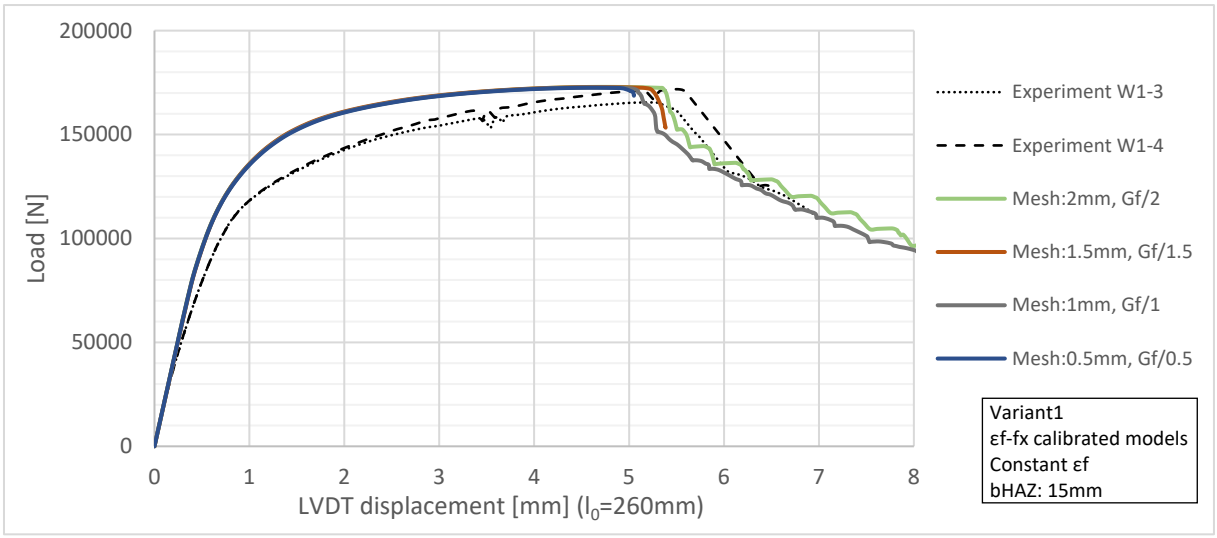

Figure 5.51: Load-displacement graph of the mesh sensitivity study analyses for variant 1.

From the results of the mesh sensitivity study as presented in Figure 5.51, it is observed that the influence of the mesh size is very limited. A smaller mesh size resulted in less deformation up to failure. This despite the fact that the fracture energy was uniformly adjusted. Strain localization, incorrect fracture energy adjustment, or the overall mesh configuration may cause the small deviation. Since no large mesh influence is found and the material and damage model were calibrated based on the dogbone specimens with a mesh size of 1.0mm, this mesh size will be maintained in the critical zones for the up-following models.

As mentioned, the exact dimensions of the HAZ in the case of the welded cruciforms is unknown. Therefore, the HAZ width b_{HAZ} was varied in four different analyses around the value of 15 mm, which was obtained from the transversely welded dogbones. The results of the analyses and the results of two experiments are plotted in Figure 5.52.

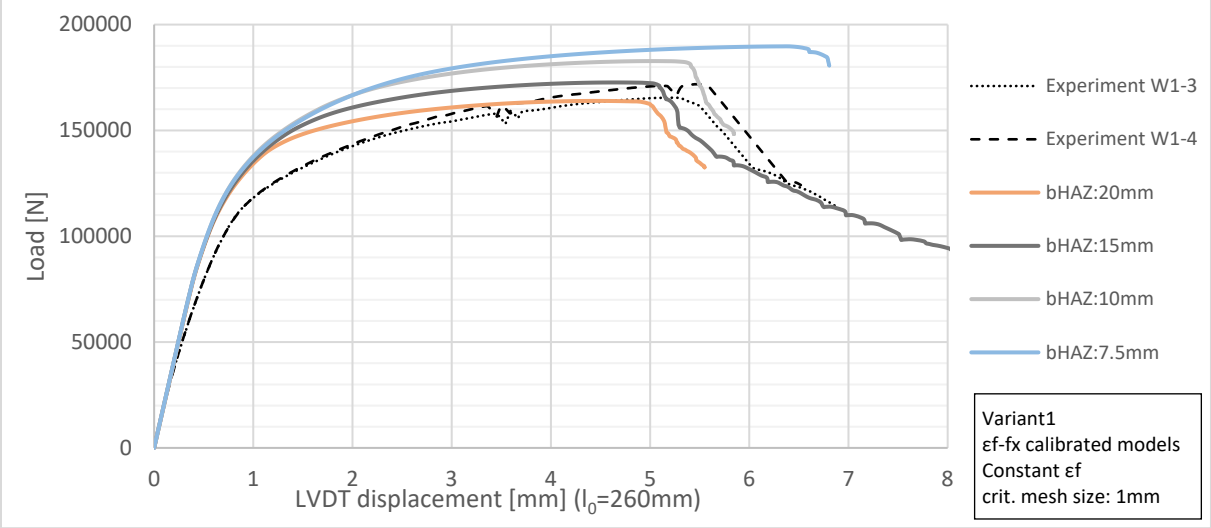

Figure 5.52: Load-displacement graph of the varying HAZ width analyses of variant 1.

First of all, it can be noticed from the results, that both the ultimate resistance and the ultimate displacement were dependent on the HAZ width. This is explained by the fact that a smaller HAZ width will result in more contribution of the base material. By confining the zone, a larger part of the strains concentrate in the base material which contains a higher strength and strain at rupture. Therefore, it appeared that applying more ductile material by means of a HAZ will not directly result in an enhanced structural ductility.

Secondly, it was observed that a rather good approach of the experimental curves was reached for the analyses containing a HAZ width of 10 and 15 mm. It seemed that plastic deformation occurred somewhat later in the numerical model. However, the ultimate force and the displacement at failure were well approached. The plastic strain contour plot shown in Figure 5.53, indicates that strain concentrations localized around the toe of the finger plate and that damage started at this location. These findings correspond to the findings of the experiments where cracking started around the toe of the finger plate, as shown in Figure 5.54. Eventually, failure occurred around this location, which was also experienced in the experiments. A schematization of the failed specimen in the FEM model and a picture of the failed experimental specimen are shown in Figure 5.55 and Figure 5.56, respectively. From these figures, it is concluded that an almost identical behavior is experienced.

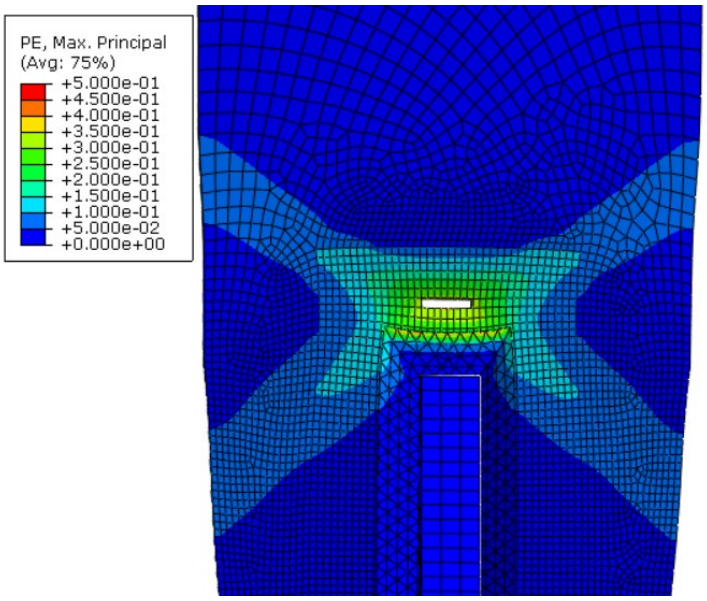

Figure 5.53: Plastic strain contour plot of variant 1 and bhaz=15mm at the beginning of failure (u_{LVDT}=5.28mm).

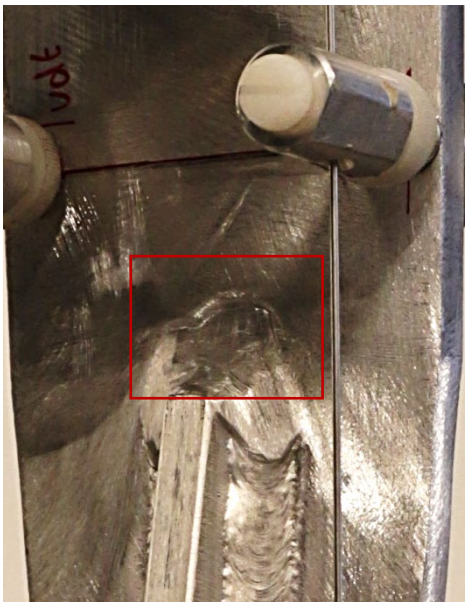

Figure 5.54: Picture of specimen W1-2 at the beginning of failure.

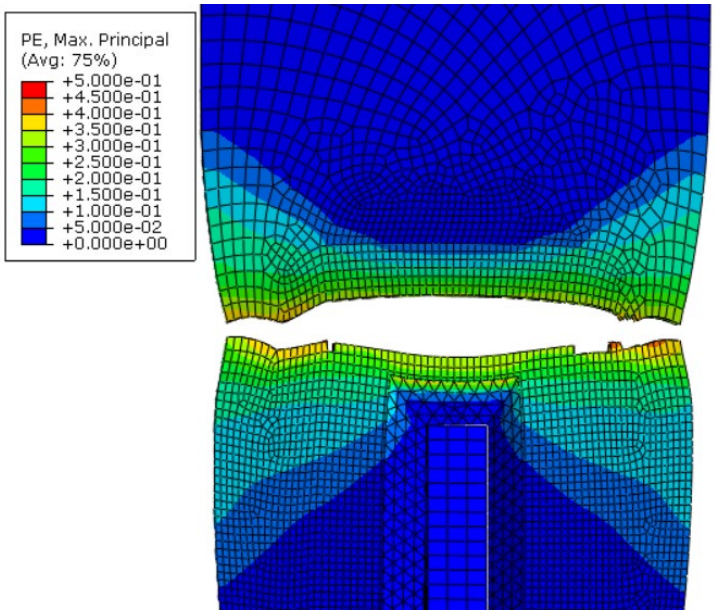

Figure 5.55: Plastic strain contour plot of variant 1 and bhaz=15mm at the moment of complete failure (u_{LVDT}=11.7 mm).

Figure 5.56: Picture of specimen W1-3 at the moment of complete failure.

Since a fracture model was constructed which is based on the stress-triaxialities, also an analysis was performed using this fracture locus. For this analysis a HAZ width of 15 mm was maintained. The results of the analysis with the use of a fracture locus and the analysis with the use of a constant fracture strain are plotted together in Figure 5.57.

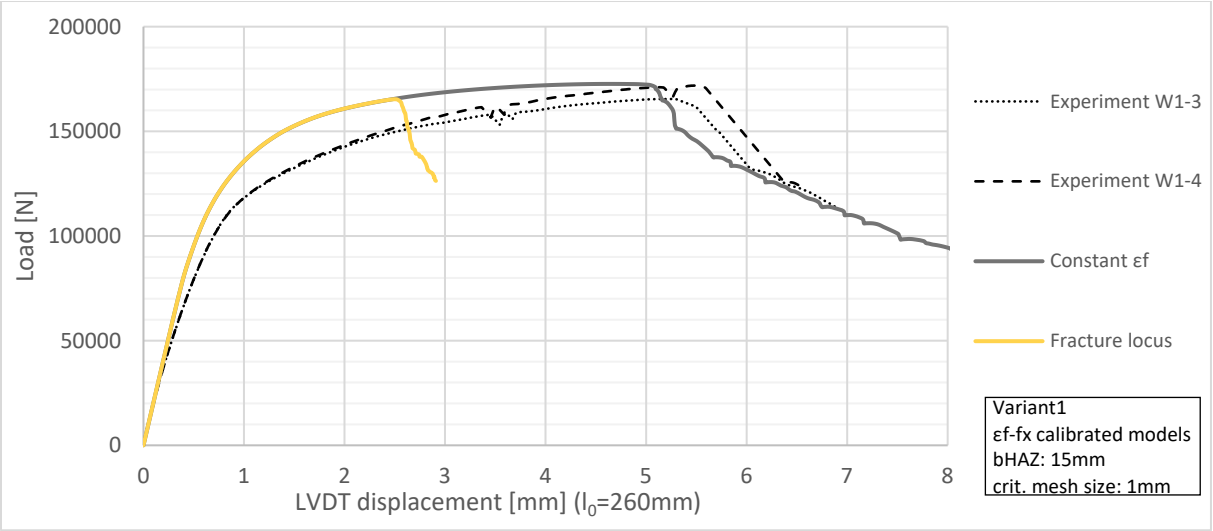

Figure 5.57: Load-displacement graph of the constant and the triaxiality dependent fracture strain analysis of variant 1.

From the results it is obtained that applying a fracture locus will result in early failure of the welded cruciform. The displacement at the moment of damage onset was about 2.6 mm in the fracture locus model and 5.2 mm in the constant fracture strain model. This premature failure proves that the fracture locus model has not yet been properly calibrated. This fracture locus model was calibrated based on stress triaxialities of about 0.33 as experienced in the dogbone models. However, from the stress triaxiality contour plot shown in Figure 5.58 it is observed that different values for the stress triaxiality were experienced for the welded cruciform. The elements in the critical zone experienced stress triaxiality values in the range 0.40 to 0.55 compared to a value of 0.33 as experienced in the dogbone calibration models.

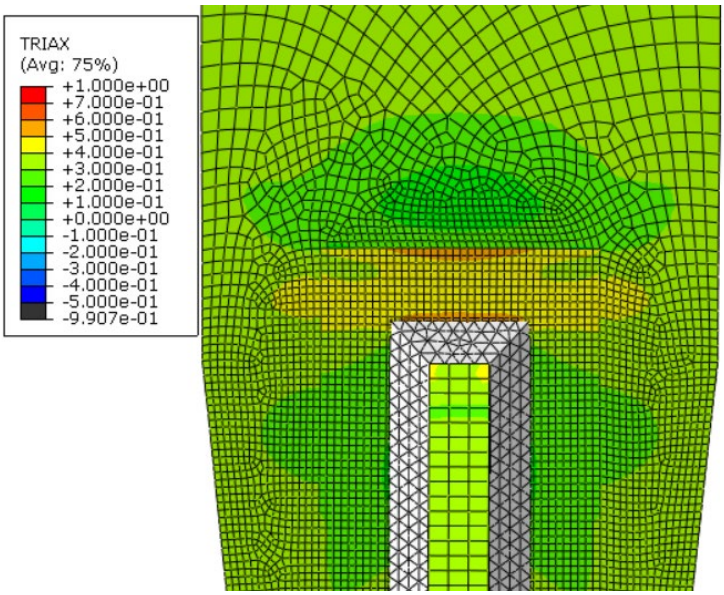

Figure 5.58: Stress triaxiality contour plot of variant 1 specimen at the moment before damage initiation (u_{LVDT}=2.4mm).

5.3.3. Cruciform with failure in fully heat-affected cross-section

Next to the first variant also the cruciform with failure occurring in the fully heat-affected cross-section was modeled and analyzed. For this variant also failure will occur in the member plate. Since the cross-section is smaller, as known for variant 1, the ultimate force will be significantly lower.

5.3.3.1. Dimensions and layout

The used dimensions of the model are shown in Figure 5.59. The thickness of both plates was equal to 8 mm. The elements in the member plate had a minimum size of 1.0 mm around the critical points and a maximum of 6 mm around the end of the plate. A total of six elements was applied over the thickness. For the finger plate, which was considered to be uncritical, a minimum size of 2 mm was applied around the welds and a maximum size of 6 mm around the end of the plate. A total of three elements was applied over the thickness. The HAZ width was also, in this case, varied with values of 7.5, 10, 15, and 20 mm. Since it was assumed that due to the limited width of the member, the complete cross-section was fully heat-affected, the HAZ extended only in the longitudinal direction as schematized in Figure 5.59.

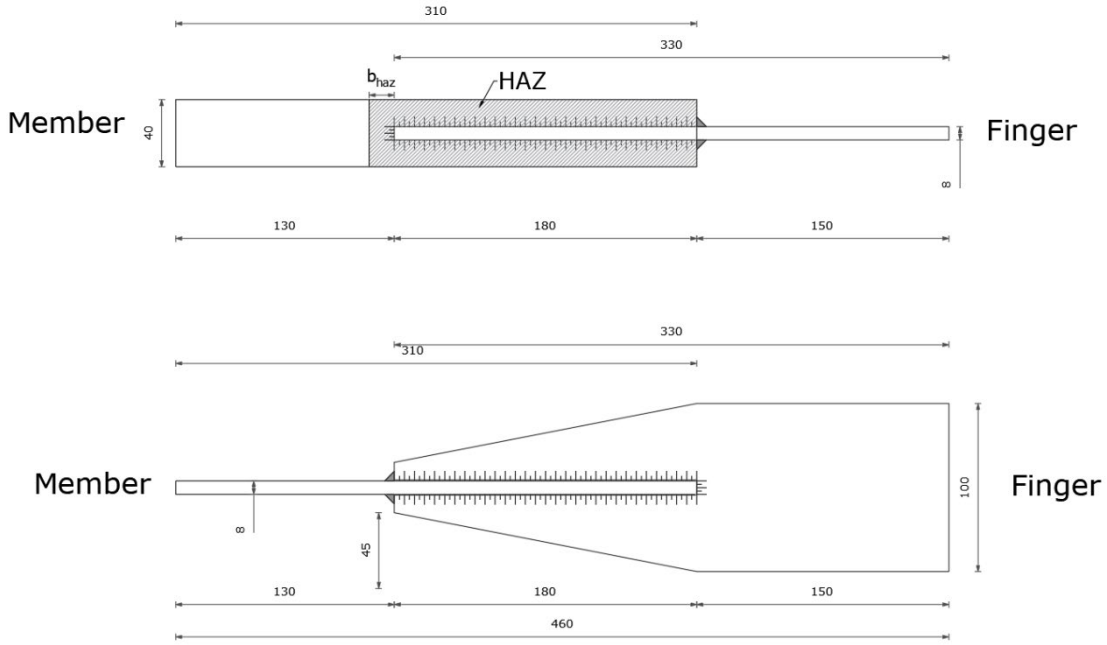

Figure 5.59: Applied dimensions in the numerical model for the welded cruciform variant 2.

5.3.3.2. Results

The results of the analyses with the ε_f-f_x material model and varying HAZ width values are presented in Figure 5.60. In the numerical model the displacements were measured at the same locations as measured in the experiments by the LVDT's, corresponding to a total gauge length of 260 mm.

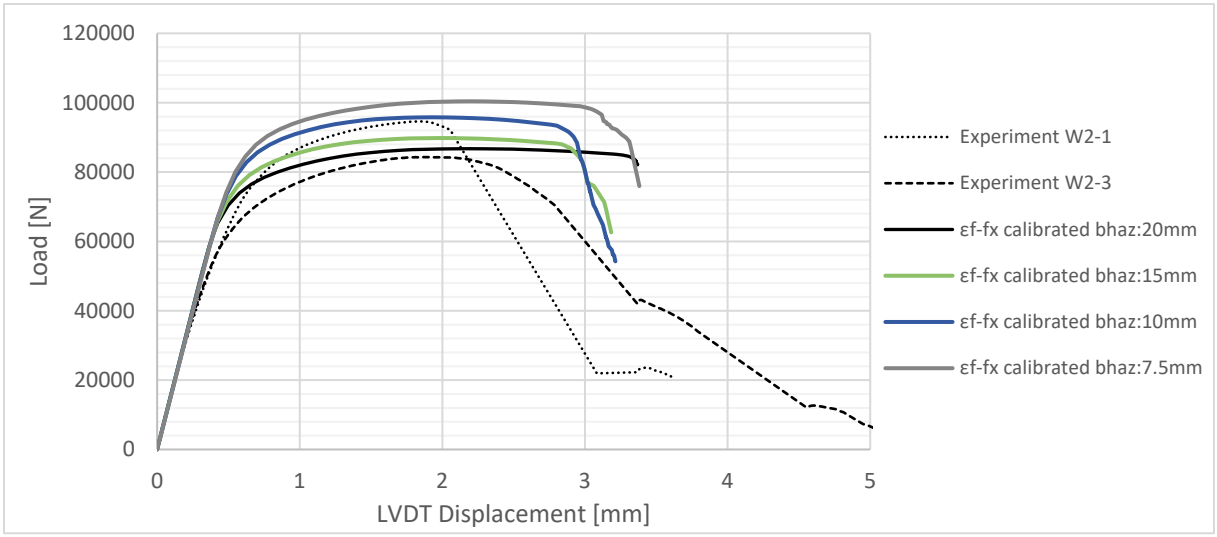

Figure 5.60: Results of the welded cruciform variant 2 analyses.

From the results it is noticed that the ultimate strength of the experiments was well approached. However, the displacement at failure was somewhat overestimated for all the different used HAZ width values. It is remarkably that a smaller extension of the HAZ in longitudinal direction led to an increase in strength. This despite the fact that the critical cross-section remained fully heat-affected. Which indicates that the unaffected region outside the HAZ can contribute to the overall resistance. In Figure 5.61 and Figure 5.62, contour plots of the plastic strains for the b_{haz}=7.5 mm and b_{haz}=20 mm variants are shown. From this it can be noticed that the strain concentrations are present in diagonal shape from the toe of the finger plate to the edges of the member plate. Therefore, in the case of a small HAZ width, a part of the strains are present in the base material. By narrowing the HAZ, more strain concentration will be present in the base material. A shift in the outlined behavior will be present around a HAZ width of 15 to 20 mm. Around this value of the HAZ width, all the strain concentrations are present in the heat-affected material, and contribution of the base material is no longer provided. By increasing the width even further, will increase the ductility performance as it enlarges the limited critical zone.

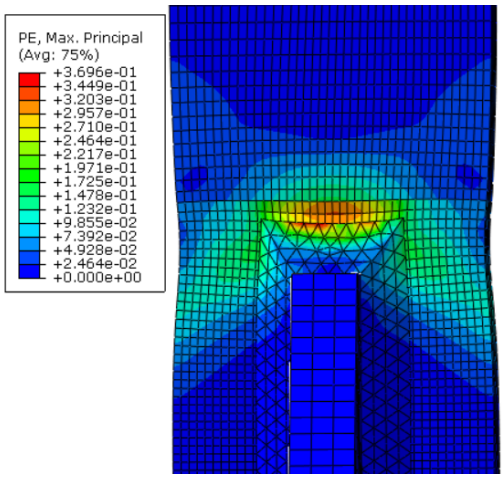

Figure 5.61: Plastic strain contour plot of variant 2 and bHAZ=7.5mm (load step=41).

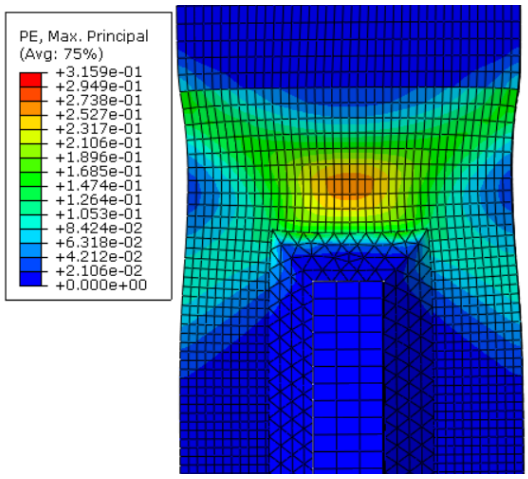

Figure 5.62: Plastic strain contour plot of variant 2 and bHAZ=20mm (load step=41).

Strain concentrations occurred around the toe of the finger plate, similar as shown for variant 1. Figure 5.63 shows that also for variant 2 damage starts at this location. The experimental tests showed that the variant 2 specimens failed just near the weld region at the toe of the finger plate as also shown in Figure 5.64. From these results it is noticed that failure occurred at the same location for both the numerical and experimental tests.

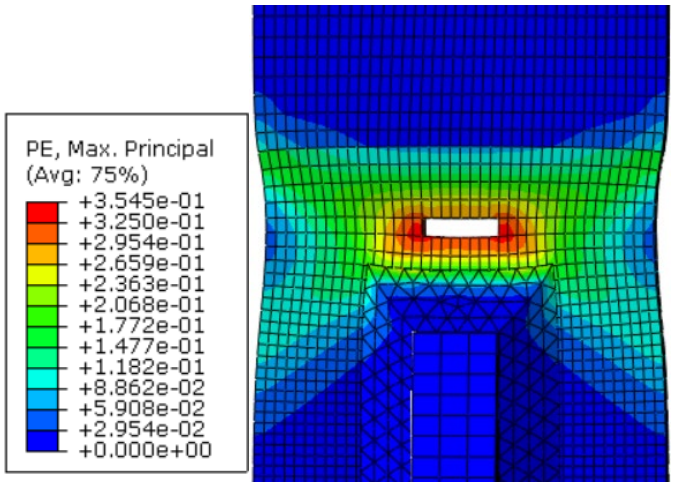

Figure 5.63: Plastic strain contour plot of variant 2 (b_{haz}:15mm) at the moment of failure (u_{LVDT}:3.18mm).

Figure 5.64: Picture of the failed W2-2 specimen.

5.3.4. Cruciform with failure in cold worked finger plate

For the third variant, failure will occur in the finger plate, which consists of aluminum alloy 5083H111. Since no heat-treatments are applied for this type of alloy it is not affected by heat of welding, and hence no HAZ is present.

5.3.4.1. Dimensions and layout

Also, for this variant an analysis was performed using the ε_f-f_x calibrated material models. The HAZ in the member plate was constructed with a width of 15 mm. The used dimensions of the model are shown in Figure 5.65. The thickness of both plates was equal to 8 mm. The elements in the finger plate had a minimum size of 1.0 mm around the critical points and a maximum of 6 mm around the end of the plate. A total of eight elements was applied over the thickness. For the member plate, which was considered to be uncritical, a minimum dimension of 2 mm was applied around the welds and a maximum dimension of 6 mm around the end of the plate. A total of three elements was applied over the thickness.

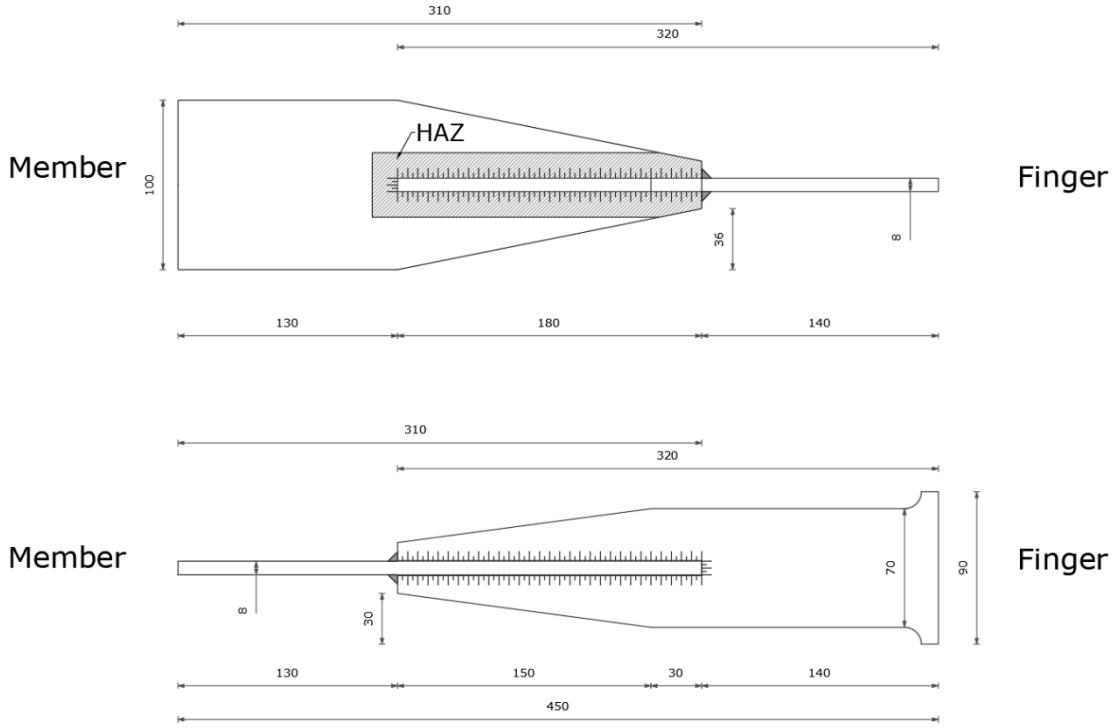

Figure 5.65: Applied dimensions in the numerical model of the welded cruciform variant 3.

5.3.4.2. Results

The result of this first analysis of variant 3 is presented in Figure 5.66. From the results it is noticed that both strength and deformation were overestimated. An deviation in predicting the restiance of about 20% was found. For the deformations this was even 70%.From this it is concluded that this numerical model could not be validated based on the experimental results.

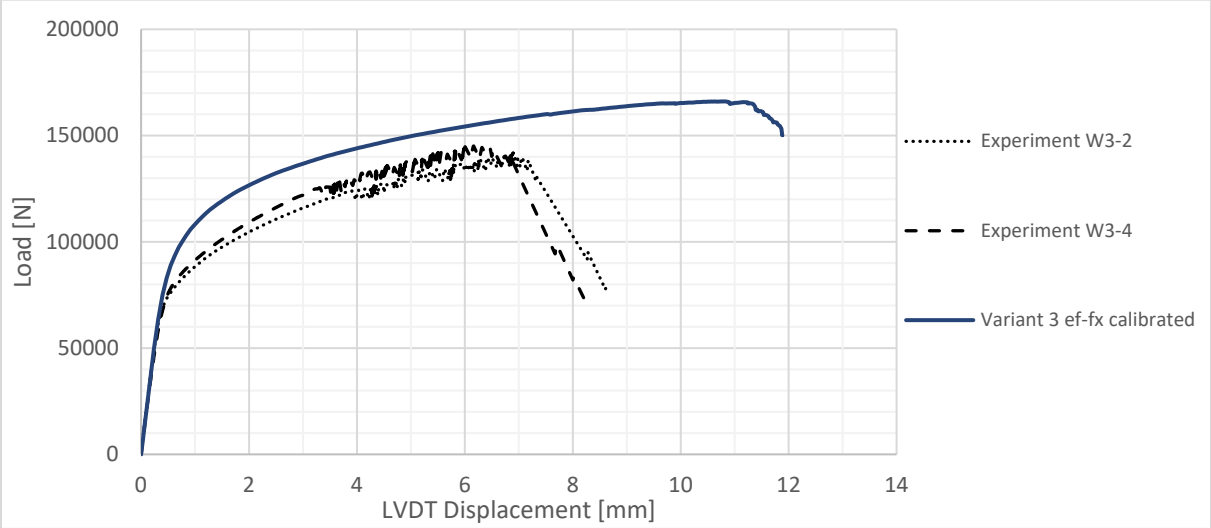

Figure 5.66: Load-displacement graph of the variant 3 analysis result.

5.3.5. Cruciform with failure in cold worked narrowed finger plate

For the fourth and final variant, failure will also occur in the finger plate, which consists of aluminum alloy 5083H111. However, in this case the sloped edges are extended, resulting in a narrowed critical cross-section.

5.3.5.1. Dimensions and layout

The analysis was performed using the ε_f-f_x calibrated material models. The HAZ in the member plate was constructed with a width of 15 mm. The used dimensions of the model are shown in Figure 5.67. The thickness of both plates was equal to 8 mm. The elements in the finger plate had a minimum size of 1.0 mm around the critical points and a maximum of 6 mm around the end of the plate. A total of eight elements was applied over the thickness. For the member plate, which was considered to be uncritical, a minimum dimension of 2 mm was applied around the welds and a maximum dimension of 6 mm around the end of the plate. A total of three elements was applied over the thickness.

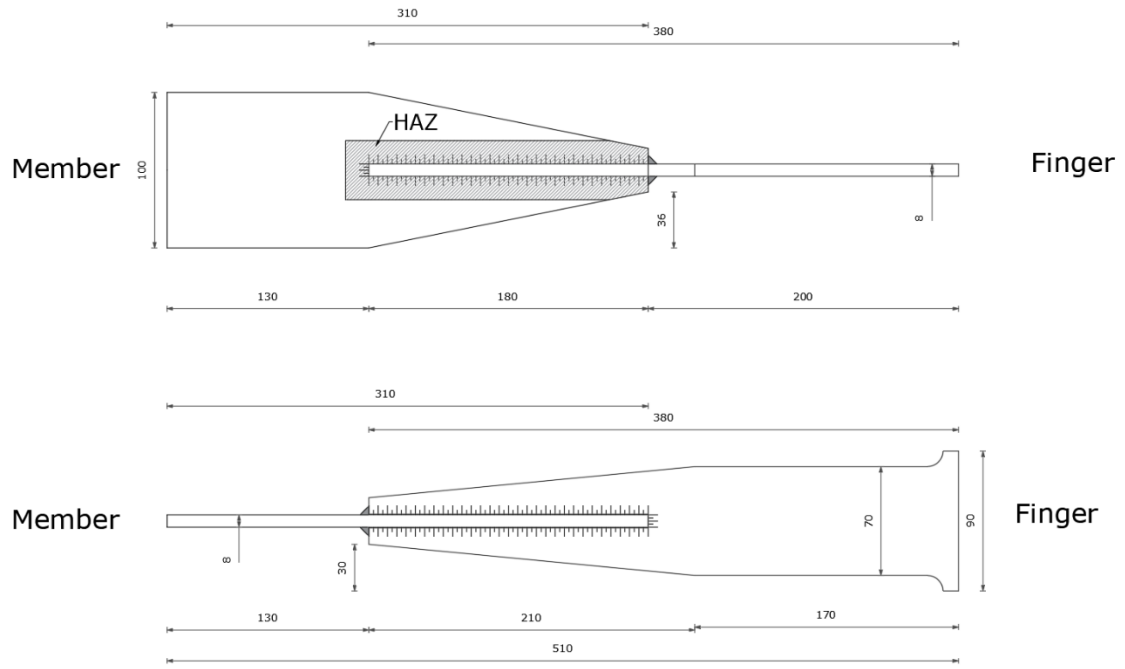

Figure 5.67: Applied dimensions in the numerical model of the welded cruciform variant 4.

5.3.5.2. Results

The result of the analysis of variant 4 is presented in Figure 5.68. From the plotted graph it is noticed that also for this variant not a good performing numerical model was obtained. Both the maximal load and the deformation at failure were overestimated, similar as shown for variant 3.A deviation in predicting of 20% is noticed for the total resistance and even 75% for the deformations. Based on these results it is concluded that a good foundation for a numerical model regarding failure in the AA5083H111 finger plate is not present yet. It is unclear if this problem arises due to a wrong calibrated material model or by the presence of a slot in the finger plate, which influences the failure behavior in the experiments.

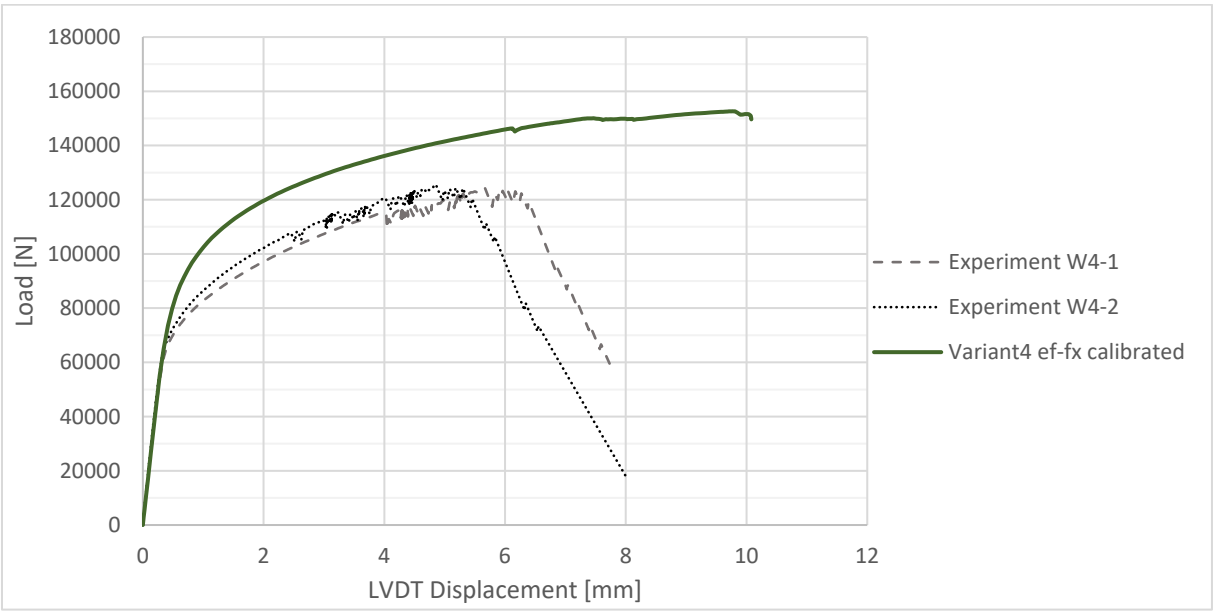

Figure 5.68: Results of the variant 4 analyses.

5.4. Conclusions from numerical modeling

From the numerical models of the welded cruciforms, it is observed that good first approximations of the resistance and deformations for variant 1 and 2 were obtained. In these variants, failure occurred in the heat-treated aluminum alloy 6082T6. The ultimate force, displacement at failure, and the location of failure were accurately matched. The best matches were obtained with a simplified HAZ model with an extent of about 15 mm. It is noticed that an accurate prediction was found with a simplified damage model using a constant value for the fracture strain. However, when a more detailed model was implemented, by using the fracture locus, a good approach was not obtained. This by the fact the fracture locus was not calibrated correctly since exact fracture properties were not yet determined.

The accurate approximation of failure in the heat-treated AA6082T6 plate was also shown for the numerical model of the plate containing two bolt holes. Using a constant fracture strain, an accurate prediction of both the ressitance and deformation up to failure was obtained. Also for this model the fractor locus model turned out not to perform well.

For failure in the cold worked AA5083H111 plate, which was unaffected by the heat of welding, a good approach was not reached yet. In this model, both the maximal failure load and the deformation up to failure were overestimated with about 20% and 70%, respectively. That for these variants the reality was not accurately approached can be caused by several aspects.

One of the possible reasons could be blamed on the welding conditions since, in these variants, the welds are more critical while failure occurs in the weld zone due to the presence of the slot. Another cause can be explained by a minimal influence of the heat input by welding. A minimal influence was also shown in the hardness experiments, but it was stated that this was negligible. Therefore, this was not considered in the numerical model. Finally, it could also be caused due to a poorly calibrated fracture locus model. It was already proved for the heat-treaded alloys that this model was not correctly calibrated for the wide variety of stress triaxialities. Since several uncertainties exist about this cold worked finger plate failure model, further research for modeling this type of alloy is needed.

6. Conclusions

This thesis presented a literature review and experimental research in the field of ductility of aluminum alloy structures. Additionally, a foundation for a numerical model was provided. Based on the findings of the different sections in this thesis, some conclusions can be drawn.

Firstly, it is concluded that transversely welded connections in the tensile zone of members must be avoided where possible for heat-treated aluminum alloys. This is concluded by the fact that transverse welds will result in a fully heat-affected critical cross-section, which is detrimental to the deformation capacity. From the literature review, it is found that some studies already indicated the lack of deformation capacity for these transversely welded connections in combination with heat-treated alloys. Several studies stated that transverse welds could better be avoided in the tensile zone of the member. The results obtained from the transversely welded dogbone experiments confirm these statements.

Secondly, in the case of longitudinal welds, it is concluded that larger deformation capacity values were experienced. The longitudinally welded connection with a partly heat-affected cross-section and the connections with failure in the cold worked AA5083H111 finger plate showed about three to five times as much deformation capacity as the transversely welded dogbone. However, in the case of the longitudinally welded cruciform, which contained a fully heat-affected cross-section, low deformation capacity values were found in the range of the transversely welded dogbone. It is therefore concluded that fully heat-affected cross-sections must be avoided where possible.

Thirdly, based on the experiments on bolted connections, it is concluded that net cross-section failure results in low deformation capacity. In the case of bearing failure, a significant increase in deformation capacity was found compared to the net cross-section failure variant. Comparing the experimental results of the bolted connections to the welded connections shows that the deformation capacity of about 4.0 in the case of a fully heat-affected cross-section connection, was in the same range of the 'badly engineered' bolted connection with a value of about 4.2. For the other longitudinally welded connections, higher deformation capacity values were experienced in the range of 8.4 up to 13.3. These values were in the range of the values as experienced for the bearing failure variant. However, the longitudinally welded connections did not achieve a high deformation capacity value of 18.0, as shown for this bolted variant.

Fourthly, it is observed that an increased material ductility by a higher $f_u/f_{0.2}$ ratio did not directly lead to an increased structural ductility. It is experienced that the extent of the zone of changed material properties has a more significant impact on ductility performance than the material properties themselves. It is also shown for bolted joints suffering from bearing failure, that a low $f_u/f_{0.2}$ ratio close to 1.0, did not lead to early failure by a possible inability of stress concentration redistribution.

Lastly, it is concluded that a reasonable approach of both the resistance and deformation capacity was obtained with the numerical models considering failure in the heat-affected member plate. Furthermore, the numerical model of the plate containing two bolt holes showed an accurate prediction of both the resistance and deformation capacity as experienced in the experiments. However, the numerical models of the longitudinally welded cruciforms with failure in the cold worked finger plate, which was unaffected by welding, performed not as expected. These models showed results with a significant deviation from the actual experimental results for both the resistance and deformation capacity. Additionally, the application of the fracture locus did not produce the intended results for both the bolted and welded variants. It is subsequently concluded that this model was not calibrated correctly for this application.

7. Recommendations

This thesis shows that welded connections that contain a heat-affected zone over the full critical cross-section result in limited deformation capacity. This limited capacity indicates that it is better to avoid connections with a HAZ present over the full cross-section where possible. Besides the designing and engineering recommendations to obtain more structural ductility, some recommendations regarding further research are drawn.

Firstly, it is recommended to study a reliable measuring method for the deformation capacity and the required ductility limits. Since currently the ductility is assessed by a self-defined deformation capacity measure and is compared with a 'badly engineered' bolted connection, no solid and grounded guidelines can be drawn. Therefore, further research into the required ductility limits and a reliable measuring method is required.

Secondly, further research in defining the transition from fully heat-affected cross-sections to partly heat-affected cross-sections is recommended to perform. This in order to quantify fully heat-affected cross-sections since it is advised to avoid connections with a HAZ present over the full cross-section. By further research, the transition from fully heat-affected to partly heat-affected can be defined by means of a ratio of member width to HAZ width. It is found that the limit member width prescribed by the standard EN-1999-1-1 of three times the prescribed HAZ width, strongly differs from the limit experienced in practice. Although this guideline ensures a safe estimation of the resistance, it is not adequate regarding the ductility. Therefore, further research on this topic seems to be of added value.

Finally, it is recommended to research the application of the fracture locus more in-depth. Additionally, specific experiments may be required to calibrate the fracture model. The current research already provides a solid foundation of the numerical models in order to easily and quickly investigate the performance of several connection types. However, more research is needed regarding the exact failure behavior.

References

[1] Soetens, F., Maljaars, J., Van Hove, B., & Pawiroredjo, F. (n.d.). *Lecture handbook Aluminum structural design*. Eindhoven, Netherlands: Eindhoven University of Technology.

[2] CEN, Eurocode 3; NEN-EN-1993-1-1; *Design of steel structures*, Brussel, 2011.

[3] CEN, Eurocode 9; NEN-EN-1999-1-1; *Design of aluminium structures*, Brussel, 2011.

[4] Mae, H., Teng, X., Bai, Y., & Wierzbicki, T. (2008). Comparison of ductile fracture properties of aluminum castings: Sand mold vs. metal mold. *International Journal of Solids and Structures*, *45*(5), 1430–1444. https://doi.org/10.1016/j.ijsolstr.2007.10.016

[5] Mechanical Properties of Materials. (n.d.). Retrieved November 7, 2018, from https://mechanicalc.com/reference/mechanical-properties-of-materials

[6] Mazzolani, F. (2003). *Aluminium Structural Design*. Udine, Italy: SpringerWienNewYork.

[7] Mathers, G. (2002). *The Welding of Aluminium and Its Alloys*. Abington, England: Woodhead Publishing Ltd.

[8] Kissell, J. R., & Ferry, R. L. (2002). *Aluminum structures: a guide to their specifications and design* (2nd ed.). New York, USA: J. Wiley.

[9] De Jongh, S. (2016). *The resistance of welded X-joints of rectangular hollow sections in aluminum.* Retrieved from https://research.tue.nl/en/studentTheses/the-resistance-of-welded-x-joints-of-rectangular-hollow-sections-

[10] Farajkhah, V., & Liu, Y. (2016). Effect of metal inert gas welding on the behaviour and strength of aluminum stiffened plates. *Marine Structures*, 50, 95–110. https://doi.org/10.1016/j.marstruc.2016.07.005

[11] De Matteis, G., Landolfo, R., Manganiello, M., & Mazzolani, F. (2004). Inelastic behaviour of I-shaped aluminium beams: numerical analysis and cross-sectional classification. *Computers & Structures*, *82*(23-26), 2157–2171. https://doi.org/10.1016/j.compstruc.2004.03.071

[12] Castaldo, P., Nastri, E., & Piluso, V. (2016). Evaluation of Rotation Capacity of RHS Aluminium Alloy Beams by FEM Simulation: Temper T6. *Key Engineering Materials*, *710*, 281–287. https://doi.org/10.4028/www.scientific.net/kem.710.281

[13] Castaldo, P., Nastri, E., & Piluso, V. (2017). FEM simulations and rotation capacity evaluation for RHS temper T4 aluminium alloy beams. *Composites Part B: Engineering*, *115*, 124–137. https://doi.org/10.1016/j.compositesb.2016.10.026

[14] Mazzolani, F., & Piluso, V. (1997). Prediction of the Rotation Capacity of Aluminium Alloy Beams. *Thin-Walled Structures*, *27*(1), 103–116. https://doi.org/10.1016/0263-8231(96)00014-6

[15] Moen, L. A., Hopperstad, O. S., & Langseth, M. (1999). Rotational capacity of aluminum beams under moment gradient. I: Experiments. *Journal of structural engineering*, *125*(8), 910-920.

[16] Moen, L. A., Matteis, G. D., Hopperstad, O. S., Langseth, M., Landolfo, R., & Mazzolani, F. M. (1999). Rotational capacity of aluminum beams under moment gradient. II: Numerical simulations. *Journal of structural engineering*, *125*(8), 921-929.

[17] Su, M., Young, B., & Gardner, L. (2014). Deformation-based design of aluminium alloy beams. *Engineering Structures*, *80*, 339–349. https://doi.org/10.1016/j.engstruct.2014.08.034

[18] Piluso, V., Pisapia, A., Nastri, E., & Montuori, R. (2019). Ultimate resistance and rotation capacity of low yielding high hardening aluminium alloy beams under non-uniform bending. *Thin-Walled Structures*, *135*, 123–136. https://doi.org/10.1016/j.tws.2018.11.006

[19] Matteis, G. D., Moen, L. A., Langseth, M., Landolfo, R., Hopperstad, O. S., & Mazzolani, F. M. (2001). Cross-sectional classification for aluminum beams—Parametric study. *Journal of structural engineering*, *127*(3), 271-279.

[20] Steenbergen, H. M. G. M., Bijlaard, F. S. K., & Daniels, B. J. (1996). The influence of material properties on plastic hinge rotational capacity and strength.

[21] Manganiello, M., De Matteis, G., & Landolfo, R. (2006). Inelastic flexural strength of aluminium alloys structures. *Engineering Structures*, *28*(4), 593–608. https://doi.org/10.1016/j.engstruct.2005.09.014

[22] Manevich, A. (2007). Effect of strain hardening on the buckling of structural members and design codes recommendations. *Thin-Walled Structures*, *45*(10-11), 810–815. https://doi.org/10.1016/j.tws.2007.08.026

[23] Van Es, S., Slot, H., Steenbergen, H., Maljaars, J., & Pijpers, R. (2018). Use of HSS and VHSS in steel structures in civil and offshore engineering. *Steel Construction*, *11*(4), 249–256. https://doi.org/10.1002/stco.201800018

[24] Matusiak, M., & Larsen, P. K. (1999). An Experimental Study of Strength and Ductility of Welded Aluminium Beams. *Light-Weight Steel and Aluminium Structures*, 449–456.

[25] Wang, T. (2006). *Modelling of Welded Thin-Walled Aluminium Structures* (Doctoral thesis for the degree of philosophiae doctor). Retrieved from https://brage.bibsys.no/xmlui/bitstream/handle/11250/236374/122367_FULLTEXT01.pdf?sequence=1

[26] Faella, C., Mazzolani, F. M., Piluso, V., & Rizzano, G. (2000). Local buckling of aluminum members: testing and classification. *Journal of Structural Engineering*, *126*(3), 353-360.

[27] Arnold, B., & Altenhof, W. (2004). Experimental observations on the crush characteristics of AA6061 T4 and T6 structural square tubes with and without circular discontinuities. *International Journal of Crashworthiness*, *9*(1), 73–87. https://doi.org/10.1533/ijcr.2004.0273

[28] Hsu, S. S., & Jones, N. (2004). Dynamic axial crushing of aluminium alloy 6063-T6 circular tubes. *Latin American Journal of Solids and Structures*, *1*(3), 277-296.

[29] Simar, A., Bréchet, Y., De Meester, B., Denquin, A., & Pardoen, T. (2007). Sequential modeling of local precipitation, strength and strain hardening in friction stir welds of an aluminum alloy 6005A-T6. *Acta Materialia*, *55*(18), 6133–6143. https://doi.org/10.1016/j.actamat.2007.07.012

[30] Çam, G., & Koçak, M. (2007). Microstructural and mechanical characterization of electron beam welded Al-alloy 7020. *Journal of Materials Science*, *42*(17), 7154–7161. https://doi.org/10.1007/s10853-007-1604-z

[31] Dekker, R. W. A., Snijder, H. H., & Maljaars, J. (2016). Numerical investigation into strong axis bending-shear interaction in rolled I-shaped steel sections. In *2016 International Colloquium on Stability and Ductility of Steel Structures (SDSS 2016), May 30–June 1, 2016, Timisoara, Romania*. Wiley Ernst&Sohn.

[32] Farajkhah, V., & Liu, Y. (2016b). Effect of metal inert gas welding on the behaviour and strength of aluminum stiffened plates. *Marine Structures*, *50*, 95–110. https://doi.org/10.1016/j.marstruc.2016.07.005

[33] Li, J., Zhang, Q., & Ding, J. (2006). Experiments on Properties of Aluminium Welding Joints. *Structural Engineering International*, *16*(4), 331–338. https://doi.org/10.2749/101686606778995209

[34] Hval, M., Thaulow, C., Lange, J. H., Hoydal, S. H., & Zhang, Z. L. (1998). Numerical modeling of ductile fracture behavior in aluminum weldments. *WELDING JOURNAL-NEW YORK-*, *77*, 208.

[35] Zheng, L., Petry, D., Rapp, H., & Wierzbicki, T. (2009). Characterization of material and fracture of AA6061 butt weld. *Thin-Walled Structures*, *47*(4), 431–441. https://doi.org/10.1016/j.tws.2008.08.008

[36] Sato, Y. S., Kokawa, H., Enomoto, M., & Jogan, S. (1999). Microstructural evolution of 6063 aluminum during friction-stir welding. *Metallurgical and Materials Transactions A*, *30*(9), 2429–2437. https://doi.org/10.1007/s11661-999-0251-1

[37] Missori, S., & Sili, A. (2000). Mechanical behaviour of 6082-T6 aluminium alloy welds. *Metallurgical science and technology*, *18*(1), 12-18.

[38] Lakshminarayanan, A. K., Balasubramanian, V., & Elangovan, K. (2009). Effect of welding processes on tensile properties of AA6061 aluminium alloy joints. *The International Journal of Advanced Manufacturing Technology*, *40*(3-4), 286–296. https://doi.org/10.1007/s00170-007-1325-0

[39] Woelke, P., Hiriyur, B., Nahshon, K., & Hutchinson, J. (2017). A practical approach to modeling aluminum weld fracture for structural applications. *Engineering Fracture Mechanics*, *175*, 72–85. https://doi.org/10.1016/j.engfracmech.2017.02.010

[40] ABAQUS inc.. (2005). Abaqus advanced topics, Lecture 9, Material Damage and Failure [Slides]. Retrieved April 2, 2019, from http://imechanica.org/files/l9-damage-failure.pdf

[41] DS Simulia. (n.d.). Abaqus Analysis User's Manual (6.10). Retrieved May 6, 2019, from https://www.sharcnet.ca/Software/Abaqus610/Documentation/docs/v6.10/books/usb/default.htm

[42] Wierzbicki, T., Bao, Y., Lee, Y., & Bai, Y. (2005). Calibration and evaluation of seven fracture models. *International Journal of Mechanical Sciences*, *47*(4-5), 719–743. https://doi.org/10.1016/j.ijmecsci.2005.03.003

[43] Manders, W. (2018). *Punching Shear Failure on welded Rectangular Hollow Section Joints in Aluminum*. Retrieved from https://research.tue.nl/en/studentTheses/punching-shear-failure-on-welded-rectangular-hollow-section-joint

[44] Chan, T. K., & Porter Goff, R. F. D. (2000). Welded aluminum alloy connections: Test results and BS8118. *Thin-Walled Structures*, *36*(4), 265–287. https://doi.org/10.1016/S0263-8231(00)00006-9

[45] Zhang, Z. L., Ødegård, J., Myhr, O. R., & Fjær, H. (2001). From microstructure to deformation and fracture behaviour of aluminium welded joints - A holistic modelling approach. *Computational Materials Science*, *21*(3), 429–435. https://doi.org/10.1016/S0927-0256(01)00181-1

[46] Bao, Y. (2003). *Prediction of ductile crack formation in uncracked bodies*. Cambridge, United States: Massachusetts Institute of Technology.

[47] Glinka, G. (2005). *ME322- Mechanical Design 1, Partial notes – Part 6 (Welded Joints).* Retrieved from https://slideplayer.com/slide/4534565/

[48] Schijve, J. (2009). *Fatigue of Structures and Materials*. New York, United States: Springer Publishing.

[49] Leoni, F., Sandness, L., Grong, Ø., & Berto, F. (2019). Mechanical behavior of gas metal arc AA6082-T6 weldments. *Procedia Structural Integrity*, *18*, 449–456. https://doi.org/10.1016/j.prostr.2019.08.187

[50] Sussman, T. (2017, November 21). Solid and shell elements [Slides]. Retrieved from http://www.ablemax.co.kr/abc/2016/homeupload/app/5_Solidandshellelements.pdf

[51] ISO, ISO-6892-1, *Metallic materials – Tensile Testing – Part 1: Method of test at room temperature,* 2009.

[52] Instron. (n.d.). Vickers Test - Instron. Retrieved September 13, 2019, from https://www.instron.us/our-company/library/test-types/hardness-test/vickers-test